Abstract

Directionality and Vector Resonances of Regular and Chaotic Dielectric Microcavities

Harald Georg Leonhard Schwefel
2004

Dielectric microcavities/ microlasers are a key component for novel opto-electronic devices. We model such devices as a dielectric rod and analyze the vector wave-equation for an infinite dielectric rod with arbitrary cross-section. Analytic results for the resonance condition and polarization properties are given for the cylinder. With the parabolic equation method we derive the resonance condition and the polarization properties for modes related to 2d stable periodic ray orbits. The polarization of hybrid emitting modes of cylindrical resonators is shown to be linear up to a polarization critical angle and elliptical beyond this angle, which always lies between the Brewster and the total-internal-reflection angles of the dielectric. Arbitrary cross-sections in general give rise to non-integrable ray dynamics. We review classical Hamiltonian dynamics and billiards and expand the theory to dielectric billiards. Analysis of periodic ray orbit bifurcations and unstable manifolds enables us to understand the emission directionality of differently deformed polymer microlasers. We report new experiments on the first whispering gallery laser from a resonator with a single reflection symmetry axis, and analyze a number of different Gallium Nitride resonators/ lasers.

Directionality and Vector Resonances of Regular and Chaotic Dielectric Microcavities

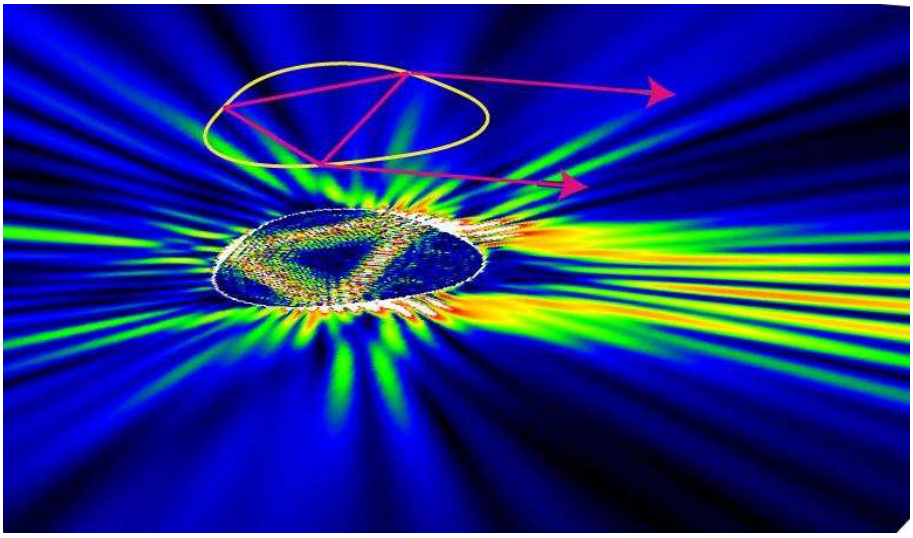

A Dissertation
Presented to the Faculty of the Graduate School
of
Yale University
in Candidacy for the Degree of
Doctor of Philosophy

by
Harald Georg Leonhard Schwefel

Dissertation Director: A. Douglas Stone

December 2004

Contents

[1]This Section is taken in part from Ref. [1]

[2]This chapter is based on work published in Ref. [2]

[3]See our paper in Ref. [3]

Acknowledgments

Various people made my life at Yale so fruitful and pleasant as it was. First of all, I would like to thank my advisor A. Douglas Stone. 'Doktorvater'[4], this German word for advisor sums up what he was and is for me. His enthusiasm, support and guidance combined with his insight and intuition has shaped me both as a physicist and as human.

I especially treasure having had Richard Chang as a mentor. His warmth and expertise, always served as a beacon of light.

My fortune of having a great friend and collaborator always right next to me in my office, Hakan Türeci, can not be rivaled. Working more than five years side by side made work less work and more fun.

I like to thank Bob Grober, whom I first met when he was teaching an optics class I took, for being the experimentalist by heart who makes the life of a theorist hard, but fruitful.

Here, I would also like to thank Yoram Alhassid, for introducing me to non-linear dynamics and Sean Barrett for the encouraging discussions during physics lab.

Special thanks go to Fritz Haake who agreed upon short notice to be my external reader; Vielen Dank!

During my time in Richard Chang's lab, I especially have to thank Grace Chern for her support, music CD's and all the great insights into the experimental setup. None of my experimental work would have been possible without her. I was also fortunate to have many great discussions with Nathan Rex, Yongle Pan and Kevin Aptowicz.

Meetings and discussions with former members of Professor Stone's group were very valuable, here I would like to thank Jens Nöckel, Evgenii Narimanov and Philippe Jacquod, who also introduced me to the taste of Belgium beer.

Visits from Martin Gutzwiller here at Yale were fantastic highlights. Knowing him as a friend and mentor, hearing physics from him, has always been a pleasure.

Chang Sub Kim, while being a visiting Professor here at Yale in 2001, got me immersed into the quantum regime, for which I am thankful.

I had many stimulating discussions with Martina Hentschel during her visit in 2000, which lead to the foundations for the classical ray-dynamics program. I would not want to miss the many fruitful discussions with and visits of and to Jan Wiersig.

[4] 'Doktorvater' = Ph.D. dad

I would not be here if it were not for all the great people at the BTU-Cottbus, where I first have to thank my mathematics professors Friedrich Sauvigny and Sabine Pickenhain who got me started and then my physics professors who pulled me away from math, Ernst Siegmund, Jürgen Reif, Ullrich Wulf and Dieter Schmeisser and finally Thomas Kolb, who taught me how to use LaTeX.

During my time at Yale my ways crossed a number of administrators who went out of their way to help and support. Here I would like to thank our registrar Jo-Ann Bonnett as well as Jayne Miller, Tanis Lea and Pam Patterson, not just for the many friendly reminders when I was again too late, but especially for being there when there was need and taking care of all the bureaucracy.

During my time in the GSA and GPSS I met a number of amazing administrators, with whom I had many discussions not just about Yale, but life in general, first of all Susan Hockfield, Peter Salovey, Richard Sleight and Thomas Burns.

The liveliness of Jakob Ulmschneider, a friend, classmate and comrade on long nights of problem sets and lunches at HGS, without whom something at Yale is missing. I would like to thank Steve, for giving every lunch that personal touch, and bringing me back to the real problems of life.

My life here at Yale would not have been what it was were it not for my roommates from my first two years, Stephen Holt, for keeping me sane my first year and Matthew Green; best American friends and housemates anyone could hope for. From them I learned how to fake (or become?) an American. Go Redskins!

Christine: for her the emotional support when I started writing, I would not have managed without her.

Detlef and Gosia, for their support and encouragement.

And finally my mom, Erika, for giving me all her love and support.

Chapter 1

Introduction

1.1 Overview

Resonators are the basis for music and speech as well as a key component in all lasers. In this thesis we will analyze the resonances of dielectric cavities used in microlasers. These lasers have a size of order 100 microns, roughly the diameter of a human hair. We focus on a type of microresonator of particular theoretical interest, known as an *Asymmetric Resonant Cavity* (ARC) [12, 13, 14, 15, 16]. ARC lasers have been shown to be among the most powerful designs for microlasers, much more powerful than the whispering gallery micro-disk lasers which preceded them, as well as providing for the first time directional emission from a resonator which uses total internal reflection to provide high enough Q-values. Therefore it is hoped that ARC-based optical devices will find application in the opto-electronics industry for telecommunications, information processing or sensing. At least one device related to the ARC, a GaN blue/ UV light source employing a spiral resonator design [17] is being actively developed at Yale and at PARC as an amplifier/ laser.

1.2 Conventional microlasers

The widest and most used macro-optical resonator is of the Fabry-Perot type, Fig. 1.1 A). Two metal coated mirrors opposite from each other at a distance l confine a light field with the reflectivity of one mirror slightly less than that of the other. All standard lasers and amplifiers are based on this resonator, for modern opto-electronic devices it is however important to reduce the size of resonators. Metal coated reflectors are very difficult to produce at micron size scales. One way to get good reflectivity at a micro scale is the *Vertical Cavity Surface Emitting Lasers* VCSEL [18] (See Fig. 1.1 B), which consists of multiple layers of different dielectric material to create a Bragg reflector at each side. The emission of the VCSEL is perpendicular to the plane. VCSELs have already found their commercial market in bar-code scanners and gigabit optical fiber communication systems. If we want to emit in plane, the standard approach is the edge emitter, see Fig. 1.1 C). But as

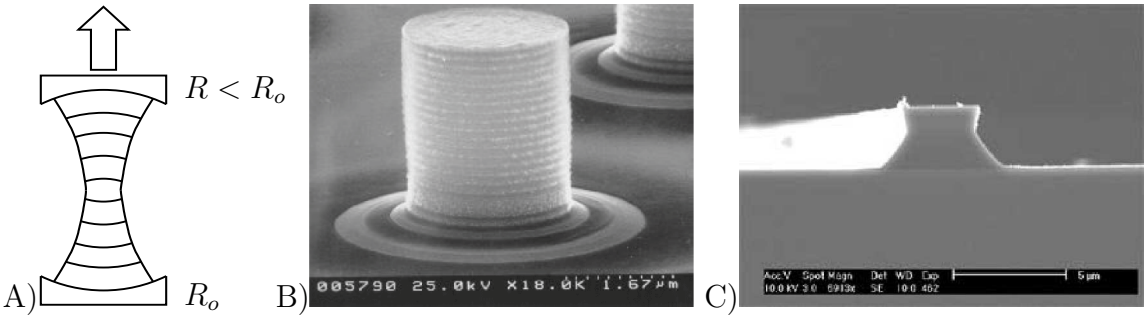

Figure 1.1: A) Schematic of Fabry-Perot resonator. B) Scanning electron micrograph picture of a VCSEL [4]. C) Edge emitting laser from the National Institute of Physics [5].

the dielectric interface at normal incidence is not a good reflector, the resonances are low Q. Thus the gain region has to be relatively long, which excludes the possibility for a true *micro*-resonator. This leads to the concept of the microdisk laser, see

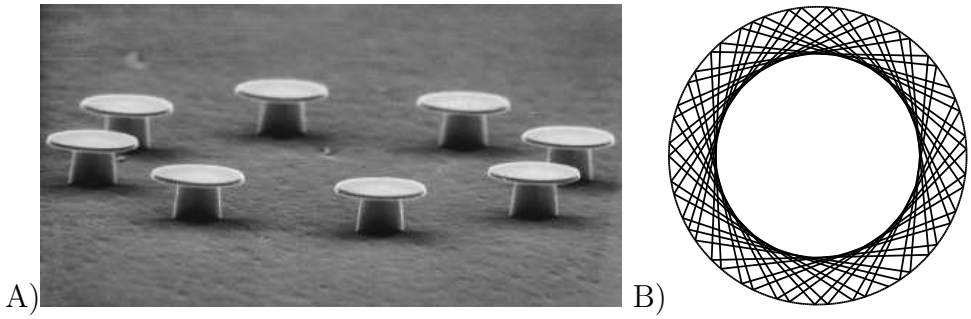

Figure 1.2: A) Edge emitting laser from the National Institute of Physics [5]. B) A field of microdisk lasers by Levi [6]. B) Schematic of whispering Gallery.

Fig. 1.2 A). In a circular dielectric, the angle of incidence χ of a ray is conserved and by employing near *total internal reflection* (TIR) the light can be trapped in a micron scale region. However, studies of the exact solutions for the dielectric disk [11], sphere [19] and for the cylinder (Section 6.3.1) show that TIR is only perfect for an infinite plane interface. This results in evanescent leakage due to curvature effects of the boundary, similar to tunneling in quantum mechanics. Resonators using this effect are the so-called *whispering gallery* type resonators, named after an acoustical analog observed and studied by Lord Rayleigh [20, 21]. Whispering gallery type resonances are strongly localized at the boundary, as are the acoustical waves studied by Lord Rayleigh, that traveled along the smooth stone surface of the St. Paul's Cathedral in London (see Fig. 1.3). A multitude of resonators have been studied that operate on these modes, e.g. droplets [22, 23], disks [24, 25, 26], and rings [27]. Some of them have been shown to have Q-values as high as 10^{10}, although in practical semiconductor lasers the values are much smaller (in the 10^3

range), apparently controlled by surface properties. Their use stretches from the study of cavity QED effects [28] to channel add-drop filters [29]. Due to the inherent symmetry of circle these resonator types do not show any preferred directionality and thus show a strong susceptibility to surface roughness and the environment.

A)  B) 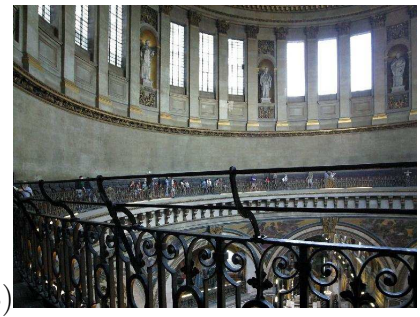

Figure 1.3: A) St. Paul's Cathedral in London on a 1754 painting from Canaletto B) Whispering Gallery in St. Paul's Cathedral in London (curtesy of Richard Seaman [7]).

Different approaches for achieving directionality have been proposed: an *extrinsic* approach by external coupling and an *intrinsic* by breaking the symmetry of the shape. Little in Ref. [29] used the extrinsic approach to create a microring resonator channel dropping filter by placing two waveguides close to the resonator. As the evanescent field decays exponentially the fabrication of these devices is extremely sensitive to the etching techniques as both waveguides need to be placed at exactly the same distance. Levi and coworkers followed the intrinsic approach by breaking the symmetry of the microdisk by adding a bump [30] to the cavity. Instead of adding Chu *et al.* [31] cut a chunk out of the cavity, producing a 'pac-man' like shape. With these methods directionality is achieved but reproduction of the same shape and prediction of the emission properties is difficult.

1.3 Asymmetric Resonant Cavities

The concept of the ARC developed as an extension of the concept of the whispering gallery microdisk lasers. A drawback of the original circular disk-shaped lasers was the isotropic emission from such modes in the absence of additional guiding elements, and this motivated the ARC concept. The key idea was to deform the cavity from circular symmetry in order to induce intrinsically directional emission from the (deformed) WG modes. The deformations were to be smooth so that ray optical concepts could be employed to predict and understand the resulting emission patterns. The particular theoretical interest of these resonators is that the ray dynamics in such a shape is complex and partially chaotic for generic deformations; the effect of shape on ARC laser emission properties is a main theme of this thesis. A number of ARC-based lasers have been fabricated and tested using a variety of gain media, starting with micro-droplets and micro-jets [22, 23], GaAs [32] and GaN

diode lasers [3], InGaAs and GaAs quantum cascade lasers [8], and polymer lasers [2]. The polymer and GaN lasers have been studied using optical pumping here at Yale; a set of measurements on a space-capsule shaped ARC are described in Chapter 8 of this thesis.

1.4 Passive vs. active cavities

A method often used to describe the laser cavity is to consider simply the resonances of a passive dielectric cavity. This will neglects effects like mode pulling and locking as well as mode competition effects, which thus makes the lasing mode difficult to predict in advance. Nonetheless the method is found to be quite adequate for explaining and even predicting the directionality of lasing modes in low-index ARCs, as we shall see below. All of the thesis is devoted to the study of passive cavities and finding their linear resonances, later we will introduce numerical and semiclassical techniques for finding the resonances. One can imagine probing the dielectric cavity in two ways:

1) Scattering experiment: An incoming wave from infinity is scattered off the cavity and collected in the far-field. Varying the frequency of the incoming wave we can probe the resonances. Resonances refer to the frequencies $\omega = ck$ (speed of light c, and the wave-vector $k = 2\pi/\lambda$ in vacuum) at which the light gets confined in the cavity for a long time. The lifetime τ is defined by the inverse of the resonance width. An important experimental quantity is the quality factor Q which relates to the lifetime as $Q = \tau\omega$. A high Q thus denotes a very sharp resonance.

2) Emission experiment: Here we have Sommerfeld boundary conditions with no incoming wave from infinity. This setup is the typical description used for laser resonances and used throughout this thesis. In an emission experiment, the cavity is excited and the emission is recorded in the far-field. A schematic of the setup is shown in Fig. 1.4. Important for a good understanding of the lasing resonance is the possibility in this setup to obtain an image of the emitting boundary. Both the far-field intensity variation and the position on the boundary from which the far-field radiation originated can be obtained. This setup was first introduced by Nathan Rex and was used to explore the GaN and Polymer cavities in diameter ranges of 10μm–50μm discussed in this thesis.[1] The study of the polymer lasers revealed that a theoretical description of such lasers introduced by Nöckel and Stone [14] had to be revised [2]; the results are discussed in Chapter 5. In this thesis, we will use the above described experimental setup to obtain experimental data for a space-capsule shaped GaN cavity. This experiment and the theoretical discussion are presented in Chapter 8.

The resonances of the passive cavity can be found from Maxwell equations with an index profile independent of the field strength. For the case of a uniform dielectric, assuming harmonic behavior of the fields these equations reduce to Helmholtz

[1]The emission for the GaN is at a wavelength of 404nm in the ultraviolet, pumped at 355nm and for the polymer at 612nm visible orange-red light, pumped with 532mn (green light).

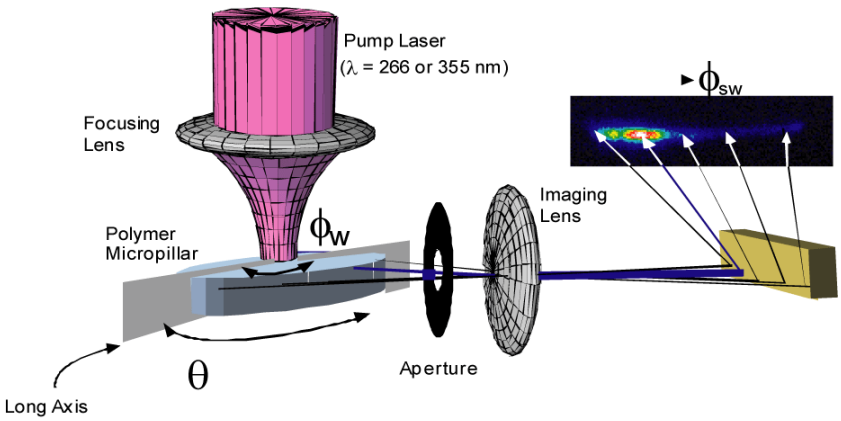

Figure 1.4: Standard experimental setup. The cavity gets pumped with a pump-beam. Emission is collected through an imaging lens onto a CCD camera for different far-field angles θ. Details are given in Chapter 8

equation

$$\left(\nabla^2 + \gamma^2\right) \begin{Bmatrix} \boldsymbol{E}(\boldsymbol{r}) \\ \boldsymbol{B}(\boldsymbol{r}) \end{Bmatrix} = 0, \quad \text{with} \quad \gamma^2 = n^2(\boldsymbol{r})k^2 - k_z^2 \tag{1.1}$$

where $n(\boldsymbol{r})$ is the index of refraction and k the wavenumber and k_z the wavenumber in the z-direction (throughout this thesis we make the approximation of a dielectric rod or pillar which is infinite in the z-direction). The reduced wavenumber γ is related to the frequency by $\omega_j = c\mathrm{Re}\left[\gamma\right]$ and the speed of light c. This is the central equation of this thesis (and for studies ranging from seismic waves trying to predict volcanos, to the search for U-boats, to quantum mechanics). The equation requires a set of suitable boundary conditions, which for a general dielectric geometry mix the electric $\boldsymbol{E}(\boldsymbol{r})$ and magnetic $\boldsymbol{B}(\boldsymbol{r})$ field components.

At a given k, k_z the solutions to this equation can in general be expanded in an expansion of incoming waves $\psi_\mu^<(\boldsymbol{r})$ and outgoing waves $\psi_\mu^>(\boldsymbol{r})$. To solve the equation an additional condition in the far-field needs to be considered. This condition at infinity relates to the two different experiments. For the scattering experiment, an incoming wave $\psi_\mu^<(\boldsymbol{r})$ is given, for the emission experiment no incoming wave $\psi_\mu^<(\boldsymbol{r})$ exists, only outgoing waves. These so called Sommerfeld boundary conditions require the Ansatz:

$$\Psi^j(\boldsymbol{r}) \sim \sum_\nu \gamma_\nu(\gamma_j)\psi_\nu^+(\gamma_j;\boldsymbol{r}) \quad |\boldsymbol{r}| \to \infty. \tag{1.2}$$

The possible values of γ_j have to be complex in this equation, coming from the fact that the energy for the outgoing waves needs to be supplied by the imaginary part of γ. These resonances occur at discrete complex frequencies and are called *quasi-normal modes* and relate to the mode frequency by $\omega_j = c\mathrm{Re}\left[\gamma\right]$ and the lifetime $\tau_j = 2/c\mathrm{Im}\left[\gamma\right]$ and thus the Q value $Q = -2\mathrm{Re}\left[\gamma\right]/\mathrm{Im}\left[\gamma\right]$. Here we can see a first simple connection to the lasing problem, as we can imagine that the pump process will provide us with the energy necessary to radiate. We will now review various approaches to finding these resonances.

1.4.1 Numerical approaches to resonances

Various approaches for calculating resonances of dielectric bodies exist. Simple geometries like the circle can be solved straight-forwardly; in Chapter 2 of this thesis we will generalize these results to the vector solutions of the cylinder. For small perturbations of the circle Lee [33] and Lai [34] used a perturbative approach. General Finite Element methods [35, 36] are used and lattice methods (finite-differences) can be used. These methods though very useful for closed resonators but are difficult to use in the open, dielectric case, where the area included in the calculations needs to be greatly expanded. A boundary matching approach was used by Nöckel [11]. Boundary Integral Methods [37] have emerged in the 1950s and where first introduced to the quantum chaos community by Berry [38]. For the dielectric case, boundary integral methods where first applied by Wiersig [39]. These methods are very flexible but involve a relatively high computational effort.

For smoothly deformed cavities which are not too far from the circle methods based on Bessel function expansions are applicable and convenient, as well as being helpful for physical interpretation. A powerful and fast approach of this type is a method based on finding the change of eigenvalues of a generalized eigenvalue problem and interpolating them to quantization; this method was used by Türeci and Schwefel [1], in Chapter 4 we present this method and generalize it for three dimensional resonators. This method is very efficient for finding a large number of resonances, but fails for too large deformations from the circle and too high values of kR (as do all the numerical methods). The method is particularly helpful for semiclassical interpretation of solutions as in this case it is often unnecessary to quantize the solutions [40, 1].

We will now consider a classical or semiclassical approach to the resonances of the microcavities.

1.4.2 Semiclassical methods

The semiclassical (or EBK, WKB, short-wavelength) limit, is the limit where a ray description is possible. As numerical solutions of the wave equation do not always reveal the physical picture and are computationally very expensive in the semiclassical regime, ray optical approaches have been shown to be very useful [14, 2]. Although direct ray tracing is often used in optics, it is in general not the right approach for microcavities, as general deformed shape will almost always exhibit chaotic dynamics. In this case most ray-tracing algorithms fail, and in any event do not give the phase space information which is most useful.

Reflection of rays at the boundary that satisfy the TIR condition follow the same laws as point mass with specular reflection. Here, we can utilize results of the non-linear dynamics community and their study of billiards. Billiards are 2d boundaries generating specular reflection of a point mass confined inside and moving ballistically. (The name is due to the obvious analogy to the billiard table [41, 42].) The important difference between dielectric billiards and classical billiards is the

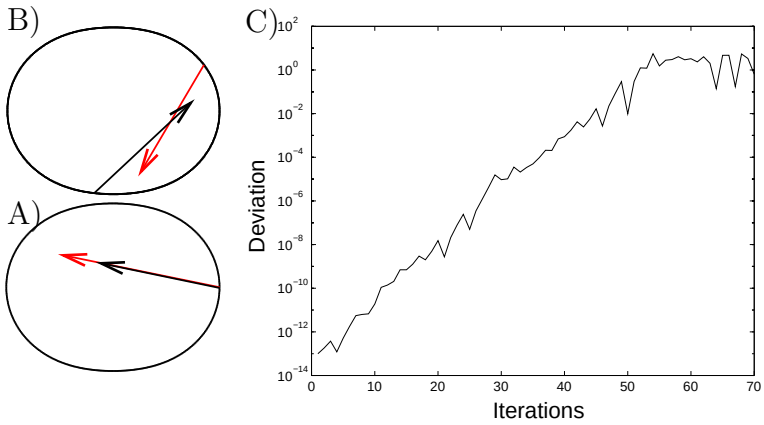

Figure 1.5: Chaotic behavior in a quadrupole billiard (see Eq. 1.3. A) two initial conditions have the same direction but deviate in position by 10^{-13} radians. B) after 70 iterations they have uncorrelated in both position and momentum, hence all information is lost. This is a mixed dynamical system and not all initial conditions for this shape would be uncorrelated, assuming an initial uncertainty of 10^{-13} radians. C) Log plot shows the exponential increase of the error. Note that it saturates, as the angular position is periodic in π.

possibility for light to refract out. The circular billiard has the property that it conserves the angle of incidence, which is proportional to the angular momentum. This additional constant of motion results in the integrability of the shape. Such a system is not very sensitivity to the initial conditions, contrary to a general system that is *chaotic*. Chaotic systems are exponentially sensitive to initial conditions, as shown for a generic billiard in Fig. 1.5. The rise of chaos by smooth general perturbations of an integrable shape has been studied by *Komogorov–Arnol'd–Moser* (KAM) [43] and is reviewed in Chapter 3. For the case of a smooth billiard system Lazutkin has refined the theory noting that the perturbation strength is not uniform in such a billiard [44] (see Section 3.3.6). The basic results of the theories is that small deformations do not break integrability everywhere, and that the chaotic component of phase space increases gradually. We shall see in Chapter 3 how chaos arises and how the structures that remain can explain emission directionality in microlasers. A further tool used is the Poincaré *surface of section*, SOS. For a 2-d dynamical system, the phase space is four dimensional. Conservation of energy reduces the dimension by one. A stroboscopic projection of the 3d motion is given by the SOS. The SOS consists of the set of points $(\phi_i, \sin\chi_i)$ taken by recording the point on the boundary in polar coordinates ϕ_i where a reflection occurs and the sine of the angle of incidence $\sin\chi_i$. This representation has all the information of the dynamics, and has a stunning beauty, see Fig. 1.6. In this plot a trajectory for which an additional constant exists will lie on a 1-d curve. If not, it will cover a 2-d region densely.

A model system for a general billiard geometry is the quadrupole billiard studied throughout the thesis both theoretically and experimentally (see Fig. 1.5); its

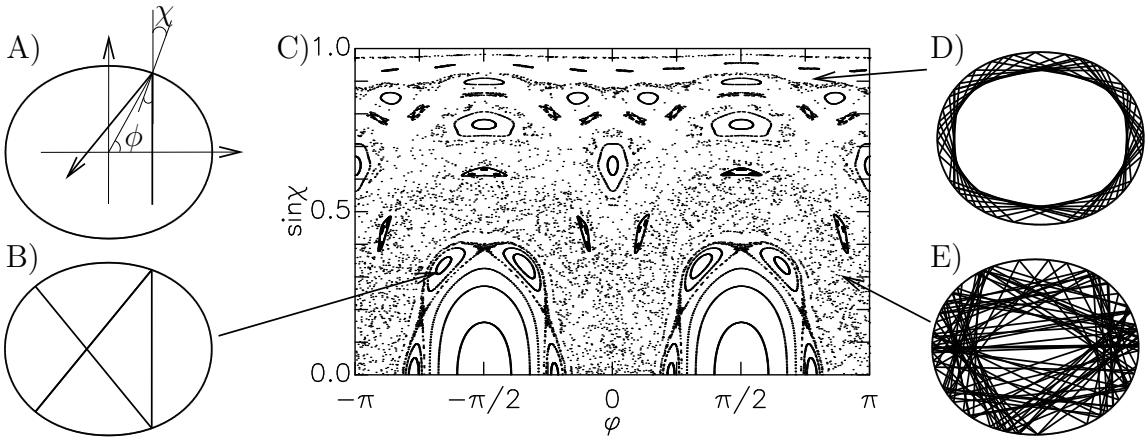

Figure 1.6: A) Schematic for the coordinates in the cavity. C) Surface of Section for the quadrupole at deformation $\varepsilon = 0.09$ for 30 different trajectories iterated for 600 reflections. B) a stable period-6 orbits, indicating an island in the SOS; D) a whispering gallery type orbit, well localized around a particular $\sin\chi$ in the SOS; E) a chaotic trajectory, filling a 2-d area in the SOS.

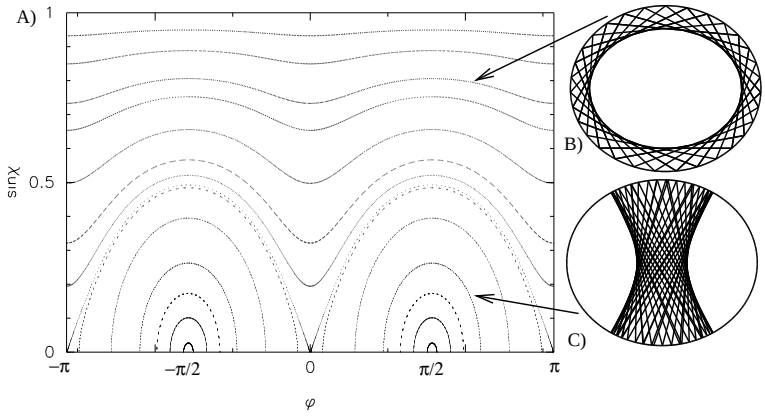

Figure 1.7: A) Surface of Section for the ellipse at deformation $\varepsilon = 0.072$ for 30 different trajectories iterated for 600 reflections. B) WG type orbit; C) Bouncing ball type orbit.

boundary shape is given by

$$r(\phi) = r_o(1 + \varepsilon \cos 2\phi). \tag{1.3}$$

In order to take the leakiness of dielectric billiards into account we have to alter the billiard dynamics to include the possibility of refractive escape. The critical angle $\sin \chi_c$ at which TIR breaks down can be plotted as a straight line onto the SOS, Fig. 1.8. The region above the critical angle is TIR, while below it the ray may refract out with a probability given by the Fresnel coefficients. This picture was first introduced by Nöckel and Stone [14]. In such a simulation the ray is given an amplitude and, using Fresnel's law, at every reflection the output is taken into account, displayed as the diameter and color change of a set of initial conditions in Fig. 1.8.

A completely different phase space structures is found for the ellipse, Fig. 1.7. The ellipse has an additional constant of motion (see Chapter 3) and therefore every trajectory lies on a one dimensional invariant curve in the SOS. Only two type of orbits are possible, the WG type (Fig. 1.7 B) and the bouncing ball type (Fig. 1.7 C).

For general ray dynamical simulations, the initial conditions of the rays are important, and an adiabatic theory [14] was devised to represent WG resonances which is discussed in the next section.

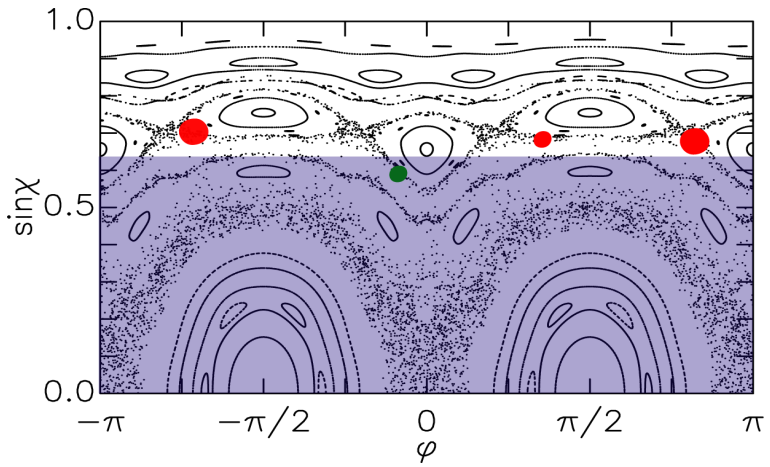

Figure 1.8: Schematic of Ray escape in a dielectric in the SOS. The shaded area marks the region below the critical angle, i.e. light will get refracted out. Starting with the right red dot we iterate to the far left side, both are total internally reflected, at the green dot we emit and continue with the smaller red dot.

1.4.3 Adiabaticity in low index material

To understand the effect of small but non-perturbative deformations from the circle/sphere on output directionality Nöckel and Stone devised an adiabatic theory [14,

45]. It was argued that the flow in the SOS of a smoothly deformed shape would follow for some time an adiabatic curve similar to the invariant curves of the ellipse. On a short time scale the rays would follow this adiabatic curve and only slowly diffuse into the lower regions of the phase-space. From this perspective ray-dynamical simulations were run by launching rays initially localized on an adiabatic curve and then propagating them into the far-field. This theory predicted directionality in agreement with numerical and experimental measurements, e.g. of deformed droplets and dye jets [46, 47]. Further it was proposed that this directionality would change dramatically if regular structures in the SOS would disrupt the adiabatic curves. The effect was termed *dynamical eclipsing* and is shown in Fig. 1.9. In this thesis we will analyze experimental data showing that the Nöckel–Stone prediction of directionality does break down for large deformation, where no regular structures persist [2]. The theory needs to be revised. We were able to show that in this regime it is not the regular structures that regulate the directionality, but rather the manifolds of the unstable fixed points, (See Chapter 5). In the low-index material experiments no spectral information was obtained and thus a linking to specific periodic orbits was not possible; such linkage was made in semiconductor experiments (see below). Experiments on low-index material were done on a number of different geometries and materials: polymers with $n \sim 1.5 - 2$ [48, 49, 17, 2], fused silica with $n \sim 1.5$ Refs [50, 51] and liquid droplets Refs [52, 53, 23, 54, 55, 56]. For these experiments the ray-dynamical approach worked very well.

1.4.4 High index materials

Work on higher index materials like the InGaAs quantum cascade micro lasers [8] with an index of $n = 3.3$ and GaN micro cavities [3] with an index of 2.65 show different behavior from the low index material. Spurred on by the success of microdisk resonators, and the directionality in the droplet experiments, Gmachl *et al.* [8] studied deformations of a flattened quadrupole shape. They found a strong increase in directional power output between circular laser and 20% deformed lasers of identical design. This sudden increase in output power combined with the spectral information could be linked to a regular structure in the SOS of the geometry. It turned out to be the stable period-4 bow-tie orbit in the quadrupole, see inset Fig. 1.10 B). The sudden onset of directionality was explained by the fact that the orbit gets born at the period doubling bifurcation of the stable two bounce orbit. Below a deformation of 14% the periodic orbit is too far below the critical line to sustain enough gain. At 15% deformation the angle of incidence of the bowtie is $\sin \chi_{\bowtie} = 0.30$ which is right at the critical line $\sin \chi_c = 1/n = 1/3.3 = 0.30$. For the 16% deformation $\sin \chi_{\bowtie} = 0.32$ the bow-tie is above the critical line and has enough gain for the lasing transition.

Another material studied was Gallium Nitride (GaN). The interest in GaN is based on its emission frequency which is in the blue to UV. In the GaN experiment strong directionality was also observed [3]. The image data was analyzed and emission from a bow-tie orbit could be ruled out. This time a triangular orbit, as shown

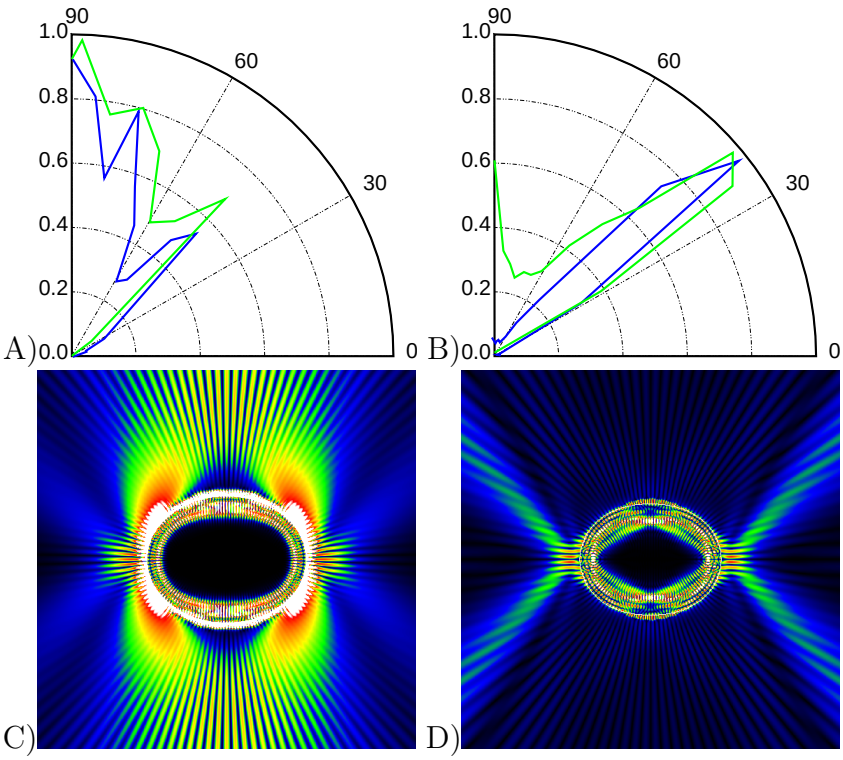

Figure 1.9: A) Emission directionality of the ellipse. B) Emission far-field for the quadrupole. Green Experimental data, blue ray-dynamical simulation. C) False color representation of the electric field intensity of a whispering gallery resonance of an ellipse at $n = 1.49$ shows generic emission pattern from points of highest curvature in the tangent direction shown. D) False color representation of the electric field intensity of a resonance of a quadrupole at $n = 1.49$.

in Fig. 1.11, gave rise to the emission. The surprising aspect of this finding was that the triangular orbit is unstable. Quantum localization on an unstable periodic orbits is known as a *scarring* in the quantum chaos community [57]. A classical ray would move away from such an orbit very rapidly.

Ray-dynamic tools need to be adjusted for high index materials as the adiabatic approximation breaks down, due to the fact that much more light is TIR. Different ray-dynamics methods can be used, where the localization of the rays is not on an adiabatic curve but on other structures of the SOS [3]. In this context, an important tool to correlate wavefunctions to classical structures in the phase space is the *Husimi distribution* [58] a smoothed Wigner projection of the wavefunction into the phase space, see Section 4.10.

A further GaN shape was studied, the hexadecapole [59]. Here it was possible to link the resonant mode at the lower deformations to a stable triangular orbit, and to follow it through its pitchfork-bifurcation into a scarred mode, see Section 8.6.4.

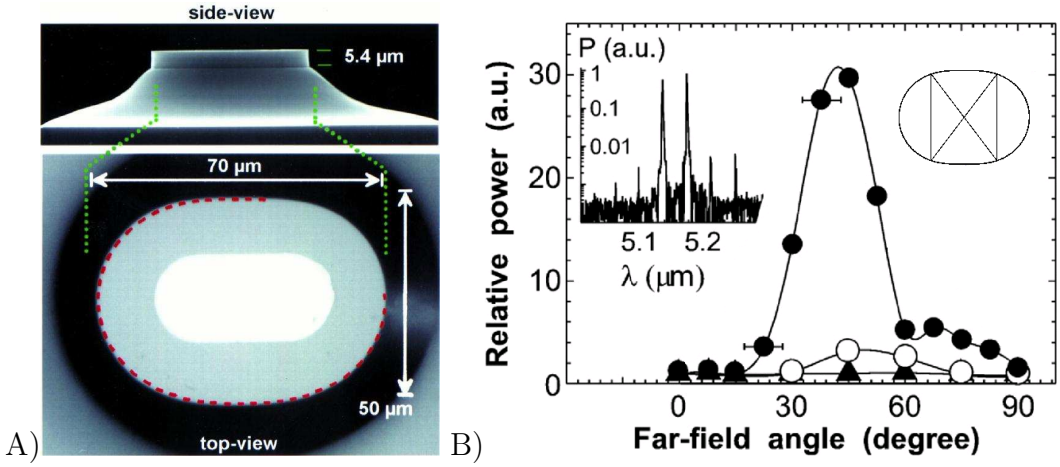

Figure 1.10: A) Scanning electron micrographs of the top and side-view of the 16% deformed cylindrical quantum cascade micro-lasers. B) Angular dependence of the emission intensity for deformations $\varepsilon = 0$ (triangles), $\varepsilon = 0.14$ (open circles), $\varepsilon = 0.16$ (filled circles). The right inset shows the bowtie orbit at 16% and the left inset shows the logarithmic plot of the measured power spectrum. The free-spectral range of the peaks is found to agree with the calculated bowtie free spectral range (Following Ref. [8]).

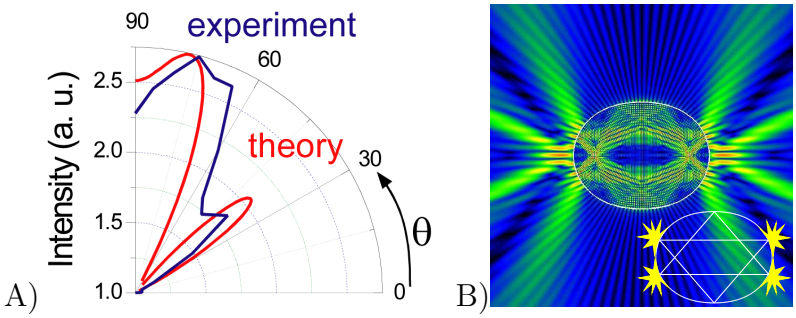

Figure 1.11: A) Experimental and theoretical far-field for a resonance in the quadrupole. B) Realspace plot of a triangular mode in the quadrupole. Following Ref. [3].

1.4.5 Three dimensional ARCs

So far all ARC experiments where analyzed with a scalar wave theory, but the real world and all experiments are on 3d structures, cylindrical, spherical or arbitrary. The theoretical considerations so far have only been based on a two dimensional cross section, which is adequate under circumstances to be discussed below. With this limitation the polarization degree of freedom of light is treated in an essentially trivial manner. This thesis will change that! The study of the polarization of resonances

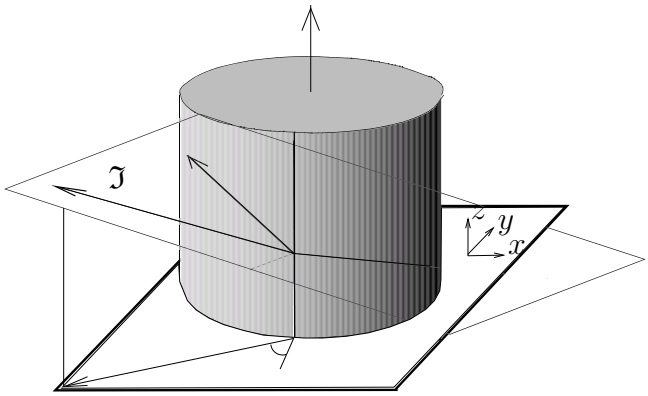

Figure 1.12: Schematic for the rays traveling in a 3-d cylinder.

is major part of this thesis. In an infinite dielectric rod of arbitrary cross-section, the solutions to the vector Helmholtz equation are fully determined by only two field components, often chosen to be E_z and B_z. They are then mixed via the boundary conditions. We can relate the wavevector along the z axis, k_z to the z-momentum of a ray spiraling up in Fig. 1.12, by $\tan\theta = k_z/\sqrt{n^2k^2 - k_z^2}$. We will show below that the general resonance condition in the cylinder can be written as

$$n^2(1-n^2)^2m^2\sin^2\theta = G^{TE}\cdot G^{TM},$$

where $G^{TE} = 0$ and $G^{TM} = 0$ define the resonance conditions for the separable TE and TM modes in the $\theta = 0$ case. In the general case polarization considering simple TM and TE modes don't exist and so-called *Hybrid* polarizations are formed. The literature mainly deals with the lowest order modes of the cylinder in this case. These modes are the relevant modes for fiber optics telecommunication and have been widely studied [60, 61]. Especially for single mode fibers the lowest mode is the only allowed mode, due to the diameter specification of the fiber. In cladded fibers the small index mismatch results effectively into rays with a very shallow angle of incidence. Here we will deal with a much more general class of "leaky" spiral modes which could be observed in elastic scattering experiments such as those of Poon *et al.* [10].

For the cylinder we will write down the Einstein-Brillouin-Keller (EBK) quantization conditions and find a polarization critical angle at which the resonance is shifted by a generalized Fresnel phase. This generalized Fresnel factor can also be

found via a polarization ray-tracing method, using a Jones matrix approach. Experiments done by Poon [10] showed a blue-shift in the resonances observed on a tilted fiber; this blue-shift is explained in Chapter 6.

For a smoothly deformed cylinder we are able to project the ray-dynamics onto a 2-d cross-section with a constant momentum along the z axis. We are thus still able to use the SOS to analyze the 3d system, noting that the general incidence angle η will be shifted due to a finite θ by

$$\cos\eta = \cos\chi\cos\theta, \tag{1.4}$$

where χ is the angle of incidence in the 2-d plane. With this the critical angle gets shifted and thus modes are more strongly confined with a finite θ.

1.4.6 Deformed cylinders

No prior work has been done on deformed three dimensional cylinders. Resonances in these structures with a projected motion that is stable are found via a Gaussian optics approach. Their polarization effects are studied and discussed in Chapter 7.

1.5 Brief survey of chapters

In Chapter 2 we discuss the wave equation in the 3d geometry. The boundary conditions on the fields are derived for the symmetry of an infinite rod of arbitrary cross-section, and we derive with the eikonal method Snell's and Fresnel's law at a semi-infinite dielectric boundary.

In Chapter 3 we discuss the ray-dynamics in deformed billiards and make the connection to ray-dynamics in dielectric media. We will first go over the necessary Hamiltonian dynamics, discuss the road to chaos via the KAM theory and understand bifurcations. The maps of the circle, ellipse and quadrupole are studied. For the latter we provide a survey of its fixed-points. The connection to the dielectric billiard is made via the Poincaré surface of section and we introduce different methods for ray-simulations and relate them to experiments.

In Chapter 4 we discuss the resonance condition in three dimensions, and derive the quasi-bound resonances for the cylinder. For a general deformed geometry we study the eigenvalues and describe a new algorithm for finding the resonances. We introduce the Husimi projection, a projection of wave-solutions into the SOS, to correlate wave solutions with classical structures in the phase space. Finally we derive the polarization of the far-field radiation.

In Chapter 5 we discuss an experiment on elliptic, quadrupolar and hexadecapolar shaped lasing polymers. The adiabatic ray model of Nöckel and Stone and dynamical eclipsing is reviewed. The failure of the model to reproduce the experimental data is shown and a new model based on the unstable manifolds of short periodic orbits is introduced. With this model we are able to interpret the data and make a prediction about directional emission from a completely chaotic shape, the stadium.

In Chapter 6 we discuss the resonance conditions of the three dimensional wave equation in the above barrier regime. We relate the resonance width to the classical Fresnel formula and calculate the resonance condition of the cylinder with the help of the EBK method. For dielectric rods with an arbitrary cross-section, we derive the quantization condition for classical structures, that have stable projections in the plane, based on the Gaussian optics approach.

In Chapter 7 we derive a method for finding the polarization states of resonances in the cylinder using the Jones algebra of spiraling rays. We then study and interpret the eigenpolarization conditions for the dielectric cylinder and compare to exact numerical results.

In Chapter 8 we describe the experimental setup for micro laser experiments. Experimental data for a space-capsule shaped GaN laser is presented and analyzed theoretically. The extreme directionality shift in experimental data for different deformations of the ellipse is explained. The first observation of lasing from a scarred orbit in GaN is reviewed and lasing of a resonance located around a period orbit in the hexadecapole is observed as the orbit becomes unstable.

In Chapter 9 we summarize the thesis and mention interesting open problems.

Chapter 2

The Wave-equation for 3d dielectric structures

2.1 Introduction

As noted in Chapter 1 the focus of this thesis is to understand the emission characteristics of micro-resonators by interpreting the resonances of dielectric cavities using semiclassical methods. We will set up the connection between the partially chaotic ray-dynamics in micro cavities to the wave solutions in the next chapter. In this chapter, we will develop the vector wave equation and derive the nessesary boundary conditions. The majority of the microcavity experiments analyzed in this thesis are performed on dielectric structures of cylindrical geometry, with the z-axis pointing along the cylinder axis. Two cases will be distinguished: 1) the solutions of the vector wave equation have zero axial momentum i.e., $k_z = 0$. In this case, the vector equations reduces to the scalar Helmholtz equation and the solutions are the standard 2-d TM and TE cases known from elementary electro-magnetism. The majority of past work on microcavities has considered only this case. 2) The solutions have nonzero momentum $k_z \neq 0$. In this case the vector equations do not separate and a simple eigenpolarization does not exist. Below we will derive from Maxwell's equation the vector wave equation for the geometry of an infinite rod with arbitrary cross-section and show that all the field information is contained in two scalar components. Within this formalism, the generalized Snell's and Fresnel's laws will be derived by the application of the Eikonal method.

2.2 Wave equation for an infinite dielectric rod

In this section we will derive the vector wave equation for the electromagnetic field in an infinitely long dielectric rod of arbitrary cross-section. The general Maxwell's

equations can be written as

$$\boldsymbol{\nabla} \times \boldsymbol{E} + \frac{\partial}{\partial t}\boldsymbol{B} = 0 \qquad \boldsymbol{\nabla} \cdot \boldsymbol{D} = 0 \tag{2.1}$$

$$\boldsymbol{\nabla} \times \boldsymbol{H} - \frac{\partial}{\partial t}\boldsymbol{D} = 0 \qquad \boldsymbol{\nabla} \cdot \boldsymbol{B} = 0 \tag{2.2}$$

Let's assume solutions have harmonic time dependence $e^{-i\omega t}$.[1] For an isotropic linear medium with $\boldsymbol{D} = \epsilon \boldsymbol{E}$ and $\boldsymbol{B} = \mu \boldsymbol{H}$, these equations reduce to

$$\boldsymbol{\nabla} \times \boldsymbol{E} - i\omega \boldsymbol{B} = 0 \qquad \boldsymbol{\nabla} \cdot \epsilon \boldsymbol{E} = 0 \tag{2.3}$$

$$\boldsymbol{\nabla} \times \boldsymbol{B} + i\omega\mu\epsilon \boldsymbol{E} = 0 \qquad \boldsymbol{\nabla} \cdot \boldsymbol{B} = 0. \tag{2.4}$$

Combining the two curl equations for a uniform dielectric with index of refraction $n^2 = \mu\epsilon$ and wave vector $ck = \omega$ (in the following we choose $c = 1$) we obtain the *general* vector *Helmholtz equation*

$$\left(\nabla^2 + n^2 k^2\right) \begin{Bmatrix} \boldsymbol{E}(x, y, z) \\ \boldsymbol{B}(x, y, z) \end{Bmatrix} = 0. \tag{2.5}$$

These six equations are in general coupled via the boundary conditions. The translational symmetry along the z-axis (see Fig. 2.1) allows us to express the z-variation of the fields as

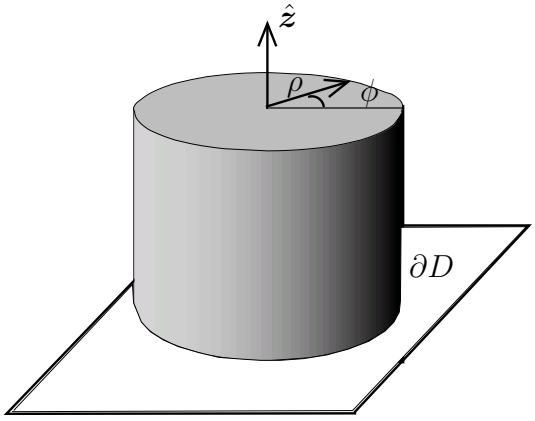

Figure 2.1: Schematic for the infinite rod with translational symmetry along the $\hat{\boldsymbol{z}}$-axis and arbitrary cross-section.

$$\boldsymbol{E}(\boldsymbol{x}) = \boldsymbol{E}(x, y)\mathrm{e}^{-ik_z z}, \quad \boldsymbol{B}(\boldsymbol{x}) = \boldsymbol{B}(x, y)\mathrm{e}^{-ik_z z} \tag{2.6}$$

Following Refs. [62, 63], we separate the fields and operators into components parallel and transverse to the z-axis:

$$\boldsymbol{E}(x, y) = \boldsymbol{E}_z(x, y) + \boldsymbol{E}_\perp(x, y) = \boldsymbol{E}_\perp + \hat{\boldsymbol{z}} E_z, \quad \boldsymbol{\nabla} = \boldsymbol{\nabla}_\perp + \hat{\boldsymbol{z}} \frac{\partial}{\partial z} \tag{2.7}$$

[1] Since any arbitrary solution can be found by Fourier superposition of harmonic functions.

With this Eq. (2.3) becomes

$$\boldsymbol{\nabla}_\perp \cdot \boldsymbol{E}_\perp = ik_z E_z \tag{2.8}$$

and

$$\begin{aligned} ik\boldsymbol{B} &= \boldsymbol{\nabla} \times (\boldsymbol{E}_\perp + \hat{\boldsymbol{z}} E_z) \\ &= \left(\boldsymbol{\nabla}_\perp + \hat{\boldsymbol{z}}\frac{\partial}{\partial z}\right) \times \boldsymbol{E}_\perp + (\boldsymbol{\nabla} E_z) \times \hat{\boldsymbol{z}} \\ &= \boldsymbol{\nabla}_\perp \times \boldsymbol{E}_\perp + \hat{\boldsymbol{z}} \times (-ik_z \boldsymbol{E}_\perp) + (\boldsymbol{\nabla}_\perp E_z) \times \hat{\boldsymbol{z}} \\ &= \boldsymbol{\nabla}_\perp \times \boldsymbol{E}_\perp + (ik_z \boldsymbol{E}_\perp + \boldsymbol{\nabla}_\perp E_z) \times \hat{\boldsymbol{z}} \end{aligned} \tag{2.9}$$

as the first term is clearly in $\hat{\boldsymbol{z}}$ direction and the second in the transverse direction we can write

$$ikB_z = (\boldsymbol{\nabla}_\perp \times \boldsymbol{E}_\perp)_z \tag{2.10}$$

$$ik\boldsymbol{B}_\perp = (ik_z \boldsymbol{E}_\perp + \boldsymbol{\nabla}_\perp E_z) \times \hat{\boldsymbol{z}} \tag{2.11}$$

for the $\boldsymbol{B}$ field we find similar relations:

$$\boldsymbol{\nabla}_\perp \cdot \boldsymbol{B}_\perp = ik_z B_z \tag{2.12}$$

$$-in^2 k E_z = (\boldsymbol{\nabla}_\perp \times \boldsymbol{B}_\perp)_z \tag{2.13}$$

$$-in^2 k \boldsymbol{E}_\perp = (ik_z \boldsymbol{B}_\perp + \boldsymbol{\nabla}_\perp B_z) \times \hat{\boldsymbol{z}}. \tag{2.14}$$

The reduced Helmholtz equation becomes

$$\left(\nabla^2 + \gamma^2\right) \begin{Bmatrix} \boldsymbol{E}(x,y) \\ \boldsymbol{B}(x,y) \end{Bmatrix} = 0, \quad \text{with} \quad \gamma^2 = n(\boldsymbol{x})^2 k^2 - k_z^2 \tag{2.15}$$

We will now show that we can simplify the equations even further by finding relationships between the different components of the EM fields. We write Eq. (2.11) and replace $\boldsymbol{B}_\perp$ by Eq. (2.14) to get a relation between $\boldsymbol{E}_\perp$ and E_z, B_z,

$$\begin{aligned} -in^2 k \boldsymbol{E}_\perp &= (ik_z \boldsymbol{B}_\perp + \boldsymbol{\nabla}_\perp B_z) \times \hat{\boldsymbol{z}} \\ &= \left[ik_z \frac{1}{ik}(ik_z \boldsymbol{E}_\perp + \boldsymbol{\nabla}_\perp E_z) \times \hat{\boldsymbol{z}} + \boldsymbol{\nabla}_\perp B_z\right] \times \hat{\boldsymbol{z}} \\ &= \frac{k_z}{k}\left[(ik_z \boldsymbol{E}_\perp + \boldsymbol{\nabla}_\perp E_z) \times \hat{\boldsymbol{z}}\right] \times \hat{\boldsymbol{z}} + \boldsymbol{\nabla}_\perp B_z \times \hat{\boldsymbol{z}} \\ &= \frac{k_z}{k}\left[- (ik_z \boldsymbol{E}_\perp + \boldsymbol{\nabla}_\perp E_z)\right] + \boldsymbol{\nabla}_\perp B_z \times \hat{\boldsymbol{z}} \\ -i(n^2 k^2 - k_z^2)\boldsymbol{E}_\perp &= -k_z \boldsymbol{\nabla}_\perp E_z - k\hat{\boldsymbol{z}} \times \boldsymbol{\nabla}_\perp B_z \\ \boldsymbol{E}_\perp &= -\frac{i}{\gamma^2}(k\hat{\boldsymbol{z}} \times \boldsymbol{\nabla}_\perp B_z + k_z \boldsymbol{\nabla}_\perp E_z) \end{aligned} \tag{2.16}$$

doing the same for $\boldsymbol{B}_\perp$

$$\begin{aligned}
ik\boldsymbol{B}_\perp &= (ik_z\boldsymbol{E}_\perp + \boldsymbol{\nabla}_\perp E_z)\times\hat{\boldsymbol{z}} \\
&= \left[ik_z\frac{1}{-in^2k}(ik_z\boldsymbol{B}_\perp + \boldsymbol{\nabla}_\perp B_z)\times\hat{\boldsymbol{z}} + \boldsymbol{\nabla}_\perp E_z\right]\times\hat{\boldsymbol{z}} \\
&= \frac{k_z}{-n^2k}\big[(ik_z\boldsymbol{B}_\perp + \boldsymbol{\nabla}_\perp B_z)\times\hat{\boldsymbol{z}}\big]\times\hat{\boldsymbol{z}} + \boldsymbol{\nabla}_\perp E_z\times\hat{\boldsymbol{z}} \\
&= \frac{k_z}{-n^2k}\big[-(ik_z\boldsymbol{B}_\perp + \boldsymbol{\nabla}_\perp B_z)\big] + \boldsymbol{\nabla}_\perp E_z\times\hat{\boldsymbol{z}} \\
-in^2k^2\boldsymbol{B}_\perp + ik_z^2\boldsymbol{B}_\perp &= -k_z\boldsymbol{\nabla}_\perp B_z - n^2k\boldsymbol{\nabla}_\perp E_z\times\hat{\boldsymbol{z}} \\
-i(n^2k^2 - k_z^2)\boldsymbol{B}_\perp &= -k_z\boldsymbol{\nabla}_\perp B_z + n^2k\hat{\boldsymbol{z}}\times\boldsymbol{\nabla}_\perp E_z \\
\boldsymbol{B}_\perp &= \frac{i}{\gamma^2}(n^2k\hat{\boldsymbol{z}}\times\boldsymbol{\nabla}_\perp E_z - k_z\boldsymbol{\nabla}_\perp B_z). \qquad (2.17)
\end{aligned}$$

Projecting the transverse fields $\boldsymbol{E}_\perp, \boldsymbol{B}_\perp$ into its normal and tangential components on the boundary, we can write these relations in a compact matrix form.

$$\begin{pmatrix} E_t \\ E_n \end{pmatrix} = -\frac{i}{\gamma}\begin{pmatrix} \partial_t & \partial_n \\ \partial_n & -\partial_t \end{pmatrix}\begin{pmatrix} k_z/\gamma & 0 \\ 0 & k/\gamma \end{pmatrix}\begin{pmatrix} E_z \\ B_z \end{pmatrix} \qquad (2.18)$$

and

$$\begin{pmatrix} B_t \\ B_n \end{pmatrix} = -\frac{i}{\gamma}\begin{pmatrix} -\partial_n & \partial_t \\ \partial_t & \partial_n \end{pmatrix}\begin{pmatrix} n^2k/\gamma & 0 \\ 0 & k_z/\gamma \end{pmatrix}\begin{pmatrix} E_z \\ B_z \end{pmatrix} \qquad (2.19)$$

It's evident from these equations that we can take E_z and B_z as the fundamental fields which fully determine the other four components. We can now focus on the 2-component wave equation for the E_z and B_z component of the field.

$$\left(\nabla^2 + \gamma^2\right)\begin{Bmatrix} E_z(x,y) \\ B_z(x,y) \end{Bmatrix} = 0, \quad \text{with} \quad \gamma^2 = n(\boldsymbol{x})^2k^2 - k_z^2 \qquad (2.20)$$

2.3 Boundary conditions

The actual complication of solving the vector Helmholtz equation stems from the fact that the *boundary conditions* are coupled. We should remind ourselves that the Maxwell boundary conditions, in the absence of surface currents and charges for a linear, isotropic medium are given by

$$\hat{\boldsymbol{n}}\times(\boldsymbol{E}_1 - \boldsymbol{E}_2) = 0, \qquad \hat{\boldsymbol{n}}\cdot(n_1^2\boldsymbol{E}_1 - n_2^2\boldsymbol{E}_2) = 0 \qquad (2.21)$$

$$\hat{\boldsymbol{n}}\times(\boldsymbol{B}_1 - \boldsymbol{B}_2) = 0, \qquad \hat{\boldsymbol{n}}\cdot(\boldsymbol{B}_1 - \boldsymbol{B}_2) = 0. \qquad (2.22)$$

The subscripts denote the media on respective sides of the interface. $\hat{\boldsymbol{n}}$ is the unit normal on the interface, pointing away from the cylinder. We will assume $n_1 = n >$

$n_2 = 1$. Note that these are six conditions altogether. With the transverse field projected onto normal $\hat{\boldsymbol{n}}$ and tangential $\hat{\boldsymbol{t}}$ components

$$E_{z1} = E_{z2}, \qquad B_{z1} = B_{z2} \tag{2.23}$$
$$E_{t1} = E_{t2}, \qquad B_{t1} = B_{t2} \tag{2.24}$$
$$n_1^2 E_{n1} = n_2^2 E_{n2}, \qquad B_{n1} = B_{n2} \tag{2.25}$$

To obtain the boundary conditions in terms of E_z and B_z we use Eq. (2.16) and Eq. (2.17) projected onto the normal and tangent direction with $\hat{\boldsymbol{t}} = \hat{\boldsymbol{z}} \times \hat{\boldsymbol{n}}$. We also define $\partial_n = \hat{\boldsymbol{n}} \cdot \boldsymbol{\nabla}$ and $\partial_t = \hat{\boldsymbol{t}} \cdot \boldsymbol{\nabla}$.

$$E_t = \hat{\boldsymbol{t}} \cdot \boldsymbol{E}_\perp = \hat{\boldsymbol{t}} \cdot -\frac{i}{\gamma^2}(k\hat{\boldsymbol{z}} \times \boldsymbol{\nabla}_\perp B_z + k_z \boldsymbol{\nabla}_\perp E_z) \tag{2.26}$$
$$= -\frac{i}{\gamma^2}(k\hat{\boldsymbol{n}} \cdot \boldsymbol{\nabla}_\perp B_z + k_z \hat{\boldsymbol{t}} \cdot \boldsymbol{\nabla}_\perp E_z) \tag{2.27}$$
$$= -\frac{i}{\gamma^2}(k\partial_n B_z + k_z \partial_t E_z) \tag{2.28}$$

Following the idea through we get

$$E_n = \hat{\boldsymbol{n}} \cdot \boldsymbol{E}_\perp = \frac{i}{\gamma^2}(k\partial_t B_z - k_z \partial_n E_z) \tag{2.29}$$
$$B_t = \hat{\boldsymbol{t}} \cdot \boldsymbol{B}_\perp = \frac{i}{\gamma^2}(n^2 k\partial_n E_z - k_z \partial_t B_z) \tag{2.30}$$
$$B_n = \hat{\boldsymbol{n}} \cdot \boldsymbol{B}_\perp = -\frac{i}{\gamma^2}(n^2 k\partial_t E_z + k_z \partial_n B_z) \tag{2.31}$$

and combining these leads to

$$\frac{1}{\gamma_1^2}(k\partial_n B_{z1} + k_z \partial_t E_{z1}) = \frac{1}{\gamma_2^2}(k\partial_n B_{z2} + k_z \partial_t E_{z2}) \tag{2.32}$$
$$\frac{n_1^2}{\gamma_1^2}(k\partial_t B_{z1} - k_z \partial_n E_{z1}) = \frac{n_2^2}{\gamma_2^2}(k\partial_t B_{z2} - k_z \partial_n E_{z2}) \tag{2.33}$$
$$\frac{1}{\gamma_1^2}(n_1^2 k\partial_n E_{z1} - k_z \partial_t B_{z1}) = \frac{1}{\gamma_2^2}(n_2^2 k\partial_n E_{z2} - k_z \partial_t B_{z2}) \tag{2.34}$$
$$\frac{1}{\gamma_1^2}(n_1^2 k\partial_t E_{z1} + k_z \partial_n B_{z1}) = \frac{1}{\gamma_2^2}(n_2^2 k\partial_t E_{z2} + k_z \partial_n B_{z2}) \tag{2.35}$$

note that adding Eq. (2.32) $\times k_z +$ Eq. (2.35) $\times -k$ as well as Eq. (2.33) $\times k +$ Eq. (2.34) $\times k_z$, we get the continuity of the tangential derivatives of the E_z and B_z fields,

$$\partial_t E_{z1} = \partial_t E_{z2} \tag{2.36}$$
$$\partial_t B_{z1} = \partial_t B_{z2} \tag{2.37}$$

using $\gamma^2 = n^2k^2 - k_z^2$. These two equations are equivalent to Eq. (2.23) which we can see writing a Taylor expansion for the E_z field on an arbitrary point s on the boundary

$$E_{z1}(s_2) = E_{z1}(s_1) + \hat{\boldsymbol{t}} \cdot \boldsymbol{\nabla} E_{z1}(s_1 - s_2) \tag{2.38}$$
$$E_{z2}(s_2) = E_{z2}(s_1) + \hat{\boldsymbol{t}} \cdot \boldsymbol{\nabla} E_{z2}(s_1 - s_2) \tag{2.39}$$

subtracting both equations and using the continuity of E_z at positions s_1, s_2 we get

$$\hat{\boldsymbol{t}} \cdot \boldsymbol{\nabla} E_{z1}(s_1 - s_2) - \hat{\boldsymbol{t}} \cdot \boldsymbol{\nabla} E_{z2}(s_1 - s_2) = 0 \quad \Rightarrow \quad \partial_t E_{z1} = \partial_t E_{z2} \tag{2.40}$$

The same holds for B_z. Thus, there are only four independent boundary conditions. To clearly see the limiting $k_z = 0$ case we write the BCs Eq. (2.32) and Eq. (2.34) with the substitution of the continuity of the tangent derivatives of the fields Eqs (2.36) and (2.37)

$$E_{z1} = E_{z2} \quad \text{or} \quad \partial_t E_{z1} = \partial_t E_{z2} \tag{2.41}$$
$$B_{z1} = B_{z2} \quad \text{or} \quad \partial_t B_{z1} = \partial_t B_{z2} \tag{2.42}$$
$$\frac{k}{\gamma_1^2}\partial_n B_{z1} - \frac{k}{\gamma_2^2}\partial_n B_{z2} = -\left(\frac{k_z}{\gamma_1^2} - \frac{k_z}{\gamma_2^2}\right)\partial_t E_{z1} \tag{2.43}$$
$$\frac{n_1^2 k}{\gamma_1^2}\partial_n E_{z1} - \frac{n_2^2 k}{\gamma_2^2}\partial_n E_{z2} = +\left(\frac{k_z}{\gamma_1^2} - \frac{k_z}{\gamma_2^2}\right)\partial_t B_{z1} \tag{2.44}$$

We will now look at some special cases of these conditions.

2.3.1 Transverse Magnetic TM

If we have $B_z = 0$ and $k_z = 0$ we get from Eq. (2.16) $\boldsymbol{E}_\perp = 0$ and

$$\boldsymbol{B}_\perp = \frac{i}{\gamma^2} n^2 k \begin{pmatrix} -\partial_y E_z \\ \partial_x E_z \end{pmatrix}. \tag{2.45}$$

The equations Eqs (2.41)-(2.44) completely decouple and we only have to solve for E_z. The electromagnetic field is *linearly polarized* and the polarization is said to be *transverse magnetic* (TM).

2.3.2 Transverse Electric TE

If we have $E_z = 0$ and $k_z = 0$ we get from Eq. (2.17) $\boldsymbol{B}_\perp = 0$ and

$$\boldsymbol{E}_\perp = -\frac{i}{\gamma^2} k \begin{pmatrix} -\partial_y B_z \\ \partial_x B_z \end{pmatrix}. \tag{2.46}$$

Again,the equations Eqs (2.41)-(2.44) completely decouple and we only have to solve for B_z. The electromagnetic field is *linearly polarized* and called *transverse electric* (TE).

2.3.3 Transverse Electromagnetic TEM

We have one remaining special class of solutions, the so called *transverse electromagnetic* TEM case. In this case the field is only propagating in the z direction, with $B_z = E_z = 0$ and we get that $\gamma = 0$. This case is important in transmission lines but not relevant to our main focus below and will not be discussed further.

2.3.4 Hybrid Modes

The most general type of solutions have both $k \neq k_z$ and $k_z \neq 0$, as well as non-vanishing B_z and E_z. These modes are called *hybrid modes*, HE or EH modes. These field configurations correspond in the semiclassical limit to "skew ray" modes. It is these modes that we will study and classify further in this thesis. The classical literatrue has in general avoided a general treatment and mainly looked at the "weakly guiding waveguides" where modes are only guided with very shallow classical angles. Below, we will analyse this general case via a semiclassical approach.

2.4 Eikonal theory for scattering off a dielectric rod

In this section we will try to solve the reduced vector Helmholtz Equation (2.20) in the semiclassical limit. We have seen in Section 2.2 that in the case for $k_z = 0$ the vector solutions seperate into two cases $(E_z(x,y), 0)$ and $(0, B_z(x,y))$, the standard 2-d TM and TE solutions. For the general $k_z \neq 0$ case we will have to solve

$$\left(\nabla^2 + \gamma^2\right) \begin{Bmatrix} E_z(x,y) \\ B_z(x,y) \end{Bmatrix} = 0, \quad \text{with} \quad \gamma^2 = n(\boldsymbol{x})^2 k^2 - k_z^2. \tag{2.47}$$

In the limit of $\gamma \to \infty$ (*semiclassical limit*) we expect the vector wave solution to have strong fluctuations in the phase and but slow variation in the amplitude, captured in the ansatz

$$\Psi(x,y) \sim \begin{Bmatrix} E_z^o(x,y) \\ B_z^o(x,y) \end{Bmatrix} e^{i\gamma S(x,y)} \tag{2.48}$$

It was first shown by Sommerfeld [64] following a suggestion from Debye that using this Ansatz in Eq. (2.20) we can derive the *Eikonal equation* and the *transport equation* of optics. Here we state the results

$$(\nabla S)^2 = n^2(\boldsymbol{r}) \qquad \text{Eikonal Eq.} \tag{2.49}$$

$$2\nabla \cdot S\, \nabla \cdot A + A\, \nabla^2 S = 0 \qquad \text{Transport Eq.} \tag{2.50}$$

From the knowledge of the optical properties of the medium through $n(\boldsymbol{r})$ the *Eikonal*[2] $S(\boldsymbol{r})$ can be obtained via the eikonal equation, and subsequently the amplitude $A(\boldsymbol{r})$ via the transport equation. The surfaces

$$S(\boldsymbol{r}) = \text{constant} \tag{2.51}$$

[2]The term *eikonal* from Greek $\varepsilon\iota\kappa\tilde{\omega}\nu$ = image was introduced in 1895 by H. Bruns [65].

are called the *geometrical wave-fronts*.[3] As we can identify the eikonal equation to be the time-independent Hamilton-Jacobi equation of mechanics with $S(\boldsymbol{r})$ defined as the *action*, we can map the ray dynamics onto the motion of a point particle of mass $m = 1$ and energy $E = 0$ moving in a potential of the form $V(\boldsymbol{r}) = -1/2n(\boldsymbol{r})^2$, where $n(\boldsymbol{r})$ is the local index of refraction. The Ansatz in Eq. (2.48), when used to find bound solutions, is known as the EBK method, following work of Einstein, Brillouin and Keller [67, 68, 69], in which the quantized γ values will be determined by topologically invariant loop integrals (see Section 6.4.1).

2.4.1 Generalized Snell's law

The conditions above describe waves in an infinte medium. We will now derive the necessary modifications for semi-infinte media, specifically scattering of the EM field at a curved interface separating two semi-infinite media of different index of refraction (See Fig. 2.2). Using this, we will later derive the EBK quantization conditions for EM waves in a semi-bounded medium, an infinitely long dielectric rod.

In order to satisfy the boundary conditions we need to have an incoming and an outgoing field inside. As we deal with emitting cavities, one outgoing field outside is enough to fullfill the outgoing boundary conditions at infinity. The Ansatz Eq. (2.48) can be interpreted following the classical ray path of an incoming, reflected and transmitted ray at the boundary. The schematic is shown in Fig. 2.2, where i denotes

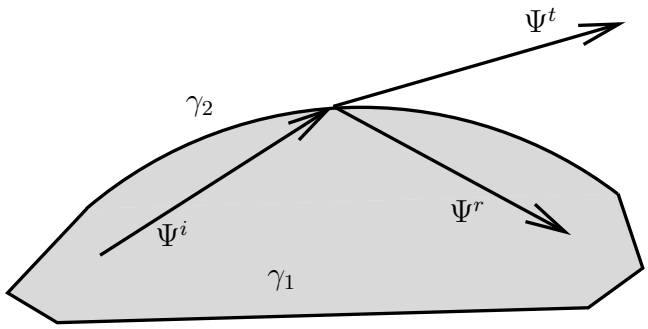

Figure 2.2: Schematic for EBK. We will expand the wave solution inside into an incoming component Ψ^i and a reflected Ψ^r. The outside into Ψ^t.

the incoming ray, r the reflected and t the transmitted. The Ansatz for each of the fields is given by

$$\Psi^m = \begin{pmatrix} E_{z,m} \\ B_{z,m} \end{pmatrix} e^{i\gamma S_m}, \quad \text{with} \quad m \in \{i, r, t\} \tag{2.52}$$

The gradient of the Eikonal ∇S gives the direction of the the ray and is of constant length $|\nabla S| = n$. Using Fig. 2.3 C) we find

[3] We can also recognize the eikonal equation as the *Hamilton-Jacobi* equation of the variational problem [66] going back to Fermat. (Fermat's variational problem of the shortest optical path $\delta = \int ds\ n(\boldsymbol{r})$. For a relevant derivation refer to Ref. [65] Appendix I.)

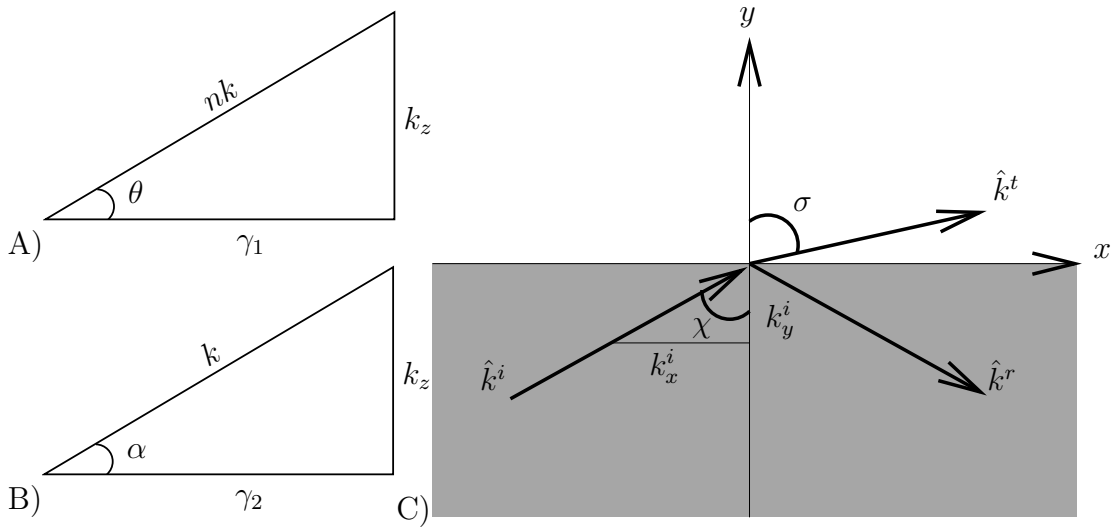

Figure 2.3: A), B) Schematic for the relations along the z-axis, inside (outside) of the cylinder of $k, k_z, \gamma_1, (\gamma_2)$ to the angles $\theta(\alpha)$. α is given by $n \sin\theta = \sin\alpha$ C) Angles in the projection of the rays in the xy-plane.

$$\begin{array}{lll} \partial_n \boldsymbol{S}^i = i\gamma_1 \cos\chi & \partial_n \boldsymbol{S}^r = -i\gamma_1 \cos\chi & \partial_n \boldsymbol{S}^t = i\gamma_2 \cos\sigma \\ \partial_t \boldsymbol{S}^i = i\gamma_1 \sin\chi & \partial_t \boldsymbol{S}^r = \quad i\gamma_1 \sin\chi & \partial_t \boldsymbol{S}^t = i\gamma_2 \sin\sigma \end{array} . \tag{2.53}$$

The first set of boundary conditions, the continuity of the field across the boundary, Eqs (2.41) and (2.42) becomes:

$$\begin{pmatrix} E_z \\ B_z \end{pmatrix}^i e^{i\gamma_1 S^i} + \begin{pmatrix} E_z \\ B_z \end{pmatrix}^r e^{i\gamma_1 S^r} = \begin{pmatrix} E_z \\ B_z \end{pmatrix}^t e^{i\gamma_2 S^t}. \tag{2.54}$$

Since these equations need to hold everywhere on the boundary, the phases need to be equal, thus yielding

$$\gamma_1 S^i = \gamma_1 S^r = \gamma_2 S^t. \tag{2.55}$$

Using the fact that the tangent components are continuous, we obtain

$$\gamma_1 \sin\chi = \gamma_1 \sin\chi = \gamma_2 \sin\sigma \quad \Rightarrow \quad \sin\chi = \frac{\gamma_2}{\gamma_1} \sin\sigma. \tag{2.56}$$

This equation can be identified as the generalized *Snell's Law* projected into the transverse plane. Noting that $\gamma_1^2 = n^2k^2 - k_z^2$ and $\gamma_2^2 = k^2 - k_z^2$. For $k_z = 0$, $\gamma_1 = nk$ and $\gamma_2 = k$, yielding then the well known Snell's law for a 2-d planar interface

$$n \sin\chi = \sin\sigma. \tag{2.57}$$

We can write the generalized Snell's Law in a completely geometric fashion noting (Fig. 2.3 for the geometry)

$$\frac{\gamma_2}{\gamma_1} = \frac{\gamma_2}{k_z}\frac{k_z}{\gamma_1} = \frac{\tan\theta}{\tan\alpha} \tag{2.58}$$

and for the 3d farfield angle $\sin\sigma$

$$\sin\sigma = \frac{\gamma_1}{\gamma_2}\sin\chi = \frac{\sin\alpha\,\cos\theta}{\cos\alpha\,\sin\theta}\sin\chi = \frac{n\cos\theta\,\sin\chi}{\sqrt{1-n^2\sin^2\theta}}. \tag{2.59}$$

The usual Snell's law hold also in the new geometry, in appropriate coordinates. In

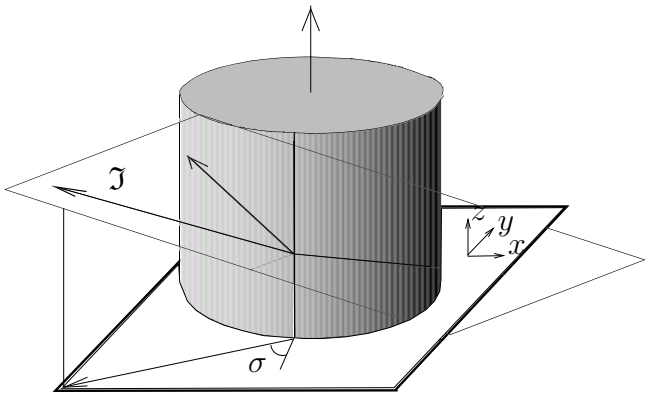

Figure 2.4: Schematics for semiclassical scattering. We will describe the semiclassical wave solution, with the coordinates (x, y) and a constant momentum in z. σ denotes the projected angle of the refracted.

the classical ray picture, the incident light spans together with the normal on the boundary a plane of incidence $\mathfrak{I}$, in which the reflection is governed by Snell's law

$$n\sin\eta_{in} = n_o\sin\eta_{out}. \tag{2.60}$$

n, n_o are the indices of refraction in each medium. The angle σ that we derived above is the projected emission angle in the (x, y) plane (see Fig. 2.4). Another geometric derivation is given in Appendix B. Snell's law already hints to an interesting feature of dielectric interfaces. If the angle of incidence $\sin\chi > \gamma_2/\gamma_1$ then the outside angle $\sigma = \frac{\pi}{2} + i\eta$ is complex. While the normal component of the ray is purely imaginary, the tangent component is purely real. Thus, locally the outside solution decays away from the interface as it should and propagates along the surface. This gives rise to a generalized *critical angle* (CA). We now analyse the transport properties across the interface.

2.4.2 Generalized Fresnel coefficients

All the results in the last section have been derived just from the first set of boundary conditions, the continuity of the tangential components. Now we will investigate the boundary conditions Eqs (2.43) and (2.44)

$$\mathfrak{B}^i \begin{pmatrix} E_z \\ B_z \end{pmatrix}^i e^{i\gamma_1 S^i} + \mathfrak{B}^r \begin{pmatrix} E_z \\ B_z \end{pmatrix}^r e^{i\gamma_1 S^r} = \mathfrak{B}^t \begin{pmatrix} E_z \\ B_z \end{pmatrix}^t e^{i\gamma_2 S^t} \tag{2.61}$$

where the matrices $\mathfrak{B}$ are given by

$$\mathfrak{B}^{(i,r)} = \begin{pmatrix} (n-n^3)\sin\theta\cdot\partial_t & \cos^2\alpha\cdot\partial_n \\ n^2\cos^2\alpha\cdot\partial_t & (n^3-n)\sin\theta\cdot\partial_n \end{pmatrix} \tag{2.62}$$

$$\mathfrak{B}^{t} = \begin{pmatrix} 0 & n^2\cos^2\theta\cdot\partial_n \\ n^2\cos^2\theta\cdot\partial_n & 0 \end{pmatrix} \tag{2.63}$$

With the derivative of the eikonal from Eq. (2.53) we get:

$$\mathfrak{B}^{i} = \begin{pmatrix} (n-n^3)\sin\theta\sin\chi & \cos^2\alpha\cos\chi \\ n^2\cos^2\alpha\cos\chi & (n^3-n)\sin\theta\sin\chi \end{pmatrix} \tag{2.64}$$

$$\mathfrak{B}^{r} = \begin{pmatrix} (n-n^3)\sin\theta\sin\chi & -\cos^2\alpha\cos\chi \\ -n^2\cos^2\alpha\cos\chi & (n^3-n)\sin\theta\sin\chi \end{pmatrix} \tag{2.65}$$

$$\mathfrak{B}^{t} = \begin{pmatrix} 0 & n\cos\sigma\cos^2\theta \\ n\cos\sigma\cos^2\theta & 0 \end{pmatrix} \tag{2.66}$$

We can now relate the incoming field to the outgoing and the reflected using the boundary conditions Eq. (2.54) and Eq. (2.61)

$$\Psi^r = R\Psi^i \tag{2.67}$$

$$\Psi^t = T\Psi^i \tag{2.68}$$

where R and T are the general Fresnel coefficients (matrices) given by

$$\begin{aligned} & \mathfrak{B}^i\Psi^i + \mathfrak{B}^r\Psi^r = \mathfrak{B}^t\Psi^i + \mathfrak{B}^t\Psi^r \\ \Rightarrow \quad & \left(\mathfrak{B}^r - \mathfrak{B}^t\right)\Psi^r = \left(\mathfrak{B}^t - \mathfrak{B}^i\right)\Psi^i \\ & \Rightarrow \quad \Psi^r = \left(\mathfrak{B}^r - \mathfrak{B}^t\right)^{-1}\left(\mathfrak{B}^t - \mathfrak{B}^i\right)\Psi^i \\ & \Rightarrow R = \left(\mathfrak{B}^r - \mathfrak{B}^t\right)^{-1}\left(\mathfrak{B}^t - \mathfrak{B}^i\right) \end{aligned} \tag{2.69}$$

and similarly

$$T = \left(\mathfrak{B}^t - \mathfrak{B}^r\right)^{-1}\left(\mathfrak{B}^i - \mathfrak{B}^r\right) \tag{2.70}$$

we can check that these are indeed the well known Fresnel equations by taking

$$\theta = 0 \quad \Rightarrow \quad \alpha = 0. \tag{2.71}$$

Resulting in the well-known classical Fresnel coefficients for a 2-d plane interface

$$R = \begin{pmatrix} \frac{n\cos\chi-\cos\sigma}{n\cos\chi+\cos\sigma} & 0 \\ 0 & \frac{\cos\chi-n\cos\sigma}{\cos\chi+n\cos\sigma} \end{pmatrix} \quad \widehat{=} \quad R = \begin{pmatrix} r_s & 0 \\ 0 & -r_p \end{pmatrix} \tag{2.72}$$

$$T = \begin{pmatrix} \frac{2n\cos\chi}{n\cos\chi+\cos\sigma} & 0 \\ 0 & \frac{2\cos\chi}{\cos\chi+n\cos\sigma} \end{pmatrix} \quad \widehat{=} \quad T = \begin{pmatrix} t_s & 0 \\ 0 & t_p \end{pmatrix}. \tag{2.73}$$

Returning to the comment made in the last Section, we will now investigate the region where the angle of incidence is larger than the critical angle. Let us rewrite the reflection matrix R in Eq. (2.72) using

$$\cos\sigma = i\sqrt{n^2 \sin\chi^2 - 1} \quad \forall \quad \left(\sin\chi > \frac{1}{n}\right) \tag{2.74}$$

we can see that both r_s and r_p are of the from $\frac{a+ib}{a-ib}$, with $a, b \in \mathbb{R}$. We know that the absolute value of such a complex number is 1. We will therefore have perfect reflection on the boundary. Note however that the polarization will change upon reflection. For the transmission matrix we can show that the outgoing field decays exponentially and that the energy transfer vanishes [70]. These observations also hold true for $\theta \neq 0$.

In the subsequent chapters we will solve for the resonances of the circular dielectric rod and numerically find solutions for a deformed rod. We will make ample use of these solutions in Chapter 5 where we will discuss experiments on polymer microlasers and in Chapter 8 where GaN cavities are covered. The solutions for the vector wave-equation will enable us to discuss the polarization of hybrid modes in Chapter 7. In the following Chapter 3 we will go over the underlying ray-dynamics for generally deformed cavities, to form a basis for discussion of the semiclassical aproximations and correspondence.

Chapter 3

Ray-dynamics in deformed Cavities

3.1 Introduction

Ray-dynamics (geometric optics) is a powerful tool used for many applications in everyday optics. The application we are going to be interested in is the description of dielectric microcavities. In Chapter 1, we made the connection between wave solutions of dielectric cavities in the short-wave-length limit and ray-dynamics in those cavities. In many cases the motion of rays corresponds to the classical mechanics of a point mass, e.g. reflection elastically from a boundary. In the non-linear dynamics community these systems are termed billiards. The 'leakyness' of dielectric billiards represents an extension to the canonical billiard system. The microcavities that we will investigate in this thesis will have a general non-integrable shape. Since billiards represent a class of Hamiltonian systems, it will be useful to discuss Hamiltonian systems and specifically the transition from integrability to partially chaotic (mixed) dynamics first. Action-angle variables will help us illustrate the breakdown of perturbation theory for non-integrable systems, as described by the KAM theory. A powerful tool, the surface of section, is introduced to facilitate the discovery of unbroken tori. The three classes of fixed-points are analyzed in general and for special maps. Next, we discuss discrete maps and their fixed-point analysis. Bifurcations will be explained in this context and we will follow the bifurcation diagram of a stable orbit in a generic shape. We conclude with the effects of an open system with refractive escape and describe the numerical simulations and its relation to experiments. A good review of the Hamiltonian dynamics can be found in Ref. [71]. Some parts of the discussion might be a bit dry, but bear with us, as the understanding of ray-dynamics will help us explain and predict the lasing emission of micro cavity lasers.

3.2 Hamiltonian Dynamics

We consider here classical systems governed by a Hamiltonian function

$$H(\boldsymbol{q}, \boldsymbol{p}) = E \tag{3.1}$$

where $\boldsymbol{q} = (q_1, \ldots, q_N)$ and $\boldsymbol{p} = (p_1, \ldots, p_N)$ are generalized positions and momenta of a system with N-degrees of freedom and the energy E. Solving Hamilton's equation

$$\dot{\boldsymbol{q}} = \quad \nabla_{\boldsymbol{p}} H \tag{3.2}$$
$$\dot{\boldsymbol{p}} = -\nabla_{\boldsymbol{q}} H \tag{3.3}$$

given some initial conditions $\{\boldsymbol{q}(0), \boldsymbol{p}(0)\}$ we can find the history $\boldsymbol{q}(t)$ of this system. A Hamiltonian system is called *integrable* if we can find N independent analytic single-valued functions that are constant along any trajectory

$$F_m(\boldsymbol{q}, \boldsymbol{p}) = f_m, \quad 1 \leq m \leq N. \tag{3.4}$$

Furthermore the constants of motion F_m must be 'in involution', i.e. they need to fulfill the *Poisson bracket* [72]

$$\{F_m, F_n\} \equiv \nabla_{\boldsymbol{p}} F_m \cdot \nabla_{\boldsymbol{q}} F_n - \nabla_{\boldsymbol{p}} F_n \cdot \nabla_{\boldsymbol{q}} F_m = 0. \tag{3.5}$$

With this equation we can solve for $\boldsymbol{p}$ in terms of $(\boldsymbol{q}, \boldsymbol{f})$. A *canonical transformation* is a transformation from one set of Hamiltonian variables $(\boldsymbol{p}, \boldsymbol{q})$ to another set $(\boldsymbol{P}, \boldsymbol{Q})$, which leaves the equations of motion unchanged. We can regard the F_m as new momenta $\tilde{\boldsymbol{p}} = \boldsymbol{F}$ in a canonical transformation to new variables $(\tilde{\boldsymbol{q}}, \tilde{\boldsymbol{p}})$. As $\boldsymbol{p}$ is constant Eq. (3.3) gives us the independence of the new Hamiltonian to $\tilde{\boldsymbol{q}}$ and thus it follows from Eq. (3.2)

$$\tilde{\boldsymbol{q}}(t) = \nabla_{\boldsymbol{f}} H(\boldsymbol{f})\, t + \boldsymbol{c}, \quad \text{with} \quad \boldsymbol{c} \text{ and } \nabla_{\boldsymbol{f}} H(\boldsymbol{f}) = \text{const.} \tag{3.6}$$

The problem is solved once we can express $\tilde{\boldsymbol{q}}$ in terms of $\boldsymbol{q}$ which can be done with the generating function $G(\boldsymbol{q}, \tilde{\boldsymbol{p}})$

$$G(\boldsymbol{q}, \tilde{\boldsymbol{p}}) = \int_{q_0}^{q} \boldsymbol{p}(\boldsymbol{q}, \tilde{\boldsymbol{p}})\, d\boldsymbol{q} = \int_{q_0}^{q} \boldsymbol{p}(\boldsymbol{q}, \boldsymbol{f})\, d\boldsymbol{q} = G(\boldsymbol{q}, \boldsymbol{f}) \tag{3.7}$$

where $\boldsymbol{p}(\boldsymbol{q}, \boldsymbol{f})$ is obtained from Eq. (3.4), yielding

$$\tilde{\boldsymbol{q}}(t) = \nabla_{\boldsymbol{f}} G(\boldsymbol{q}, \boldsymbol{f}). \tag{3.8}$$

Any classically integrable system can be solved in this fashion. The N constants of motion restrict each trajectory to lie on a N-dimensional manifold $\mathcal{M}$. In any *conservative system* the energy is conserved and we are guaranteed one constant of motion

$$F_1(\boldsymbol{q}, \boldsymbol{p}) = f_1 = E(\boldsymbol{q}, \boldsymbol{p}) = \text{const.} \tag{3.9}$$

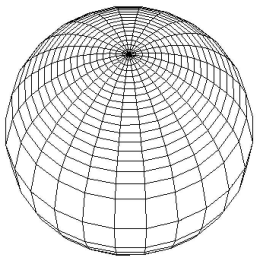
A)

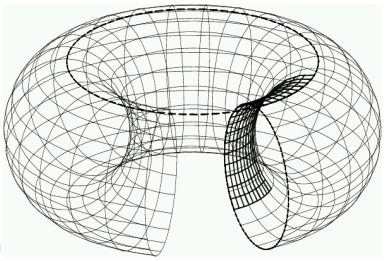
B)

Figure 3.1: 2-d Manifolds. The sphere A) is clearly not a 'parallelizable' manifold, the 2-d Torus B) is. We could not comb the sphere without a singularity.

The energy surface upon which motion in a conserved system can take place is thus $2N-1$ dimensional. The topological structure of the manifold $\mathcal{M}$ is going to be important, we will investigate it now. The manifold $\mathcal{M}$ is defined by fixing the f_m. The normals of the manifold are given by $\hat{\boldsymbol{n}}_n = (\nabla_{\boldsymbol{q}} F_n, \nabla_{\boldsymbol{p}} F_n)$. Consider N $2N$-component-vector fields in phase space

$$V_m \equiv \begin{pmatrix} \nabla_{\boldsymbol{p}} F_m \\ -\nabla_{\boldsymbol{q}} F_m \end{pmatrix}, \tag{3.10}$$

and we can see that the vector field V_m is perpendicular to the normals of the manifold $\mathcal{M}$

$$\begin{aligned} \hat{\boldsymbol{n}}_n \cdot V_m &= (\nabla_{\boldsymbol{q}} F_n, \nabla_{\boldsymbol{p}} F_n) \begin{pmatrix} \nabla_{\boldsymbol{p}} F_m \\ -\nabla_{\boldsymbol{q}} F_m \end{pmatrix} \\ &= \{F_m, F_n\} = 0. \end{aligned} \tag{3.11}$$

Thus the vector field V_m is *parallel* to the manifold $\mathcal{M}$. If we restrict ourselfs to a finite phase space, i.e. bounded motion, the manifold is thus compact and 'parallelizable' with a smooth and independent vector field. A theorem from topology states that any such object is a N-torus (Fig. 3.1). The systems we will be dealing with are either 2-d or 3-d. In the 3-d case we will only consider dynamics which we can project on a 2-d space with a contant motion along the third dimension. The dimensionality of the phase space is thus 4, the energy surface 3-d and the manifolds $\mathcal{M}$ on which the motion in an integrable system will take place, 2-d. The tori are called *invariant tori* as the motion started on one will remain on it forever. Naturally we want to use as coordinates $(\tilde{\boldsymbol{q}}, \tilde{\boldsymbol{p}})$. Every constant of motion, or generalized momentum $\tilde{\boldsymbol{p}} = \boldsymbol{f}$ defines a torus, on which $\tilde{\boldsymbol{q}}$ are the coordinates. A natural set of variables well-suited for integrable systems are the *action-angle variables*. They can be obtained by a canonical transform and are chosen such that

$$\boldsymbol{J} \mathrel{\widehat{=}} \tilde{\boldsymbol{p}} \quad \textit{action} \text{ of the torus} \tag{3.12}$$

$$\boldsymbol{\Theta} \mathrel{\widehat{=}} \tilde{\boldsymbol{q}} \quad \textit{angles} \text{ on the torus.} \tag{3.13}$$

The action variable $\boldsymbol{J}$ defines the torus and the $\boldsymbol{\Theta}$ are the coordinates on the torus which are periodic with period 2π. The equations of motion in terms of action-angle

variable are

$$\boldsymbol{J} = \text{ const.}, \quad \text{and} \quad \boldsymbol{\omega} = \nabla_{\boldsymbol{J}} H(\boldsymbol{J}) = \text{ const.} \tag{3.14}$$

with the frequency vector on the torus $\boldsymbol{\omega}(\boldsymbol{J}) = \nabla_{\boldsymbol{J}} H(\boldsymbol{J})$ we can finally write

$$\boldsymbol{\Theta} = \boldsymbol{\omega}(\boldsymbol{J})\, t + \boldsymbol{c}, \quad \text{with} \quad \boldsymbol{c} = \text{ const.} \tag{3.15}$$

There are two different possibilities for the orbit on the manifold $\mathcal{M}$. If the frequencies are commensurable,

$$\boldsymbol{\omega} \cdot \boldsymbol{m} = 0, \quad \text{for some} \quad \boldsymbol{m} = (m_1, \ldots, m_N) \in \mathbb{N}^N \tag{3.16}$$

the orbit on $\mathcal{M}$ is *closed*, i.e. it will wrap arount the torus on a 1-d region on $\mathcal{M}$. If the frequencies are not commensurable, the orbit *never closes* and will trace out a helix on $\mathcal{M}$ till it covers it densely after an infinite time.

3.2.1 Perturbation theory on tori

We will now discuss the effect of a generic non-integrable perturbation $\varepsilon H_1(\boldsymbol{J}, \boldsymbol{\Theta})$ on an integrable system. The new Hamiltonian reads

$$H(\boldsymbol{J}, \boldsymbol{\Theta}) = H_o(\boldsymbol{J}) + \varepsilon H_1(\boldsymbol{J}, \boldsymbol{\Theta}). \tag{3.17}$$

$\boldsymbol{J}$ and $\boldsymbol{\Theta}$ are no longer action-angle variables as $\boldsymbol{\Theta}$ appears in H. If the perturbed system is still integrable there must be a new set of variables $(\boldsymbol{J'}, \boldsymbol{\Theta'})$ such that

$$H(\boldsymbol{J}, \boldsymbol{\Theta}) = H'(\boldsymbol{J'}). \tag{3.18}$$

This should be achieved via a generating function $G(\boldsymbol{J'}, \boldsymbol{\Theta})$ such that

$$\begin{pmatrix} \boldsymbol{J} \\ \boldsymbol{\Theta} \end{pmatrix} \quad \leftarrow \quad \begin{matrix} \boldsymbol{J} = \nabla_{\boldsymbol{\Theta'}} G \\ \nabla_{\boldsymbol{J'}} G = \boldsymbol{\Theta} \end{matrix} \quad \rightarrow \quad \begin{pmatrix} \boldsymbol{J'} \\ \boldsymbol{\Theta'} \end{pmatrix} \tag{3.19}$$

resulting in

$$H\left(\nabla_{\boldsymbol{\Theta}} G(\boldsymbol{J'}, \boldsymbol{\Theta}), \boldsymbol{\Theta}\right) = H'\left(\boldsymbol{J'}\right). \tag{3.20}$$

Expanding G in powers of ε and keeping only the first order terms

$$G = \boldsymbol{\Theta} \cdot \boldsymbol{J'} + \varepsilon G_1(\boldsymbol{J'}, \boldsymbol{\Theta}) + \ldots \tag{3.21}$$

we can write for the Hamiltonian

$$H_o(\boldsymbol{J'}) + \varepsilon \nabla_{\boldsymbol{J'}} H_o(\boldsymbol{J'}) \cdot \nabla_{\boldsymbol{\Theta}} G_1 + \varepsilon H_1(\boldsymbol{J'}, \boldsymbol{\Theta}) = H'(\boldsymbol{J'}). \tag{3.22}$$

Remembering that $\nabla_{\boldsymbol{J'}} H_o = \boldsymbol{\omega}_o(\boldsymbol{J'})$ and that both H_1 and G_1 are functions of $\boldsymbol{p}$ and $\boldsymbol{q}$ and which are themselves periodic in $\boldsymbol{\Theta}$, we can fourier expand H_1 and G_1 in $\boldsymbol{\Theta}$

$$H_1(\boldsymbol{J}, \boldsymbol{\Theta}) = \sum_{m} H_{1m}(\boldsymbol{J}) e^{i\boldsymbol{m}\cdot\boldsymbol{\Theta}}, \quad \text{and} \quad G_1(\boldsymbol{J'}, \boldsymbol{\Theta}) = \sum_{m} G_{1m}(\boldsymbol{J'}) e^{i\boldsymbol{m}\cdot\boldsymbol{\Theta}}. \tag{3.23}$$

With this, the generator G reads as

$$G(\boldsymbol{J'}, \boldsymbol{\Theta}) = \boldsymbol{J'} \cdot \boldsymbol{\Theta} + i\varepsilon \sum_{m \neq 0} \frac{H_{1m}(\boldsymbol{J'})}{\boldsymbol{m} \cdot \boldsymbol{\omega}_o(\boldsymbol{J'})} e^{i\boldsymbol{m}\cdot\boldsymbol{\Theta}} + \dots \ . \tag{3.24}$$

Can we now continue with this method and write a perturbation theory for non-integrable systems? The problem that we will encounter is the quotient $\boldsymbol{m} \cdot \boldsymbol{\omega}_o$. We have noted above that if the frequencies are commensurable this product vanishes and thus the sum should diverge. Even if the frequencies are non-commensurable we can find $\boldsymbol{m}$ such that the product is arbitrary small. This is the *problem of small divisors* that has been around for a long time. Thankfully, Kolmogorov [73], Arnol'd [74] and Moser [75] (KAM) solved this problem and showed that for a given perturbation the sum can still converge most of the time. For a 4-d phase space and thus on a 2-d manifold $\mathcal{M}$ we will sketch the problem here. KAM have shown that the series in Eq. (3.24) converges for all tori with *sufficiently irrational* frequencies (ω_1, ω_2) such that

$$\left| \frac{\omega_1}{\omega_2} - \frac{r}{s} \right| \geq \frac{K(\varepsilon)}{s^{2.5}}, \quad \forall \{r, s\} \in \mathbb{N} \tag{3.25}$$

where K is just some function of the perturbation strength independent of r and s.

3.2.2 Digression on Irrationality

Now what do we really mean by sufficiently irrational? Can different irrational numbers be better approximated with rational numbers than others? The surprising answer is, yes, indeed. A simple way of finding rational approximations in our decimal system is to just take the first few digits and divide by the corresponding power of 10, i.e. for $\sigma \in \mathbb{R} \setminus \mathbb{Q}$

$$\sigma = e = 2.71828182845905\ldots \approx \frac{r}{s} = \frac{2}{1}, \frac{27}{10}, \frac{278}{100}, \frac{2782}{1000}, \frac{27821}{10000}, \ldots \tag{3.26}$$

This error of this approximation is trivially

$$\left| \sigma - \frac{r}{s} \right| < \frac{1}{s}. \tag{3.27}$$

It can be shown that a much better approximation can be achieved through the *continued fraction* given by

$$\sigma = e = 2 + \cfrac{1}{1 + \cfrac{1}{2 + \cfrac{1}{1 + \cfrac{1}{1 + \cfrac{1}{4 + \cdots}}}}}. \tag{3.28}$$

It can be shown that the ratio produced by this fashion is the *best* approximation such that there is no better approximation with smaller denominators. One can show that for continued fraction

$$\left|\sigma - \frac{r_n}{s_n}\right| \leq \frac{1}{s_n s_{n-1}}. \tag{3.29}$$

With this we can construct the 'worst-to-approximate' irrational number, namely

$$\frac{\sqrt{5}+1}{2} = 1.6180339887\ldots = 1 + \cfrac{1}{1 + \cfrac{1}{1 + \cfrac{1}{1 + \cfrac{1}{1 + \cfrac{1}{1+\cdots}}}}}, \tag{3.30}$$

the *golden mean*. The torus with the frequency ratios being the golden mean is thus the last torus to break under a perturbation! For small perturbations how many tori will break? We can study this by asking the inverse to Eq. (3.25), namely how many 'too rational' numbers exits at which the tori will break. Around each of the 'too rational' ratios r/s between $[0,\ldots,1]$ we exclude a line of length $K(\varepsilon)/s^{2.5}$. These are the tori which will definitely break under a perturbation ε. The total length of this line, with an upper limit of s ratios r/s, is at least

$$L \leq \sum_{s=1} \frac{K(\varepsilon)}{s^{2.5}} s = K(\varepsilon) \sum_{s=1} \frac{1}{s^{1.5}} = K(\varepsilon) \cdot \text{ const.} \tag{3.31}$$

For $K(\varepsilon) \to 0$ this line tends to vanish, thus for small perturbations most tori remain unbroken. Conversely there is a maximal perturbation ε at which *all* tori are broken.

3.2.3 Poincaré Surface of Section & discrete maps

How can we study the effect of such a perturbation and determine if there are remaining local constants of motion in the phase space? It can be very difficult to determine all constants of motion, for a 2-d system by direct analysis. A particularly good method to study phase space structures was devised by Poincaré in 1890 [76]. Consider the 4-d phase space with Hamiltonian

$$H(q_1, p_1, q_2, p_2), \tag{3.32}$$

for our conservative systems, the energy E is a first constant of motion and we can write one of the momenta as $p_2 = p_2(q_1, p_1, q_2, E)$. Trajectories will thus lie on a 3-d volume within the 4-d phase space (note that the structure is in general not that of the Euclidian $\mathbb{R}^3$). If we only plot the trajectory for $q_2 = Q$ =const., we will observe the motion on a 2-d section of the volume, the so called *surface of section* (SOS). The surface of section can be viewed as a discrete map T which maps the point $(q_1, p_1) \xrightarrow{T} (q_2, p_2)$. As the motion is governed by a conservative Hamiltonian, this map T is *area preserving*, i.e. an area mapped by T conserves its area.

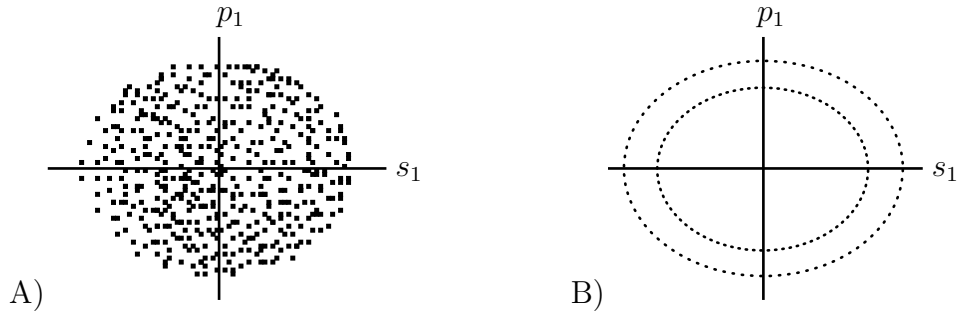

Figure 3.2: Poincaré surface of section. A) no additional constant of motion is present and the motion will produce a 2-d scatter of points. B) another constant of motion can be found, the motion is confined to a 1-d area of the surface of section.

The resulting plot can give either 1) a 2-d scatter of points, indicating broken tori (Fig. 3.2 A), or 2) a 1-d curve indicating the existence of a second (local) constant of motion. This constant of motion is specified by the curve $T(\mathcal{C}) = \mathcal{C}$ (Fig. 3.2 B).

3.2.4 Fixed points of general maps

If an orbit closes on the manifold $\mathcal{M}$ it will appear in the surface of section as a set of N points. These fixed-point are defined by $T^N(x) = x$, where N denotes the period of this orbit. We will later see how important the surface of section will be in understanding the ray-dynamics in micro-cavities. But first let us analyze the integrability – non-integrability transition in general area-preserving maps. For this we will study discrete area preserving maps. KAM does not tell us anything about what will happen to general fixed-points. For this purpose a simple, non-integrable *Twist Map* was devised by Moser that will help us understand what happens

$$\begin{pmatrix} p_{n+1} \\ q_{1+1} \end{pmatrix} = T_\varepsilon \begin{pmatrix} p_n \\ q_n \end{pmatrix}, \quad \text{such that} \quad \begin{cases} p_{n+1} = p_n + \varepsilon F(p_n, q_n) \\ q_{n+1} = q_n + 2\pi\alpha(p_n) + \varepsilon G(p_n, q_n) \end{cases} . \tag{3.33}$$

We require F and G to be periodic in 2π, that it keeps the map area preserving and that for $p = 0$, $F = G = 0$ such that a fixpoint at 0 exists. As we vary p, for $\varepsilon = 0$, the points will lie on different concentric circles. When the *winding number* α is equal to a rational number $\alpha = r/s$ with r and s coprime, the map will consist of s discrete points on a circle. We will now show that for a fixed-point of this map of order N, an even multiple of N fixed-points will remain after a small pertubation. This is known as the *Poincaré-Birkhoff fixed point theorem*. To show this we plot the twist map for three different values of α, see Fig. 3.3. On $\mathcal{C}$ the we have $\alpha = r/s$, the curve $\mathcal{C}^+$ and $\mathcal{C}^-$ are above and below with an α bigger and smaller than r/s. A map T^s will leave a point on $\mathcal{C}$ invariant. The same map T^s will move a point on $\mathcal{C}^+$ clockwise and on $\mathcal{C}^-$ counter-clockwise. This behavior will remain even after a small perturbation ε, thus a point R_ε in the vicinity of $\mathcal{C}$ will have a point that is unchanged by T^s_ε. The curve R_ε spanned by these points will under iteration of T^s_ε intersect

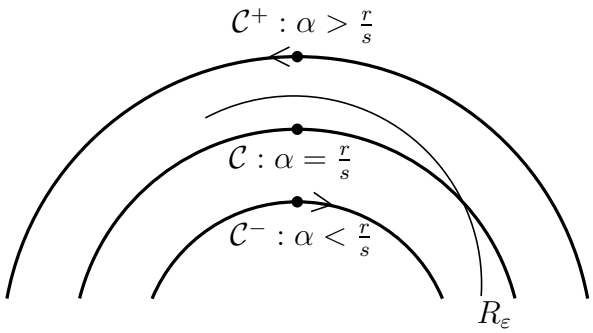

Figure 3.3: The action of the twist map (Eq. (3.33)) on the different invariant curves. The map curve $\mathcal{C}$ is invariant under T^s. The map T^s will move a point on $\mathcal{C}^+$ clockwise and on $\mathcal{C}^-$ counter-clockwise. A perturbed mapping T_ε preserves these relative twists for small ε. The curve R_ε must have at least one point in common with $\mathcal{C}$.

with itself and due to the area preservation be of same size and centered around the origin, see Fig. 3.4. Therefore an even number of fixed-points are preserved under the perturbation. As the flow in the vicinity of the fixed-points is conserved we can already see from Fig. 3.4 that there are two different types of fixed-points. One type, $\mathcal{E}$ where the flow circulates around the fixed-point; the second type, $\mathcal{H}$ where the flow diverges.

3.2.5 Tangent Map

To analyze the behavior around the fixed-points more quantitatively it is useful to look at the linearized map M, the *tangent map* of T_ε. Let (q_o, p_o) be a fixed-point of the map M, of order μ i. e. $(q_o, p_o) = (q_\mu, p_\mu) = T_\varepsilon^\mu(q_o, p_o)$. The linearized map M is defined by

$$M = \frac{\partial(q_\mu, p_\mu)}{\partial(q_o, p_o)} = \begin{pmatrix} \frac{\partial q_\mu}{\partial q_o} & \frac{\partial q_\mu}{\partial p_o} \\ \frac{\partial p_\mu}{\partial q_o} & \frac{\partial p_\mu}{\partial p_o} \end{pmatrix}. \tag{3.34}$$

This map is also known as the *monodromy matrix* or in optics as the *ABCD matrix* for reflections from a curved mirror (assuming a billiard geometry). The behavior of a deviation $(\delta q, \delta p)$ around the fixed-point (q_o, p_o) can be determined by finding the eigenvalues of the linearized map M.

$$\begin{pmatrix} \delta q_\mu \\ \delta p_\mu \end{pmatrix} = \begin{pmatrix} \frac{\partial q_\mu}{\partial q_o} & \frac{\partial q_\mu}{\partial p_o} \\ \frac{\partial p_\mu}{\partial q_o} & \frac{\partial p_\mu}{\partial p_o} \end{pmatrix} \begin{pmatrix} \delta q_o \\ \delta p_o \end{pmatrix}. \tag{3.35}$$

The eigenvalues of every 2×2 matrix are given by the trace and the determinant, (since the map is area preserving $\det M = 1$)

$$\lambda^2 - (\mathrm{Tr} M)\lambda + \det M = 0 \tag{3.36}$$

$$\lambda_\pm = \frac{1}{2}\Big(\mathrm{Tr} M \pm \sqrt{\mathrm{Tr}^2 M - 4}\Big). \tag{3.37}$$

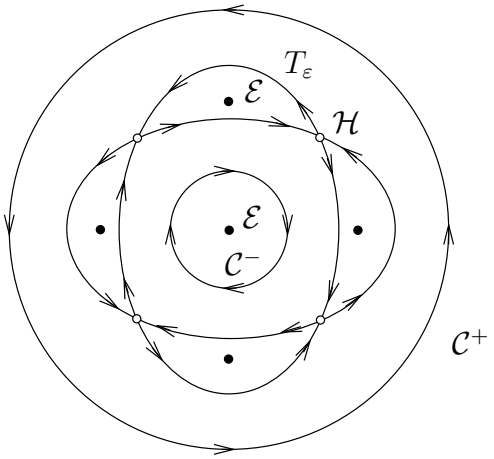

Figure 3.4: The curves $\mathcal{C}^+$ and $\mathcal{C}^-$ are on the outside and inside. Inside we show R_ε and $T_\varepsilon R_\varepsilon$. These curves must intersect an even number of times. The flow on the curves is indicated by the arrows. We see that the flow around $\mathcal{E}$ (solid points) is *elliptic* and around $\mathcal{H}$ (hollow points) *hyperbolic*.

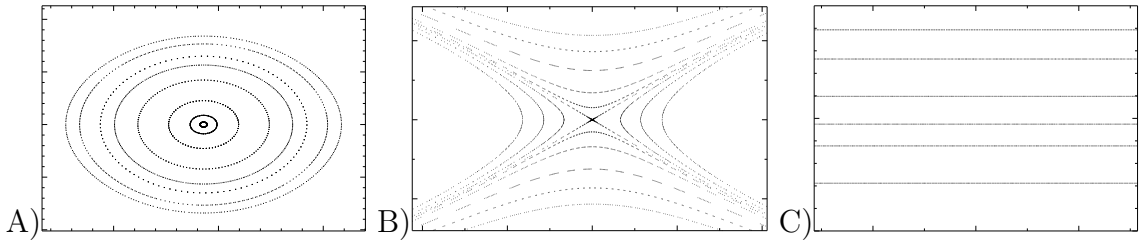

Figure 3.5: Motion in the vicinity of fixed-points. A) When the eigenvalues of the monodromy matrix are complex conjugates, the fixed-point is stable, motion around the fixed-point proceeds on ellipses. B) Near a hyperbolic fixed-point the eigenvalues are real and the motion proceeds on hyperbolas. C) Parabolic fixed-point define marginally stable motion. The invariant curves are straight lines.

The eigenvalues are thus either *real* reciprocals $\lambda_+\lambda_- = 1$ or *complex conjugates* on the unit circle, or else degenerate with $\lambda_+ = \lambda_- = \pm 1$.

- For $\lambda_+ = \lambda_-^*$ we can write

$$\lambda_+ = e^{i\phi}, \quad \text{and} \quad \lambda_- = e^{-i\phi}; \tag{3.38}$$

thus the eigenvectors must be complex conjugates $\mathfrak{u}, \mathfrak{u}^*$. In this case we can write the map as

$$M = e^{i\phi}\mathfrak{u} + e^{-i\phi}\mathfrak{u}^* \tag{3.39}$$

which just describes motion on an ellipse. Thus iterations of a small deviation in the vicinity of such a fixed-point will rotate around an ellipse as shown in Fig. 3.5 A). Such a fixed-point is of *elliptic* type. Motion around an elliptic fixed-point is *stable*, as any point near them will remain near them for an arbitrary number of iterations of the map.

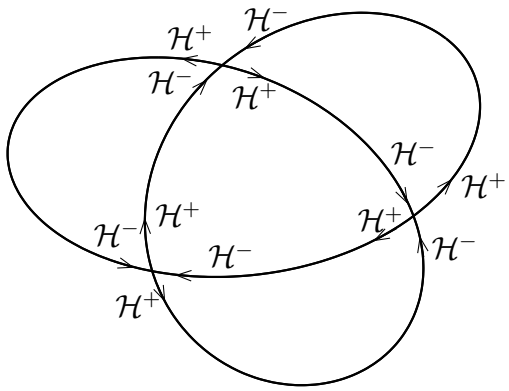

Figure 3.6: Hyperbolic fixed-point in an integrable system. The invariant curves $\mathcal{H}^+$ of the fixed-point join smoothly with $\mathcal{H}^-$.

- For real eigenvalues $\left\{\lambda_+ = \lambda_-^{-1}\right\} \in \mathbb{R}$ the map can be reduced to

$$M = \lambda_{1/2}\mathfrak{u} \quad \text{with} \quad \lambda_{1/2} = \left\{\lambda, \lambda^{-1}\right\}. \tag{3.40}$$

  The invariant curves are thus hyperbolae as shown in Fig. 3.5 B) and the corresponding fixed-point is called a *hyperbolic fixed-point*. Two different types of hyperbolic fixed-points exist. For $\lambda > 0$ the fixed point is said to be *ordinary hyperbolic* as the iterates remain on one branch of the hyperbola. For $\lambda < 0$ the fixed-point is of *inversion hyperbolic* type, where iterates jump back and forth between opposite branches. Hyperbolic fixed-points are said to be *unstable* as motion in their vicinity is not confined. Motion on one branch approaches the fixed-point, while the other repells exponentially.

- In the degenerate case where $\lambda_+ = \lambda_- = \pm 1$ we have a *parabolic fixed-point*. Any deviation will increase linearly. Invariant curves corresponding to this type of fixed-point are straight lines as shown in Fig. 3.5 C). This type of motion is often referred to as *marginably stable* motion.

3.2.6 Manifolds and their crossings

We will now leave the realm of linear motion and enter the non-linear regime, i.e. the exact map. At any hyperbolic fixed-point $\mathcal{H}$, four branches meet. Two are incoming ($\mathcal{H}^-$) and two are outgoing ($\mathcal{H}^+$). A point on an incoming branch will move exponentially close to the fixed-point, whereas a point on the outgoing branch will move away exponentially. In the case of an integrable system the outgoing invariant curve $\mathcal{H}^+$ joins the incoming invariant curves $\mathcal{H}^-$ of a neigbouring hyperbolic point. Compare to Fig. 3.6 where we have illustrated this behavior. This smooth joining is only present in integrable systems, as we will see in Section 3.3.3 the elliptic billiard will feature such a hyperbolic fixed-point. In the generic case where they do not smoothly connect they have to intersect. Every intersection of a branch with itself has to be a fixed-point. The invariant curve $\mathcal{H}^+$ represents an *unstable manifold*

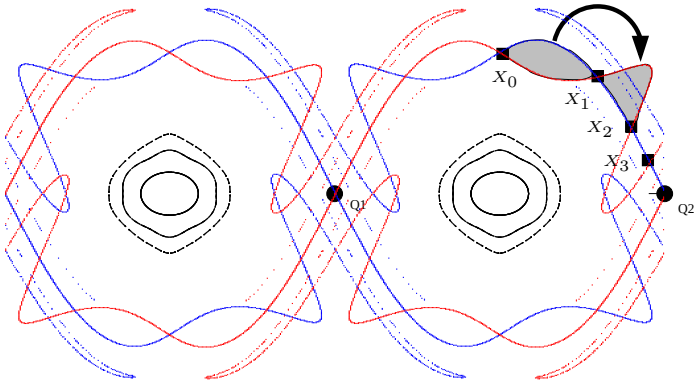

Figure 3.7: Motion close to a Hyperbolic fixed-point in a non-integrable system. The (blue) invariant curves $\mathcal{H}^+$ of the fixed-point intersects the (red) invariant curve $\mathcal{H}^-$ at the homoclinic points $\{X_0, X_1, X_2, X_3, \ldots, X_\infty\}$. The grey shaded area has to remain constant due to the area preserving character of the map T.

while $\mathcal{H}^-$ is a *stable manifold*. What happens if two different branches, $\mathcal{H}^+$ and $\mathcal{H}^-$ intersect each other? The intersections are called *homoclinic* if the manifolds emanate from the same fixed-point $\mathcal{H}$ or to different points of the same unstable closed orbit. Intersection of invariant curves of different hyperbolic fixed-points are called *heteroclinic*. As homoclinic points lie on the stable and unstable manifold of the fixed-point, so must its iterate through the map T, thus one homoclinic point implies an infinite number. We will later see that unstable manifolds play a significant role in the emission directionality of micro-cavities (see Section 5.7) and that wavefunctions in microcavities can localize around homoclinic points (see Fig. 4.10).

3.2.7 Onset of Chaos

In this section we will finally understand from where chaos originates! The area preservation combined with the existence of *one* homoclinic point is enough. As we have seen above, the existence of one homoclinic point implies an infite number, due to the area preserving property of the map, the area enclosed by the invariant curves between two such homoclinic points must be preserved. In Fig. 3.7 we show this behavior. As the homoclinic points will come closer and closer to each, the loop around the area (shaded in grey) must become longer and longer. It becomes clear that these invariant curves are *area filling*, as they need to explore more and more of the phase space. No torus exists in this region. A proof of this for the simplified 'horseshoe map' has been given by Smale [77]. They can nevertheless be bounded by other stable tori, such that they are limited to a finite area of the phase space. This is at least true in the 4-d phase space, in higher dimensions we expect *Arnol'd diffusion*, where chaotic areas do not need to be separated by invariant curves.

3.3 Billiards – Discrete Maps

In this section we want to apply the theory reviewed in the previous section to billiard maps and with that we get closer to the goal of describing the ray-dynamics in a microcavity. Ray-dynamics in cavities of arbitrary (convex) shape can be looked upon as the motion of a particle elastically scattered from the boundary if we neglect refraction. We will first consider motion in a closed resonator, the fully classical billiard problem. In order to be able to describe the motion in a billiard as a discrete map we need to introduce *Birkhoff coordinates* [41]. A self-contained treatment of classical mechanics in various billiard systems has been given by Berry in Ref. [42].

3.3.1 Birkhoff Coordinates

The motion in a classical billiard consists of straight line segments and specular reflections from the boundary. Two coordinates describe this system exactly. We record at each collision with the boundary the arc-length s and the tangential momentum p_t of the incident particle. Each consecutive collision is marked with ascending integers n. The set of collisions is given by the discrete map T. This map is area preserving as the Hamililtonian of the system is conservative. It is convenient to use the radial angle ϕ instead of s.[1] The coordinates are then not anymore canonical conjugates but the information obtainable from the map is not changed. For the transverse momentum it is convenient to scale out the energy of the particle and instead use the variable

$$\sin\chi = \frac{p_t}{\sqrt{2mE}} \tag{3.41}$$

for the transverse momentum. Here χ is the angle of incidence with respect to the normal at position ϕ on the boundary, m the mass and E the energy of the particle.

3.3.2 Circle map

The first map we want to consider is the map of ray motion inside a circle. In Section 1.2 we have seen that an important group of resonators are based on microdisks, which have the cross section of a circle. In the circle the normal at each point on the boundary goes through the origin. The angle of incidence will thus be conserved and hence also the angular momentum. For the map we write

$$\sin\chi_{n+1} = \sin\chi_n \tag{3.42}$$

$$\begin{aligned}\phi_{n+1} &= \pi - 2\chi \\ &= 2\arccos(\sin\chi) + \phi_n.\end{aligned} \tag{3.43}$$

The eigenvalues of the monodromy matrix are degenerate for all χ and we have only *parabolic* fixed-points. In Fig. 3.8 we show the SOS of the circle and indicate a

[1] This holds true for star shaped objects, objects where every point on the boundary can be connected with a straight line to the origin.

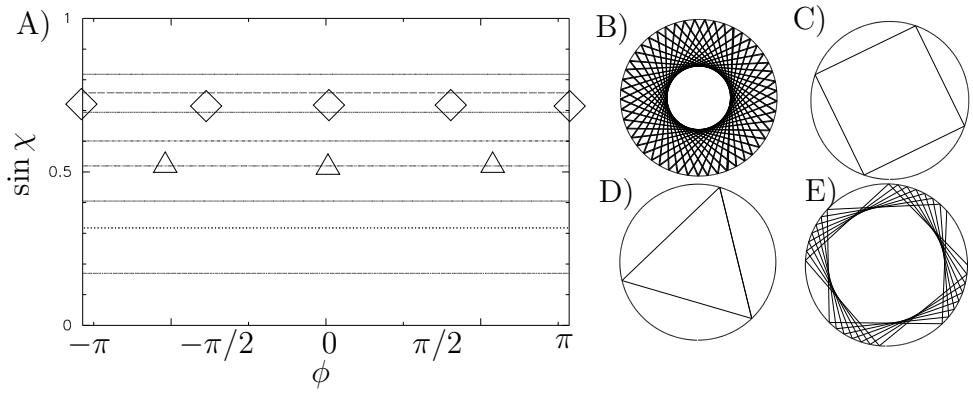

Figure 3.8: A) Surface of Section of the ray-dynamics in the circle. B) real space pictures of the whispering gallery type orbit, C) the rectangular orbit where the torus has the exact ratio of $r/s = 1/4$. D) the triangle with $r/s = 1/3$. E) a quasi periodic orbit close to the rectangular orbit with a frequency slightly above the one in C).

number of different fixed-points. On the right hand side of the figure we show four real space trajectories.

3.3.3 Ellipse map

The ellipse is the only other integrable convex billiard besides the circle [78].[2] The existence of a second conserved quantity besides the energy, namely the product of the angular momenta around the two foci, guarantees the integrability of the ellipse. For later reference, we will define here the equation of the ellipse in polar coordinates, scaled to area π

$$r(\phi) = \frac{1+\varepsilon}{\sqrt{1+[(1+\varepsilon)^4-1]\sin^2\phi}}, \tag{3.44}$$

here ε corresponds to the deformation (major to minor axis ratio) of the ellipse. Another way of writing the ellipse is by $\Gamma(x,y) = x^2/a^2 + y^2/b^2 - 1 = 0$. Using this we can write an algebraic map

$$\begin{pmatrix} x_1 \\ y_1 \end{pmatrix} = \begin{pmatrix} x_o + s\cdot e_x \\ y_o + s\cdot e_y \end{pmatrix}, \quad \text{with} \quad s = -2\frac{x_o e_x b^2 + y_o e_y a^2}{e_x^2 b^2 + e_y^2 a^2} \tag{3.45}$$

with $\mathfrak{e} = (e_x, e_y)$ defined by

$$\mathfrak{e} = \frac{1}{2\sqrt{x^2/a^2 + y^2/b^2}} \begin{pmatrix} -y_o/b^2 \sin\chi - x_o/a^2 \cos\chi \\ -y_o/b^2 \cos\chi + x_o/a^2 \sin\chi \end{pmatrix}. \tag{3.46}$$

The invariant curves of this map in the SOS can be derived from the constant of motion in the ellipse:

$$\sin\chi(\phi) = \sqrt{1 + (S^2-1)\kappa^{2/3}(\phi,\varepsilon)} \tag{3.47}$$

[2] Also know as the *Birkhoff-Poritsky conjecture*.

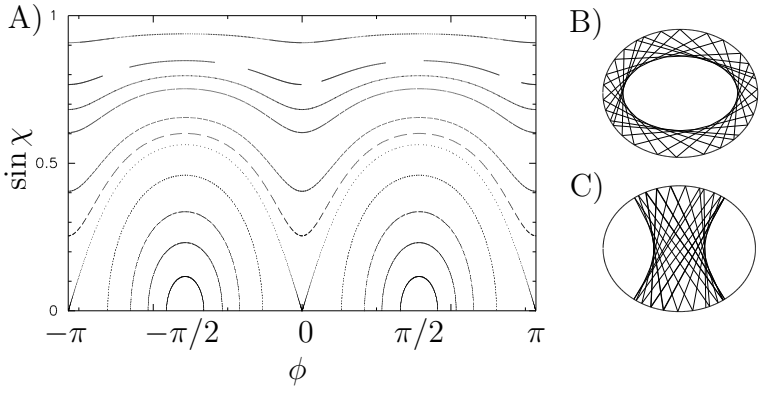

Figure 3.9: Surface of Section A) and realspace images of the ray-dynamics in the ellipse. B) is of whispering gallery type orbit, C) a bouncing Ball type orbit, the only family of stable orbits in the ellipse. The ellipse here at an deformation $\varepsilon = 0.1$.

κ denotes the curvature and ε is the deformation of the ellipse. The motion in the ellipse is more interesting that in the circular case, which only has parabolic fixed-points. Besides all the parabolic fixed-points, it has exactly one stable and one unstable fixed-point. The stable one is at $(\phi = \pm\pi/2, \sin\chi = 0)$ and the unstable at $(\phi = \{0, \pm\pi\}, \sin\chi = 0)$. The shape of the ellipse is given in polar coordinates

$$r(\phi) = \frac{1+\varepsilon}{\sqrt{1 + [(1+\varepsilon)^4 - 1]\sin^2\phi}}. \tag{3.48}$$

Around the origin in Fig. 3.9 we can see the invariant curve corresponding to the hyperbolic fixed-point that we have already seen in Fig. 3.5 B in a close-up. We can see here that $\mathcal{H}^+$ and $\mathcal{H}^-$ connect smoothly. This curve is also known as the *separatrix* as it separates the two types of orbits that can exist. The *whispering gallery* type orbits, where the sign of the angular momentum is constant, and the 'bouncing ball' type orbits, where the angular momentum changes the sign at every reflection, such orbits are called *librational*[3].

3.3.4 Classical Ray-tracing – a non analytic discrete map

For the circle we were able to write down a simple expression for the map. The map for the ellipse proved to be a bit harder but is still analytic. The map of the motion in a general convex shape however cannot be expressed analytically. Here we provide a numerical procedure for the map corresponding to a generic boundary, which involves a non-linear root search. This routine is the core for all ray calculations done in this thesis. Let $\mathfrak{r} = \mathfrak{r}(\varphi)$ describe the boundary and

$$\mathfrak{r}' = \frac{d\mathfrak{r}}{d\varphi} \tag{3.49}$$

[3]The PO can be seen as librational as zero has no sign.

the first derivative with respect to φ. The tangent vector is given by

$$\mathfrak{r} = \begin{pmatrix} r_x \\ r_y \end{pmatrix}, \quad r = |\mathfrak{r}|, \quad r_x = r\cos\varphi, \quad r_y = r\sin\varphi \tag{3.50}$$

taking φ derivative we get the tangent vector

$$\mathfrak{t} = \begin{pmatrix} t_x \\ t_y \end{pmatrix}, \quad t_x = -r\sin\varphi + r'\cos\varphi, \quad t_y = r\cos\varphi + r'\sin\varphi. \tag{3.51}$$

In general, we want to have our tangent vector $\mathfrak{t}$ to be normalized, so we calculate

$$|\mathfrak{t}| = \sqrt{t_x^2 + t_y^2} = \sqrt{r^2 + r'^2} = \Gamma \tag{3.52}$$

and define

$$\mathfrak{t} = \frac{1}{\Gamma}\mathfrak{t} \tag{3.53}$$

The same holds for the normal

$$\mathfrak{n} = \frac{1}{\Gamma}\begin{pmatrix} n_x \\ n_y \end{pmatrix}, \quad n_x = r\cos\varphi + r'\sin\varphi, \quad n_y = r\sin\varphi - r'\cos\varphi. \tag{3.54}$$

If the angle of incidence is given by χ, then the reflected ray will have the direction of the tangent $\mathfrak{t}$ rotated by $\pi/2 - \chi$ to the left. The required rotation matrix is:

$$\begin{pmatrix} \cos\theta & -\sin\theta \\ \sin\theta & \cos\theta \end{pmatrix} \text{ with } \theta = \pi/2 - \chi \rightarrow \begin{pmatrix} \sin\chi & -\cos\chi \\ \cos\chi & \sin\chi \end{pmatrix} = R(\chi) \tag{3.55}$$

$$R(\chi)\mathfrak{t} = \mathfrak{e} = \begin{pmatrix} e_x \\ e_y \end{pmatrix}, \quad e_x = t_x\sin\chi - t_y\cos\chi, \quad e_y = t_x\cos\chi + t_y\sin\chi \tag{3.56}$$

With this we can write the map

$$(\varphi_0, \sin\chi_0) \xrightarrow{M} (\varphi_1, \sin\chi_1) \tag{3.57}$$

by finding the intersection of $\mathfrak{e}$ with the boundary $\boldsymbol{R}$, i.e. solving the non-linear equation

$$\boldsymbol{R} - \lambda\mathfrak{e} = 0 \tag{3.58}$$

where the length λ and the position of $\boldsymbol{R}$ has to be found.

3.3.5 Fixed-points in billiards – periodic orbits

Now that we have a tool to generate the ray-dynamics in an arbitrary shape we need a tool to analyse the type of periodic orbits that this map will create. In Section 3.2.5 we learned that the monodromy matrix is the linearized map. The monodromy matrix can be written as a product of matrices for each separate reflection. In order

to calculate each matrix we need to know the length of the segment x, the radius of curvature $\mathfrak{R}$ and the angle of incidence χ at each reflection point. The radius of curvature is given by

$$\mathfrak{R} = 1/\kappa = \frac{(r^2 + \dot{r}^2)^{3/2}}{r^2 + 2\dot{r}^2 - r\ddot{r}} \tag{3.59}$$

For the one segments of length x_o, with the radius of curvature at the beginning (end) of the segment $\mathfrak{R}_o$ ($\mathfrak{R}_1$), the matrix is given by

$$m_{10} = \begin{pmatrix} \frac{(x_o - y_o)\mathfrak{R}_1}{y_1 \mathfrak{R}_o} & -\frac{x_o \mathfrak{R}_1 \mathfrak{R}_o}{y_o y_1} \\ \frac{y_o + y_1 - x_o}{\mathfrak{R}_o \mathfrak{R}_1} & \frac{(x_o - y_1)\mathfrak{R}_o}{y_o \mathfrak{R}_1} \end{pmatrix}, \quad \text{with} \quad y_i = \mathfrak{R}_i \cos\chi_i \tag{3.60}$$

We can now calculate the monodromy matrix for an *N-periodic orbit* (PO) by simply multiplying the matrices for each of the segments.

$$M = \prod_{n=1}^{N-1} m_{n,n-1} \tag{3.61}$$

The eigenvalues of the resulting monodromy matrix can be analyzed in the fashion of Section 3.2.5.

3.3.6 Lazutkin's theorem – why is a billiard not as chaotic as it should be

This discussion is important to us as we will study micro cavities with a deformation large enough such that the last torus should have already been broken, see Section 3.2.7. This would have occured at the torus with a ratio of the golden mean. We do however still find whispering gallery type orbits, a clear indication that the last torus is not broken. The statement from Section 3.2.2 is only true if we have a uniform perturbation of the map, but for the convex billiard this is not the case. Motion very close to the boundary has an effective perturbation that is reduced as $\sin\chi \to 1$. We can quantify this following Ref. [79] by writing the map as

$$\sin\chi_{n+1} = \sin\chi_n + F(\phi_{n+1}, \sin\chi_n) \tag{3.62}$$

$$\phi_{n+1} = 2\pi\alpha + \phi_n + G(\phi_n, \sin\chi_n). \tag{3.63}$$

The terms F, G in this map contain the nonlinearity of the map, $\alpha = \arccos(\sin\chi)$. As the perturbation factors F, G depend on $\sin\chi$ we see that the perturbation is not uniform. Close to the boundary we expect the change in the polar angle ϕ to be small for $\sin\chi \to 1$. Furthermore we show in Fig. 3.10 that the perturbation strength F for an actual whispering gallery mode in a general convex billiard is indeed dependent on $\sin\chi$. The average perturbation scales as $\cos^3\chi$ [79]. We can also argue that as the curvature becomes tangent to the boundary, the expression for the invariant curves of the ellipse from Section 3.3.3 will hold true. If we see the parameter S in Eq. (3.47) as the average $\sin\chi$ and let it approach $S \to 1$ the effect of the curvature κ

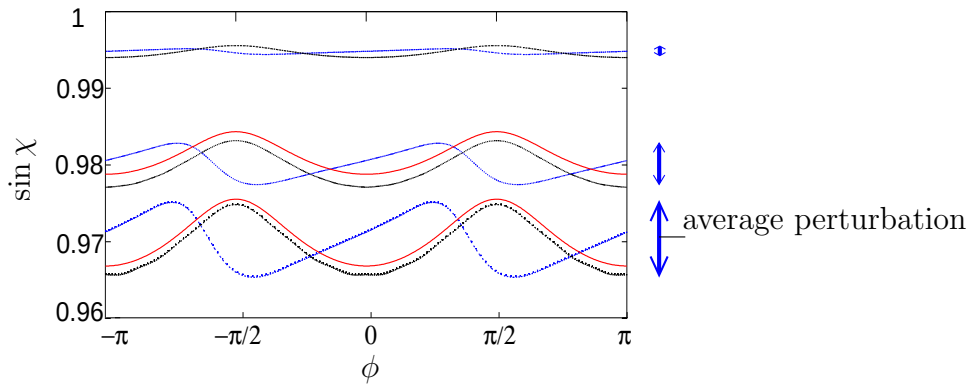

Figure 3.10: The top region of the SOS for a non-elliptical convex billiard (quadrupole $\varepsilon = 0.07$). The black curves indicate four different tori. In blue we we indicate the nonlinear perturbation $F(s_{n+1}, \sin\chi_n)$ from Eq. (3.62) shifted up by the average $\sin\chi$ of the orbit. In red we compare the adiabatic curve from Eq. (3.47). The blue arrows on the side indicate the perturbation strength. We can see how it decreases as $\sin\chi \to 1$.

reduces and $\sin\chi_{adiab}$ is almost constant. From this we conclude that even long after the golden torus is broken ($\sin\chi \approx 0.36$) there still exist whispering gallery orbits, as the effective perturbation close to the boundary goes to zero. This hold true for as long as the shape is convex. These statements are all implied by Lazutkin's theorem [44], where he however requires the boundary to possess 553 continuous derivatives ($r(\phi) \in C^{553}$). Douady showed in 1982 however that only six derivatives are enough [80].

3.3.7 Bifurcation of fixed-points

Bifurcations have the most dramatic effect on a billiard. It is through a bifurcation that we can see the strong power increase in the Bell Labs experiment described in Section 1.4.4, or the switching of emission directionality in a polymer laser in Section 5.8. The physics of bifurcations can already be discussed at the level of the simple Twist map. As we will see, it is through bifurcations that new fixed-points are generated in the map as a function of a smooth perturbation parameter. A general type of bifurcation in the twist map is illustrated in Fig. 3.11.

The type of bifurcations that we can encounter can be determined from the tangent map of Section 3.2.5. To facilitate it Greene [81] introduced the *residue* of an orbit defined by

$$R = \frac{2 - \mathrm{Tr}M}{4} \tag{3.64}$$

As the residue is only dependent on the trace of the monodromy matrix, it is independent of the point at which we evaluate M. The eigenvalues can be expressed as

$$\lambda_\pm = (1 - 2R) \pm 2\sqrt{R(R-1)}. \tag{3.65}$$

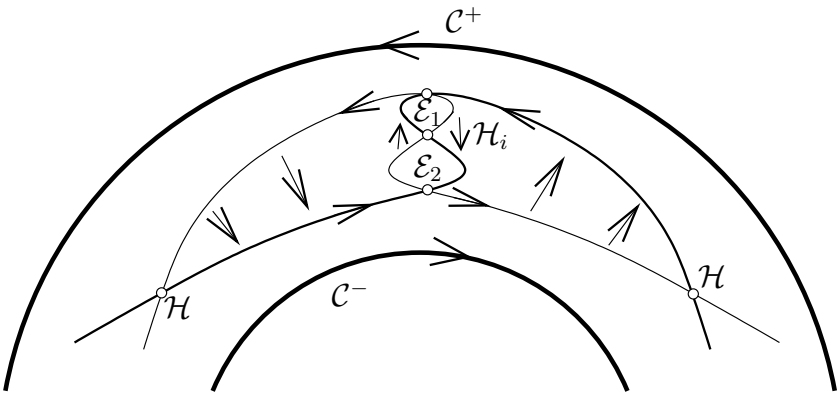

Figure 3.11: The same phase plot as in Fig. 3.4, but for stronger perturbation (following Ref. [9]). The original fixed-point $\mathcal{E}$ has vanished and was replaced by an inversion hyperbolic fixed-point $\mathcal{H}_i$. Two new elliptic orbits are born $\mathcal{E}_1$ and $\mathcal{E}_2$. Both of the elliptic fixed-points contain to the same orbit, of double period, thus a period doubling bifurcation has occurred.

We can translate the stability criteria in terms of R. If $R < 0$ we have an *ordinary hyperbolic* orbit, for $0 < R < 1$ it is *elliptic* and for $R > 1$ it is *inversion hyperbolic*. Right at $R = 0$ and $R = 1$ the fixed-point is *parabolic*. For an elliptic orbit to become unstable it has to pass through being a parabolic fixed-point, at which it bifurcates. "The possibility of bifurcations are limited by the requirement that the so called *Poincaré index* be conserved. The index of a fixed point is the sign of its residue, apart from exceptional cases with residue 0." [82] Meyer gives in Ref. [83] a proof that there only exist five 'typical' cases of bifurcations of two-dimensional area-preserving maps. These results where extended by Mao [84] to systems where the Poincaré map has discrete symmetries, as we will find in the quadrupole. We still have only five classes of bifurcations and we will discover all of them from the center orbit in the quadrupole, later in this Chapter, Section 3.4.1.

The location of bifurcations is directly related to the eigenvalues of the monodromy matrix and its complex roots. In order to see this we can write a general complex root of one as

$$\begin{aligned}\lambda &= e^{\pm i2\pi l/m}, \quad \text{with} \quad \{l,m\} \in \mathbb{N} \\ &= \cos(2\pi l/m) \pm i\sin(2\pi l/m) \\ &= \cos(2\pi l/m) \pm 2i\sin(\pi l/m)\cos(\pi l/m) \\ &= \left(1 - 2\sin^2(\pi l/m)\right) \pm 2i\sqrt{\sin^2(\pi l/m)\left(1-\sin^2(\pi l/m)\right)}, \end{aligned} \tag{3.66}$$

comparing this to Eq. (3.65) we see that

$$R_{l,m} = \sin^2\left(\pi\frac{l}{m}\right), \quad l,m \in \mathbb{Z}\setminus\{0\}. \tag{3.67}$$

For these values of R the eigenvalue λ is a complex root of one. A m-bifurcation occurs at every $l, m \in \mathbb{N}$ coprime, where we have a complex root of 1 for the eigenvalue

λ. Only the first m-bifurcations will be of different types and we give the corresponding residues and TrM in Table 3.1 The five types of bifurcations in a symmetric SOS

Table 3.1: The six bifurcations types.

l/m	R	TrM
1/1	0	+2
1/2	1	-2
1/3	3/4	-1
1/4	1/2	0
1/5	$\frac{5-\sqrt{5}}{8}$	$\frac{\sqrt{5}-1}{2}$
2/5	$\frac{5+\sqrt{5}}{8}$	$-\frac{\sqrt{5}+1}{2}$

are:

- $m = 1$, *Pitchfork bifurcation*, $R = 0$, the orbit goes from stable to unstable and a pair of stable orbits with the same period appears.
- $m = 2$, *Period doubling*, $R = 1$, the orbit becomes unstable (marginally stable) and a new stable orbit of $2N$ appears, where N is the period of the bifurcating orbit. Period doubling can also be regarded as a "pitch-fork" bifrucation of the $2N$-map. In special cases where the initial orbit continues to be stable and $\partial R/\partial\varepsilon = 0$, a stable and an unstable $2m$-orbit are created.
- $m = 3$, *Symmetric period tripling (touch and go)*, $R = 3/4$, the orbit stays stable. Four orbits of period-3 are created *near* the fixed-point, two of them stable, and the other two unstable. (For a discussion of the definition of *near* see Ref. [84].)
- $m = 4$, *Four-island chain bifurcation*, $R = 1/2$, a pair of new period-$4N$ orbits, one stable and one unstable, are created. They form a chain with the hyperbolic fixpoints between them
- $m \geq 5$ *m-island chain bifurcation for even m*, same as $m = 4$, *Doubled m-island chain bifurcation for odd m* Analogous to the symmetric period tripling.

A detailed discussion of the 2-bounce periodic orbit in the quadrupole can be found further below in Section 3.4.1.

3.3.8 Homoclinic Points

In the last section we discussed the bifurcation of an elliptic fixed-point. Let us here explore the behaviour of hyperbolic fixed-points in more detail. In Section 3.2.5 we learnt that it is through the complex behaviour of the unstable manifolds that chaotic motion sets in. The vicinity of one homoclinic point will get mapped into the vicinity of the next under one iteration of the map. We have illustrated this in Fig. 3.12. The

unstable (stable) manifolds shown in Fig. 3.12 can easily be calculated by starting a Gaussian distribution of small radius ($r \approx 0.001$) and propagating it for ≈ 10 iterations. This will give us only the unstable manifolds. To find the stable manifolds we use the trick that unstable manifolds are under time reversal the stable manifolds. Numbering the homoclinic intersections we can further distinguish between even and odd Homoclinic points. This classification is invariant under iteration along the manifold. We will encounter homoclinic points again in Section 4.11, where we will find that they can have a significant effect time on wavefunction localization!

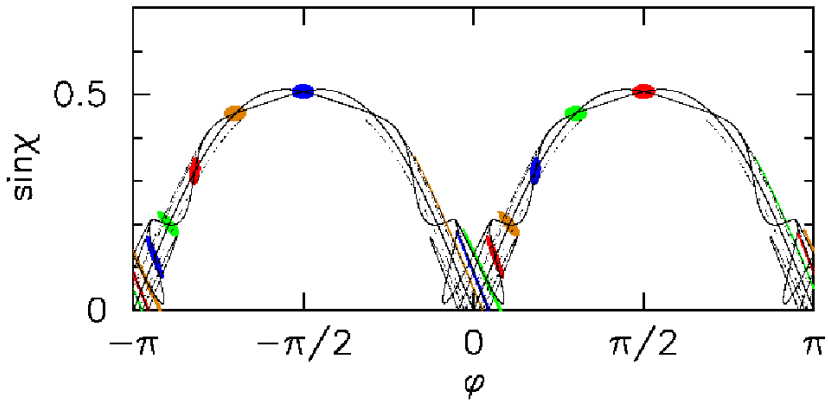

Figure 3.12: Four Gaussian distribution around the 0^{th} (blue and red) and 1^{st} (orange and green) Homoclinic point are iterated four times. The unstable and stable manifolds of the unstable two bounce orbit of the Quadrupole with $\varepsilon = 0.08$ are plotted in black.

3.4 Fixed-points, Periodic Orbits in the Quadrupole

Any convex shape can be written in polar coordinates and expanded by a Fourier series

$$r(\phi) = \frac{1}{2}a_o + \sum_{k=1}^{\infty} a_k \cos k\phi + \sum_{k=1}^{\infty} b_k \sin k\phi \tag{3.68}$$

First we want to analyze billiards with reflection symmetry $\Rightarrow b_k = 0, \forall k \in \mathbb{N}$. The first nontrivial deformation is going to be that of the quadrupole which is relevant to the microcavity experiments we have analyzed with the choice $a_o = 2, a_1 = \varepsilon$ and $a_k = 0 \quad \forall 1 < k \in \mathbb{N}$. We define the quadrupolar shape by

$$r(\phi)/R_o = \frac{1}{\sqrt{1 + 1/2\varepsilon^2}}(1 + \cos 2\phi) \tag{3.69}$$

where the prefactor insures that the area of the quadrupole is fixed to a constant value π and R_o is just an overall scale.

In the following we will analyze the properties of a few relevant periodic orbits in the quadrupole.

3.4.1 Bouncing Ball type orbits

The bouncing ball (BB) orbit is the dominant elliptic fixed-point in the quadrupole. It is the shorter diametral orbit at $\phi = \pm\pi/2$. As the nearby orbits do not have a definite sign of angular momentum we will treat this as a *librational orbit*. For this orbit we want to analyze the bifurcation theory laid out Section 3.3.7. It will be useful to know the trace of a higher repetition orbit, for the trace of the monodromy matrix of the the 4-bounce orbit we write $\mathrm{Tr}(M_4) = \mathrm{Tr}^2(M_2) - 2$. Clearly the 4-bounce orbit will stay stable as long as the 2-bounce orbit is stable ($|\mathrm{Tr}M_2| \leq 2$), and similarly any $2n-$*bounce* orbit. All the librational orbits in the quadrupole are born out of a bifurcation from the center 2-bounce orbit. Every bifurcation creates an orbit with a period equal to a multiple of the initial orbit, thus there can only be librational type orbits with an even number of bounces.[4]

Period-2 Orbits: Bouncing Ball Orbit

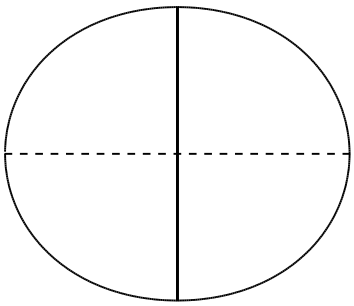

Figure 3.13: Both bouncing ball orbits in the quadrupole of $\varepsilon = 0.08$. The solid orbit is the stable two-bounce, the dashed the unstable orbits.

At $\varepsilon = 0$ we have an infinite number of period-2 orbits. For a small non-integrable perturbation $\varepsilon \neq 0$ we have seen that the infinite set breaks down and only two remain. One stable orbit along the minor axis of the quadrupole and one unstable along the major axis (Fig. 3.13). In Fig. 3.14 we explore the birth of all orbits with period $m \leq 8$ which are born directly out of the 2-bounce orbit. We call the map for the 2-bounce orbit M^2, with the residue R_2. The center graph shows the residue of M^2, M^4, M^6 and M^8 vs. deformation. Now we consider special values of the residue R of the bouncing ball orbit. Whenever the residue touches $R = 1$ (period doubling bifurcation), an orbit of double its period will be produced, for $R = 0$ (pitchfork bifurcation) an orbit of same period will appear. The first bifurcation that we show is at $\varepsilon = 0.0353$ where $R = 1/2$ (4-island chain bifurcation), a pair of $4N$, period-8 orbits appears. Above the graph we show the stable orbits that are generated, while below the unstable. If self-retracing orbits are produced we show the symmetric

[4]This might not be true if we have some external force acting, like gravity or a magnetic field. In this case there can exist 1 bounce orbits.

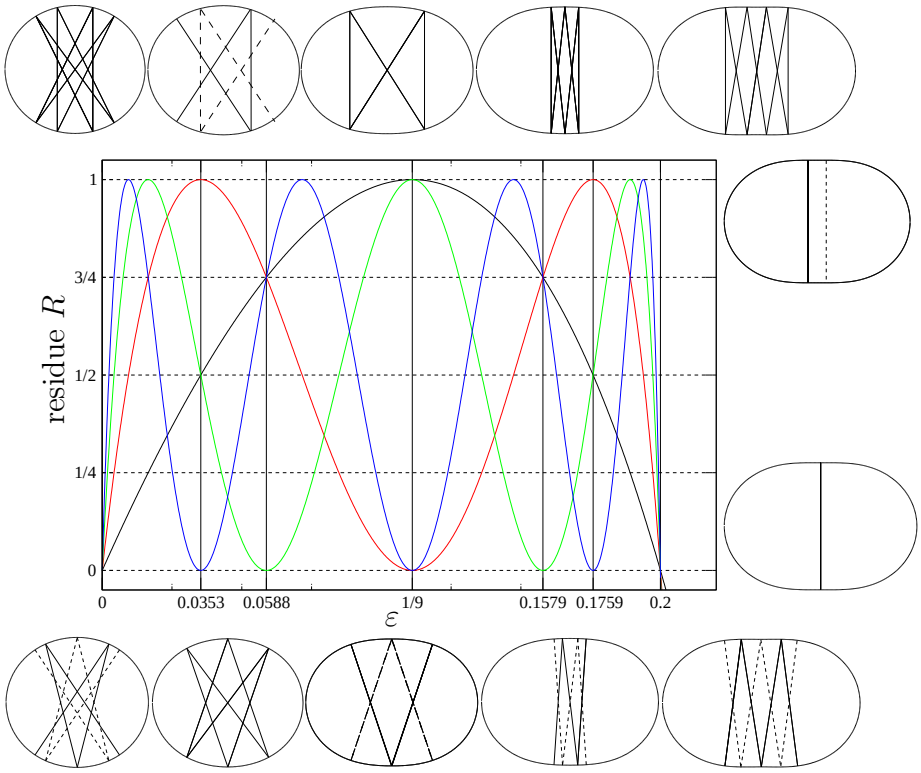

Figure 3.14: (center) The residue of the stable 'bouncing ball' orbit in the quadrupole vs. the deformation. The 2-bounce (black), 4-bounce (red), 6-bounce (green), 8-bounce orbit (blue). Above are the stable orbits born through the bifurcation, below the unstable orbits. If self-retracing orbits are produced we show the symmetric partner with a dashed line. The first bifurcation that we show occurs at $\varepsilon = 0.0353$, two period-8 orbits are born. At $\varepsilon = 0.0588$ a pair of period-6 orbits are born. At $\varepsilon = 1/9$ the 'bowtie' a period-4 orbit comes into existence, and we generate another period-6 orbit at $\varepsilon = 0.1579$ and a period-8 orbit at $\varepsilon = 0.1759$. The bouncing ball orbit becomes unstable at a pitchfork bifurcation at $\varepsilon = 0.2$. The two resulting orbits of period-2 are shown on the right.

partner with a dashed line. At $\varepsilon = 0.588$ $R = 3/4$ (Symmetric period tripling bifurcation), four period-6 orbits, two stable 'Fish' and two unstable Hexagrams (time reversal gives the other) are born *near* the fixed-point. See Appendix A.1.1 for more information on this orbit. At $\varepsilon = 1/9$ we have $R = 1$, a period doubling bifurcation of the main 2-bounce orbit. This bifurcation is a 'un-typical' period doubling bifurcation as the original orbit does not get unstable. Two period-4 'Bowtie' orbits and two 'Bird' orbit appear, see Appendix A.1.1. The other two bifurcations follow the same rules. At $\varepsilon = 0.2$ the center 2-bounce orbit bifurcates $R = 0$ with a pitchfork bifurcation and becomes unstable, as two new stable period-2 orbits are born. This denotes also the point at which the quadrupole stops being convex. We will investigate these special orbits in Appendix A.

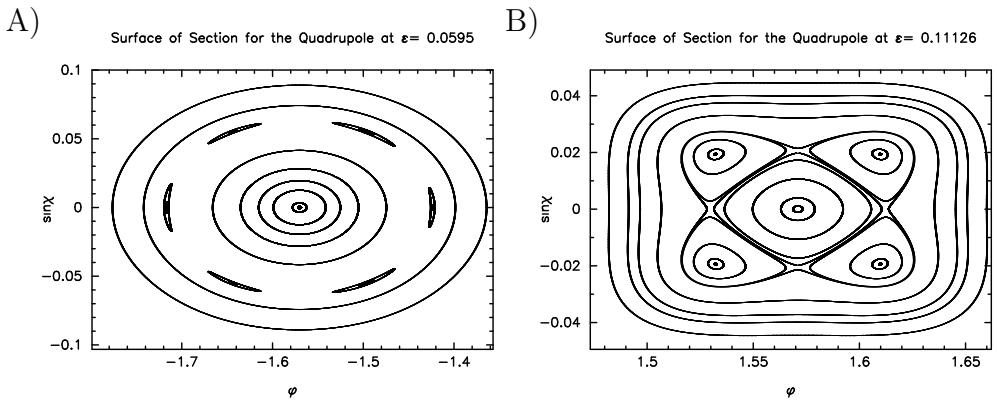

Figure 3.15: Surface of Section for the Quadrupole. A) At $\varepsilon \sim 0.0588$ the residue of the BB $R = 3/4$ a *symmetric period tripling bifurcation*, the islands are born close to the center fixed-point. B) At $\varepsilon \sim 1/9$ the residue of the BB $R = 1$ a *period doubling bifurcation* resulting in the 4-bounce Bow-tie orbit.

3.4.2 Whispering Gallery type orbits

The name *whispering gallery* terms from Lord Rayleigh [21] who analyzed the corresponding acoustic phenomenon in the St. Peters Cathedral in London (Fig. 1.3). Following Lazutkin in Section 3.3.6, every convex billiard will have whispering gallery type orbits. The shortest WG orbit that can span a convex shape is a three bounce orbit. A whispering gallery type orbit will have the sign of the angular momentum conserved. All the fixed-points that are non-librational are initially whispering gallery orbits or are born through a bifurcation from them.

3.4.3 Unstable Manifolds – a survey

So far we have discussed the elliptic fixed-points and their position and bifurcations in the SOS. What can we say about unstable fixed-points? We have seen that stable and unstable manifolds can cross and we have shown the resulting homoclinic points in Fig. 3.12. The manifolds we showed there is for the unstable 2-bounce orbit in the quadrupole of $\varepsilon = 0.08$. We have stated that different unstable manifolds can not cross each other and in Fig. 3.16 we give a survey of manifolds for the short periodic orbits in the quadrupole with a deformation of $\varepsilon = 0.18$. Clearly the unstable manifold of the 2-bounce orbit is the dominant boundary in phase space. Later in Section 5.7 we will see that these unstable manifolds change the emission pattern of polymer microlaser.

3.4.4 Mixed Phase Space in the Quadrupole

The last sections introduced and covered different stable and unstable periodic orbits. In this section we will see the interaction of both in the SOS for a generic mixed phase space. This gallery of SOS is given in Fig. 3.17 and explained in the caption.

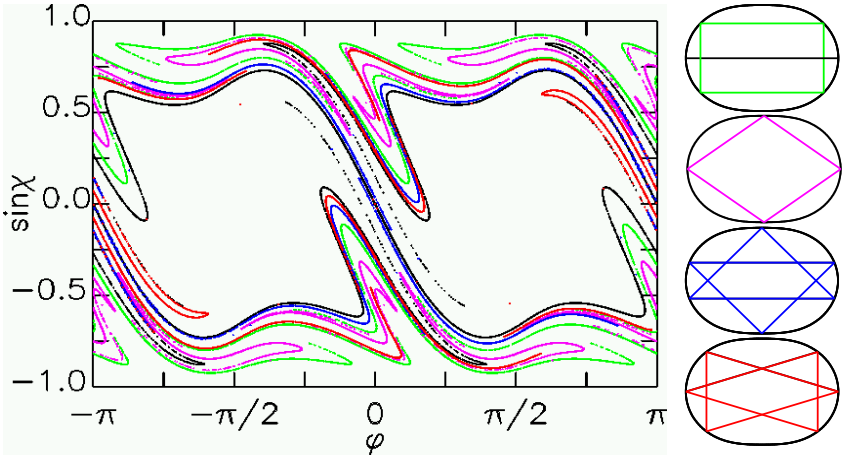

Figure 3.16: Survey of unstable manifolds in the quadrupole with $\varepsilon = 0.18$. The colors of the orbits on the right refer to the manifolds in the SOS. Note that the unstable manifolds do not intersect each other.

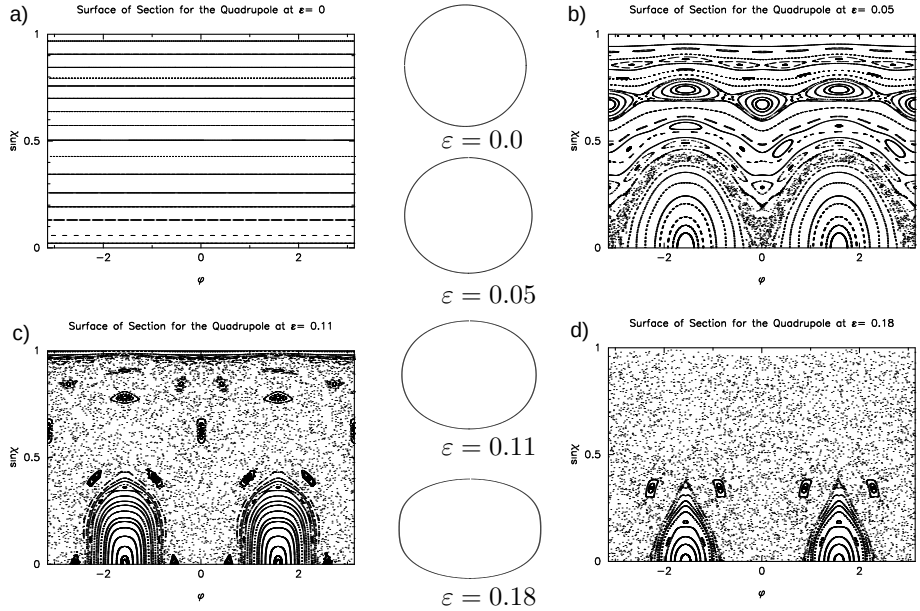

Figure 3.17: The SOS of a quadrupole at fractional deformations $\varepsilon = 0, 0.05, 0.11, 0.18$. The closed curves and the curves crossing the SOS represent two types of regular motion, motion near a stable periodic orbit and quasi-periodic motion respectively. The regions of scattered points represent chaotic portions of phase space. A single trajectory in this "chaotic component" will explore the entire chaotic region. With increasing deformation the chaotic component of the SOS (scattered points) grows with respect to regular components and is already dominant at 11% deformation. Note in (b) the separatrix region associated with the two-bounce unstable orbit along the major axis where the transition to chaotic motion sets in first.

3.5 Ray-dynamics in cylinders

In three dimensions, the dynamics is even more complicated. The generic phase space for a 3-d system is 6 dimensional and the Poincaré surface of section isn't anymore two dimensional. Arnol'd diffusion can take place as unbroken tori do not bound motion the anymore [43].

All theoretical work based on ray-dynamics for micro cavities has been based on 2-d dynamics, but all experiments are based on rods of deformed cross sections. These structures are three dimensional but, an axis exists along which we have translational symmetry (see Fig. 3.18 and Chapter 1) If we restrict ourself to such geometries, we can still characterize the dynamics by projecting the 3-d dynamics onto a 2-d dynamics, (see Fig. 3.19 and Fig. 3.20). Although the dynamics can in fact be reduced to 2-d, the additional degree of freedom gives rise to polarization mixing for the case of the vector wave-equation. These effects will be studied in detail in Chapter 7. We will assume translational symmetry along the z axis, and project the motion onto the 2-d (x, y) plane. In the (x, y) plane we write the projection vector as

$$\boldsymbol{p} = \begin{pmatrix} p_x \\ p_y \end{pmatrix}, \quad \text{with} \quad |\boldsymbol{p}| = 1 \tag{3.70}$$

knowing the two vectors $\boldsymbol{p}^1$ and $\boldsymbol{p}^2$ we can calculate the angle they span by means

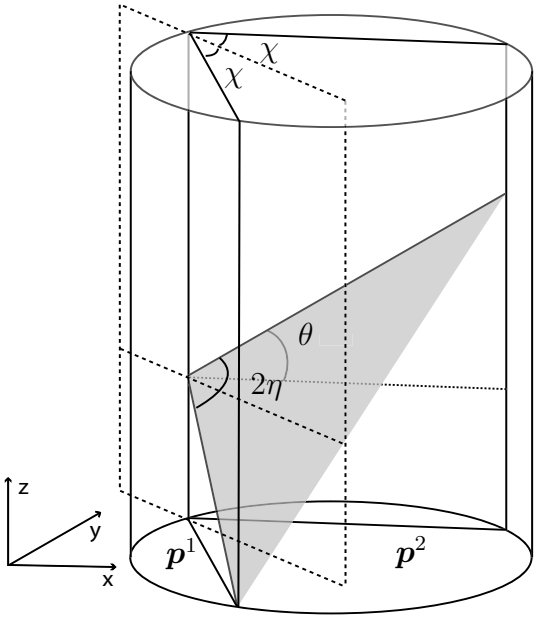

Figure 3.18: Schematic for the rays traveling in a 3-d cylinder.

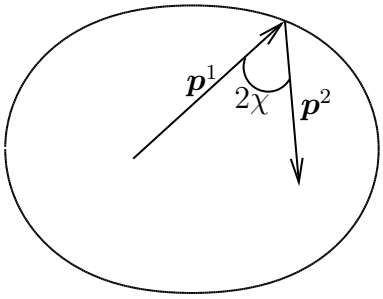

Figure 3.19: Schematic for the rays in (x, y) plane.

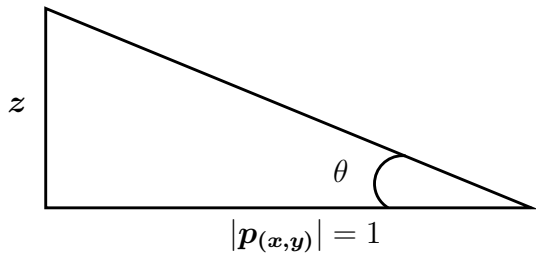

Figure 3.20: Schematic for the rays in the plane perpendicular to (x, y).

of the scalar product

$$\langle -\boldsymbol{p}^1 | \boldsymbol{p}^2 \rangle = \cos 2\chi \tag{3.71}$$
$$-(p_x^1 p_x^2 + p_y^1 p_y^2) = \cos 2\chi. \tag{3.72}$$

We write the 3-d vector as

$$\mathfrak{P} = \begin{pmatrix} p_x \\ p_y \\ \tan\theta \end{pmatrix}, \quad \text{with} \quad |\mathfrak{P}| = \sqrt{1 + \tan^2\theta} \tag{3.73}$$

and calculate the scalar product

$$\begin{aligned} \langle -\mathfrak{P}^1 | \mathfrak{P}^2 \rangle &= |\mathfrak{P}^1||\mathfrak{P}^2| \cos 2\eta \\ -(p_x^1 p_x^2 + p_y^1 p_y^2) - \tan^2\theta &= |\mathfrak{P}^1||\mathfrak{P}^2| \cos 2\eta \\ \cos 2\chi - \tan^2\theta &= (1 + \tan^2\theta) \cos 2\eta \\ \frac{\cos 2\chi - \tan^2\theta}{1 + \tan^2\theta} &= \cos 2\eta \end{aligned} \tag{3.74}$$

a number of trigonometric identities later we find a shorter form

$$\cos\eta = \cos\theta \cos\chi. \tag{3.75}$$

From this equation we can see that when we consider the critical angle in the plane of incidence η, that the corresponding critical angle χ in the (x, y) plane would not be critical, were it not for a finite θ. With a $\theta \neq 0$ we can see that the critical angle will become steeper. The total internally reflected region in the surface of section thus will become larger (see below).

3.6 Ray-dynamics in the 'open' billiard

Here, we finally get to deal with the actual problem of a dielectric resonator. So far we have analyzed the ray-dynamics in a closed resonator, where we have perfect

specular reflection and more importantly no escape. As seen in Section 2.4.2 any dielectric resonator will have some outcoupling loss at each reflection, but when the angle of incidence $\sin\chi > \sin\chi_c = 1/n$ the light is total internally reflected (TIR) and the loss is evanescent leakage and we typically neglected it. Below the critical angle, the fraction of incoming radiation that escapes is given by Fresnel coeficients (for a general derivation see Section 2.4.2). The emission directionality is given by Snell's law derived in Section 2.4.1. We will restate the law for a 2-d interface

$$n\sin\chi = n_o\sin\alpha, \quad \text{with} \quad n_o = 1. \tag{3.76}$$

The critical angle of incidence manifests itself in a very simple and intuitive way in the SOS as a straight line at $\sin\chi_c$. An orbit started above the critical line will be total internally reflected as long as the angle of incidence stays above the critical line; when it drops below, some light will get emitted from the cavity.

For the three dimensional rod we have derived the generalized Snell's law in two ways, via the EBK method in Section 2.4.1 and in a geometric fashion in Appendix B. The far-field angle σ in this case is the projected far-field angle onto the (x, y) plane.

We have used a number of different methods for analyzing the emission properties of open resonators. The classical ray simulation is done without phase information and thus neither diffraction nor interference effects can be accounted for.

3.6.1 Ray simulation

The goal for ray simulations in microcavities is to be able to make some predictions about the resonances of microcavities: 1) the emission directionality, 2) the lifetime or path-length of a ray before it is emitted, 3) classical position-momenum correlations in escape. In classical ray-simulation problems the initial conditions for the rays to be traced are clear, define a light source and trace all the rays starting from this source. For ray-simulations in microcavities the initial conditions are not that simple. Initial work on ray-simulations in microcavities with high index of refraction by Nöckel [14] followed the idea of starting rays on adiabatic curves in the surface of section. The rays were then propagated and at every reflection of the boundary a random number generator, biased with the Fresnel coefficiants, decided if the ray would refract or reflect. All emitted rays were binned in discrete far-field angle segments. Our ray-simulation avoids the Monte-Carlo aproach by giving every ray an initial amplitude of one. The ray is then propagated through the algorithm of Section 3.3.4. At each reflection from the boundary, the intensity is reduced by the Fresnel coefficients, and the outgoing intensity and far-field direction is recorded and binned. Once the amplitude drops below a minimum, the propagation is terminated. As discussed above, critical for ray simulations are their starting conditions. Different methods have been used throughout our research.

1. Starting a number of rays as Gaussian ensemble in the SOS. For closed resonator problems this method is especially useful for plotting the invariant curves of hyperbolic fixed-points, the unstable manifolds and for analyzing the

flow in the phase space (see Fig. 5.12). In the open resonator for simulation of stable periodic orbits, the initial Gaussian is located on an island.

2. Starting a number of rays on a line or set of 1-d curves. For the simulations of an elliptic cavity we started rays on a set of adiabatic curves following Eq. (3.47)

3. Starting a number of rays randomly in a given region. For the open resonator of low index of refraction (see Chapter 5) we used this method to simulate flood-pumping of the resonator. In the case of the closed resonator we used it to understand the general flow in the phase space.

4. Starting a number of rays randomly in a given region. The emission intensity at $(\phi, \sin\chi)$ is recored and projected in to the SOS. This can be directly related to the image data in experiments reported in Chapter 5, (see Fig. 5.13).

5. Starting a number of rays with density depending on a Husimi-Projection of a mode. This was used as a ray-test for the numerical calculation of the lasing 'Scar-of-David' mode, (see Fig. 8.26 B).

3.6.2 Classical lifetime in a cavity

For resonantor and lasers in particular an important value is the Q-value. We can find the Q-value of an open cavity via the associated lifetime τ

$$Q = \omega_o \tau = kL \tag{3.77}$$

where we can deterine the lifetime τ by the pathlength in the cavity till the amplitude drops from 1 to e^{-1}. Some example simulations are shown in Figs 3.21 and 3.22.

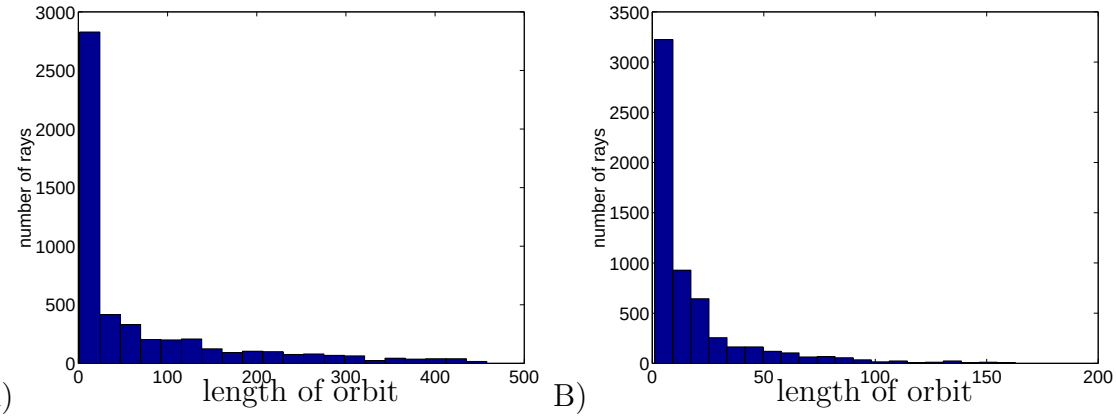

A) B)

Figure 3.21: Distribution of path length in quadrupole with the area π and $\varepsilon = 0.12, 0.18$ and $n = 1.49$ for 6000 random rays started above the critical line. The average length is 68.437 (17.414), the median 15.234 (7.554).

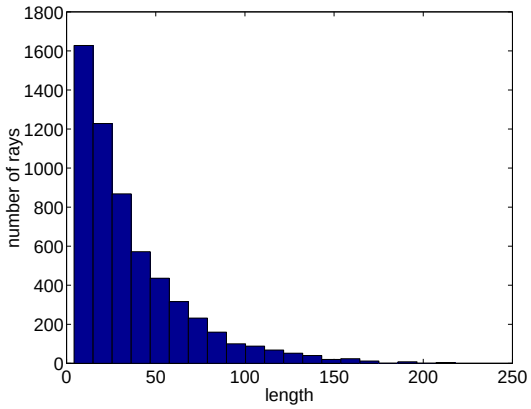

Figure 3.22: Distribution of path length in quadrupole with $\varepsilon = 0.18$ and $n = 1.49$ for 6000 random rays started above $\sin\chi = 0.909$. The average length is 36.491, the median 26.089.

3.6.3 Experiment – Theory

Far-field

From ray simulations the simplest information one can extract is the "classical" prediction for the emitted intensity in the far-field, used extensively in Chapter 5. Here we just bin the far-field angle and add the intensities obtained from the ray simulation. This is compared with the experimental setup where we place a CCD camera into the far-field of the cavity and report the intensity as a function of the far-field angle. (See Chapter 8)

Image-field

An experimental setup which yields more information is the imaging experiment, described in Chapter 8. With the help of an imaging lens and a CCD camera in the far field, the sidewall intensity is recorded and then plotted as boundary angle vs. far-field angle. This can be back projected onto the SOS and compared with a "ray-escape" simulation. In such a simulation we record the outgoing intensity at each point in the SOS and project it as a color scale on top of the SOS. We shall see in Fig. 5.13 that for the experiments described there, impressive agreement is found between this ray simulation and the experiment.

Chapter 4

Resonant Solutions of the Wave-equation

4.1 Introduction

In Chapter 2 we have reduced the Maxwell equations to the vector Helmholtz equation appropriate for the study of dielectric resonators. We learned that the actual difficulty in solving this equation arises through the boundary conditions, which in the general ($k_z \neq 0$) case, couple various field components. In this chapter we will review the two approaches for finding the resonances of a cavity and devise a new numerical algorithm for this task. We will study the resonator with Sommerfeld boundary conditions, where we will learn about quasi-normal modes. Here we will follow the approach laid out in Ref. [66, 1]. For the symmetric geometry of the cylinder we will write a resonance condition and find the quasi-normal modes via a complex root finding method. This method will work for more general geometries for which we will analyze the eigenphases of the S-matrix and devise a new numerical algorithm to find a large number of quasi-normal modes with a single calculation. The connection to experimental observables, the far-field and boundary image field are then developed via the large argument expansion of the Hankel function and the Husimi-Poincaré phase-space projection.

4.2 The Resonance problem – two Philosophies, one Solution

To illustrate the different approaches in solving the resonance problems we will start with the general vector Helmholtz equation for a dielectric (2.20)

$$\left(\nabla^2 + \gamma^2\right) \begin{Bmatrix} E_z(x,y) \\ B_z(x,y) \end{Bmatrix} = 0, \quad \text{with} \quad \gamma^2 = n(\boldsymbol{x})^2 k^2 - k_z^2, \tag{4.1}$$

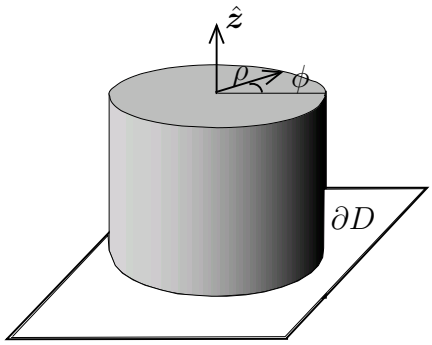

Figure 4.1: Schematic for the infinite rod with translational symmetry along the $\hat{\boldsymbol{z}}$-axis and arbitrary convex cross-section, with the boundary $R(z, \phi)$.

where we assume the resonator to be bounded by the interface ∂D given by (see Fig. 4.1)

$$\partial D = R(z, \phi) \quad \forall \quad z \in \mathbb{R}, \quad \phi \in \{0..2\pi\}. \tag{4.2}$$

The boundary conditions have been derived in Section 2.3. As we will deal with general convex shapes a good way to decompose the internal and external E_z and B_z fields is by their decomposition into cylindrical harmonics

$$\begin{pmatrix} E_z^< \\ B_z^< \end{pmatrix}(r, \phi) = \sum_{m=-\infty}^{\infty} \left[\begin{pmatrix} \alpha_m \\ \xi_m \end{pmatrix} H_m^+(\gamma_1 r) + \begin{pmatrix} \beta_m \\ \eta_m \end{pmatrix} H_m^-(\gamma_1 r) \right] e^{im\phi} \tag{4.3}$$

$$\begin{pmatrix} E_z^> \\ B_z^> \end{pmatrix}(r, \phi) = \sum_{m=-\infty}^{\infty} \left[\begin{pmatrix} \upsilon_m \\ \zeta_m \end{pmatrix} H_m^+(\gamma_2 r) + \begin{pmatrix} \delta_m \\ \vartheta_m \end{pmatrix} H_m^-(\gamma_2 r) \right] e^{im\phi}, \tag{4.4}$$

where $H^{\pm}$ are the cylindrical Hankel-functions, H^- representing an incoming wave from infinity and H^+ an outgoing wave.

There are two approaches for solving this linear problem with fixed index of refraction n for the resonances: the first is to calculate the real k unitary S-matrix, in the usual way, matching an incoming wave from infinity to an outgoing wave at infinity. The other approach is the Sommerfeld boundary condition where we only allow for outgoing waves

$$\begin{pmatrix} E_z^> \\ B_z^> \end{pmatrix}(r) = \sum_{m=-\infty}^{\infty} \begin{pmatrix} \upsilon_m \\ \zeta_m \end{pmatrix} H_m^+(\gamma_2 r), \quad r \to \infty. \tag{4.5}$$

This problem is not current conserving and can only be solved for complex k. There is a subtle relationship between these two classes of solutions. It can be shown that the complex $k = x + iy, k \in \mathbb{C} \setminus \mathbb{R}$ are the poles of the S-matrix continued to the complex plane [66, 1]. This relationship is illustrated in Fig. 4.2. These discrete solutions are known as *quasi-normal modes*. The real part x of the wave-vector determines the frequency $\omega = cx$ and the imaginary part represents the lifetime $\tau = 1/cy$. An experimentally relevant factor always reported in experiments involving resonators

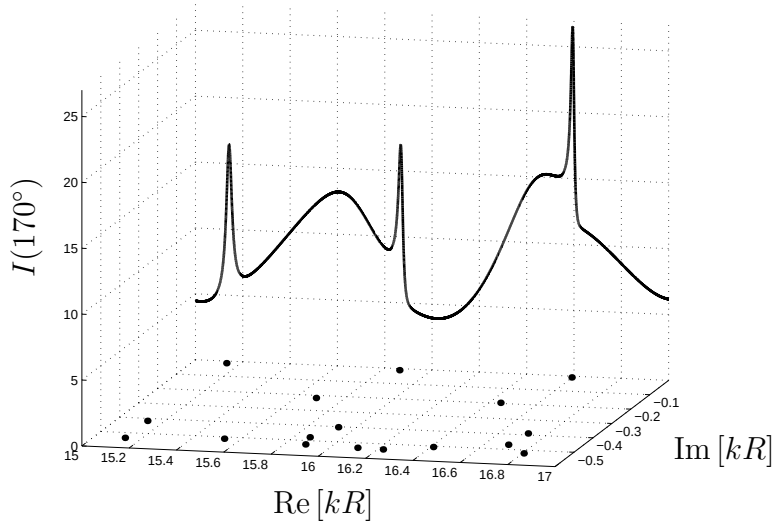

Figure 4.2: A comparison of scattering and emission pictures for quasi-bound modes. The complex quasi-bound mode frequencies are plotted on the $\mathrm{Re}\,[kR] - \mathrm{Im}\,[kR]$ plane. On the back panel we plot the real k S-matrix, scattering cross-section at 170° with respect to the incoming wave direction. Notice that the most prominent peaks in scattering intensity are found at the values of k where a quasi-bound mode frequency is closest to the real-axis. These are the long-lived resonances of the cavity. Also visible is the contribution of resonances with shorter lifetimes (higher values of $\mathrm{Im}\,[kR]$) to broader peaks and the scattering background.

is the so called Q-value of the resonator. It is defined by the number of cycles it takes for the optical field at frequency ω to decay to its half value: $Q = \omega\tau = -2\mathrm{Re}\,[\gamma R]\,/\mathrm{Im}\,[\gamma R]$.

The physical problem that we are typically interested in however, is that of a laser cavity, which contains a non-linear gain medium. For a laser above threshold however, the index becomes a non-linear function of the field strength. Here, we will confine our discussion to the linear resonances, as is frequently done in laser theory [85]. In that case, a simple model to take into account gain, albeit at a linear level, is to look for solutions of the Helmholtz equation with a complex index of refraction. For certain discrete values of n, it is possible to find stationary solutions with a real k. Such solutions are continuously related to the quasi-bound modes with real n. We have studied these solutions but do not present the results here.

4.3 Quasi-bound resonances in the Cylinder

In this section we want to explicitly calculate the quasi-bound modes for the cylinder. In the following we will simplify the notation:

$$J_m := J_m(\gamma_1 R) \quad \text{and} \quad H_m := H_m^+(\gamma_2 R) \tag{4.6}$$

where $\gamma_i = \sqrt{n_i^2 k^2 - k_z^2}, i \in \{0, 1\}$ and R is taken on the boundary of the domain. With this convention we can write the ansatz for the cylinder

$$E_z^<(\boldsymbol{r}; m, j) = \alpha_m J_m(\gamma_1^{m,j}\boldsymbol{r})e^{im\varphi} \quad B_z^<(\boldsymbol{r}; m, j) = \xi_m J_m(\gamma_1^{m,j}\boldsymbol{r})e^{im\varphi} \quad \boldsymbol{r} < R \quad (4.7)$$

$$E_z^>(\boldsymbol{r}; m, j) = \upsilon_m H_m^+(\gamma_2^{m,j}\boldsymbol{r})e^{im\varphi} \quad B_z^>(\boldsymbol{r}; m, j) = \zeta_m H_m^+(\gamma_2^{m,j}\boldsymbol{r})e^{im\varphi} \quad \boldsymbol{r} > R. \quad (4.8)$$

Using the continuity of the field boundary conditions Eq. (2.41) and Eq. (2.42) we get the relations

$$\upsilon_m = \frac{J_m}{H_m}\alpha_m \qquad \zeta_m = \frac{J_m}{H_m}\xi_m \quad (4.9)$$

using this Eqs. (2.43), (2.44) can be rewritten in the following way

$$\begin{pmatrix} ik_z\tau m J_m H_m & \frac{k}{\gamma_1^2}H_m\partial_\rho J_m - \frac{k}{\gamma_2^2}J_m\partial_\rho H_m \\ \frac{n_1^2 k}{\gamma_1^2}H_m\partial_\rho J_m - \frac{n_2^2 k}{\gamma_2^2}J_m\partial_\rho H_m & -ik_z\tau m J_m H_m \end{pmatrix}\begin{pmatrix}\alpha_m \\ \xi_m\end{pmatrix} = 0 \quad (4.10)$$

where $\tau = (1/\gamma_1^2 - 1/\gamma_2^2)$. Some of the pre-factors in Eq. 4.10 should only depend on geometric quantities, independent of k. This formulation will be useful for semi-classical considerations, following the idea in Eq. (2.62) we can write

$$\begin{pmatrix} im(n-n^3)\sin\theta J_m H_m & \cos^2\alpha H_m\partial_\rho J_m - n^2\cos^2\theta J_m\partial_\rho H_m \\ n^2\cos^2\alpha H_m\partial_\rho J_m - n^2\cos^2\theta J_m\partial_\rho H_m & im(n^3-n)\sin\theta J_m H_m \end{pmatrix}\begin{pmatrix}\alpha_m \\ \xi_m\end{pmatrix} = 0. \quad (4.11)$$

Where $\tan\theta = k_z\gamma_1$, the angle inside of the ray spiraling up with respect to the (x, y) axis and α the angle outside, see Fig. 2.3. In order for this system to have a non-trivial solution the determinant needs to vanish, resulting in

$$k_z^2\tau^2 m^2 J_m^2 H_m^2 = \left[\frac{1}{\gamma_1^2}H_m\partial_\rho J_m - \frac{1}{\gamma_2^2}J_m\partial_\rho H_m\right]\left[\frac{n_1^2k^2}{\gamma_1^2}H_m\partial_\rho J_m - \frac{n_2^2k^2}{\gamma_2^2}J_m\partial_\rho H_m\right], \quad (4.12)$$

or in the geometric form:

$$\begin{aligned} n^2(1-n^2)^2 m^2\sin^2\theta &= \frac{1}{J_m H_m}\left[n^2\cos^2\alpha H_m\partial_\rho J_m - n^2\cos^2\theta J_m\partial_\rho H_m\right] \\ &\times \frac{1}{J_m H_m}\left[\cos^2\alpha H_m\partial_\rho J_m - n^2\cos^2\theta J_m\partial_\rho H_m\right] \\ &\equiv G^{TE}\cdot G^{TM} \end{aligned} \quad (4.13)$$

Where we have defined:

$$\begin{aligned} G^{TE} &= \frac{1}{J_m H_m}\left[\frac{1}{\gamma_1^2}H_m\partial_\rho J_m - \frac{1}{\gamma_2^2}J_m\partial_\rho H_m\right] \\ G^{TM} &= \frac{1}{J_m H_m}\left[\frac{n_1^2}{\gamma_1^2}H_m\partial_\rho J_m - \frac{n_2^2}{\gamma_2^2}J_m\partial_\rho H_m\right]. \end{aligned} \quad (4.14)$$

In this form the resonance conditions Eq. (4.12), (4.13) bear a simple relation to the familiar resonance conditions for the TM and TE modes for $k_z = 0$. For $k_z = 0$,

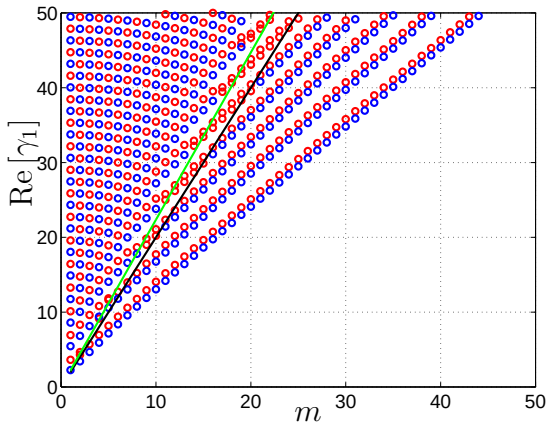

Figure 4.3: TE like resonances (red circles) and TM like resonances (blue circles) for a cylinder with $n = 2, \theta = 0.2$, solid black line corresponds to the critical angle defined by $\gamma_1 = mn$ and the green line to the Brewster condition $\gamma_1 = m\sqrt{n^2+1}$.

$\theta = 0$ ($\tau = 0, \gamma_1 = n_1 k, \gamma_2 = n_2 k$), the left hand side of Eq. (4.12), (4.13) vanishes, giving

$$0 = G^{TE} \cdot G^{TM} = \left[\frac{1}{n_1^2} H_m \partial_\rho J_m - \frac{1}{n_2^2} J_m \partial_\rho H_m\right] \left[H_m \partial_\rho J_m - J_m \partial_\rho H_m\right]. \tag{4.15}$$

The vanishing of the left bracket describes the resonance condition for the TE modes and the vanishing of the right bracket that for the TM modes [66, 1].

In order to find the resonances in the cylinder, all we need to do is to solve

$$n^2(1-n^2)^2 m^2 \sin^2\theta = G^{TE} \cdot G^{TM}. \tag{4.16}$$

The resonances are found numerically by complex root searching on a 2d grid. We use the `SLATEC` routine `dnsqe` [86]. In Fig. 4.3 the real part of the resonances found in this manner are plotted. The coloring represents the TE or TM "character" of these hybrid modes, determined by the relative magnitudes of $|G^{TE}|$ and $|G^{TM}|$ (see below).

4.4 Quasi-bound modes in an arbitrary shape with $k_z \neq 0$

In this section we will generalize the above treatment and apply it to a dielectric rod of arbitrary cross-section. We will formulate it in such a way that we can solve it numerically. From Chapter 2 we know that the complication of the problem arises through the mixing of the E_z and B_z fields via the boundary conditions Eq. (2.41)-(2.44). We will now apply the Sommerfeld boundary conditions upon the general

ansatz Eq. (4.3)

$$\begin{pmatrix} E_z^< \\ B_z^< \end{pmatrix}(r,\phi) = \sum_{m=-\infty}^{\infty} \left[\begin{pmatrix} \alpha_m \\ \xi_m \end{pmatrix} H_m^+(\gamma_1 r) + \begin{pmatrix} \beta_m \\ \eta_m \end{pmatrix} H_m^-(\gamma_1 r) \right] e^{im\phi} \qquad \boldsymbol{r} < R \tag{4.17}$$

$$\begin{pmatrix} E_z^> \\ B_z^> \end{pmatrix}(r,\phi) = \sum_{m=-\infty}^{\infty} \begin{pmatrix} \upsilon_m \\ \zeta_m \end{pmatrix} H_m^+(\gamma_2 r)\, e^{im\phi} \qquad \boldsymbol{r} > R. \tag{4.18}$$

Due to the completeness of the cylindrical harmonics we know that the expansion for $r < R_{min}$ and $r > R_{max}$, where $R_{min} = \min\{R(\phi)\,|\,\phi \in (-\pi,\pi]\}$ and $R_{max} = \max\{R(\phi)\,|\,\phi \in (-\pi,\pi]\}$, is exact as long as the sum runs over an infinite number of terms. The assumptions that the expansion can analytically be continued to the region $R_{min} < r < R_{max}$ is known as the the Rayleigh hypothesis [87]. It has been shown [88] that for a family of deformations of a circle parameterized by δ there exists a δ_c such that the expansion will become non-analytic in the interval $R(\delta)_{min} < r < R(\delta)_{max}$. For us this will have no practical relevance as the breakdown only occurs at deformations where the domain D would already be concave. We will however notice a numerical instability in the vicinity of $r \approx R_{min}$, which is a precursor of this effect.

To handle the problem efficiently numerically we will discretize the boundary at this point. We have also analyzed in depth the possibility of matching in the Fourier space of the angle coordinate. We found that both methods give us the same resonances numerically; the formergives the benefit of a speed increase.[1]

We will now impose the boundary conditions Eq. (2.41)-(2.44) at $\partial D = R(\phi) \quad \forall\phi \in \{0..2\pi\}$ and write the equations in their discretized version

$$\mathfrak{C} \begin{pmatrix} |\alpha\rangle \\ |\upsilon\rangle \\ |\xi\rangle \\ |\zeta\rangle \end{pmatrix} = \mathfrak{B} \begin{pmatrix} |\beta\rangle \\ |\upsilon\rangle \\ |\eta\rangle \\ |\zeta\rangle \end{pmatrix}, \tag{4.19}$$

where

$$\mathfrak{C}^T = \begin{pmatrix} 0 & \frac{k_z}{\gamma_2^2} TC(l,m) & -C(l,m) & -\frac{kR}{\gamma_2^2} NC(l,m) \\ 0 & -\frac{k_z}{\gamma_1^2} TA(l,m) & A(l,m) & \frac{kR}{\gamma_1^2} NA(l,m) \\ -C(l,m) & -\frac{kR}{\gamma_2^2} NC(l,m) & 0 & -\frac{k_z}{\gamma_2^2} TC(l,m) \\ A(l,m) & n^2 \frac{kR}{\gamma_1^2} NA(l,m) & 0 & \frac{k_z}{\gamma_1^2} TA(l,m) \end{pmatrix} \tag{4.20}$$

and

$$\mathfrak{B}^T = \begin{pmatrix} 0 & 0 & 0 & 0 \\ 0 & 0 & 0 & 0 \\ 0 & \frac{k_z}{\gamma_1^2} TB(l,m) & -B(l,m) & -\frac{kR}{\gamma_1^2} NB(l,m) \\ -B(l,m) & -n^2 \frac{kR}{\gamma_1^2} NB(l,m) & 0 & -\frac{k_z}{\gamma_1^2} TB(l,m) \end{pmatrix} \tag{4.21}$$

[1] $\sim$ 240% increase for a generally configured system.

with $\gamma_1 = \sqrt{n^2 k R^2(\phi) - k_z^2}$ and $\gamma_2 = \sqrt{k R^2(\phi) - k_z^2}$ and the block matrices are given by

$$A(l,m) = H_m^+(\gamma_1) e^{im\phi_l} \tag{4.22}$$
$$B(l,m) = H_m^-(\gamma_1) e^{im\phi_l} \tag{4.23}$$
$$C(l,m) = H_m^+(\gamma_2) e^{im\phi_l}. \tag{4.24}$$

The T (N) denotes the tangential (normal) derivative, given in Appendix D with $\Gamma = \sqrt{r^2 + r'^2}$ here the normal derivatives, using the recursion relation for Hankel-functions from Appendix G,

$$NA(l,m) = \frac{1}{\Gamma}\left[R\gamma_1 H_{m-1}^+(\gamma_1) - m\frac{R + iR'}{R} H_m^+(\gamma_1)\right] e^{im\phi_l} \tag{4.25}$$
$$NB(l,m) = \frac{1}{\Gamma}\left[R\gamma_1 H_{m-1}^-(\gamma_1) - m\frac{R + iR'}{R} H_m^-(\gamma_1)\right] e^{im\phi_l} \tag{4.26}$$
$$NC(l,m) = \frac{1}{\Gamma}\left[R\gamma_2 H_{m-1}^+(\gamma_2) - m\frac{R + iR'}{R} H_m^+(\gamma_2)\right] e^{im\phi_l} \tag{4.27}$$

and the tangential derivatives

$$TA(l,m) = \frac{1}{\Gamma}\left[R'\gamma_1 H_{m-1}^+(\gamma_1) - m\frac{R' - iR}{R} H_m^+(\gamma_1)\right] e^{im\phi_l} \tag{4.28}$$
$$TB(l,m) = \frac{1}{\Gamma}\left[R'\gamma_1 H_{m-1}^-(\gamma_1) - m\frac{R' - iR}{R} H_m^-(\gamma_1)\right] e^{im\phi_l} \tag{4.29}$$
$$TC(l,m) = \frac{1}{\Gamma}\left[R'\gamma_2 H_{m-1}^+(\gamma_2) - m\frac{R' - iR}{R} H_m^+(\gamma_2)\right] e^{im\phi_l} \tag{4.30}$$

where $R = R(\phi_l)$ denotes the boundary. From these relations we can define an 'internal' S-matrix

$$S(k)\begin{pmatrix}|\alpha\rangle \\ |\xi\rangle\end{pmatrix} = \begin{pmatrix}|\beta\rangle \\ |\eta\rangle\end{pmatrix} \tag{4.31}$$

As the interior field $\binom{E_z}{B_z}^<$ needs to be regular at the origin, we need to impose $|\alpha\rangle = |\beta\rangle$ and $|\xi\rangle = |\eta\rangle$. The interior field can then be described just by the Bessel functions of the first kind J_m.

$$H_m^+ + H_m^- = (J_m + iN_m) + (J_m - iN_m) = 2J_m \tag{4.32}$$

We will later return to this point and keep $|\beta\rangle$ and $|\eta\rangle$ to use a numerical trick that will help us to increase the speed and stability of the numerical routine. But for now we write the Eq. (4.31) as

$$S(k)\begin{pmatrix}|\alpha\rangle \\ |\xi\rangle\end{pmatrix} = \begin{pmatrix}|\alpha\rangle \\ |\xi\rangle\end{pmatrix} \tag{4.33}$$

This S-matrix is different from the usual S-matrix in that it non-unitary.[2] We need to note that as we are considering the 3d system, the matrix is of order $2N \times 2N$. The standard approach to this problem lies now in solving the eigenvalue problem

$$S(k) \begin{pmatrix} |\alpha\rangle \\ |\xi\rangle \end{pmatrix} = e^{i\theta} \begin{pmatrix} |\alpha\rangle \\ |\xi\rangle \end{pmatrix} \tag{4.34}$$

and finding the complex values of k for which $\theta = 2m\pi, (m \in \mathbb{Z})$. As we have noted above, the resonances associated to the quasi-normal modes only exist in the complex plane, thus we expect a complex phase $\theta = \xi + i\eta$ with $\{\xi, \eta\} \in \mathbb{R}$, if we attempt to solve Eq. (4.34) for $k \in \mathbb{R}$. The solutions are in general [89] written in terms of the roots of the secular function $\boldsymbol{\zeta}(k)$

$$\boldsymbol{\zeta}(k) = \det(1 - S(k)). \tag{4.35}$$

4.5 Numerical Strategies

The resonances that are of interest to us are in general well into the semiclassical regime where we know that the angular momentum of ray-trajectories is related to the wave properties by $L = \sin\chi = m/\gamma$ [11, 66]. The dynamics within a ball of radius R_{min} is the well know scattering problem of a circle, with the incoming field defined by the region between R_{min} and R_{max}. The number of scattering channels is thus given by $\Lambda_{sc} = [\![\gamma_{1min}]\!]$ where $[\![\cdot]\!]$ denotes the integer part of γ_{1min}. Modes which have angular momentum with $m > \gamma_{1max}$ correspond to *evanescent* that are classically forbidden. Such modes will not factor in significantly into the scattering problem. To calculate the S-Matrix numerically we need to truncate it, and these evanescent channels determine an appropriate cutoff. Modes corresponding to angular momentum of the order $\sin\chi \gtrsim m/\gamma_{1min}$ are only partially evanescent and have to be included [89]. A good cutoff is thus $m = \Lambda = [\![\gamma_{1max}]\!] + \Delta$ where Δ is of the order of 5% of Λ_{sc}.

Calculating the S-matrix $S(\gamma)$ can involve the inversion of a number of matrices. In consideration of speed and numerical stability we want to employ here a different approach. Taking the regularity of the origin into account ($|\alpha\rangle = |\beta\rangle$ and $|\xi\rangle = |\eta\rangle$) we can write Eq. (4.19) as a generalized eigenvalue problem

$$\mathfrak{C} \begin{pmatrix} |\alpha\rangle \\ |\upsilon\rangle \\ |\xi\rangle \\ |\zeta\rangle \end{pmatrix} = e^{i\theta} \mathfrak{B} \begin{pmatrix} |\alpha\rangle \\ |\upsilon\rangle \\ |\xi\rangle \\ |\zeta\rangle \end{pmatrix}. \tag{4.36}$$

Efficient numerical methods have been developed and there exist powerful generalized eigenvalue solvers such as `ZGGEV` in the `LAPACK` library [91].

Solving the equation in this manner has a nice side benefit, both, the inside and outside vectors of the E_z and B_z fields $|\alpha\rangle, |\upsilon\rangle, |\xi\rangle, |\zeta\rangle$ are obtained at one shot! For

[2] We use the symbol S here for historical reasons comparing to the S-matrix from Refs [89, 90].

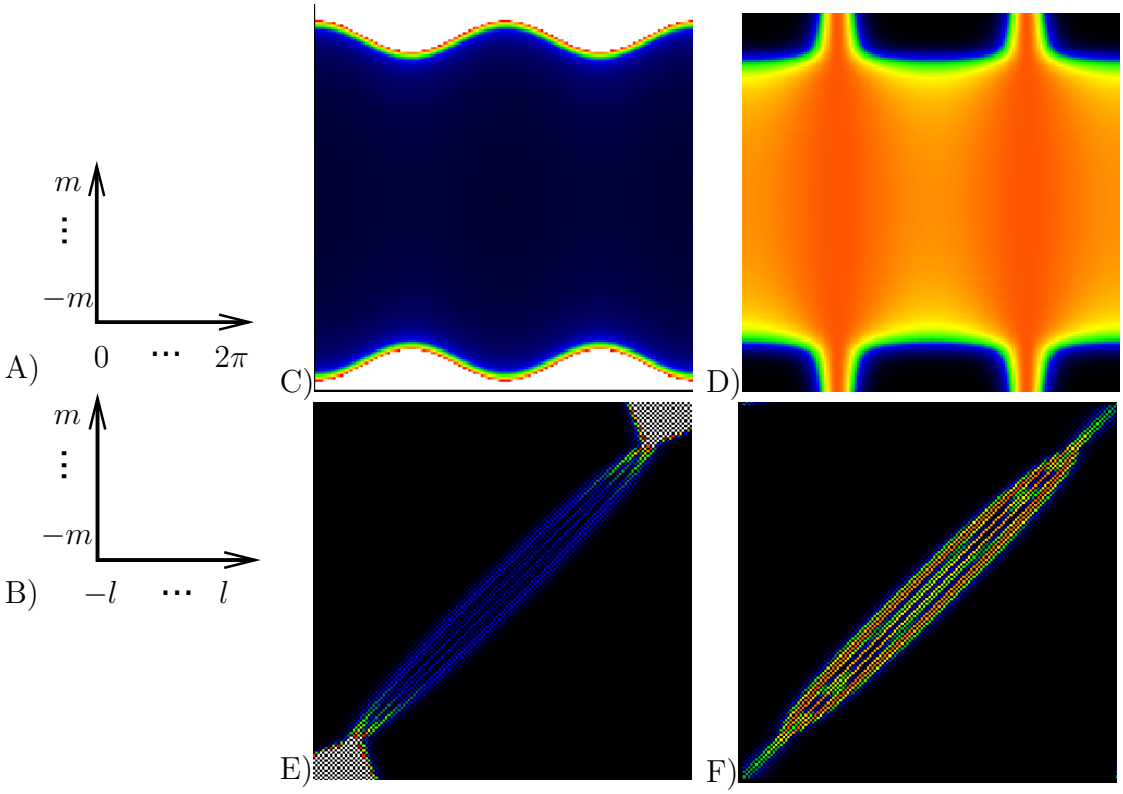

Figure 4.4: Magnitude of the elements in the A matrix. Due to the large span of magnitude encountered in the matrices we devise a scaling scheme by which we scale every angular momentum component m with the corresponding Hankel function with argument at the minimum radius. In A) we show the reference frame for the matrix values for the direct boundary matching, in B) for the integrating method. C) Direct boundary matching method without scaling, D) with scaling. E) Integrating method without scaling, F) Integrating method with scaling.

numerical evaluation we should check the magnitude of the elements in both of the matrices. We will focus in the following on the block matrix A. In Fig. 4.4 C) we see, that the magnitude can vary significantly (the color scale has a sharp cutoff). The elements nearly explode in the region of smallest radius ($\pm\pi/2$) with large m. A reduction scheme was originally introduced by Phillipe Jacquod by simply scaling every angular momentum component by the corresponding Hankel function at the smallest radius. The results are shown in Fig. 4.4 D) where the color scale does not have a cutoff. An interesting fact is that we can see the regions with the contribution of the evanescent modes nicely. The Fourier space matrix becomes almost diagonal. We show the magnitudes in the whole $\mathfrak{C}$ matrix in Fig. 4.5

At this point in principle we need to do a complex search to find the quantized modes with $\theta = 2\pi n$. However we have devised a very powerful method to bypass this search by studying the behavior of the eigenphases with respect to variation of

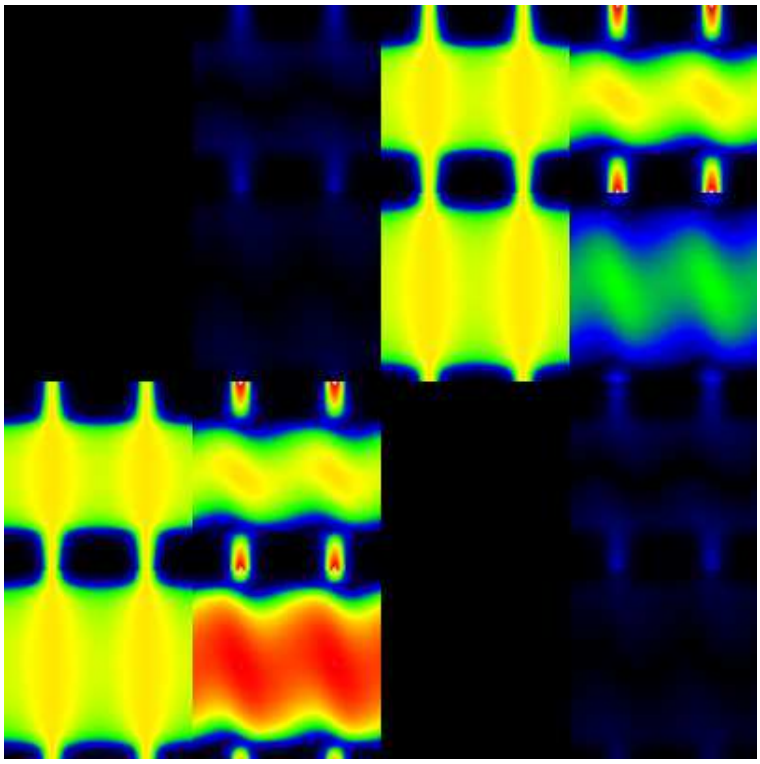

Figure 4.5: Magnitudes of the $\mathfrak{C}^T$ matrix from Eq. (4.20), with $kR = 30$, $k_z = 5$, $n = 1.5$ for the quadrupole with $\varepsilon = 0.1$.

the wave-vector. We quote from Refs [66, 1] that the average phase velocity is

$$\frac{d\overline{\theta}}{d(\gamma_1 R)} = 2\sin\overline{\beta}, \quad \text{with} \quad \overline{\beta} = \arccos\frac{\overline{m}}{\gamma_1 R}. \tag{4.37}$$

This behavior is shown in Fig. 4.6 and we state here again, that a change in $\mathrm{Re}\,[\gamma]$ will change the angle of the eigenvalue and a change in the imaginary $-\mathrm{Im}\,[\gamma]$ will move it radially outwards. With all this at hand we can predict the exact location of zeros of the secular function Eq. (4.35), at least within a reasonable range of deformation of the circle and reliably for a fraction of the resonances.

4.6 Adiabaticity of eigenvectors

But our argument goes further. We claim that the eigenvector $|\alpha\rangle$ ($|\xi\rangle$) associated to the $E_z^<$ ($B_z^<$) field has for a given γ has an identity when the mode is quantized, but also off quantization [40]. To quantify this claim we introduce a simple scalar product between two eigenvectors of the S-matrix

$$\langle\alpha(k)|\alpha(k+\Delta k)\rangle = \sum_m \alpha_m(k)\alpha_m^*(k+\Delta k). \tag{4.38}$$

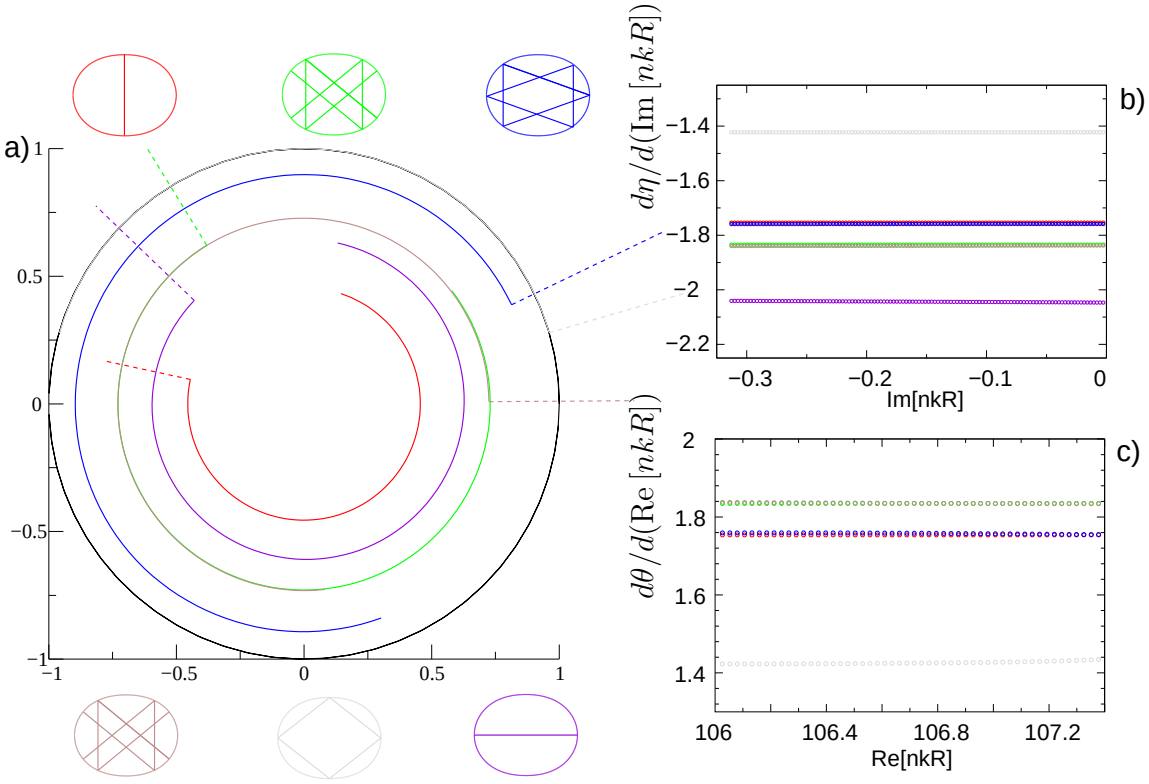

Figure 4.6: Several representative eigenvalues z (corresponding to states associated with the ray orbits above and below via color code) traced in the complex plane as one changes the real and imaginary values of k. First $\mathrm{Re}\,[k]$ is varied resulting in the circular arcs of fixed radius ($\mathrm{Im}\,[z]$); subsequently $\mathrm{Im}\,[k]$ is varied resulting in a radial motion and fixed $\mathrm{Re}\,[k]$. On the right hand side we show the constancy of the derivative of the phase angle θ with respect to $\mathrm{Re}\,[nkR]$ and of the derivative of the logarithm of the radius $\eta(k)$ with respect to $\mathrm{Im}\,[nkR]$, implying constant speed of the eigenphases as a function of k in the complex plane. The simulations are performed at $\varepsilon = 0.12$ quadrupolar deformation, $n = 2.65$.

We have analyzed this in Fig. 4.7[3] where we used the scalar product to calculate the overlap of each eigenvector with that of the eigenvector belonging to a 'fish' type eigenmode vs. the phase of the eigenvalue ξ. We choose the effective wave vector to be $kR = 120$ for the closed and $kR = 80, n = 1.5$ for the open calculation. The orthogonality relation is clearly fulfilled for the closed resonator, as we would expect, but also to a certain extent in the open resonator. This holds in the open resonator not only for a mode well localized on a stable periodic orbit, i.e. the 'fish' orbit, but also for a scarred rectangular orbit.

Seeing that states are quasi-orthogonal away from quantization we might ask how a state that is off quantization looks like in the real-space projection. We know that

[3]Note: The calculation shown in this Section have been obtained for the 2-d system, improving speed and efficiency. It has been however confirmed for the 3-d system too.

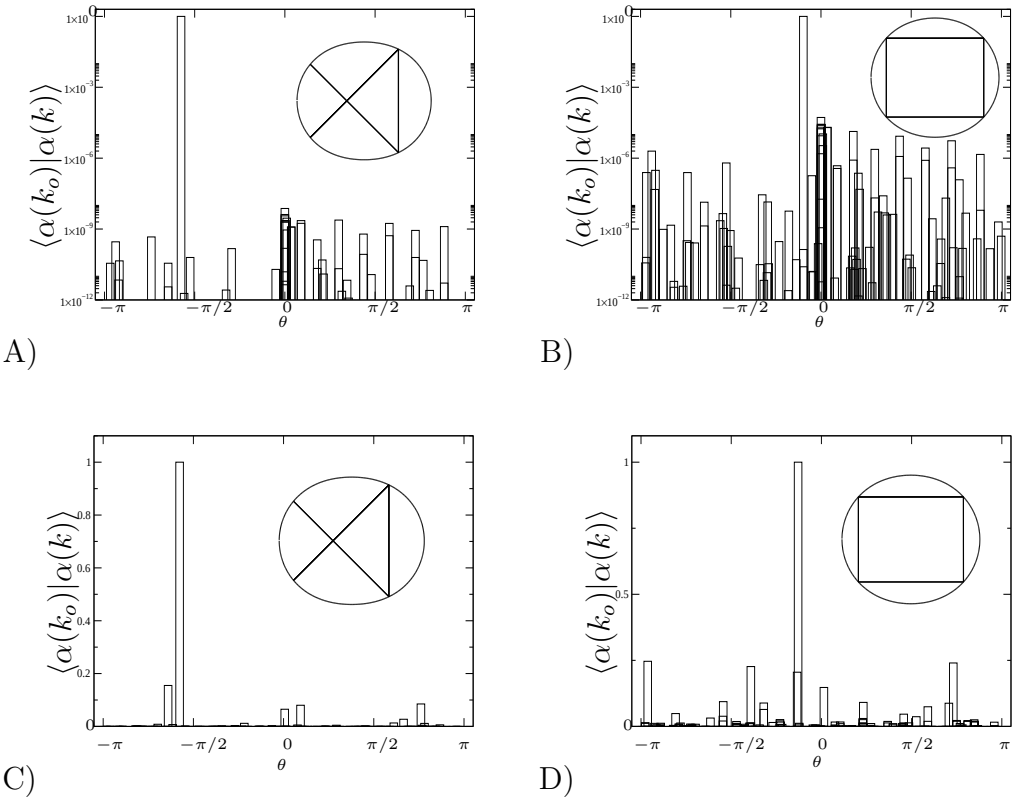

Figure 4.7: Orthogonality of eigenvectors $|\alpha\rangle$. Overlap defined by the scalar product in Eq. (4.38) with a stable 'fish' type orbit and the unstable rectangular orbit (see insets) in the quadrupole with $\varepsilon = 0.10$ vs. the phase of the eigenvalue θ. A) 'fish', B) rectangle in the closed cavity (note the log-scale) with $kR = 120$ and C) the 'fish', D) rectangle in the open cavity with $nkR = 120$, $n = 1.5$ (linear scale). Even the scarred rectangular orbit has a well defined identity.

the quantization condition is not fulfilled and when we write the internal field as

$$E_z^<(r,\phi) = \sum_m \alpha_m \left(H_m^+(\gamma_1 R) + e^{i\theta} H_m^-(\gamma_1 R) \right) e^{im\phi} \tag{4.39}$$

the existence of the $e^{i\theta}$ would leave us exposed to the r^{-m} singularity of the Neumann function at the origin. This limitation is an artifact of the particular choice of basis we might nevertheless be naïve and plot the state ignoring the phase using

$$E_z^<(r,\phi) = \sum_m \alpha_m 2J_m(\gamma_1 R) e^{im\phi}. \tag{4.40}$$

From this we can learn a bit of what happens in-between two quantized states. In Fig. 4.9 we explore it for the closed resonator, where we plot the internal field even beyond the boundary. The boundary is indicated by the white line. We can see

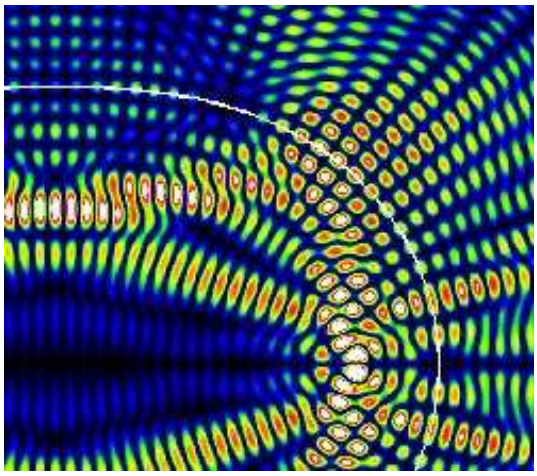

Figure 4.8: Un-quantized State calculated in the closed 2-d cavity at $kR = 70$, $\lambda = -(0.9978 + 0.0657i)$ the quantized values are at $kR = 68.2653$ and $kR = 72.0626$. We see that the boundary condition is not fulfilled. At $\lambda \sim -1$ we are exactly between quantization.

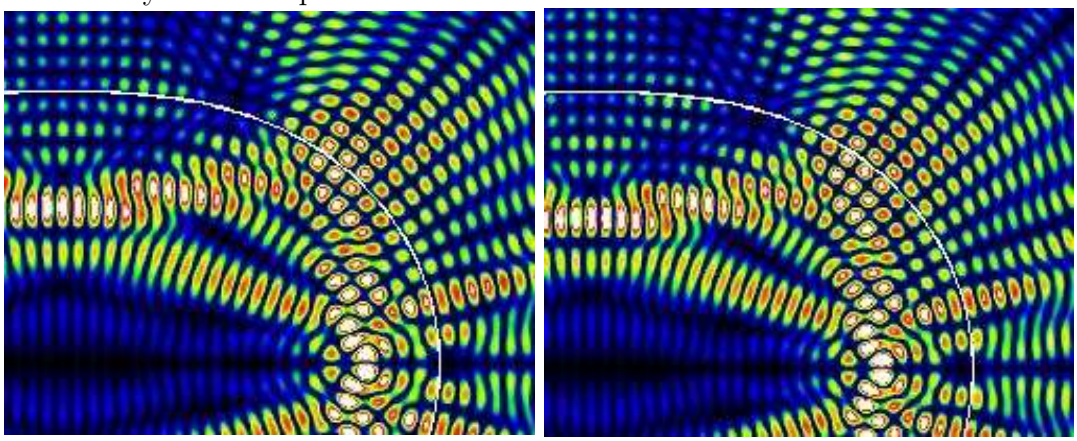

Figure 4.9: On the left the state quantized at $kR = 68.2653$, on the right at $kR = 72.0626$.

that at the point of quantization the boundary is on a nodal line, for the state off quantization the boundary is somewhere in-between. With a simple picture this can be understood. Every point in the field always depends on the product of the wave-vector k and the position $\boldsymbol{r}$. For the circular case this would just be the distance r from the origin. Increasing k can thus be seen as rescaling the coordinates or moving the boundary smoothly to the next nodal line.

To understand the 'identity' of a state even in the case when it is not simply related to a stable or unstable periodic orbit, we can use the powerful method of the Husimi-Poincaré projection technique, (see Section 4.10) where we can associate each mode with a certain area of the phase-space.

We will renew our claim that an eigenvector has an identity and that the identity will remain for small changes in k (small with respect to mean level spacing), thus

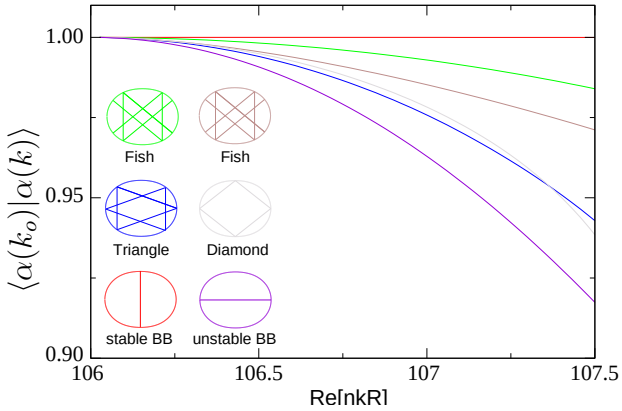

Figure 4.10: The overlap calculated for a set of states in the interval $nkR = 106 - 107.5$, for $\varepsilon = 0.12$ and $n = 2.65$. The associated classical structures are found from the Husimi projections of the respective states (see Fig. 4.11). The schematics identify the ray orbits with which they are associated (see discussion in text). At this deformation the short two-bounce orbit is stable, the long one unstable; the diamond orbit is stable and the fish and triangle orbits are unstable.

the behavior of the scalar product $\langle\alpha(k)|\alpha(k+\Delta k)\rangle$ is adiabatic. (This in general is not true for eigenvectors associated to the class of evanescent modes.) In Fig. 4.10 we confirm this claim numerically for a set of five different orbits, where we trace the overlap of the eigenvectors with the initial eigenvector at $kR_o = 106$ over an interval of the order of the mean-level spacing. We solve the S-matrix eigenvalue system first at $kR_o = 106$ where the eigenvectors $|\alpha(k)_o\rangle$ are obtained. We repeat this with a step size $n\Delta kR = 0.03$.

We can even extend this strategy to higher deformations, where the SOS is mainly chaotic and the Husimi projection localizes in the chaotic sea. An often encountered scenario is the *avoided crossing* of two scattering eigenvectors, as captured in Fig. 4.11. Two eigenvectors are traced over a a mean-level spacing. Both of the states are initially well-distinguished, their overlap is near zero. We follow both states adiabatically, and show the overlap with the initial 'fish' state $|\alpha_o\rangle$. The other state is concentrated in the seperatix region and associated with the unstable two bounce diametral orbit; we have plotted the unstable manifold (see Section 3.4.3) as a reference. If we follow the states long enough, we see that both of the states change identity. We note however that there is still going to be a state which has a considerable 80% overlap with the initial $|\alpha_o\rangle$. In the bottom right graph we see that states do like to localize in the phase space on homoclinic points, as suggested in Section 3.2.5

This simple behavior can be understood from the fact that the classical channels, angular momentum in our case, preserve their identity over a mean level spacing [66, 1]. In conclusion the radial and angular speeds of the eigenvalues are approximately 'decoupled'. To high accuracy the speed of the eigenphase is constant as is the log of the magnitude.

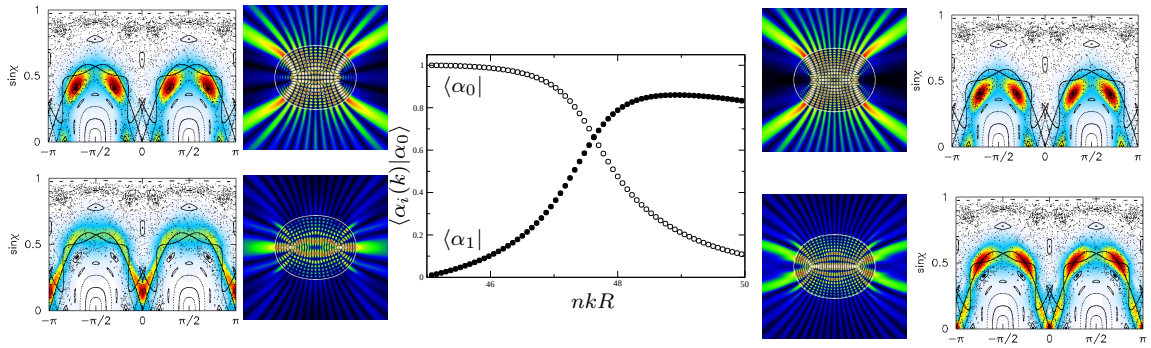

Figure 4.11: Two eigenvectors (quadrupole $\varepsilon = 0.11$) are traced by the criterion that the overlap is largest in two *consecutive* iterations. The figure shows the overlap of the two sets of states resulting with respect to one of the *initial* states, $\langle\alpha_0|$.

4.7 The Algorithm

With the last remarks in the preceeding section we can now establish an efficient numerical algorithm. The idea is demonstrated in Fig. 4.6, where first, the initial eigenvalues are followed while varying the real part of γ; each of the eigenvalues follow approximately a circular trajectory. Second, a purely imaginary change in γ, results in a change of the eigenvalues following an almost precisely radial path.

We thus state the algorithm:

1. Diagonalize $S(\gamma)$ at a given γ, with an eigensystem of size $(4N_{trunc} \times 4N_{trunc})$ and get $2N_{trunc}$ eigenphases θ^l and eigenvectors, $\left|\begin{smallmatrix}\alpha\\ \xi\end{smallmatrix}\right\rangle_o^{(l)}$, $l = 1, \ldots, N_{trunc}$.

2. Diagonalize $S(\gamma + \Delta\gamma)$ a second time at $\gamma = \gamma_o + \Delta\gamma$, where $\gamma \in \mathbb{C}$ and $|\Delta\gamma| \ll \gamma$ and associate each eigenvector $\left|\begin{smallmatrix}\alpha\\ \xi\end{smallmatrix}\right\rangle_o^{(l)}(\gamma + \Delta\gamma)$ with an initial eigenvector $\left|\begin{smallmatrix}\alpha^l\\ \xi\end{smallmatrix}\right\rangle_o^{(l)}(\gamma)$.

3. Approximate radial and angular speed of the eigenphase.

4. Assume constancy of speeds and approximate quantization wave-vector $\gamma_q^{(l)}$ for each initial eigenvector.

5. Construct the quasi-bound using the non-quantized eigenvector $\left|\begin{smallmatrix}\alpha^l\\ \xi\end{smallmatrix}\right\rangle_o^{(l)}$ mode via

$$\begin{pmatrix} E_z \\ B_z \end{pmatrix}_q^{(l)<} (r, \phi) = \sum_{m=-N}^{N} \begin{pmatrix} \alpha_m \\ \xi_m \end{pmatrix}^{(l)} J_m\left(\gamma_q^{(l)} r\right) e^{im\phi}. \qquad (4.41)$$

The last statement is valid due to the adiabaticity of the eigenvectors. In the ideal case we can construct $2N_{trunc}$ quasi-bound modes by only two diagonalization. This

limit is not always attained. The algorithm can be adapted for the particular interest. If the quantization of a single state is desired, multiple scans can be performed in a Newton's root-search like fashion and the quantization can be achieved to arbitrary precision. The real power nevertheless lies in the fact that we get a full discrete set of order $[\![\gamma]\!]$ discrete eigenmodes, compared to the external scattering approach; second, the calculated eigenstates have in general a physical identity, conserved over the mean-spacing. This identity relates them directly to the actual quasi-bound modes. A physically relevant quantity is the far-field distribution which we will describe below. A second one is the Husimi projection; we find that the off-quantized Husimi projection of the eigenvector is very close to that of the quantized one.

4.8 An experimental observable – The Far-field

The most common micro-laser measurement carried out in experiments is the so called *far-field* measurement. For this we position a CCD camera in the far-field of the cavity and record the emission intensity measured as a function dependent on the far-field angle Θ. We will explain this experimental method in detail in Chapter 8. The far-field information was the only information at hand for the famous 'Bow-tie' experiment in Ref. [8] Our algorithm is very efficient in calculating all possible far-fields achievable with a given resonator shape and index of refraction. We solve the S-matrix problem at a given γ close to the lasing frequency $\omega = c\gamma$. The far-field intensity of the E_z (B_z) component can be extracted from the outside field via the large argument expansion Eq. (G.12) and written as

$$I(\phi) = |E_z^>|^2 \propto \left| \sum_m \zeta_m e^{im\left(\phi - \frac{\pi}{2}\right)} \right|^2 , \tag{4.42}$$

where we have extracted all quantities independent of ϕ. The results are shown in Fig. 4.12 where we computed the far-field for the 'fish' mode at different quantization points over two level-spacings. We see that the far-field intensity distribution is very well-behaved and insensitive to small variations in γ used, as the strongly varying Hankel functions dropped out of the quantity. We have already seen above that the eigenstates $|\alpha\rangle$ ($|\xi\rangle$) have adiabatic behavior for small variations of γ and as $|\alpha\rangle$ ($|\xi\rangle$) is directly related to $|\upsilon\rangle$ ($|\zeta\rangle$) via Eq. (4.9) this comes as no surprise. Nevertheless it is very powerful as it allows us to obtain all possible emission patterns for a wide range of dielectric resonators very rapidly.

4.9 Polarization in the far-field

So far we have only considered the magnitude of each of the components of the solutions to vector wave-equation in the far-field. Polarization in general cannot be defined close to the cavity. In the far-field on the other hand, where the radiation is well approximated by a plane-wave-type field, we should be able to analyze the

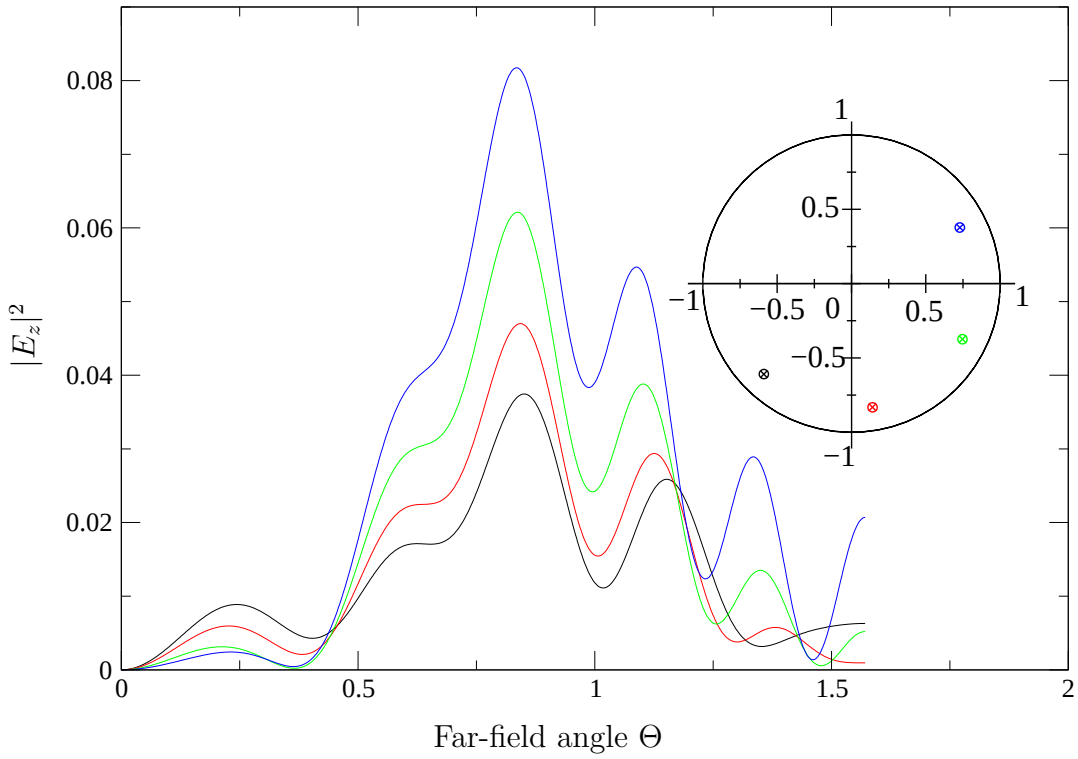

Figure 4.12: Far-field emission intensity pattern for a 'fish' mode in the quadrupolar rod with $\varepsilon = 0.1$, $\theta = 0.2 = \arctan k_z/\gamma_1$, at four different values of $\gamma = 40.0, 40.5, 41.0, 41.5$. Clearly the essential features of the emission patterns are calculable with non-quantized modes. In the inset we show the eigenvalues z in the unit circle.

polarization of the radiation in the far-field in conventional terms. For this, we need to expand each component of the three dimensional $\boldsymbol{E}$-field using the large argument Hankel-expansion. First we need to project the normal field component $\boldsymbol{E}_\perp$ into a suitable geometry, for which we will choose polar coordinates (ρ, φ) due the symmetry of our problem. Then, the gradient takes the form

$$\boldsymbol{\nabla}_\perp = \begin{pmatrix} \partial_\rho \\ \frac{1}{\rho}\partial_\varphi \end{pmatrix}. \tag{4.43}$$

The first task is to write the Eq. (2.16) and Eq. (2.17) in polar coordinates.

$$E_\rho = \frac{ik}{\gamma^2}\frac{1}{\rho}\partial_\varphi B_z - \frac{ik_z}{\gamma^2}\partial_\rho E_z \tag{4.44}$$

$$E_\varphi = -\frac{ik}{\gamma^2}\partial_\rho B_z - \frac{ik_z}{\gamma^2}\frac{1}{\rho}\partial_\varphi E_z \tag{4.45}$$

$$B_\rho = -\frac{in^2k}{\gamma^2}\frac{1}{\rho}\partial_\varphi E_z - \frac{ik_z}{\gamma^2}\partial_\rho B_z \tag{4.46}$$

$$B_\varphi = \frac{in^2k}{\gamma^2}\partial_\rho E_z - \frac{ik_z}{\gamma^2}\frac{1}{\rho}\partial_\varphi B_z \tag{4.47}$$

As we are interested in the far-field, we only investigate the field outside and write the the outgoing component of E_z and B_z as

$$E_z^>(\rho,\varphi) = \sum \upsilon_m H_m^+(\gamma_2 k\rho)e^{im\varphi} \tag{4.48}$$

$$B_z^>(\rho,\varphi) = \sum \zeta_m H_m^+(\gamma_2 k\rho)e^{im\varphi} \tag{4.49}$$

$$\tag{4.50}$$

Using the recursion relations of the Bessel-functions we can write the derivatives as

$$\partial_\rho H(\gamma_2 k\rho) = \gamma_2\left(H_{m-1}^+ - \frac{m}{\gamma_2\rho}H_m^+\right) \tag{4.51}$$

using the large argument expansion we get

$$H_m^+ \quad\rightarrow\quad \sqrt{\frac{2}{\pi\gamma_2\rho}}\exp i(\gamma_2\rho - \pi/4)\cdot e^{-im\pi/2} \tag{4.52}$$

$$\partial_\rho H_m^+ \quad\rightarrow\quad \sqrt{\frac{2}{\pi\gamma_2\rho}}\exp i(\gamma_2\rho - \pi/4)\cdot e^{-im\pi/2}\left\{e^{-i\pi/2} - \frac{m}{\gamma_2\rho}\right\} \tag{4.53}$$

Extracting the angular part of the field at a constant $\rho\rightarrow\infty$

$$|\boldsymbol{E}|^2 = \left|\begin{pmatrix}E_\rho\\E_\varphi\\E_z\end{pmatrix}\right|^2 \sim \left|\begin{pmatrix}k_z/\gamma_2\sum\upsilon_m e^{im(\varphi-\pi/2)}\\ k/\gamma_2\sum\zeta_m e^{im(\varphi-\pi/2)}\\ \sum\upsilon_m e^{im(\varphi-\pi/2)}\end{pmatrix}\right|^2 = \left|\begin{pmatrix}k_z/\gamma_2 E_z\\ k/\gamma_2 B_z\\ E_z\end{pmatrix}\right|^2 \tag{4.54}$$

The coefficient in front of the field are all related to each other, following Fig. 2.3 B) we can substitute $k_z/\gamma_2 = \tan\alpha$ and $\gamma_2/k = \cos\alpha$. In the far-field the $\boldsymbol{E}$ and $\boldsymbol{B}$ fields must be fully transverse to the propagation direction, which will have both a (2d) radial component and a z-component. Thus the transverse direction is tilted by the angle α to our original coordinate system and we need to rotate the ρ and φ component of the $\boldsymbol{E}$-field by

$$\begin{pmatrix}\cos\alpha & 0 & -\sin\alpha\\ 0 & 1 & 0\\ \sin\alpha & 0 & \cos\alpha\end{pmatrix}\begin{pmatrix}\tan\alpha E_z\\ \sec\alpha B_z\\ E_z\end{pmatrix} = \begin{pmatrix}0\\ \sec\alpha B_z\\ \sec\alpha E_z\end{pmatrix} \tag{4.55}$$

This yields a two-component transverse vector and the polarization phase in the far-field is found to be equal to the phase difference Δ of B_z and E_z. We have *linear polarization* for $\Delta = 0$, *circular polarization* for $\Delta = \pi/2$ and equal magnitude of the fields $|B_z|^2 = |E_z|^2$. The most general case is *elliptic polarization*.

Another possible setup used recently in a number of experiments [92, 3, 2, 17] and Chapter 8 is the imaging technique. A CCD camera in the far-field records the intensity profile of a sidewall viewed at an angle Θ. This information can be mapped to a two dimensional *boundary image-field* plot, from which we can extract the radiation coming from a position ϕ at the boundary going into a direction Θ in the far-field. Knowing the point on the boundary from where light originates and the far-field angle into which the light propagates, one can easily convert this into the inside angle of incidence $\sin\chi$, thus retrieving a phase space projection of the emitted field — the Husimi Projection, described in the next section.

4.10 Husimi Projection[4]

In this section, we will briefly review the Husimi Projection technique [58], which allows us to relate a given mode to the phase space structures in the SOS. Just as for quantum wavefunctions, for these two-dimensional electromagnetic fields we can represent the solutions in real space (the solutions we have been calculating) or, by Fourier transforming them, in momentum space. However we are interested in representing the solutions in the phase-space of the problem so that we can understand their ray-dynamical meaning, and ultimately in projecting such phase space densities onto the SOS which is our standard interpretive tool. Just as in quantum mechanics, we cannot have full information about real-space and momentum space at the same time due to the analog of the uncertainty principle, which here is reflected by the property of Fourier transforms:

$$\Delta x \cdot \Delta p \geq \frac{1}{2k} \tag{4.56}$$

where Δx and Δp are the widths of $\psi(\boldsymbol{x})$ and $\tilde{\psi}(p)$ in real and momentum space. Thus our goal is to take the solution $\psi(\boldsymbol{x})$ and associate with it a momentum content in some region around each point $\boldsymbol{x}$, recognizing that our resolution in real space is limited by the uncertainty relation. To interpret the quantized wavefunction classically we define the Husimi distribution

$$\rho_\psi(\bar{\boldsymbol{x}}, \bar{\boldsymbol{p}}) = |\langle z|\psi\rangle|^2 = \left| \int d^2\boldsymbol{x} Z^*_{\bar{\boldsymbol{x}}\bar{\boldsymbol{p}}}(\boldsymbol{x})\psi(\boldsymbol{x}) \right|^2, \tag{4.57}$$

where the real-space representation of a coherent state is given by

$$Z_{\bar{\boldsymbol{x}}\bar{\boldsymbol{p}}}(\boldsymbol{x}) = \left(\frac{1}{\pi\eta^2}\right)^{1/4} \exp(ik\bar{\boldsymbol{p}}\cdot\boldsymbol{x}) \exp\left(-\frac{1}{2\eta^2}|\boldsymbol{x}-\bar{\boldsymbol{x}}|^2\right). \tag{4.58}$$

[4]This Section is taken in part from Ref. [1]

This defines a function in the 3d phase space if we fix $|\rho|$. By projecting the Husimi distribution onto a circle of a constant radius and integrating over the momentum, we obtain a 2-d density distribution that we can project onto the SOS

$$H_\psi(\bar{\phi}, \sin\bar{\chi}) = \left| \sum_{-\infty}^{\infty} \alpha_m H_m^+(nkR_c) \mathrm{e}^{-inkR_c(\sin\chi - \sin\bar{\chi})\bar{\phi}} \mathrm{e}^{-\frac{\sigma^2}{2}(\sin\chi - \sin\bar{\chi})^2} \right|^2 . \tag{4.59}$$

For optimal resolution in both SOS coordinates, we choose $\sigma \sim 1/\sqrt{nkR_c}$ (R_c can be chosen at any convenient value). Finally, in order to calculate the distribution on a section on the boundary $r = R(\phi)$ instead of the circle, we choose R_c slightly outside the boundary, and extrapolate the Husimi distribution Eq. (4.59) to the boundary using the classical equations of motion; i.e. every pair $(\sin\bar{\chi}, \bar{\phi})$ on the circle maps uniquely to a different pair $(\sin\chi, \phi)$ on the boundary. We can regard this mapping as simply a change of variables so that the Husimi-SOS distribution on the boundary, $H_\psi(\phi, \sin\chi)$, satisfies:

$$H_\psi\left(\phi(\bar{\phi}, \sin\bar{\chi}), \sin\chi(\bar{\phi}, \sin\bar{\chi})\right) = H_\psi\left(\bar{\phi}, \sin\bar{\chi}\right) . \tag{4.60}$$

4.11 Quasi-bound modes and classical phase space structures

In this section we will present a few representative quasi-normal modes generated by our numerical algorithm (Section 4.7) in their real space and phase space representation. We will put special emphasis on the connection with classical phase-space structures. All the wavefunction plots and Husimi distributions are generated with the *non-quantized* scattering eigenvectors, as described above.

The first test will be the unperturbed circle. In the circle only *whispering gallery*-type orbits exist. In Fig. 4.13 A) we show such a whispering gallery mode, its Husimi distribution is shown in Fig. 4.13 B). We see, as the angle of incidence in the circle is conserved, so is the Husimi distribution – spread out along a straight line. As the Husimi distribution is localized well above the critical line the light undergoes classic total internal reflection. The effect of a small change of $\Delta\varepsilon = 0.03$ is shown in Fig. 4.13 C), D) where a quasi-bound mode corresponding to a deformed whispering gallery mode is portrayed. From close inspection of the Husimi projection we note that this mode follows an invariant adiabatic curve given by Eq. (5.1). This line is not anymore straight and we observe its touching the critical line at the points of highest curvature. It had been predicted [12, 13, 14] that such modes might show directional emission radiating from the points of highest curvature in tangent direction. For a in-depth discussion and expansion of this theory see Chapter 5.

Already at 3% deformation we see another structure in the SOS. Large stable islands are formed, right above the Husimi projection band in Fig. 4.13 D) we see the four islands of the 'diamond' orbit and centered around $\pm\pi/2$ the stable two bounce 'bouncing ball' orbit Fig. 4.13 E). Such large islands can support multiple

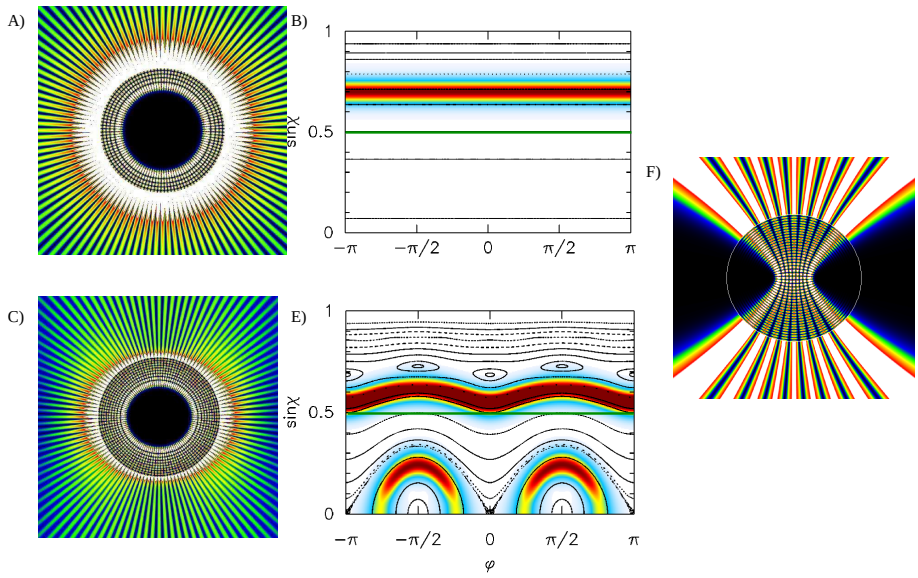

Figure 4.13: Real-space false color plot of a solution at of the circle A) $\varepsilon = 0$ and its Husimi projection. C), E) solutions of a quadrupole with $\varepsilon = 0.03$. D) Husimi projections of states C) (higher) and E) (lower). The solutions are obtained at $nkR = 82$ and $n = 2$. The solid line green at $\sin\chi = \sin\chi_c = 1/n = 0.5$ indicates the critical line, above which light is classically total internally reflected.

modes. An intensive study and theory describing these modes has been given by us elsewhere [93].

Periodic orbits are not just of importance when they are stable fixed-points. It has been shown a while ago that even unstable periodic orbits can support a wave-function [94, 95] in a closed cavity. Such *scarred* modes are shown in Fig. 4.14. Here we show the unstable bouncing ball orbit. In panels (a) and (b) the 'fundamental' mode is shown, which has its highest intensity located on the unstable fix-point. The consecutive modes are higher excited unstable bouncing ball orbits. In order to be able to associate them to the unstable bouncing ball orbit, we plot the *unstable/stable manifolds* onto the SOS. (For a detailed description of unstable/ stable manifolds see Section 3.4.3.) As we have motivated there, the intersection points of the manifolds, so called *homoclinic points* (Section 3.3.8) pose as attractors and localize the mode on them. This is clearly seen in Fig. 4.14 (d) and (f). It is interesting to note here that the corresponding real-space plots Fig. 4.14 (c) and (e) do not reveal any distinct structure contrary to the Husimi projection. For the closed system such a localization on homoclinic points has been earlier reported in Ref. [40].

At large deformations the spectrum contains chaotic modes which cannot easily be associated with any particular classical phase space structure. One of such modes is plotted in Fig. 4.15. Here the support of the mode in the phase space lies completely in the chaotic regime and a close observation of the nodal structures in the real space

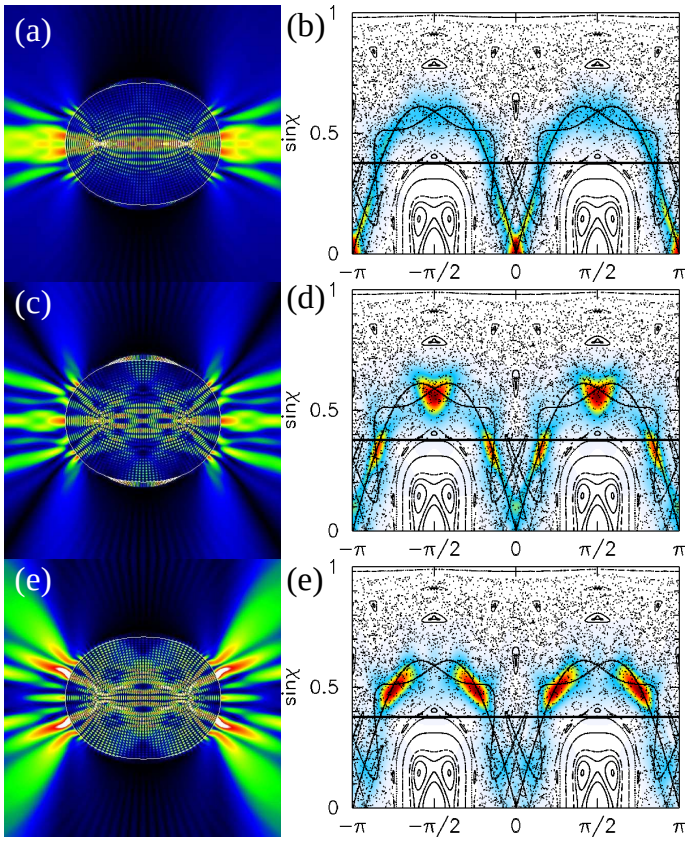

Figure 4.14: Real-space plots and Husimi distributions of scattering eigenvectors scarred by the unstable bouncing ball orbit. Superimposed on the SOS are the stable and unstable manifolds. (a),(b) fundamental mode; (c),(d) eigenvector scarred by (c),(d) the primary intersection and (e),(f) the secondary intersection. These solutions are found at $nkR = 106$, $\varepsilon = 0.12$ and $n = 2.65$.

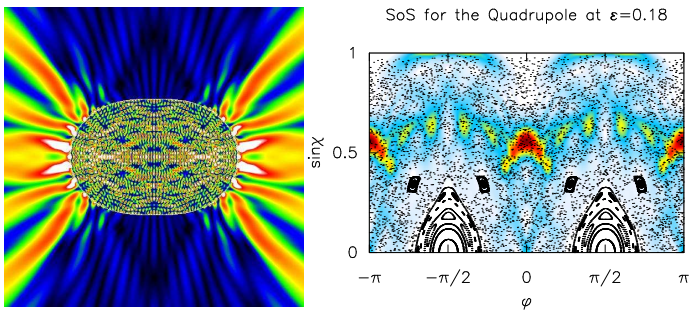

Figure 4.15: Real-space false-color plot and Husimi distribution of a chaotic mode at a quadrupolar deformation of $\varepsilon = 0.18$ and $n = 2.65$, quantized at $kR = 32.6638 - 0.06964i$.

plot reveals that there is no regularity above the scale of the wavelength.

4.12 Symmetry reduction

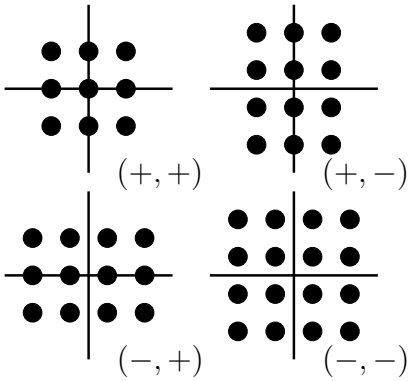

Figure 4.16: Nodal appearance in the wavefunction for the four different symmetries.

We can considerably reduce the calculation speed by taking symmetries into account. Often the symmetry group of the system we consider (e.g. the quadrupole) have two reflection symmetries and can be written as $\{1, \sigma_x, \sigma_y, \sigma_{xy}\}$. We apply this group to the Helmholtz equation to construct the symmetrized wave functions. Here we will encounter four different types, classified as $(+,+), (+,-), (-,+), (-,-)$. The symmetry operators will reduce the number of components for each wave-function from $2N$ to $\frac{1}{2}N$. We have not only noticed a huge speed increase for the calculation, but also an increase in numerical stability. The effect of the symmetry can easily be seen in a wavefunction plot, when we compare the nodal structure. In Fig. 4.16 we have related the nodal structure of the real space wave function to our definition of the symmetries for the convenience of the reader.

A comparison of different methods for the example of the non-symmetrized integrating method with the symmetrized is shown in Fig. 4.17. The values are compared in the Table below Fig. 4.17. We note that the resonance agree to $10^{-5}kR$.

4.13 Quality of numerically generated resonances

In this section we want to compare the two methods of calculating the resonances of the cylinder presented in this Chapter. The first method uses separability to arrive at Eqs (4.12), (4.13) and then perform a complex γ root search. The second method is based on Eqs (4.17), (4.18), is of general applicability, and uses the root extrapolation algorithm given in Section 4.7. In Fig. 4.18 we compare the quality of the resonances found by the S-matrix method of Section 4.7 and the solutions to Eq. (4.13). It can be seen that the S-matrix program can find the resonances extremely well in the region close to where the search is started, here at $kR_o = 20$. Even one spectral length away the error is still less than 2%. For the imaginary part of the resonance we need to note that the values span a wide region and a relative error of order unity is still acceptable.

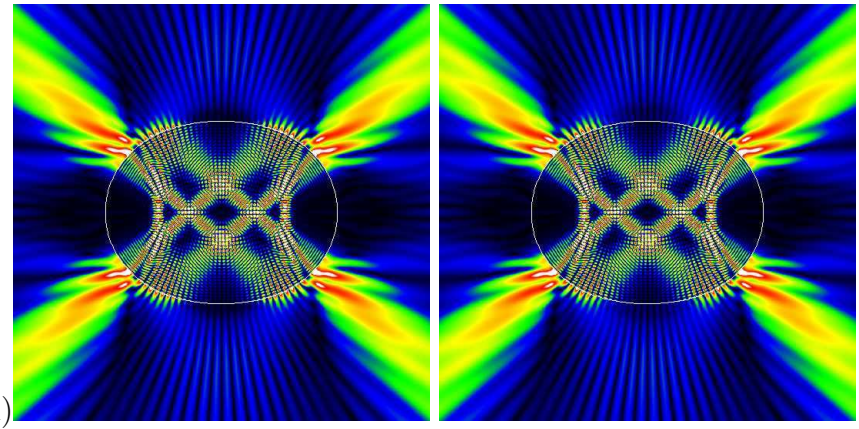

method	kR
A) no-sym int	49.4304084 -0.0717921i
B) sym no-int	49.4304122 -0.0717936i

Figure 4.17: Comparison of the wavefunction plots for the 'fish' mode in the 2-d quadrupole. A) solution to the over the boundary integrated non-symmetry-reduced system at $kR = 49.4304084 - 0.0717921i$; B) solution to the $(-+)$ symmetry reduced direct boundary matching problem at $kR = 49.4304122 - 0.0717936i$.

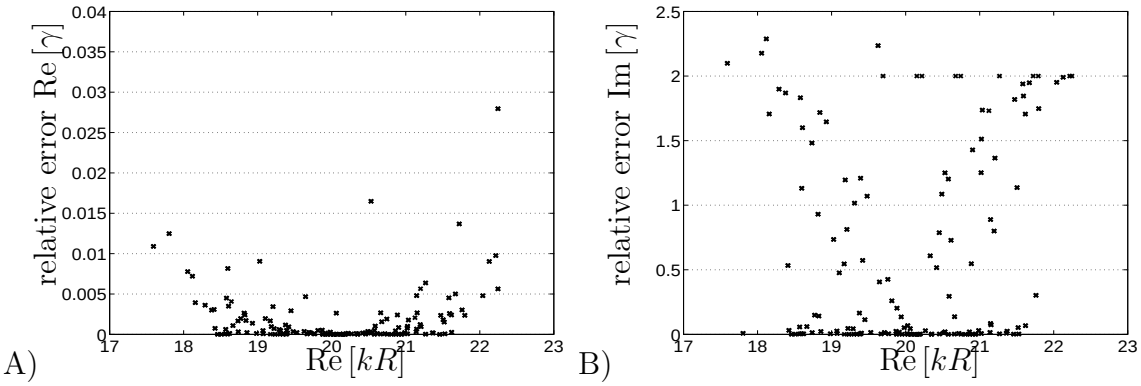

Figure 4.18: Comparison of the S-matrix method ($n = 2$, $k_z = 5$, $kR_o = 20$, $m^{max} = 40$) with the solutions to the quasi-bound resonances Eq. (4.16) for a circular rod with $n = 2$, $k_z = 5$ A) relative error in the real part of the resonance $\mathrm{Re}\,[kR]$ and B) relative error in the imaginary part of the resonance $\mathrm{Im}\,[kR]$. Here we note that $\mathrm{Im}\,[kR]$ spans a wide region from $10^{-1} \sim 10^{-10}$, thus even finding the width with a relative error of a factor of two represents a useful result.

4.14 Conclusion and Outlook

In this chapter we have presented numerical methods for calculating resonances in dielectric resonators. We rephrased the S-matrix diagonalization problem as a general eigenvalue problem for the benefit of avoiding the inversion of matrices. For this system we observed that the eigenvalues have decoupled speeds in the the radial

(angular) directions for a imaginary (real) shift in γ. This and the adiabatic behavior of the eigenvectors was used to devise an algorithm to find $\mathcal{O}[\gamma]$ resonances with only two diagonalizations. The method is highly efficient for the problems we focus on, however it will become unreliable for large deformations from the circle and large values of γ. This limitation is related to the basis used for our ansatz, the Hankel functions. Although they have a nice semiclassical interpretation, the expansion in Hankel functions is ill conditioned. We can observe the breakdown already in the real-space plots at the points that are just outside the boundary with smallest radius $r = R_{min}$. Here the evanescent components ($m > kR_{min}$) take on very large values and thus the solutions become very sensitive to the numerical errors of the coefficients $|\gamma\rangle$. This can not just be avoided by including fewer evanescent channels, as these areas are exactly in the highest overlap regime. An often used strategy is to include more evanescent channels in the diagonalization problem, but use less for the plotting of the wave functions.[5]

[5]One thought would be to use a different basis to expand in, maybe the Mathieu functions[96] which seem a good choice as they are eccentricity adapted. Unfortunately these functions are much less converging than the Bessel functions and in order to calculate them more efficiently are mostly expanded in Bessel functions. Thus any hope of using them must be in vain.

Chapter 5

Dramatic Shape Sensitivity[1]

5.1 Introduction

In this chapter we examine in detail the question of shape sensitivity of the emission patterns from ARC lasers operating on 2-d modes ($K_z = 0$). The ray-dynamical approach suggests such sensitivity as first shown by Nöckel, Stone and Chang [12, 13, 14]. In 2002 a series of experiments were done at Yale to test these ideas and led to a significant revision of the qualitative interpretation of the ray-simulations.

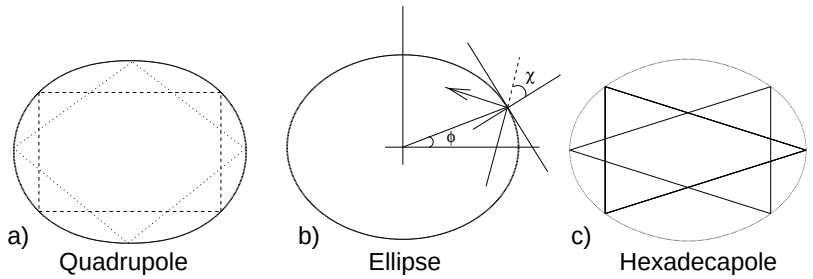

Figure 5.1: Cross-sectional shapes of micro-pillar resonators studied: (a) The quadrupole, defined in polar coordinates by $R = R_0(1+\varepsilon\cos 2\phi)$, (b) The ellipse, defined by $R = R_0(1+((1+\varepsilon)^4-1)\sin^2\phi)^{-1/2}$ and (c) The Quadrupole-Hexadecapole, defined by $R = R_0(1+\varepsilon(\cos^2\phi+\frac{3}{2}\cos^4\phi))$ all at a deformation of $\varepsilon = 0.12$. Note that all shapes have horizontal and vertical reflection symmetry and have been defined so that the same value of ε corresponds to approximately the same major to minor axis ratio. In (b) χ is the angle of incidence of a ray with respect to the local normal. In (a) and (c) we show short periodic orbits ("diamond, rectangle, triangle") relevant to the discussion below.

One might naively assume that such chaotic ray dynamics would generate a fluctuating and pseudo-random emission pattern, but in fact the ray motion follows a dominant flow pattern in the phase space favoring escape at certain points on the boundary and in certain directions in the far-field. For the quadrupole and related

[1]This chapter is based on work published in Ref. [2]

ARCs Nöckel and Stone originally argued that the flow pattern was approximately describable as rapid motion along adiabatic invariant curves (which could be calculated from knowledge of the boundary shape) and slow diffusion in the transverse direction. Major deviations from the flow pattern would occur in the vicinity of stable periodic ray orbits for reasons to be discussed in detail below. As the shape of the adiabatic curves and the location of stable and unstable periodic orbits is quite sensitive to boundary shapes, this theory did predict a rather dramatic sensitivity of the emission patterns from ARC micro-lasers to the shape of the boundary. The Yale experiments represented the first series of experiments with well-controlled boundary shapes in the low-index regime, to test these theoretical ideas. The shapes considered were the quadrupole, elliptical and hexadecapole ARCs (see definitions, caption of Fig. 5.1). It was found that; 1) There is a remarkable and reproducible difference in the lasing emission patterns from ARC lasers with very similar boundary shapes. 2) The basic difference between chaotic (quadrupole) and non-chaotic (elliptical) ARC emission patterns is in agreement with the predictions of Nöckel and Stone based on the adiabatic model. 3) Nonetheless the *persistence* of highly directional emission patterns for highly deformed quadrupolar ARCs is inconsistent with the adiabatic model and is a quite surprising experimental discovery. We propose a new theoretical model which attributes the high emission directions observed for the chaotic shapes to the flow pattern produced by the unstable manifolds of short periodic orbits; this flow pattern differs significantly from the adiabatic model. This model is shown to explain both the persistence of narrow emission peaks in the quadrupole at high deformation and the major shift in emission directionality at large deformation for ARCs with hexadecapole deformation. It also predicts that completely chaotic boundary shapes, such as the stadium, can nonetheless exhibit highly directional emission.

5.2 Dynamical Eclipsing

In Chapter 3 we discussed the ray dynamics of ARCs using the surface of section to illustrate the generic properties of mixed phase space and contrast them with integrable dynamics. The idea of dielectric cavities as "leaky" billiards with refractive escape was introduced as well as the technique of ray escape simulations.

In a series of papers beginning in 1994, Nöckel, Stone and Chang [12, 97, 13, 14] proposed the first version of that ray escape model.

A challenging point for the general definition of such a model is that in the case of chaotic dynamics there is no simple correspondence between a set of rays and a set of modes of the wave equation (as there is in the integrable case – see Section 3.6.1). Nöckel and Stone proposed [97, 14] that an appropriate set of initial conditions for ARCs would be to start a uniform distribution of rays on an adiabatic curve of the boundary [44, 45], which can be thought of as the curve in the SOS that a ray *would* follow in the absence of chaos (this approximation describes the exact flow in the ellipse, see Fig. 3.9 for an example). Using this model they were able to predict a

striking difference in the emission patterns from quadrupole resonators with index $n = 1.5$ as opposed to index $n = 2.0$. Due to the difference of the flow in the ellipse and the quadrupole they where also able to predict that quadrupole resonators with deformations in the range of 10-12% and index of refraction $n = 1.5$ would emit very differently than elliptical resonators with the same major to minor axis ratio. Specifically the elliptical resonators would emit from the points of highest curvature on the boundary roughly in the tangent direction (90°) while the quadrupoles of the same index would emit at roughly a $35° - 45°$ angle to the major axes. It was argued that the origin of this effect is the presence in the quadrupole of a stable four-bounce periodic ray orbit which prevents emission from the highest curvature points in the tangent direction, an effect they termed "dynamical eclipsing" [13, 14]. This finding was supported by numerical solutions of the linear wave equation for the quasi-bound states and their far-field emission patterns. A subsequent experiment on lasing droplets by Chang *et al.* [47] was successfully interpreted as strong evidence for such dynamically eclipsed lasing modes. However this experiment was less direct than desirable for two reasons. First, the droplet was a deformed sphere with many possible lasing modes, most of which were not of the two-dimensional type considered in references [13, 14]; it was argued, but not experimentally shown, that the 2-d "chaotic" modes dominated the lasing emission. Second, the droplet shape deformation was not controlled and could not be manipulated to turn the effect on and off. Recently, Lacey *et al.* [98] reported an experiment on nearly spherical resonators where they addressed the former but not latter problem. The experiments generalized here remedy both of these shortcomings. First the lasers are deformed cylinders and the lasing modes are truly two-dimensional. Second the boundary shapes were fabricated using a mask to conform to the desired cross-sectional profile. Hence we can directly compare e.g. quadrupolar and elliptical ARC lasers and observe the presence or absence of the dynamical eclipsing effect over a range of deformations.

5.3 The imaging technique for the study of microcavity resonators

The detection part of the experiment was designed in accordance with the information contained in the SOS diagram. The detector must be able to extract two pieces of information: 1) where along the sidewalls the light is emerging from the microcavity, that is, the angle ϕ, and 2) what the angle of the emitted ray is which is related to the internal incident angle χ by Snell's law of refraction. A detector that can only measure the far-field radiation pattern is insufficient because it misses where the light emerges along the sidewall. The far-field pattern alone is not unique in that the same pattern can occur for different sidewall distributions of emission. Any detection system ought to be able to distinguish between the two different emission types shown in Fig. 5.2, where the far-field patterns are similar, but the image patterns along the sidewalls are different.

Figure 5.3 shows the detection system that was settled upon as the best com-

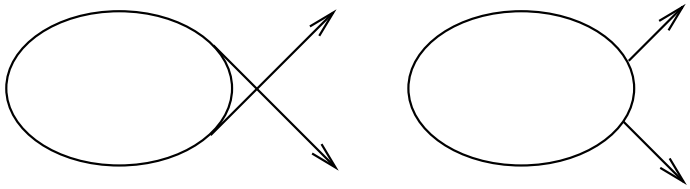

Figure 5.2: Two possible emission patterns with different emitting points on the boundary, which yet can result in identical far-field distributions.

promise between obtaining the far-field pattern while maintaining spatial resolution along the sidewalls. In this setup, microlaser devices are optically pumped normal to the plane of the pillar and light emitted from the side-walls is collected through an aperture in the far-field, passed through a lens and collected on a CCD camera. The key element in this detection system is the aperture placed before the collection lens. The aperture accomplishes two purposes: 1) it limits the solid angle of the collected light; and 2) it extends the depth of field that the light is collected from. The aperture sets a solid-angle limitation and restricts the far-field profile to an angular resolution of 5 degrees. The small aperture extends the depth of field to be larger than the longest diameter of the microstructure. The depth of field associated with the numerical aperture (NA = 0.047) is 200 μm. The largest microcavity being imaged has the longest dimension of 120 μm. Thus the entire microcavity is in focus at the same time, regardless of the rotational alignment of the microcavity with respect to the camera.

The relative angle between the CCD camera and the major axis of the quadrupolar shaped microcavity is designated as θ. At any given camera angle, the horizontal axis corresponds to different locations along the sidewalls. That horizontal strip gives false color coded intensity information as a function of pixels on the CCD camera, which can be converted to a position ϕ on the resonator boundary. The next angle

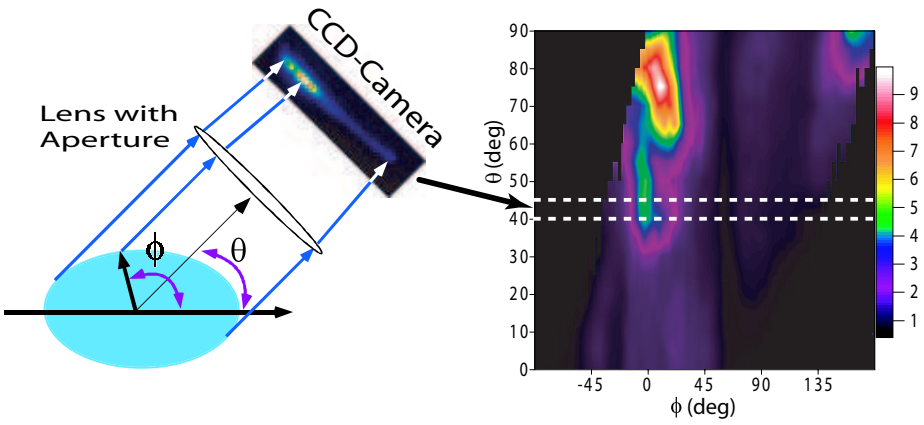

Figure 5.3: Experimental setup for measuring simultaneously far-field intensity patterns and images of the sidewall emission.

forms another strip which is placed directly under the former strip. Measurement of the intensity is made every 5 degrees from 0 to 360. This yields a two-dimensional plot, called the *imagefield*, where a given data point $I(\phi, \theta)$ denotes the intensity emitted from sidewall position ϕ towards the far-field angle θ. The latter can easily be converted to an incidence angle $\sin\chi$, using Snell's law and basic trigonometry. Hence, what is recorded is actually a phase space plot of the emitted radiation. This correspondence is put into a rigorous basis in Ref. [1]. Such 2D imagefield plots will be presented throughout the text for many of the experiments.

The far-field intensity at any angle is obtained by summing up all the pixels within the horizontal strip. This sum at a given angle is called the far-field intensity at that camera angle; we show many such plots below. This way of obtaining the far-field intensity is subtly different from placing a photomultiplier (with a pin hole) to define the angular resolution. Similarly, the *boundary image field* is obtained by integrating over all far-field angles for a fixed point ϕ on the boundary. This allows us to identify the brightest emission points on the sidewall (we rarely show these plots below, but they are used in the interpretation of the data).

5.4 Experimental Data

The experiments we studied were performed on differently shaped dye (DCM)-doped polymer (PMMA) samples that are fabricated on top of a spin-on-glass buffer layer coated over a silicon substrate via a sequence of microlithography and O_2 reactive ionic etching steps. The effective index of refraction of these microcavities is 1.49, much lower than for experiments performed using a similar set-up on GaN, to be discussed in Chapter 8, where the index of refraction is $n = 2.65$ [99, 3]. They are optically pumped by a Q-switched Nd:YAG laser at $\lambda = 532$ nm incident normal to the plane of the micropillar. Light emitted from the laser is imaged through an aperture subtending a 5° angle and lens onto a ICCD camera which is rotated by an angle θ in the far-field from the major axis. A bandpass filter restricts the imaged light to the stimulated emission region of the spectrum. The ICCD camera records an image of the intensity profile on the sidewall of the pillar as viewed from the angle ϕ which is converted from pixels to angular position ϕ. In this chapter we studied micro-cavities with elliptic, quadrupolar and quadrupolar-hexadecapolar shape of an average radius $R_o = 100\mu$m (see formulas in Fig. 5.1 caption). The observed modes have a linewidth that is below the resolution of the spectrometer, this indicates that the Q-factors must be larger than $Q_{sp} = \lambda/\Delta\lambda \approx 3 \times 10^4$. Each shape was analyzed at eccentricities of $\varepsilon = 0.12, 0.14, 0.16, 0.18$ and 0.20. The lasing is most likely multi-mode although there was no direct evidence for this.

In Fig. 5.4 we show the experimental results in a color scaled ICCD image. The two angles are the sidewall angle ϕ (for the horizontal coordinate) and the camera angle θ (for the vertical coordinate). We omit the data for $\varepsilon = 0.14$ deformation as it does not exhibit any effect not captured by the data at the other deformations. To obtain the *far-field* pattern with respect to θ, we integrate the image over all

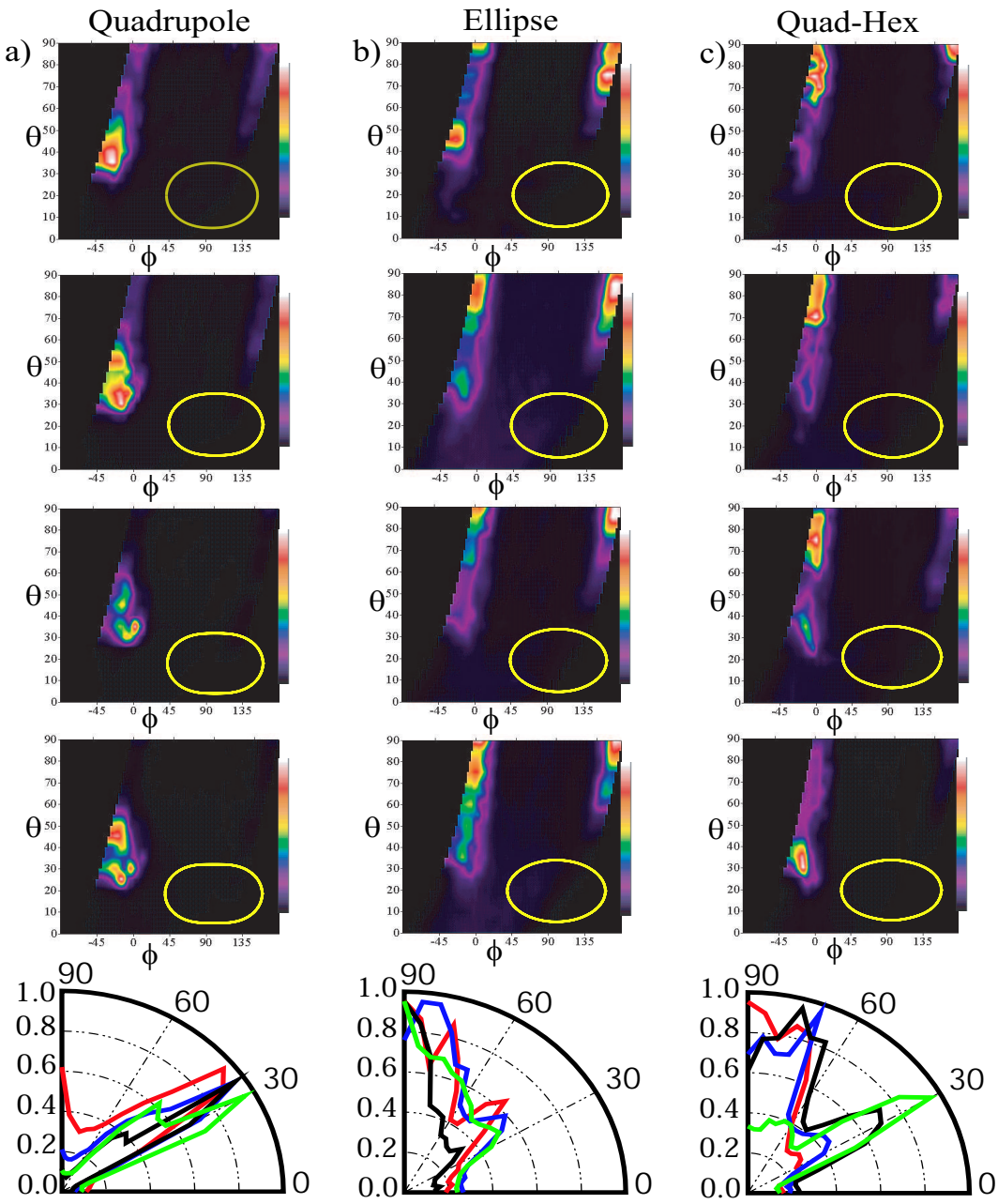

Figure 5.4: Two-dimensional display of the experimental data showing in false color scale the emission intensity as a function of sidewall angle ϕ (converted from ICCD images) and of the far-field angle θ (camera angle). Columns from left to right represent the quadrupole, ellipse and quadrupole-hexadecapole respectively. Insets show the cross-sectional shapes of the pillars in each case (for definitions see Fig. 5.1). The graphs at the bottom show the far-field patterns obtained by integration over ϕ for each θ, normalized to unity in the direction of maximal intensity. The deformations are $\varepsilon = 0.12, 0.16, 0.18, 0.20$ (red, blue, black and green respectively)

sidewall angles ϕ. The *boundary image field* is calculated by integrating over θ for each ϕ. As insets we show the exact shape of each of the microcavities. Although the shapes appear very similar to the eye, we find dramatic differences in the far-field emission patterns, which in the case of the ellipse vs. the quadrupole, persist over a wide range of deformations. Specifically, the far-field emission intensity for the quadrupole exhibits a strong peak at $\theta = 34^\circ - 40^\circ$ which remains rather narrow over the observed range of deformations. Over the same range of deformation the boundary image field for the quadrupole changes substantially and does not exhibit one localized point of emission. In contrast, the ellipse emits into the $\theta \sim 90^\circ$ direction in the far-field, but with a much broader angular intensity distribution, while the boundary image field remains well-localized around $\phi \sim 0^\circ$ (the point of highest curvature in the imaged field). For the quadrupole-hexadecapole we see a far-field directionality peak which shifts from $\theta \sim 90^\circ$ to $\theta \sim 30^\circ$ and an almost constant boundary image field. Thus we see three qualitatively different behaviors for the three shapes studied over the same range of variation of the major to minor axis ratios.

Several different samples with the same boundary shape were measured in each case and confirmed that the basic features of this data set just described are reproduced within each class (with small fluctuations) [59]. This shows that the effects measured are a property of the boundary shape and not of uncontrollable aspects of the fabrication process. Moreover the theoretical calculations, which we will present next, are based on uniform dielectric rods with the ideal cross-sectional shape specified by the mask; therefore the agreement of these calculations with the measurements also confirms that the differences are due to controllable shape differences.

5.5 Theoretical Calculations

In Figs. 5.5–5.7 we compare the experimental results for the far-field emission patterns for the three shapes measured at $\varepsilon = 0.12, 0.18$ to both ray simulations following Chapter 3 and wave resonances obtained by the method of Chapter 4. The agreement in both cases is quite good. We briefly summarize here the two models used.

In the current case we can model the passive cavity as a 2-d resonator because the penetration depth of the pump laser is of the order of μm and amplification due to reflection from the sidewall occurs primarily within the horizontal plane of the resonator. As noted above the numerical solutions of the wave equation with Sommerfeld boundary conditions yields a large set of resonances over the entire range of Q-values; the real part of the wavevector giving the resonance frequency and the imaginary part giving its width. Experiments have indicated that mode selection is complicated in these dielectric resonators and that there is no simple rule relating the observed lasing mode to the Q-value of the mode in the passive cavity. Due to the low output coupling, high Q-modes are not necessarily the observed lasing modes in the far-field. Thus from the set of calculated resonances we choose the resonance which coincides well with the observed far-field pattern and has a relatively high

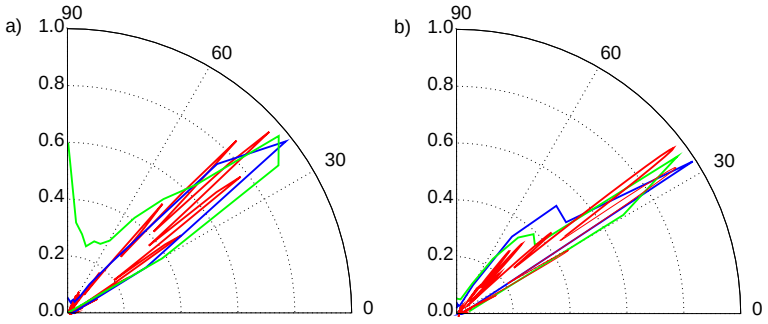

Figure 5.5: Far-field intensity for the quadrupole with $\varepsilon = 0.12$ (a) and 0.18 (b). The green curve is the experimental result, blue the ray simulation and red a numerical solution of the wave equation. The ray simulation was performed starting with 6000 random initial conditions above the critical line and then propagated into the far-field in the manner described in the text. The numerical solutions selected have $kR_0 = 49.0847 - 0.0379i$ with a $Q = 2593.05$ and $kR_0 = 49.5927 - 0.0679i$ with $Q = 1460.72$ for $\varepsilon = 0.12$ and 0.18 respectively.

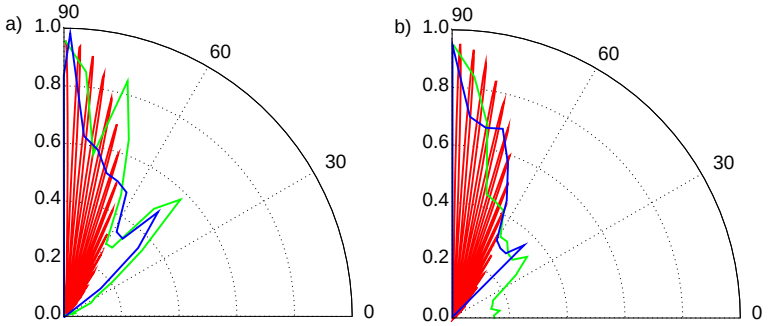

Figure 5.6: Far-field intensity for the ellipse with $\varepsilon = 0.12$ (a) and 0.18 (b). Green, blue and red curves are experiment, ray simulation and wave solution. The ray simulation was performed starting with 6000 initial conditions spread over seven KAM curves separated by $\Delta \sin\chi = 0.02$ below the critical KAM curve (that just touches the critical line). The numerical wave solutions shown correspond to $kR_0 = 49.1787 - 0.0028i$ with $Q = 17481.38$ and $kR_0 = 49.2491 - 0.0110i$ with $Q = 4488.20$ for $\varepsilon = 0.12$ and 0.18 respectively.

$Q = -2\mathrm{Re}\,[k]\,/\mathrm{Im}\,[k]$. We also confirmed that theoretical boundary image data [3] coincides well with the experimental results. Moreover in all cases discussed here, there were many resonances which gave good agreement with the data, indicating the existence of a robust class of modes any of which could be the lasing mode. In Fig. 5.5–5.7 we show as solid line the numerical far-field by calculating the asymptotic expansion of our wavefunction in the far-field. Numerical limitations prevent us from performing the calculations at the experimental values of $kR_0 \sim 1000$ but the major features of the emission pattern are not sensitive to kR_0 over the range we can study numerically. The finding (discussed next) that we can reproduce these patterns from

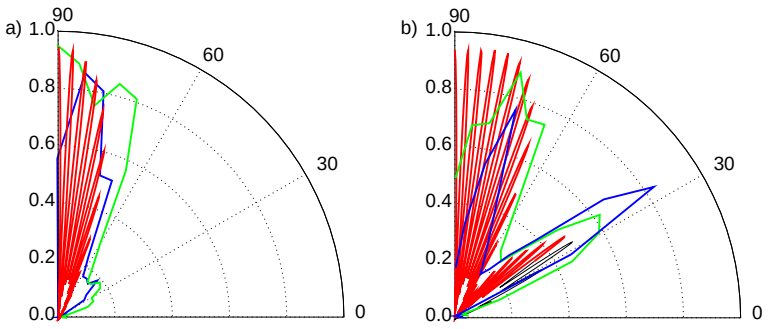

Figure 5.7: Far-field intensity for the quadrupole-hexadecapole with $\varepsilon = 0.12$ (a) and 0.18 (b). Green, blue and red curves are experiment, ray simulation and wave solution as described in the caption to Fig. 5.5. The numerical wave solutions shown correspond to $kR_0 = 50.5761 - 0.0024i$ with $Q = 42573.77$ and $kR_0 = 49.5642 - 0.0092i$ with $Q = 10741.93$ for $\varepsilon = 0.12$ and 0.18 respectively.

ray escape simulations also suggests that the wavelength is not a relevant parameter for the features we are studying. With a dash-dotted line we show the experimental results. We see that the numerical calculations agree with the measured far-field very well.

In the ray simulations an initial distribution of rays is assumed and each ray is given unit initial amplitude. At each reflection on the boundary the amplitude is reduced according to Fresnel formulas. The outgoing amplitude is recorded in the direction determined by Snell's law and the reflected ray is followed until its amplitude falls below 10^{-4}. To compare to the experimental data we collected the transmitted rays in 5° bins. A subtle issue in the calculations is the choice of the initial ray distribution. In Figs. 5.5 and 5.7 we show the far-field distribution for a randomly chosen set of initial conditions above the critical angle; in the case of the ellipse (Fig. 5.6) we chose initial uniform conditions on an invariant curve in the SOS, appropriate to its integrable dynamics (see the discussion below). The ray model is also found to reproduce the main features of the data quite well. In Section 5.7 we show that the far-field emission pattern for chaotic shapes is insensitive to the initial ray distribution over a wide range. Specifically, in Fig. 5.11 below we compare the far-field patterns for different possible initial distributions, confirming the approximate independence of the patterns to this choice.

5.6 Novel features of the Data

In the previous section we showed that we can reproduce the experimental data with both ray and wave calculations. This gives us confidence that the major differences in the experimental emission patterns are due to the different shapes of the laser cavities. The strong sensitivity of the emission patterns to small differences in boundary shape is quite striking and is a major result of this study. This sensitivity was predicted by Nöckel and Stone in the earlier work of references [13, 14, 47] and was not unexpected.

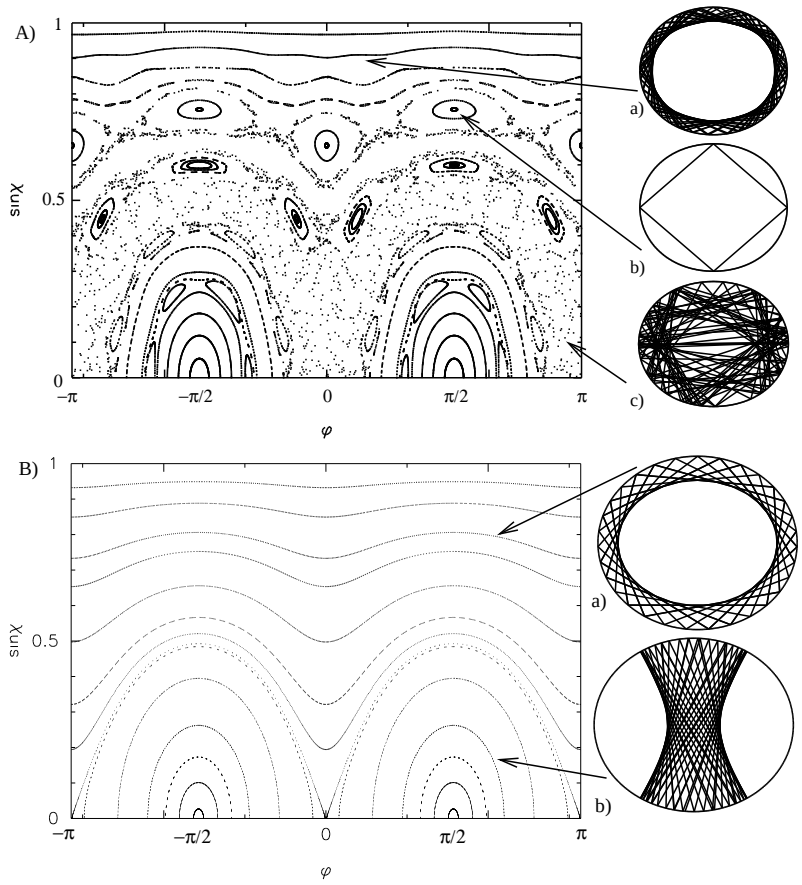

Figure 5.8: The Poincaré surface of section for the quadrupole (A) and the ellipse (B) with $\varepsilon = 0.072$. The schematics (A)(a-c) on right show three classes of orbits for the quadrupole, (A)(a) a quasi-periodic orbit on a KAM curve, (A)(b) a stable period-four orbit, (the 'diamond'), and (A)(c) a chaotic orbit. Schematic (B)(a, b) show the two types of orbits which exist in the ellipse, the whispering gallery type, with an elliptical (B)(a) and (B)(b), the bouncing ball type, with a hyperbolic.

However there are major aspects of the experimental data which are quite surprising even in the light of the earlier work on ARCs. In particular, the persistence of highly directional emission in the quadrupolar shapes at quite high deformations was not predicted theoretically and was unexpected for reasons we will now discuss.

In Fig. 5.8 we compare the SOS for the ellipse and the quadrupole at the same minor to major axis ratio. In Chapter 3 we showed that the ellipse is an integrable shape, whereas the quadrupole has a mixed phase space. This difference shows in Figure 5.8 A), the SOS of the quadrupole. Regions with a 2-d scatter of points are chaotic, islands indicate regions of regular motion; here especially to note the stable 'diamond' orbit. Due to its integrability, phase space flow in the ellipse is particularly simple: every initial condition lies on one of the invariant curves given by Eq. (5.1) below, and the trajectory retraces this curve indefinitely (see Fig. 5.8(B)). Curves which extend along the entire horizontal interval of the SOS correspond to real-

space motion tangent to a confocal elliptical caustic Fig. 5.8(B)(a); curves which are bounded in a smaller interval of ϕ represent motion tangent to a hyperbolic caustic in real space Fig. 5.8(B)(b). These two types of curves are separated by a critical curve called a *separatrix*.

A key property of mixed dynamical systems is that the different dynamical structures in phase space are disjoint; this implies that in two dimensions KAM curves and islands divide phase space into regions which cannot be connected by the chaotic orbits. This puts constraints on phase space flow despite the existence of chaos in a significant fraction of the phase space. For small deformations ($\sim 5\%$) most of phase space is covered by KAM curves, the form of which can be determined using an adiabatic approximation [14] (see Section 3.3.3). This approximation gives the exact result for all deformations in the case of the ellipse (compare Eq. (3.47)); it can be written in the following form:

$$\sin\chi(\phi) = \sqrt{1 + (S^2 - 1)\kappa^{2/3}(\phi, \varepsilon)} \tag{5.1}$$

where κ is the radius of curvature along the boundary and S is a constant. Plotting this equation for different values of S, ε gives an SOS of the type shown in Fig. 5.8(B). For the mixed case, exemplified by the quadrupole billiard in Fig. 5.8(A), Eq. (5.1) describes quite accurately the behavior for values of $\sin\chi$ near unity, but doesn't work well at lower $\sin\chi$ where chaos is more prevalent.

In Refs. [11, 14] a model was proposed based on an adiabatic theory to describe the ray-wave correspondence in the generic case of mixed dynamics. Initial conditions on the adiabatic invariant curves, e.g. of the quadrupole were chosen. Due to the presence of chaos in the true dynamics, rays initially on such a curve diffuse in phase space until they escape by refraction. The resulting emission pattern can be calculated by ray simulations of the type we have presented above. Moreover this model led to qualitative predictions about the emission patterns without doing any simulations. The adiabatic invariant curves for the quadrupole have their minimum values of $\sin\chi$ at the points of highest curvature on the boundary $\phi = 0, \pm\pi$, just as they do in the ellipse. If the diffusion in phase space is sufficiently slow, emission would be near these points of highest curvature and at the critical angle, i.e. in the tangent direction, as in the ellipse. This reasoning held as long as the escape points $\sin\chi = 1/n, \phi = 0, \pm\pi$ occurred in the chaotic region and were reachable from the totally-internally-reflected region of $\sin\chi > 1/n$. However for $n = 1.5$ and deformations around 10%, these points are enclosed by the stable island corresponding to the four-bounce "diamond" orbit and due to the disjoint nature of the dynamics, "chaotic" rays cannot escape there. Instead they will escape at higher or lower values of ϕ leading to a large change in the emission pattern from that of the ellipse with similar minor-major axis ratio. This is the phenomenon termed "dynamical eclipsing", and it was predicted to occur for the $n = 1.5$ quadrupole at $\varepsilon \sim 0.12$ some time ago [14, 13]. The experimental data confirms this prediction for the $\varepsilon = 0.12$ case. Figure 5.9 contrasts the phase space for the ellipse and the quadrupole for this deformation. The island associated with the stable diamond orbit is smaller than

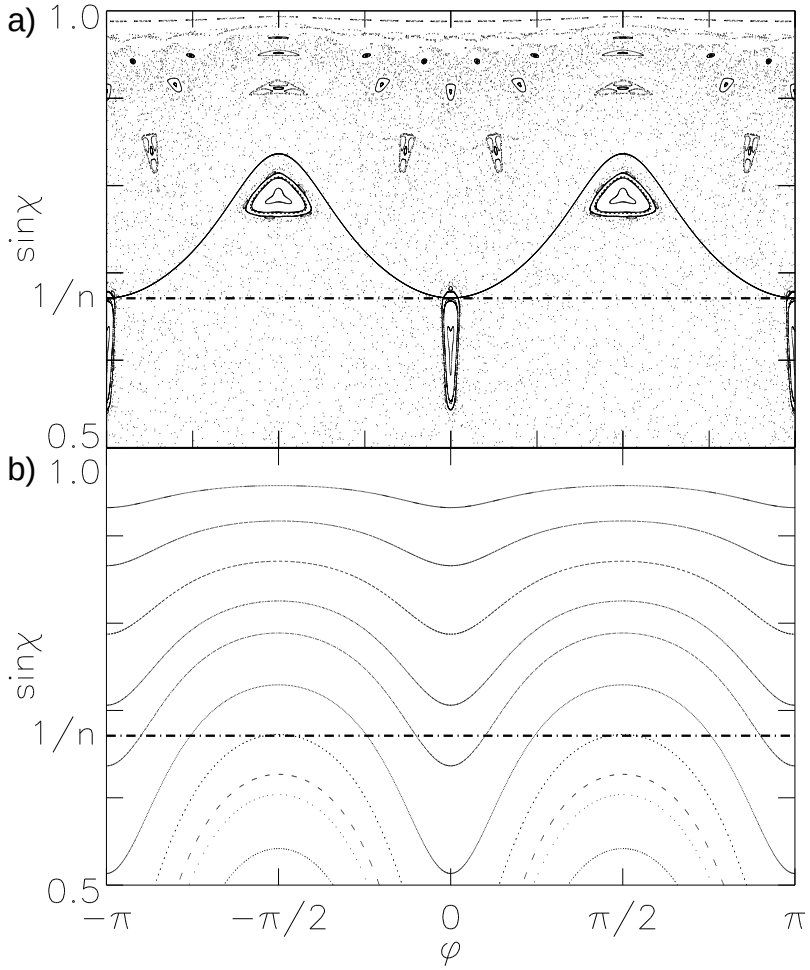

Figure 5.9: Comparison of the Poincaré surface of section for (a) the quadrupole and (b) the ellipse with $\varepsilon = 0.12$ showing mostly chaotic behavior in the former case and completely regular motion in the latter. The dash-dotted line denotes $\sin\chi_c = 1/n$, the critical value for total internal reflection; rays above that line are trapped and those below escape rapidly by refraction. The quadrupole still exhibits stable islands at $\phi = 0, \pi$ and $\sin\chi = \sin\chi_c$ which prevent escape at the points of highest curvature in the tangent direction. In (a) we show an adiabatic curve (solid black line) that has the minimum on the critical line.

at $\varepsilon = 0.072$, but still present for the quadrupole; there is no such island at any deformation for the ellipse. Note that in the experimental data for the quadrupole at $\varepsilon = 0.12$ we do not see a bright spot at the boundary at $\phi = 0$, consistent with the dynamical eclipsing model in which the island structure forces the chaotic WG modes to emit away from the point of highest curvature. In contrast the bright spot in the ellipse which emits to $\theta = 90^\circ$ clearly is at $\phi = 0$ for $\varepsilon = 0.12$. Thus the adiabatic model of Refs. [14, 13] does seem to provide a reasonable description of the data for $\varepsilon = 0.12$ and the observed dramatic difference between the ellipse and

quadrupole shapes is as predicted.

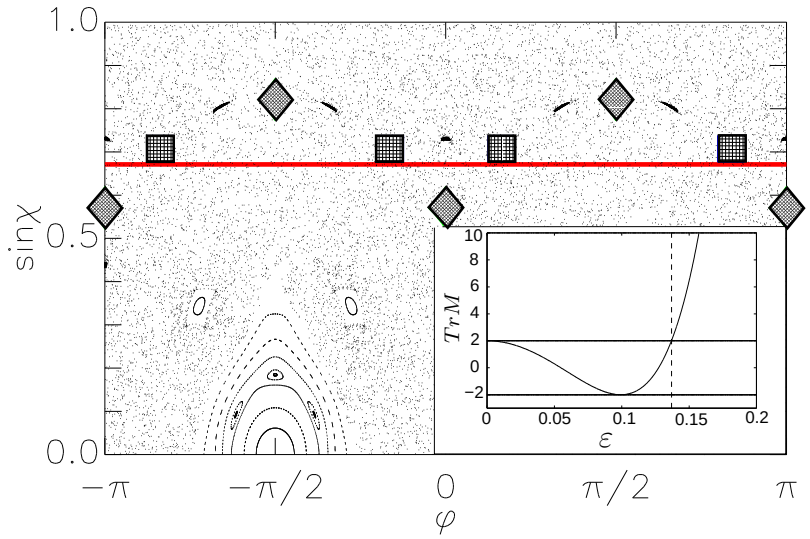

Figure 5.10: Poincaré surface of section for the quadrupole with $\varepsilon = 0.18$. The grey line indicates the critical angle of incidence. The diamonds indicate the location of the fixed points of the (now) unstable "diamond" orbit and the squares the fixed points of the unstable rectangular orbit. In the inset we show the trace of the monodromy (stability) matrix (see Section 5.7) for the diamond orbit versus deformation. When $|Tr[M]| > 2$ its eigenvalues become real, the periodic motion becomes unstable and the associated islands vanish. For the diamond this happens at $\varepsilon = 0.1369$ (see dashed vertical line in the inset) and the simple dynamical eclipsing picture of Fig. 5.9 does not apply at larger deformations.

The earlier work on ARCs did not look extensively at deformations above $\varepsilon = 0.12$ for the case of low index materials such as polymers. The belief was that the adiabatic model would become questionable at higher deformations as the phase space became more chaotic and the ray motion departed from the adiabatic curves very rapidly. A natural expectation was that due to increased chaos the emission patterns in the far-field would become less directional and more pseudo-random. More specifically, for the $n = 1.5$ quadrupole one finds that the "diamond" orbit becomes unstable at $\varepsilon \approx 0.1369$ (the associated islands shrink to zero) and one would not expect highly directional emission at higher deformations (see inset in Fig. 5.10). Thus a plausible extrapolation of the adiabatic model suggests a steady broadening of the quadrupole emission with deformation with at least some significant emission in the tangent (90°) direction. The experimental data strongly contradicts this expectation, as the observed emission patterns remain peaked around 35° and do not broaden at all up to $\varepsilon = 0.20$. A similar analysis would show that the adiabatic theory provides no qualitative explanation for the switch in the far-field directionality for the quadrupole-hexadecapole at high deformations. Thus we were motivated to look for a model of the phase space flow which can explain the persistence in highly

directional emission at high deformations where almost all of the phase space is chaotic. This model will be presented in the next section.

5.7 Short-time dynamics and Unstable Manifolds

An indication that the emission patterns we observe are not closely linked to adiabatic curves is obtained by looking at the dependence of the ray emission directionality on initial conditions. The original work of Nöckel and Stone began the ray simulations with an ensemble of rays uniformly distributed on the adiabatic curves. This is obviously correct for the ellipse as one can use the eikonal method to calculate modes corresponding to the different invariant curves. However, as already noted, the ellipse is special since chaotic diffusion is absent. In Fig. 5.11 we compare ray emission patterns arising from three different choices of initial conditions in the quadrupole: uniform on the adiabatic curve (green), initial conditions localized on the unstable fixed points associated with the rectangular periodic orbit shown in Fig. 5.1 (blue), and finally, initial conditions chosen *randomly* above the critical angle for escape (red). These three quite different choices all lead to similar far-field intensity patterns, in good agreement with the experimental measurements (dash-dotted). More generally, we found that the ray simulations are quite insensitive to the choice of initial conditions, as long as a significant fraction of the rays are started within the chaotic sea. (Ray bundles only started in an island would obviously lead to different results.) We now explain the qualitative origin of this insensitivity.

In a mixed system such as the quadrupole and hexadecapole billiards we have been discussing a single trajectory beginning in a chaotic component of the phase space will cover that component uniformly for long times. However for short times the motion is not simply uniform diffusion but instead can be analyzed conveniently by looking at the unstable fixed points (periodic orbits) of the billiard or SOS map and constructing the linearized map, M near these points. (See Section 3.2.5 for a deeper treatment of this material.)

One can argue qualitatively that the unstable manifolds of the short periodic orbits ought to control the ray escape dynamics at large deformations. The manifolds of short periodic orbits are the least convoluted as they are typically the least unstable; hence the unstable direction is fairly linear over a large region in the SOS. A typical ray will only make small excursions in phase space until it approaches one of these manifolds and then it will rather rapidly flow along it. If the direction leads across the critical line for escape, that crossing point and the portion just below will be highly favored as escape points in phase space. We can check this qualitative argument with a few simple numerical experiments.

In Fig. 5.12(a) we show the results of a short time iteration of a uniform random set of initial conditions above the critical line in comparison to the unstable manifolds of the various relevant short periodic orbits. Note that the different unstable manifolds must fit together in a consistent manner and cannot cross one another; if they did, such a crossing point would define a ray which asymptotically in the

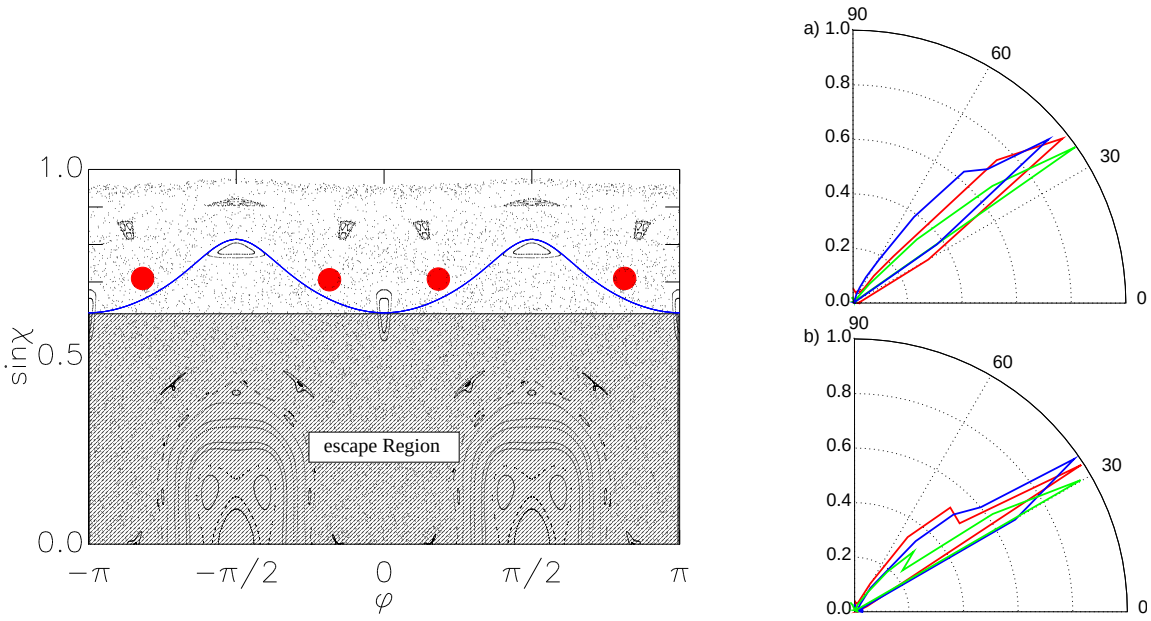

Figure 5.11: left: Surface of section of the quadrupole ARC with $\varepsilon = 0.12$ and index of refraction $n = 1.5$. The portion of the SOS below $\sin\chi_c = 1/n$ is shaded to indicate that in this region rays escape rapidly by refraction. In color we have indicated two possible types of initial conditions used in the ray escape model; the blue curve represents one of the possible adiabatic curves which were used as initial conditions in the Nöckel-Stone model and the red circles initial conditions localized on the unstable 4-bounce orbit. A third initial condition used extensively below is simply to start randomly on all possible points in the SOS originating in the trapped region above the critical line. Right: far-field emission plots calculated using the ray escape model for this system with the three possible choices of initial conditions just described. The qualitative and semi-quantitative features of the emission patterns are seen to be independent of the choice of initial conditions for this system. right: Ray simulations of the far-field emission patterns for the quadrupole with $\varepsilon = 0.12$ (a), $\varepsilon = 0.18$ (b) with different types of initial conditions. The red curve is the result of choosing random initial conditions about the critical line $\sin\chi = 1/n$, the green curve is for initial conditions on the adiabatic curve with minimum value at the critical line. The blue curve is for initial conditions localized around the unstable fixed point of the rectangle periodic orbit. In each of the ray simulations 6000 rays were started with unit amplitude and the amplitude was reduced according to Fresnel's law upon each reflection, with the refracted amplitude "collected" in the far-field. The emission pattern found by the ray model agrees well with microlaser experiments.

past approaches two different sets of fixed points, which is not possible. Because of this non-crossing property the unstable manifolds define just a few major flow directions in the SOS. We see clearly in the simulation that the actual short-time flow of random points in the chaotic sea is controlled and approximately bounded

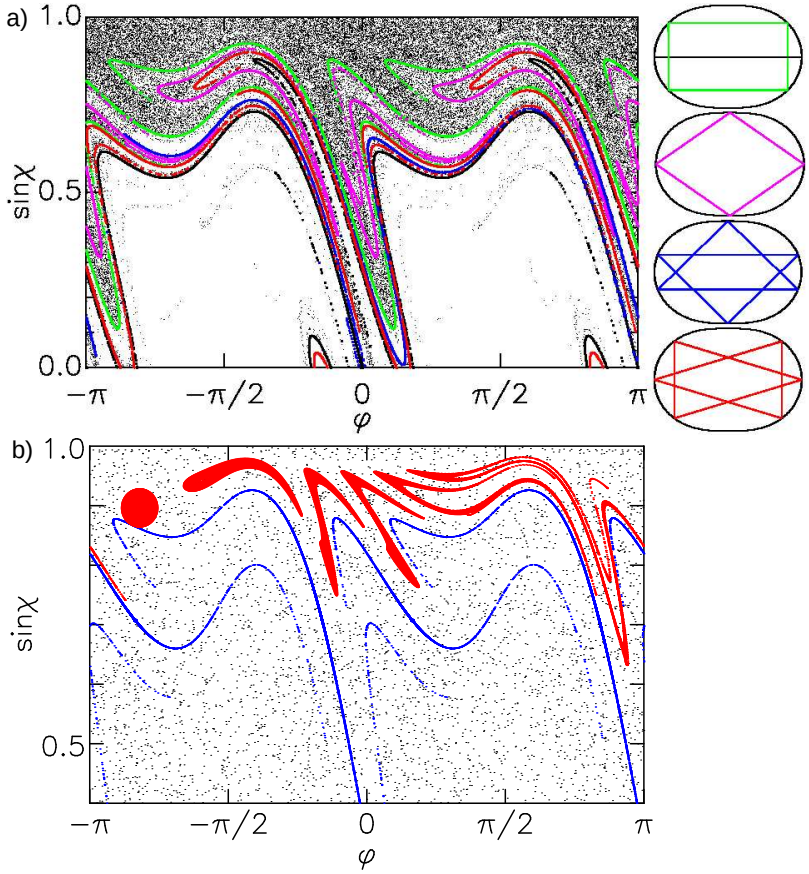

Figure 5.12: (a) Ray simulations of short-term dynamics for random initial conditions above the critical line, propagated for 10 iterations, plotted on the surface of section for the quadrupole with $\varepsilon = 0.18$. The areas of the SOS covered are delineated very accurately by the unstable manifolds of the short periodic orbits which are indicated in the schematics at right. These manifolds are overlaid in the figure with appropriate color coding. (b) Flow of phase space volume in the surface of section of the quadrupole with $\varepsilon = 0.18$. A localized but arbitrary cloud of initial conditions (red) is iterated six times to illustrate the flow. The initial volume is the circle at the far left, successive iterations are increasingly stretched by the chaotic map. The stretching clearly follows closely the unstable manifold of the rectangle orbit which we have plotted in blue.

by these unstable manifolds. To further support our statement that the general motion in phase space is governed by the unstable manifolds of these short orbits, in Fig. 5.12(b) we propagated an arbitrary but localized set of initial conditions and confirmed that they are stretched along and parallel to nearby unstable manifolds. Thus it appears that for the highly deformed case the phase space flow of a generic ray is much better predicted by simply plotting these manifolds.

As a confirmation that these manifolds do control escape, we perform a further ray simulation for the "open" billiard. We propagate, as before, an ensemble of rays

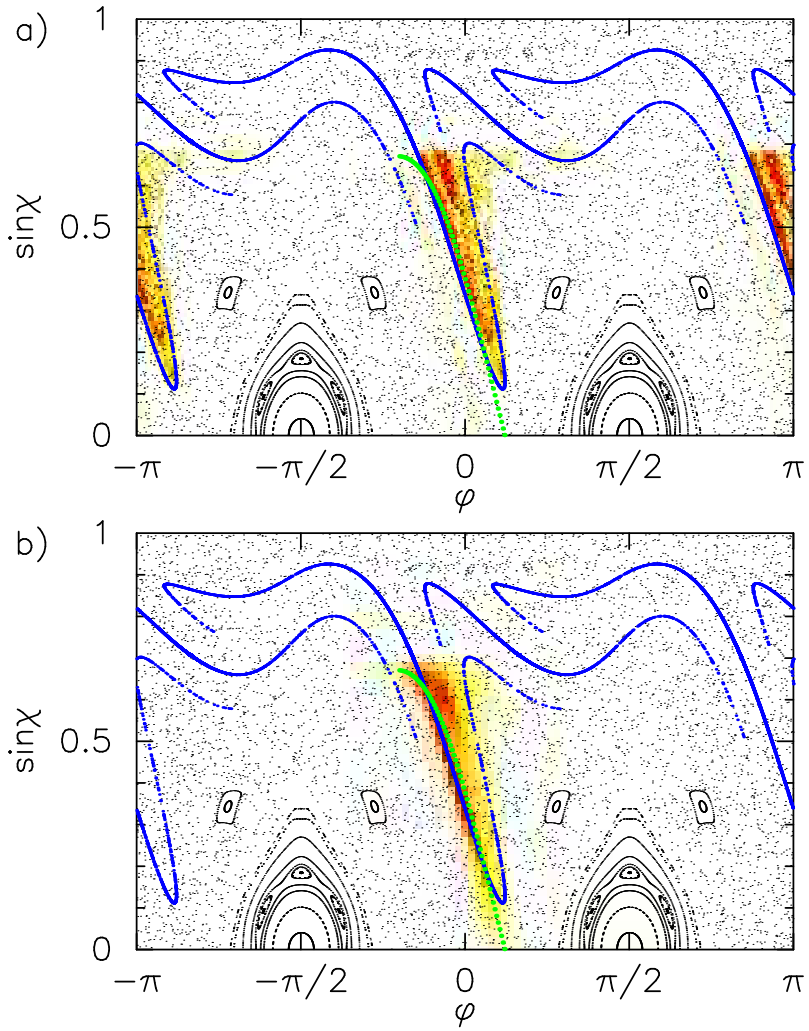

Figure 5.13: (a) Ray simulation of emission: emitted ray amplitude (color scale) overlaid on the surface of section for the quadrupole with $\varepsilon = 0.18$. (b) Far-field intensity from experimental image data Fig. 5.4 projected in false color scale onto the surface of section for the quadrupole with $\varepsilon = 0.18$. The blue line is the unstable manifold of the periodic rectangle orbit. In green we have the line of constant 34° far-field (see the discussion in Section 5.8). Absence of projected intensity near $\phi = \pm\pi$ in (b) is due to collection of experimental data only in the first quadrant.

with a uniform random distribution above the critical angle. As we have done in calculating the ray emission pattern, we associate to every starting ray in the surface of section an amplitude which decreases as the ray propagates forward in time according to Fresnel's law (if the point falls below the critical line). Instead of following the refracted amplitude into the far-field, in this case we plot the *emitted* amplitude onto the surface of section, as shown in Fig. 5.13(a). The emission amplitude is almost completely confined within the two downwards "fingers" created by the unstable manifold of the four-bounce rectangular orbit. As noted earlier, the availability of

the two-dimensional data obtained from the imaging technique (see Fig. 5.4), gives us a unique ability to reconstruct the emitting part of the lasing mode both in real space and momentum space directly from experimental data. It is therefore possible to check directly this ray simulation in phase space against experimental data. The intensity data is sorted into intensity pixels according to both its sidewall location (the angle ϕ from which emitted intensity originated) and its far-field angle, which by geometric considerations and Snell's law can be converted to the internal angle of incidence $\sin\chi$. Therefore we can project this data "back" onto the SOS for emission. In Fig. 5.13(b) we show this projection for the same deformation as in Fig. 5.13(a); we find remarkable agreement between the projected data and the ray simulation. We note that this is a much more demanding test of agreement between theory and experiment than simply reproducing the experimental far-field patterns.

5.8 Ray Dynamical Explanation of the Experimental Data

In the last section we established that typical rays above the critical angle escape by following closely the unstable manifolds of the short periodic orbits. This leads to a ray escape probability which is relatively localized in the surface of section (Fig. 5.13(a)). However despite the non-random character of this escape, there is still a significant spread of angles of incidence for escape. In fact the spread of escape angle we see in Fig. 5.13 would lead to an angular spread of nearly 80° in the far-field if all the escape occurred from the same point on the boundary. However as we see from Fig. 5.13, the point of escape and the angle of incidence are correlated and vary together according to the shape of the unstable manifold. Because the boundary is curved, different angles of incidence can lead to the same angular direction in the far-field. It is straightforward to calculate the curves of constant far-field for a given shape; for the quadruple at $\varepsilon = 0.18$ and for the peak observed emission angle of 34° this curve is plotted in green in Fig. 5.13. The curve tends to lie remarkably close to the unstable manifold. Therefore we find that the curvature of the boundary tends to compensate almost completely for the dispersion in the angle of incidence at escape.

As a further test of the explanatory power of plotting the unstable manifolds, we can use this method to explain the large shift in the far-field directionality in the quadrupole-hexadecapole (QHD) with deformation shown in Fig. 5.4. The QHD shape is an interesting contrast to the quadrupole as the diamond and rectangle periodic orbits interchange their roles. For the QHD at small deformations the diamond orbit is unstable and gives no islands whereas the rectangle is stable and gives rather large islands at $\varepsilon = 0.12$ (see Fig. 5.14(a)). Since there is no island at the point of highest curvature for this deformation the original adiabatic theory would predict emission from the point of highest curvature approximately in the tangent (90°) direction. We see in Fig. 5.7 that we indeed have such behavior experimentally. The same prediction would come from looking at the unstable manifolds; in Fig. 5.14(a)

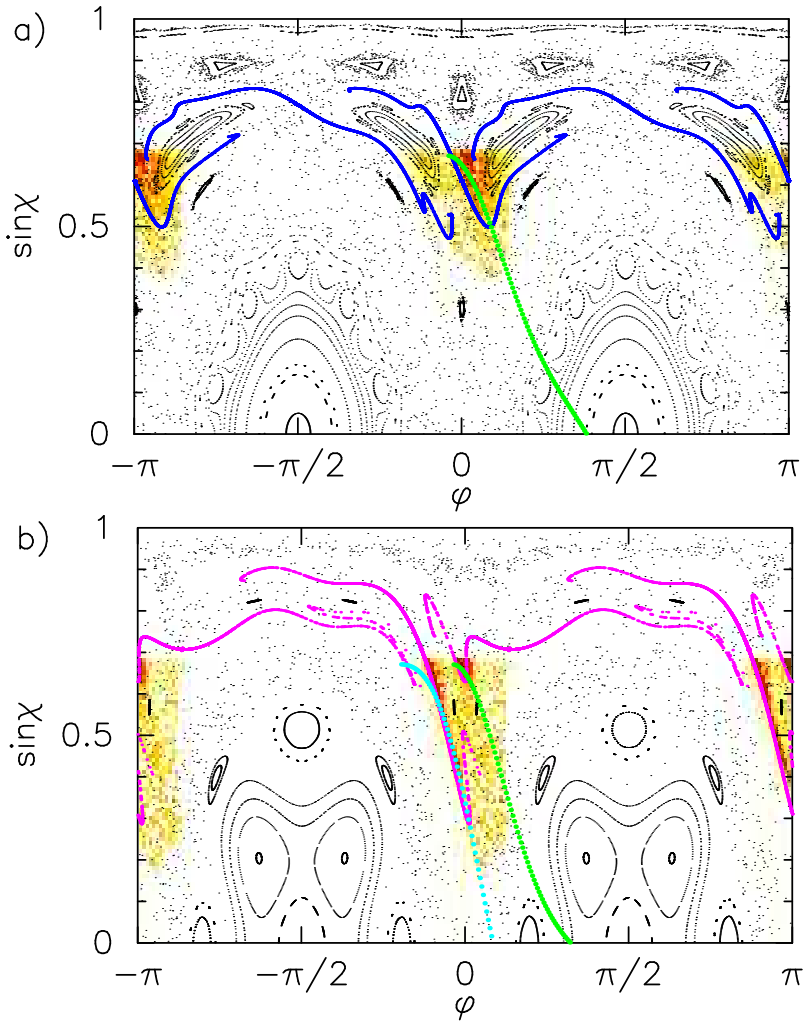

Figure 5.14: Ray emission amplitude (color scale) overlaid on the surface of section for the quadrupole-hexadecapole with $\varepsilon = 0.12$ (a) and $\varepsilon = 0.20$ (b). Solid blue and magenta curves are the unstable manifold of the diamond orbit (a) and of the unstable rectangular orbit (b). In green and turquoise we plot the line of constant emission in the 75° and 30° directions in the far-field.

we find the maximum ray escape amplitude comes from near $\phi = 0$ and is bounded by the unstable manifold of the diamond orbit. The relevant unstable manifolds rearrange as the deformation is increased to $\varepsilon = 0.20$. The stable rectangle bifurcates at $\varepsilon \sim 0.1115$ into two stable, period four, "parallelogram" orbits. As the deformation increases the islands associated with these orbits move closer to $\phi = 0$, and although the islands themselves are quite small, they cause the unstable manifolds of the diamond to become steeper (as the fixed point of the diamond orbit sits right between the two period four islands). Due to the non-crossing property the rest of the unstable manifolds in this region of the phase space also become steeper. At $\varepsilon = 0.20$, Figure 5.14(b) shows that the unstable manifold of the rectangular orbit dictates

the flow of the escaping rays, which now are emitted into the $\theta = 30^\circ$ direction in the far-field for essentially the same reason as in the quadrupole. Thus the QHD is a shape which behaves like the ellipse at low deformations and as the quadrupole at high deformations; this can be attributed to the evolution in the geometry of its unstable manifolds.

5.9 Directional Emission from Completely Chaotic Resonators

The existence of highly directional emission for the highly deformed quadrupole ($\varepsilon = 0.20$) suggests that the slow diffusion in phase space, characteristic of mixed systems, is not essential to get this effect. Therefore we decided to study theoretically resonators for which the corresponding billiard is completely chaotic and for which there exist no stable periodic orbits at all. The Bunimovich Stadium (see inset in Fig. 5.15), mentioned above, was a natural choice due to its similarity to the quadrupole. As before we did both ray escape simulations and numerical solutions of the wave equation. In Fig. 5.15 we show our predictions. We find again highly directional emission with a peak direction ($\sim 55^\circ$) slightly shifted from the quadrupole; the narrowness of the far-field peak in the stadium is comparable to that of the far-field peak in the quadrupole. We can associate this peak with the slope and position of the manifold of the unstable rectangular orbit in the stadium, Fig. 5.16(a). The noticeable shift between the $\varepsilon = 0.12$ and $\varepsilon = 0.18$ deformation (see inset in Fig. 5.15) originates from the change in the slope of the unstable manifold of the rectangular orbit, Fig. 5.16(b). The discontinuities of slope in the unstable manifolds of the periodic orbits in the stadium result from its non-smooth boundary. These results indicate clearly that a fully chaotic dielectric resonator can nonetheless sustain highly directional lasing modes. It would be interesting to test this in future experiments.

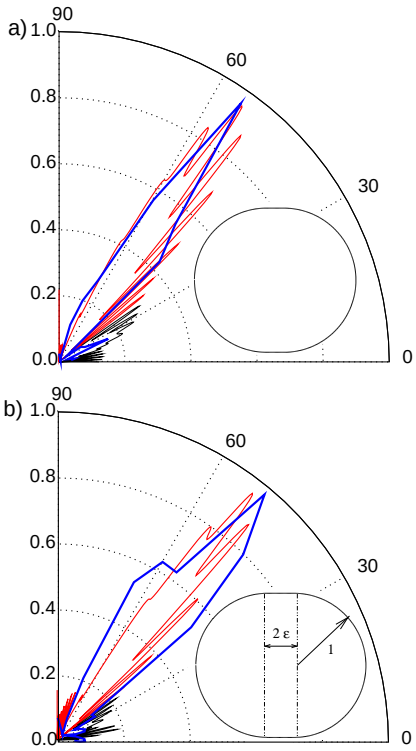

Figure 5.15: Far-field emission patterns for the stadium with $\varepsilon = 0.12, 0.18$. The blue curve is the ray simulation and the red a numerical solution of the wave equation; no experimental data was taken for this shape. The ray simulation was performed with random initial conditions exactly as in Fig. 5.5. The numerical solutions were for resonances with $kR = 50.5401 - 0.0431i$ with $Q = 2342.71$ and $kR = 48.7988 - 0.1192i$ with $Q = 818.83$ for $\varepsilon = 0.12$ and 0.18 respectively. The inset shows the shape of the stadium; it is defined by two half circles with radius one and a straight line segment of length 2ε.

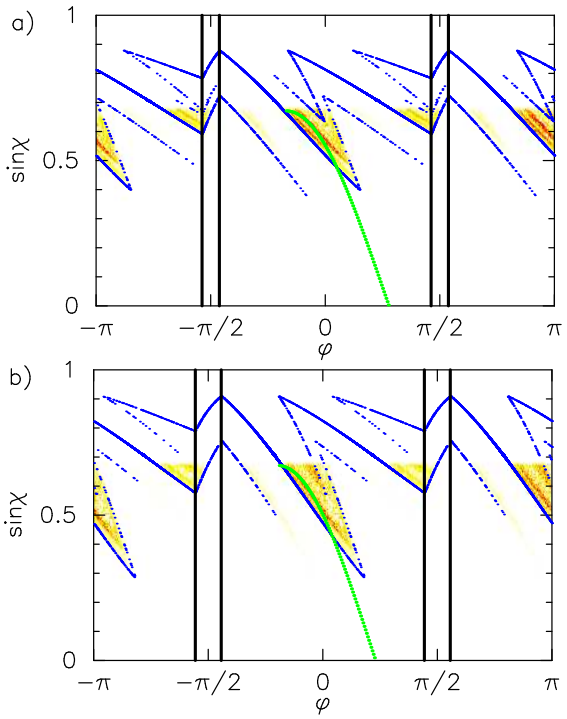

Figure 5.16: Ray emission amplitude (color scale) overlaid on the surface of section for the stadium with $\varepsilon = 0.12$ (a) and $\varepsilon = 0.18$ (b). Solid blue curve is the unstable manifold of the periodic rectangle orbit. The green curve is the line of constant 55°(a) and 48° (b) emission direction into the far-field. The thick black lines mark the end of the circle segments of the boundary and coincide with discontinuities in the manifolds.

Chapter 6

Hybrid Resonances of the dielectric Rod

As noted Chapter 2, the vector resonances of dielectric rods of arbitrary cross-section correspond to definite TM and TE polarization states for the solutions with $k_z = 0$; however for $k_z \neq 0$ the solutions are modes of hybrid polarization, whether or not the rod is circular (the cylinder) or deformed. In the next two chapters we explore in more detail these hybrid resonances, focusing on two analytically tractable cases, the cylinder and the stable orbit modes of deformed cylinders. In this chapter we analyze the resonance quantization conditions and their dependence on tilt angle θ, $(\tan\theta = k_z/\sqrt{n^2k^2 - k_z^2})$ for these two cases. As shown earlier, when $k_z = 0$ the resonance solutions are the usual TE and TM modes. Therefore when the modes are totally-internally-reflected they will suffer a real wavevector shift corresponding to the well-known phase shifts for TIR in the TE and TM modes; there is also a small $\mathrm{Im}\,[k]$ in the TIR case due to the curvature of the surface which represents evanescent leakage and is evaluated below. When the modes are below TIR their lifetimes correspond to the usual Fresnel escape probability for the TE and TM cases, with small curvature corrections (also evaluated below). This picture needs to be generalized to the $k_z \neq 0$ case for which TE and TM are not good polarization states. Below we will derive the shift of the real part of the resonance for this case and the shift in its imaginary part which together define a generalized Fresnel Law. This is done initially by expansions relating to the exact resonance condition for the separable case of the cylinder. Closely related results for the cylinder are obtained by the generalized Einstein–Brillouin–Keller (EBK) method which will also give both the resonance wavevectors (in an equivalent approximation) and the polarization states of the hybrid modes of the cylinder, discussed in the following chapter. Finally we discuss the resonances corresponding to 2d stable periodic orbits using a generalization of the Gaussian optical method; this method gives both the resonance wavevectors and the polarization states of a subset of the modes for the deformed case.

6.1 Asymptotic expansion for resonances in the above barrier regime

As we showed in Chapter 4, the vector wave equation can be separated in (z, ρ, ϕ) coordinates for the cylinder and a resonance condition can be derived of the form, Eq. 4.16:

$$n^2(1-n^2)^2 m^2 \sin^2\theta = G^{TE} \cdot G^{TM}, \tag{6.1}$$

where we found (using the recursion relations for the derivative of the Bessel-functions in Section G.3.1)

$$\begin{aligned} G^{TE} &= \left[\frac{1}{\gamma_1}\frac{J_{m-1}}{J_m} - \frac{m}{\gamma_1^2} - \frac{1}{\gamma_2}\frac{H_{m-1}}{H_m} + \frac{m}{\gamma_2^2}\right] \\ G^{TM} &= \left[\frac{n_1^2}{\gamma_1}\frac{J_{m-1}}{J_m} - \frac{n_1^2 m}{\gamma_1^2} - \frac{n_2^2}{\gamma_2}\frac{H_{m-1}}{H_m} + \frac{n_2^2 m}{\gamma_2^2}\right]. \end{aligned} \tag{6.2}$$

By employing asymptotic expansions of the Bessel functions we can then obtain analytic results for the resonance spectrum of the hybrid modes. For the case of the circle (or equivalently, for $k_z = 0$) this has been done previously [11, 100] and we briefly review the results, leaving details in Appendix E.1.

6.1.1 Cylinder resonances in two dimensions

For $k_z = 0$ the left-hand-side of Eq. (6.1) equals zero and the two brackets simplify using $\gamma_1 = nkR$ and $\gamma_2 = kR$. Therefore the two resonance conditions can be written

$$\begin{aligned} 0 = G^{TE} \qquad &\Rightarrow \qquad \left[\frac{J_{m-1}}{J_m} = \frac{m}{kR}\left(n - \frac{1}{n}\right) - n\frac{H_{m-1}}{H_m}\right] \\ 0 = G^{TM} \qquad &\Rightarrow \qquad \left[n\frac{J_{m-1}}{J_m} = \frac{H_{m-1}}{H_m}\right]. \end{aligned} \tag{6.3}$$

With the large argument expansion of the Bessel-functions (Appendix G)

$$J_m \approx \sqrt{\frac{2}{\pi nkR}}\cos\left(nkR - m\frac{\pi}{2} - \frac{\pi}{4}\right) \tag{6.4}$$

$$H_m \approx \sqrt{\frac{2}{\pi kR}}\exp i\left(kR - m\frac{\pi}{2} - \frac{\pi}{4}\right) \tag{6.5}$$

these reduce to the resonance conditions

$$nkR = \pi\left(j + \frac{m}{2} + \frac{1}{4}\right) - \frac{i}{2}\ln\frac{n+1}{n-1} \tag{6.6}$$

$$nkR = \pi\left(j + \frac{m+1}{2} + \frac{1}{4}\right) - \frac{i}{2}\ln\frac{n+1}{n-1} \tag{6.7}$$

It is interesting to note that both resonance conditions are the same up to a $\pi/2$ phase shift, leading to the same values. We can check the correctness of the equations with the numerical solutions from Chapter 4, see Fig. 6.1. This result can be easily understood; in the limit of $m \ll kR$ we are considering Fabry-Perot type resonances for which the resonance condition is not affected by the polarization state. We can also recognize that the value of the

$$\mathrm{Im}\,[nkR] = \ln\left(\frac{n+1}{n-1}\right) \tag{6.8}$$

to be the appropriate lifetime arising from the Fresnel coefficients, Eq. 2.72, for the case of normal incidence $\chi = 0$, (see discussion below)

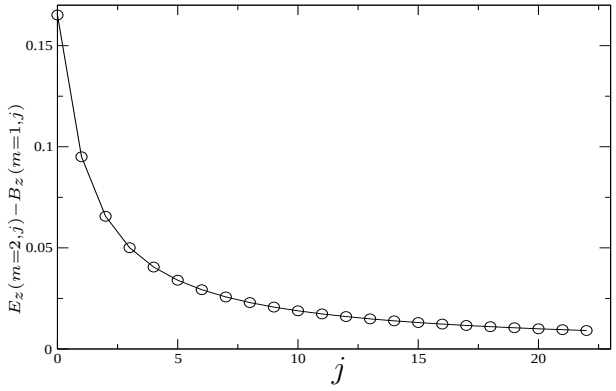

Figure 6.1: Difference between the exact numerical resonances of Chapter 4 for the TM $E_z(m = 2, j)$ and TE $B_z(m = 1, j)$ field.

6.1.2 Cylinder resonances in three dimensions

First we again take the limit $nkR \gg m$. We note that $\gamma^2 = n^2k^2 - k_z^2$ and thus in the same limit $m/\gamma \to 0$ for $k_z < kR$. In this limit the right hand side of Eq. 6.1 gives us a factor of order $\mathcal{O}(\gamma^2)$ and thus the left hand side vanishes with $m/\gamma \to 0$, so that we have again $0 = G^{TE} \cdot G^{TM}$. For the above barrier limit we found asymptotic formulas for the zeros of both resonant conditions. Following the train of thought above we get very similar relations, namely

$$\gamma_1^{TM} = \pi\left(\frac{m}{2} + \frac{1}{4} + j\right) - \frac{i}{2}\ln\frac{\gamma_1+\gamma_2}{\gamma_1-\gamma_2} \tag{6.9}$$

$$\gamma_1^{TE} = \pi\left(\frac{m+1}{2} + \frac{1}{4} + j\right) - \frac{i}{2}\ln\frac{\gamma_1+\gamma_2}{\gamma_1-\gamma_2}. \tag{6.10}$$

In order to understand the behavior of the real part up to $\pm\pi$ (the resonance condition) for small k_z we now expand both of the formulas around k_z, remembering

$\gamma = \sqrt{n^2k^2 - k_z^2}$

$$nkR^{TM} = \sqrt{\left(\pi\left[\frac{m}{2} + \frac{1}{4} + j\right] - \frac{i}{2}\ln\frac{n+1}{n-1}\right)^2 + k_z^2} \tag{6.11}$$

$$nkR^{TE} = \sqrt{\left(\pi\left[\frac{m+1}{2} + \frac{1}{4} + j\right] - \frac{i}{2}\ln\frac{n+1}{n-1}\right)^2 + k_z^2}. \tag{6.12}$$

Again, for fixed k_z, the values for the TM-like and TE-like resonances coincide due to the normal incidence property (now projected into the transverse plan).

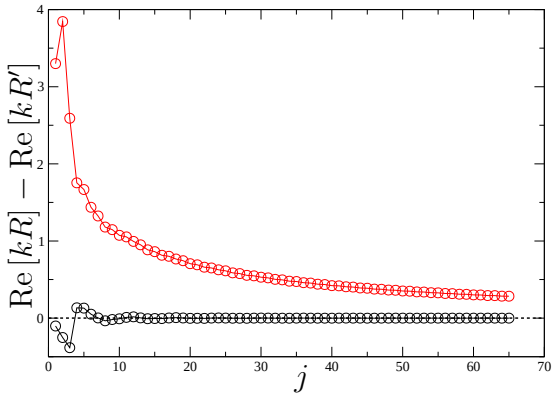

Figure 6.2: Error of the approximation Eq. (6.15) vs. the radial quantum number j in a system with $m = 10$, $k_z = 5$ and $n = 1.5$. The black curve indicates the difference between the resonances k_o calculated for the circle, the red curve using the approximation for the TE and TM resonances Eq. (E.20) and Eq. (E.23).

6.2 Blueshift for Hybrid modes

From the separability of the wave equation due to translational symmetry Eq. 2.15, we got the relation

$$\gamma = \sqrt{n^2k^2 - k_z^2}. \tag{6.13}$$

This can be interpreted as a blue shift with respect to the 2d resonances. For a solution γ_o of the Helmholtz equation we can write a continuum of solutions due to the translational symmetry in the z direction

$$nkR = \sqrt{\gamma_o^2 + k_z^2}. \tag{6.14}$$

Because kR_o is a solution for the 2-d problem it is also a solution of the three dimensional problem, we can fix $\gamma_o = kR_o$ getting

$$nkR = \sqrt{k_o^2 + k_z^2}. \tag{6.15}$$

This result can be compared to experiments done by Andrew Poon [10] where he illuminated a tilted optical glass fiber with a unfocused Gaussian beam, see Fig. 6.3. A simple argument for this blue shift is given via a wavefront matching argument,

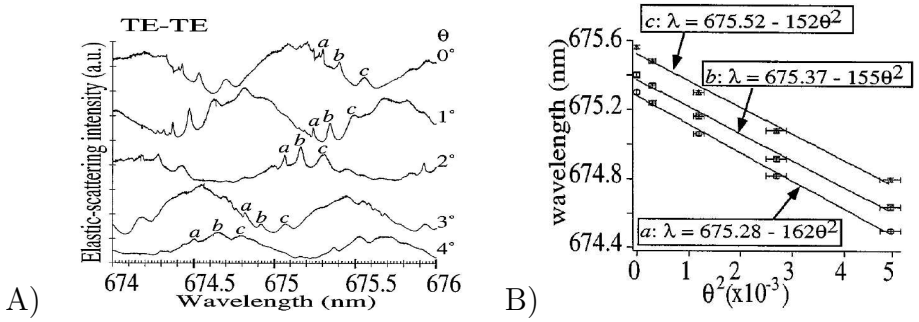

Figure 6.3: Elastic-scattering spectra detected at 90° scattering angle from a tilted fiber that is illuminated by an unfocused beam. The tilt angle is θ. A) Both the incident and scattered light were horizontally polarized (TE-TE). B) Blue-shift of the a, b and c resonances with θ^2 dependence. Note that the angle θ in this graph corresponds to the outside angle α in our notation. Figures from Poon [10].

following Fig. 6.4. The result in Eq. (6.15) is equivalent to the quadratic blue-shift

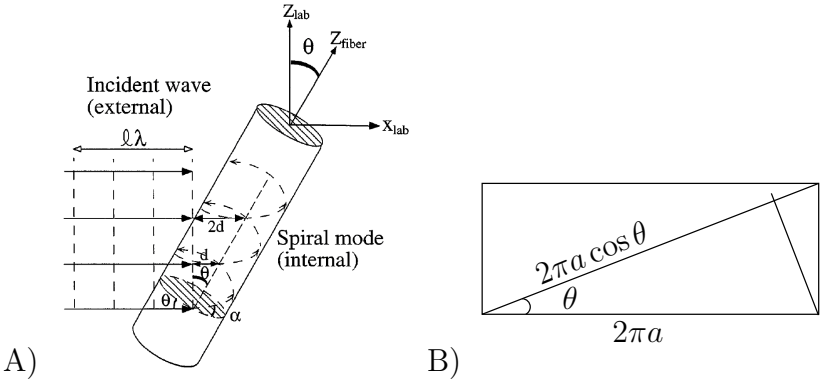

Figure 6.4: A) Schematic of wave-front-matching argument. Internal spiral wave of a tilted optical fiber with respect to. B) The effective length of for the tilted wave is $2\pi a \cos\theta$, where a is the radius of the fiber. Figures from Poon [10].

in the limit of small tilt angle $\theta \approx \sin\theta = k_z/nkR$.

$$\gamma = nk_o\sqrt{1+\frac{k_z^2}{n^2k_o^2}} = nk_o\sqrt{1+\theta^2} \approx nk_o\left(1+\frac{1}{2}\theta^2\right) \approx nk_o + \frac{nk_o}{2}\theta^2 \qquad (6.16)$$

We confirm the adequacy of the approximation Eq. (6.15) in Fig. 6.2.

6.3 Resonance width and modified Fresnel Laws

The imaginary part of a resonance wave-vector is related to the lifetime of the mode. This can be related to the classical emission probability which is just the Fresnel transmission probability. Similar considerations were established done by Nöckel in his thesis [11] and by Hentschel [100] where a relation to the Goos-Hänchen Shift was reported. Here we will review this connection. In the short wavelength limit a ray travels between two reflections for a length $L = 2R\cos\chi n$. If we assume μ bounces the corresponding time is $t = 2R\cos\chi n\mu/c$ and thus the probability of remaining in the cavity is

$$P(t) = p_o^\mu = \exp(\mu \ln p_o) \tag{6.17}$$

$$= \exp\left\{tc\frac{\ln p_o}{2nR\cos\chi}\right\} = e^{-2t/\tau}, \quad \text{with} \quad \mu = \frac{tc}{2nR\cos\chi} \tag{6.18}$$

We can thus write the reflection probability at each reflection in terms of the decay rate τ

$$p_o = \exp\left\{-\frac{4nR\cos\chi}{c\tau}\right\} \tag{6.19}$$

But the decay rate is related to the imaginary part of kR by $|y| = R/c\tau$, thus

$$p_o = \exp\{-4n|y|\cos\chi\}. \tag{6.20}$$

By inserting the exact numerics from Section 4.3 we obtain the exact Fresnel reflection probability. In the Fig. 6.5 we compare the modified Fresnel results (from Ref. [11]) with the classical Fresnel relation. The reflection probability in the modified Fresnel equation does not go to one directly at the critical angle, but has an

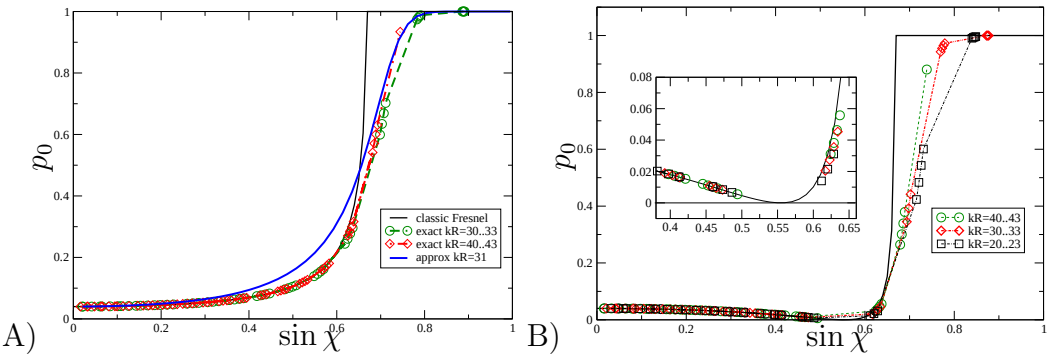

Figure 6.5: Reflection probability p_o at each collision with a circular interface versus the sine of the angle of incidence, assuming $n = 1.5$. A) for the TM polarization and B) for the TE polarization. In A) we additionally plot in blue the perturbative solution for narrow resonances Ref. [11] with $kR = 31$ In the inset of B) shows the magnification of the Brewster angle, where the resonance width diverges. Note, one does not get an exact Brewster zero for the cuved case. For comparison the Fresnel formulae for a plane interface are plotted as solid lines.

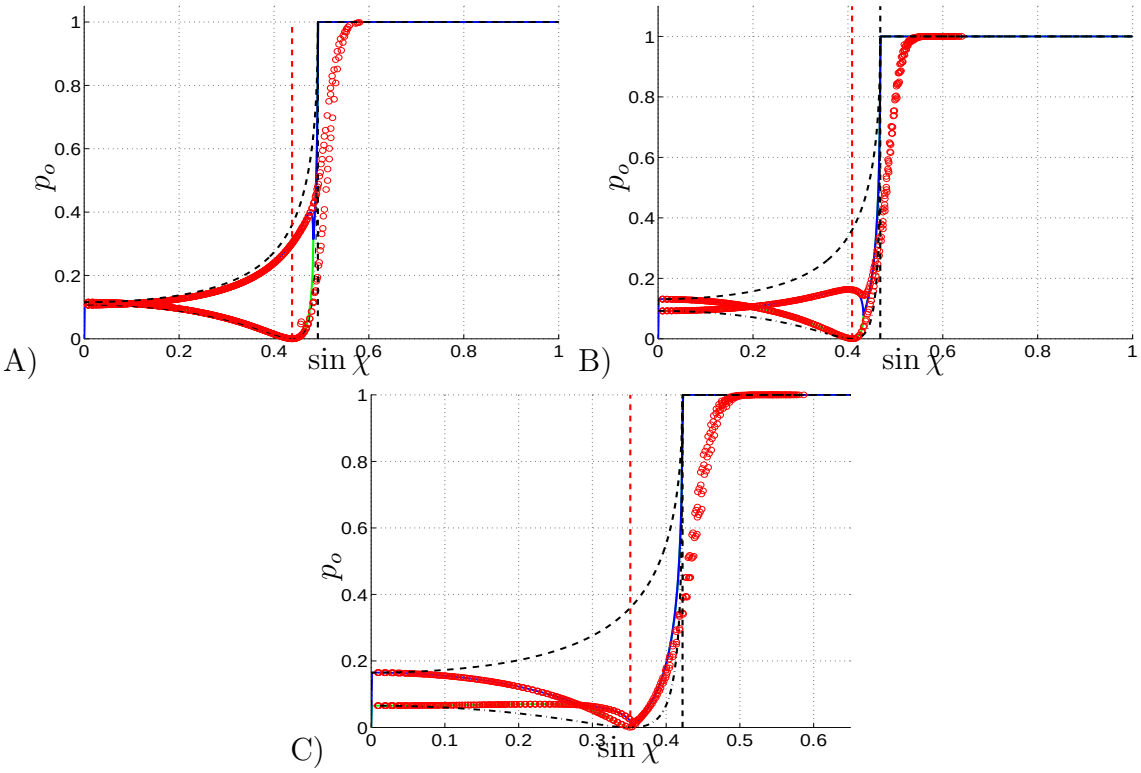

Figure 6.6: A) $\theta = 0.1$, B) $\theta = 0.2$, C) $\theta = 0.3$, Escape probability in the cylinder with $n = 2$ vs. $\sin\chi$. (red dots) exact numerical solutions with $\gamma_1 \in [98, 112]$, following Eq. (6.21), (black dashed) classical Fresnel coefficient r_s, (black dash dot) classical Fresnel coefficient r_p, (vertical red dashed) effective Brewster angle, (vertical black dashed) effective critical angle.

exponential tail. This change reflects the evanescent emission from circular microcavities, although the rays are total internally reflected.

6.3.1 Resonance width in 3d

We need to slightly modify the reflection probability from Section 6.3, due to the change in effective path length, when we include nonzero k_z. The resulting reflection probability is

$$p_o = \exp\left\{4\cos\chi \mathrm{Im}\left[\gamma_1\right]\right\} \tag{6.21}$$

In Fig. 6.6 we plot the modified Fresnel formula for $\theta \neq 0$. We can see that for small θ the exact numerical solutions follow the classical Fresnel coefficients r_s and r_p, and can clearly be associated with a TE and TM like mode. The first new feature to observe is the shift in the critical angle. This shift just stems from the increased θ and is given by Eq. (3.75). From the plotted r_p reflection coefficient we can clearly see the Brewster angle, also noted with the vertical red line. We can see that between the Brewster angle and the CA both polarization types mix.

6.4 Resonance conditions in the semiclassical limit

Up to now we have considered the above barrier regime and the long lived resonance modes. In this section we will derive the resonance conditions with semiclassical methods. First we will return to the Eikonal approach discussed already in Chapter 2 where we derived in Section 2.4 Snell's and Fresnel's law by applying the boundary conditions to the general Eikonal ansatz. In this section we will derive the quantization condition, the so called EBK quantization for the cylinder.

6.4.1 The EBK quantization conditions

In Section 2.4 we have studied the Eikonal theory for vector EM waves scattering off a dielectric interface and derived the generalized Snell's and Fresnel's law. Here we will learn what conditions need to be fulfilled to have a resonance in a dielectric cavity. Einstein in 1917 was the first to tackle the problem of semiclassical quantization for general 2d and 3d geometries within the context of the old quantum theory [67]. This work was forgotten, and then reinvented and improved by Keller in 1958 [69], who applied the general theory to the circle and other shapes in 1960 with Rubinow [101]. We will follow here the description of Türeci [66] who expanded the quantization treatment to the 2-d circular domain with dielectric boundary conditions.

The generalized EBK ansatz for the quasi-bound solutions of the vector Helmholtz Eq. 2.15 can be written as

$$\begin{pmatrix} E_z \\ B_z \end{pmatrix} = \Psi(\boldsymbol{r}) = A_1 e^{i\gamma S_1(\boldsymbol{r})} + A_2 e^{i\gamma S_2(\boldsymbol{r})} \tag{6.22}$$

where $A_{1,2}$ are two component vectors and S is the Eikonal, described in Section 2.4. Following Refs [101, 66] we can write the general quantization condition

$$\oint_{\Gamma_i} d\boldsymbol{q} \cdot \nabla S = 2\pi l_i, \quad i = 1, 2 \tag{6.23}$$

This equation is quite remarkable, as it gives the quantization condition just by integration over *any* two topologically inequivalent closed loops. It has been shown [101, 66] that for the integrable circle the topology of the problem is that of a torus and that there are only two topologically different loops. The integral gives this phase advance along the curve Γ_i, which we require to be quantized. The first loop Γ_1 (see Fig. 6.7 A)) gives the angular momentum quantization

$$\sin\chi = \frac{m}{\gamma} \tag{6.24}$$

This result is frequently used throughout this thesis. The second loop Γ_2 gives the quantization condition for the reduced wavevector and in terms of the path length L of the loop.

$$L = 2\cos\chi - 2\left(\frac{\pi}{2} - \chi\right)\sin\chi. \tag{6.25}$$

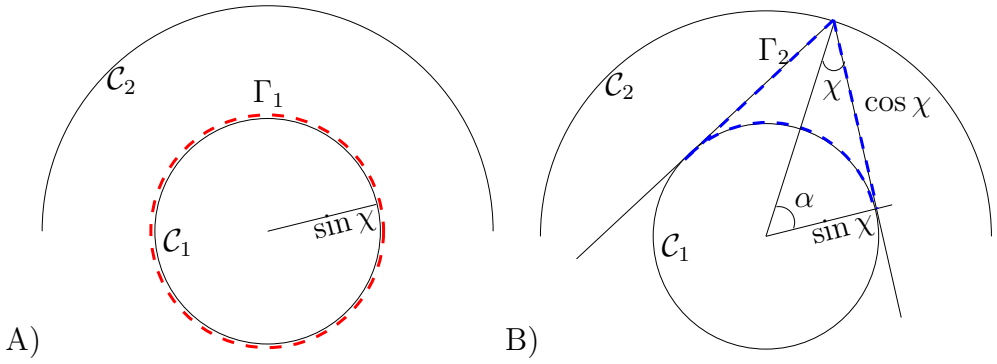

Figure 6.7: A) Path of the first curve Γ_1. B) Second path Γ_2, of length L.

We note that this effective length is the same for the cylinder and the circle. The whole information of the three dimensional problem is hidden in the reduced wavenumber $\gamma = \sqrt{n^2k^2 - k_z^2}$. We still need to consider the phase shift induced by a reflection on the boundary. In Section 2.4.2 we derived the matrix R that connects the incoming spinor wavefronts with the outgoing ones given in Eq. 2.67, which reads as

$$\Psi^r = R\Psi^i. \tag{6.26}$$

We require that each reflection from the boundary leaves the polarization invariant. (Free propagation leaves polarization invariant.) This reduces to the eigenvalue problem

$$\Lambda \mathfrak{a} = R\mathfrak{a}, \tag{6.27}$$

with the eigenvectors $\mathfrak{a}$ and the eigenvalues Λ. Noting that for the case for resonances with $k_z = 0$ the R-matrix reduces to the Fresnel reflection coefficients r_s and r_p on the diagonal.

The behaviour of the eigenvalues $\Lambda = re^{\zeta}$ of the matrix R for $k_z \neq 0$ is shown as a function of the angle $\sin\chi = m/\gamma$ is shown in Fig. 6.8. We note here that the magnitude of the eigenvalues are different up to a point between the Brewster angle (vertical dashed), and the CA (vertical dashed). At this point the the eigenvalues become complex conjugates of each other. We will call this point, the *polarization critical angle* (PCA). Not until the CA do the $\Lambda_{1,2}$ lie on the complex unit circle given TIR. Thus we have a new phenomenon, a phase shift without total internal reflection. The eigen-polarizations resulting from Eq. 6.27 will be discussed in the next Chapter. A further phase shift of $\pi/2$ has to be taken into account as the ray touches a caustic, for a detailed description see Ref. [66]. We can thus write the quantization condition for the cylinder as

$$\gamma L = 2\pi j + \frac{\pi}{2} + \zeta + i\ln|r|, \quad \text{with} \quad L = 2\left[\cos\chi - \left(\frac{\pi}{2} - \chi\right)\sin\chi\right], \tag{6.28}$$

using the quantization of the angular momentum $\sin\chi = m/\gamma$ we write the transcendental equation

$$2\gamma\sqrt{1 - \frac{m^2}{\gamma^2}} + m\arcsin\left(\frac{m}{\gamma}\right) = 2\pi j + m\pi + \zeta + i\ln|\Lambda|, \quad \text{with} \quad j, m \in \mathbb{N}. \tag{6.29}$$

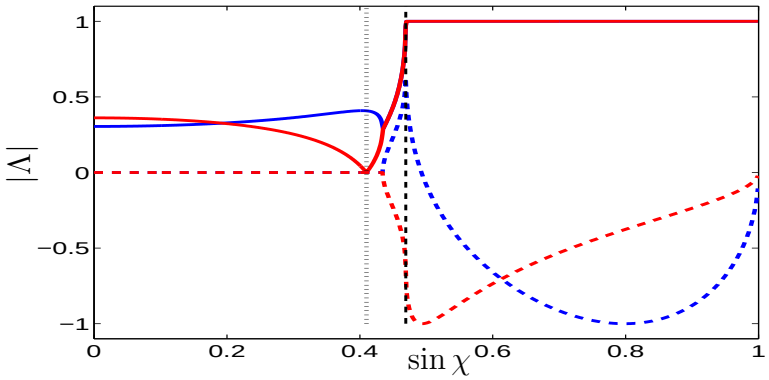

Figure 6.8: Absolute value of the eigenvalues of the R matrix (solid red and blue lines) with $n = 2$ and $\tan\theta = 0.2$ vs. $\sin\chi$. The imaginary part of the eigenvalues is also plotted in dashed. The dotted horizontal line is the Brewster angle and the dashed the critical angle. Red indicates TM like component and black the TM.

This is the full semiclassical quantization condition for the dielectric cylinder! We can compare this result to the above barrier regime by taking the limit $\cos\chi \to 1$, $\chi\sin\chi \sim 0$ and using the angular momentum quantization condition, to get

$$\gamma\left(2 - \frac{\pi}{2}\frac{m}{\gamma}\right) = 2\pi j + \frac{1}{2} + f(\chi) \tag{6.30}$$

$$\Rightarrow \quad \gamma = \pi\left[j + \frac{m}{2} + \frac{1}{4}\right] + f(\chi) \tag{6.31}$$

This equation corresponds to Eq. 6.11, 6.12. Where the contributions of the phase shift and the loss at the boundary have been combined in $f(\chi)$. We will later (Chapter 7) return to this function when we have derived a simpler R matrix based on ray considerations. This will help us to develop a physical understanding for the phase shift.

In Tab. 6.1 we compare the resonances found by three methods, the exact cylinder resonances from the Bessel functions, the S-Matrix method and the EBK quantization.

6.5 Gaussian Optics in 3d

For a deformed cylinder, there is no general analytic method to find all the modes of a cavity. There are however powerful asympthotic methods for the calculation of the fraction of modes localized on regular regions in a general, mixed phase space. We have shown in Chapter 3 that a general phase space will have three different type of trajectories. Oscillatory motion in the vicinity of a stable fixed-point, chaotic motion in the region around unstable fixed-points and marginally stable motion on families of quasi-periodic orbits. The Bell-Labs experiment [8] showed that a resonance on a stable periodic orbit can be relevant for deformed microlasers. An asymptotic

Table 6.1: Resonances in the cylinder with $n = 2, \theta = 0.1$. We compare the resonances calculated by zero finding of the Bessel functions, the S-Matrix method and the EBK method. The agreement is reasonably well. For the S-matrix calculation it is to be noted that we calculated and interpolated around $kR = 100$, thus the values further away from 100 are less exact. We have to note that as the EBK quantization is a transcendental equation, which we did not attempt to solve. We used the results from the wave numerics to calculate the $\sin\chi$ using this we checked the equation.

$\theta = 0.1$		exact	S-Matrix		EBK
m	TE/TM	kR	kR	j	kR
18		100.52083-0.27170i	100.52082-0.27168i	55	100.520468-0.271695i
20		100.42571-0.27098i	100.42570-0.27098i	54	100.425346-0.270979i
44		100.06672-0.25117i	100.06680-0.25523i	43	100.066168-0.255107i
74		100.30341-0.20475i	100.30321-0.20462i	31	100.301095-0.204629i
98		101.41861-0.09114i	101.40758-0.07870i	23	101.382400-0.075236i
$\theta = 0.2$					
5	TM	99.62235-0.59423i	99.62239-0.59427i	29	99.61990-0.59421i
17	TE	99.86057-0.55418i	99.85991-0.55355i	23	99.86699-0.55433i
20	TM	99.29851-0.56992i	99.29954-0.57074i	22	99.29473-0.56984i
34	TE	100.17837-0.84848i	100.16835-0.83978i	16	100.20152-0.85155i
39	TE	99.78148-1.35232i	99.65145-1.26193i	14	99.74088-1.36053i
57	TE	99.76787-0.00005i	99.76803-0.00005i	8	96.79993+0.00009i
62	TM	100.78974-0.00000i	100.79161-0.00000i	7	100.86339+0.00000i

approach for the calculation of wavefunctions related to periodic orbits (PO) in a 2-d dielectric cavity, was constructed in Ref. [93]. We will here expand this formalism to orbits in three dimensional translationally symmetric cavities whose 2d projection is a stable periodic orbit.

We use the vector Helmholtz equation (2.20)

$$(\nabla^2 + \gamma^2)\Psi = 0, \quad \text{with} \quad \Psi = \begin{Bmatrix} E_z(x,y) \\ B_z(x,y) \end{Bmatrix}. \tag{6.32}$$

Its solutions Ψ can be expanded along a set of arms of a ray trajectory shown in Fig. 6.9

$$\Psi(x,y) = \sum_m^N \Psi_m(x_m, y_m) \tag{6.33}$$

Following the parabolic equation approximation [102], we assume that the main

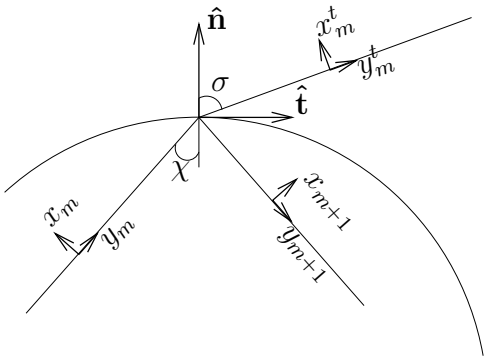

Figure 6.9: Local and global coordinate system for Gaussian optics. Here a cut on the plane of incidence. x_m and y_m are the local coordinates attached to each segment. At every point of the boundary we define a global set of coordinates in the normal $\hat{\mathbf{n}}$ and the tangent $\hat{\mathbf{t}}$ direction.

variation of the phase in the y-direction is linear and factor it out

$$\Psi_m(x_m, y_m) = u_m(x_m, y_m)e^{i\gamma y_m}. \tag{6.34}$$

Using this ansatz in the Helmholtz equation

$$(\nabla_m^2 + \gamma^2)\Psi_m = 0 \tag{6.35}$$

we obtain the following partial differential equation

$$\frac{\partial^2 u}{\partial x^2} + \frac{\partial^2 u}{\partial y^2} + 2i\gamma\frac{\partial u}{\partial y} = 0. \tag{6.36}$$

Following the reasoning in Ref. [66] we use a standard tool from the boundary layer theory [103, 104] to stretch the 'fast' variable x with the appropriate scale

$$\widetilde{x} = x/\sqrt{\gamma}. \tag{6.37}$$

This results into

$$\frac{\partial^2 u}{\partial \widetilde{x}^2} + \frac{1}{\gamma}\frac{\partial^2 u}{\partial y^2} + 2i\frac{\partial u}{\partial y} = 0, \tag{6.38}$$

which we now only keep to lowest order in γ.

$$\frac{\partial^2 u}{\partial \widetilde{x}^2} + 2i\frac{\partial u}{\partial y} = 0. \tag{6.39}$$

We now make the following Ansatz

$$u_m^o(\widetilde{x}_m, y_m) = \mathfrak{c} A(y_m) \exp\left[\frac{1}{2} i\Omega(y_m)\widetilde{x}_m^2\right] \tag{6.40}$$

where $\mathfrak{c}$ is a vector representing amplitudes of the E_z and B_z components. The exponential and the amplitude $A(y)$ are taken to be the same for both fields. This Ansatz yields two differential equations

$$\Omega^2 + \Omega' = 0 \tag{6.41}$$

$$A\Omega + 2A' = 0 \tag{6.42}$$

with $\Omega' = \frac{\partial \Omega}{\partial y}$ and $A' = \frac{\partial A}{\partial y}$. Substituting $\Omega = Q'/Q$ we obtain

$$Q'' = 0 \tag{6.43}$$

$$\frac{Q'}{Q} + 2\frac{A'}{A} = 0 \tag{6.44}$$

latter equation has the solution $A = 1/\sqrt{Q}$ and former Eq. (6.43) is the Euler equation for ray propagation in a homogeneous medium with the general solution $Q = \alpha y + \beta$. This is the connection to the underlying classical ray picture.

The boundary conditions that we have to fulfill in a three dimensional cylindrical structure are given in Eq. (2.41)–(2.44). We write them here as

$$\Psi^i(\widetilde{x}_m, y_m) + \Psi^r(\widetilde{x}_m, y_m) = \Psi^t(\widetilde{x}_m, y_m) \tag{6.45}$$

$$\mathfrak{B}^i\Psi^i(\widetilde{x}_m, y_m) + \mathfrak{B}^r\Psi^r(\widetilde{x}_m, y_m) = \mathfrak{B}^t\Psi^t(\widetilde{x}_m, y_m) \tag{6.46}$$

where $\mathfrak{B}$ are given by Eqs (2.64)–(2.66). The continuity condition on the boundary gives us with together with the Ansatz Eq. (6.40) a condition for the amplitudes and for the phases

$$\frac{\mathfrak{c}_i}{\sqrt{Q_i(y_m)}} + \frac{\mathfrak{c}_r}{\sqrt{Q_r(y_r)}} = \frac{\mathfrak{c}_t}{\sqrt{Q_t(y_t)}} \tag{6.47}$$

$$\left[\gamma_1 y_i + \frac{1}{2}\frac{Q_i'}{Q_i}\widetilde{x}_i^2\right] + \left[\gamma_1 y_r + \frac{1}{2}\frac{Q_r'}{Q_r}\widetilde{x}_r^2\right] = \left[\gamma_2 y_t + \frac{1}{2}\frac{Q_t'}{Q_t}\widetilde{x}_t^2\right]. \tag{6.48}$$

We now need to write the local coordinates in global coordinates which we scaled according to Eq. 6.37 such that $\widetilde{x} = \sqrt{\gamma}x$, $\widetilde{n} = \sqrt{\gamma}n$, $\widetilde{t} = \sqrt{\gamma}t$

$$y_i = l_m + 1/\sqrt{\gamma_1}\cos\chi\widetilde{n} + 1/\sqrt{\gamma_1}\sin\chi\widetilde{t} \qquad x_i = \sin\chi\widetilde{n} - \cos\chi\widetilde{t} \tag{6.49}$$

$$y_r = l_m - 1/\sqrt{\gamma_1}\cos\chi\widetilde{n} + 1/\sqrt{\gamma_1}\sin\chi\widetilde{t} \qquad x_r = \sin\chi\widetilde{n} + \cos\chi\widetilde{t} \tag{6.50}$$

$$y_t = l_m + 1/\sqrt{\gamma_2}\cos\sigma\widetilde{n} + 1/\sqrt{\gamma_2}\sin\sigma\widetilde{t} \qquad x_i = \sin\sigma\widetilde{n} + \cos\sigma\widetilde{t} \tag{6.51}$$

We now assume that the boundary is in the vicinity of the bounce point parabolic and follows the relation $\widetilde{n} = -\widetilde{t}^2/\gamma\rho$ where ρ is the local radius of curvature. Using the coordinate transforms Eq. (6.49)–(6.51) on the phase relation Eq. (6.48) we get to order $\mathcal{O}(1/\sqrt{\gamma})$ considering first the coefficients of t for the incoming and outgoing component we get

$$\nu\sin\chi = \sin\sigma \tag{6.52}$$

where $\nu = \gamma_1/\gamma_2 = \tan\alpha/\tan\theta$. This is the Snell's law derived in Section 2.4.1 via the EBK method. Collecting the t^2 components we get

$$\begin{pmatrix} Q_t \\ Q_t' \end{pmatrix} = \begin{pmatrix} 1/\mu & 0 \\ \frac{1/\nu-\mu}{\sqrt{\gamma_1}\rho\cos\chi} & \mu \end{pmatrix} \begin{pmatrix} Q_i \\ Q_i' \end{pmatrix} \tag{6.53}$$

where $\mu = \cos\chi/\cos\sigma$ and we have fixed $Q_i = \mu Q_t$. This matrix equation can be recognized as the ABCD matrix for transmission through a curved interface [85]. Observing now the incoming and reflected phase components we do not get new information from the t components but from the t^2 components we get

$$\begin{pmatrix} Q_r \\ Q_r' \end{pmatrix} = \begin{pmatrix} -1 & 0 \\ \frac{2}{\sqrt{\gamma_1}\rho\cos\chi} & -1 \end{pmatrix} \begin{pmatrix} Q_i \\ Q_i' \end{pmatrix} \tag{6.54}$$

where we have taken the convention that $Q_r = -Q_i$. This equation can be interpreted as the ABDC matrix or reflection matrix at a curved boundary [85].

So far we have only considered the phase relations. Now we write the amplitude conditions for the continuity at the boundary condition

$$\frac{\mathfrak{c}_i}{\sqrt{Q_i}} + \frac{\mathfrak{c}_r}{\sqrt{Q_r}} = \frac{\mathfrak{c}_t}{\sqrt{Q_t}} \tag{6.55}$$

using $Q_i = \mu Q_t$ and $Q_r = -Q_i$ we arrive at

$$\mathfrak{c}_i - i\mathfrak{c}_r = \sqrt{\mu}\mathfrak{c}_t \tag{6.56}$$

Next we need to impose the mixing boundary conditions Eq. (2.61) on the fields. The phase relation is going to be unaffected, but the amplitude condition rewrites as

$$\mathfrak{B}^i\mathfrak{c}_i - i\mathfrak{B}^r\mathfrak{c}_r = \sqrt{\mu}\mathfrak{B}^t\mathfrak{c}_t, \tag{6.57}$$

where $\mathfrak{B}^i$, $\mathfrak{B}^r$, $\mathfrak{B}^t$ are given by Eqs (2.64)–(2.66). Combining Eq. (6.56) and Eq. (6.57) we can derive a relation between the incoming and reflected field as

$$\mathfrak{c}_r = -i\left(\mathfrak{B}^r - \mathfrak{B}^t\right)^{-1}\left(\mathfrak{B}^i - \mathfrak{B}^t\right)\mathfrak{c}_i. \tag{6.58}$$

We can recognize this equation from Section 2.4, where we have defined it to be R.

Now we can write the quantization condition for a stable orbit. Having determined how an initial solution (Q, Q') is propagated an arbitrary distance, we now require that the solution be single valued after propagation around a loop of a periodic orbit (PO), with length L

$$\Psi(x, y + L) = \Psi(x, y). \tag{6.59}$$

We need now to determine the phase advance.

Contributing to the phase is the Floquet Phase φ relating to the fact that the eigenvectors of the monodromy matrix of for the PO are complex when the orbit is stable (see Section 3.2.5), another shift in the phase occurs at every reflection of the boundary by $\pi/2$ and by the eigenvalues $\Lambda = re^{i\zeta}$ of the reflection matrix $R = \Pi R_i$, when we require that after a round trip the eigenpolarizations $\mathfrak{c}$ need to be invariant in order to satisfy the translational symmetry in the z direction. We can thus write the final quantization condition for a N periodic stable periodic orbit

$$\gamma_1 L = \frac{1}{2}\varphi + 2\pi m + \frac{1}{2}\pi N + \pi N_\mu + \zeta + i \ln r. \tag{6.60}$$

Here, $\pi/2$ is the phase shift at each reflection, $\Lambda = re^{i\zeta}$ is the eigenvalue of the reflection matrix $\Pi_{i=1}^{N} R_i$ and N the number of bounces. The integer N_μ, the *Maslov index* [66, 105] which is sensitive to the number of times the phase wraps around the origin. If it is odd we can observe a π phase-shift in the resonance condition. We want to remark on this result that it is valid for *all* PO as long as they are stable in any geometry! In the next Section we want to apply the above found results for a periodic orbit in a deformed cavity.

6.5.1 Gaussian Quantization of the Bouncing Ball orbit

In the last section we derived a quantization rule for any stable periodic orbit. Here we want to apply the theory to the period-2 orbit, the bouncing ball (BB) orbit of the hexadecapole (see Chapter 5 for the definition of the shape). We can now state the quantization rule:

$$\gamma L = \frac{1}{2}\varphi - \frac{\pi}{2} + N\frac{\pi}{2} + \zeta + 2j\pi + i \ln r \tag{6.61}$$

where φ is the Floquet phase of the orbit, N the number of bounces, j some integer and the eigenvalue of the total R matrix is $re^{i\zeta}$. A comparison to calculations via the S-matrix formalism from Section 4.7 is shown in Table 6.2. We can see a good agreement between the resonance conditions and the resonance width.

6.6 Conclusion

In this chapter we have derived analytic results for the resonances. First in the cylinder using the above barrier limit and the limit of long lifetime (WG). We understood and described the experimentally observed 'blue'-shift and then derived a full

Table 6.2: Quantization for the bouncing ball orbit in the hexadecapole with $\varepsilon = 0.07$ and $\theta = 0.2$. $L = 3.71680$, $\varphi_1 = -1.53399$, $\varphi_2 = +1.53399$

$\theta = 0.2$	$n = 2$	S-Matrix		Gauss
TE/TM	sym	kR	j	kR
TE	++	96.98726-0.54882i	57	96.98652-0.54640i
TM	+−	96.99360-0.63930i	57	96.98652-0.64110i
TE	+−	98.67793-0.54882i	58	98.67701-0.54640i
TM	++	98.68409-0.63930i	58	98.67701-0.64110i
TE	++	100.36859-0.54882i	59	100.36749-0.54640i
TM	+−	100.37458-0.63930i	59	100.36749-0.64110i
TE	+−	102.05926-0.54882i	60	102.05797-0.54640i
TM	++	102.06507-0.63930i	60	102.05797-0.64110i

semiclassical quantization condition for the cylinder. These results where all compared to numerical data. In the last Section we derived a quantization method for a stable periodic orbit in an arbitrary geometry with translational symmetry along one direction. In the next Section we will use these results to understand the polarization of hybrid resonances. The important eigenvalues of the R matrix will find a more physical interpretation through a ray-dynamical interpretation using the Jones Algebra.

Chapter 7

Polarization States of Hybrid Modes

7.1 Introduction

In Chapter 6 we analyzed the resonance condition for the analytically solvable cases of the dielectric cylinder with $k_z \neq 0$ and for the stable orbit modes of arbitrarily deformed cylinders with $k_z \neq 0$, finding the quantized resonance wavevectors of these modes. In this chapter we analyze in more detail the spatial character of the resulting $\boldsymbol{E}$ and $\boldsymbol{B}$ fields and the polarization properties of the light emitted from these modes. The resonance wavevectors derived by the EBK method in Eq. (6.27) involved a contribution from the boundary reflection which we parameterized as $\Lambda = re^{i\zeta}$ and derived as eigenvalues of the EBK R-matrix. We now return to this question and for the case of the cylinder derive the relevant quantity by a different method which makes its interpretation much clearer. Similar arguments will allow us to analyze the polarization states of the stable orbit modes of the deformed cylinder. We briefly review the $k_z = 0$ case and set notation for the discussion of polarization in the general 3D case.

7.2 Polarization of a plane wave

When we talk about polarization it is important to realize that polarization only has meaning for plane waves, or fields that are perpendicular to the propagation direction $\boldsymbol{k}$. Choosing the propagation direction to be along $\hat{\boldsymbol{z}}$ we can write the electric field as

$$\boldsymbol{E} = \boldsymbol{E}_o e^{i(kz-\omega t)}, \quad \text{with} \quad \boldsymbol{E}_o = E_{ox}\hat{\boldsymbol{x}} + E_{oy}\hat{\boldsymbol{y}} \tag{7.1}$$

The relationship between E_{ox} and E_{oy} describes the *polarization* of the light. An arbitrary phase shift between the two fields is call *elliptically polarized*. There are a number of special cases that we want to remark on. If the phase difference between the two components is $\pm\pi, \pm 2m\pi,\ \forall\ m \in \mathbb{Z}$, we call it *linearly polarized*. If the magnitude of both components is equal and the phase shift is $\pm\pi/2$ i.e. $E_{ox} = iE_{oy}$

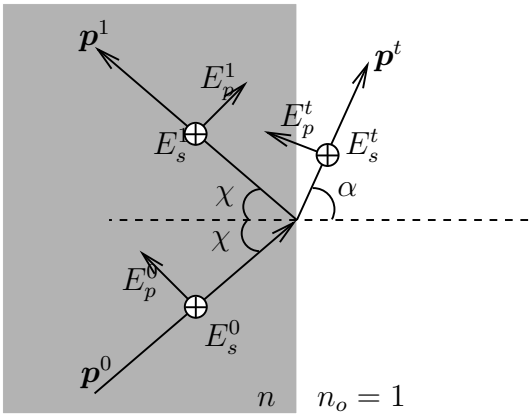

Figure 7.1: Schematic for reflection and transmission at a plane interface.

the field never goes to zero simultaneously in both dimensions and we call the light *circularly polarized*. In Section 2.4 we have studied the effect of a discontinuity in the dielectric constant for a field with 1-d translational symmetry. We will now use the results derived there for the $k_z = 0$ case to understand the phase shift encountered by reflection/ refraction at an dielectric interface. It is common to describe the electric field in coordinates with respect to the plane spanned by the incoming field and the normal at the boundary, the *plane of incidence* $\boldsymbol{p}^0 \wedge \boldsymbol{p}^1$ (see Fig. 7.1). We will choose a projection of the electric field into components parallel to the plane of incidence E_p^0, and perpendicular E_s^0.[1] Linearly polarized light with only E_s components is called *TM-polarized*, with only E_p components *TE-polarized*. From Eq. (2.18) and (2.19) it follows that in the 2-d case ($k_z = 0$) the Fresnel coefficients derived in Section 2.4.2 will hold for E_s and E_p; Snell's law Eq. (2.57) is polarization invariant. For the completeness of this chapter we will restate Snell's law:

$$n \sin\chi = n_o \sin\alpha \tag{7.2}$$

and the Fresnel coefficients:

$$r_s \equiv \frac{E_s^1}{E_s^0} = \frac{\sin(\chi-\alpha)}{\sin(\chi+\alpha)} = \frac{n\cos\chi - n_o\cos\alpha}{n\cos\chi + n_o\cos\alpha} \tag{7.3}$$

$$r_p \equiv \frac{E_p^1}{E_p^0} = -\frac{\tan(\chi-\alpha)}{\tan(\chi+\alpha)} = \frac{n\cos\alpha - n_o\cos\chi}{n\cos\alpha + n_o\cos\chi} \tag{7.4}$$

$$t_s \equiv \frac{E_s^t}{E_s^0} = \frac{2\sin\alpha\cos\chi}{\sin(\chi+\alpha)} = \frac{2n\cos\chi}{n\cos\chi + n_o\cos\alpha} \tag{7.5}$$

$$t_p \equiv \frac{E_p^t}{E_p^0} = \frac{2\sin\alpha\cos\chi}{\sin(\chi+\alpha)\cos(\chi-\alpha)} = \frac{2n\cos\chi}{n\cos\alpha + n_o\cos\chi} \tag{7.6}$$

[1] It is customary in the literature to use the subscript $_s$ to note the perpendicular field, from the German word for perpendicular *senkrecht*. This is not just the case because I am German.

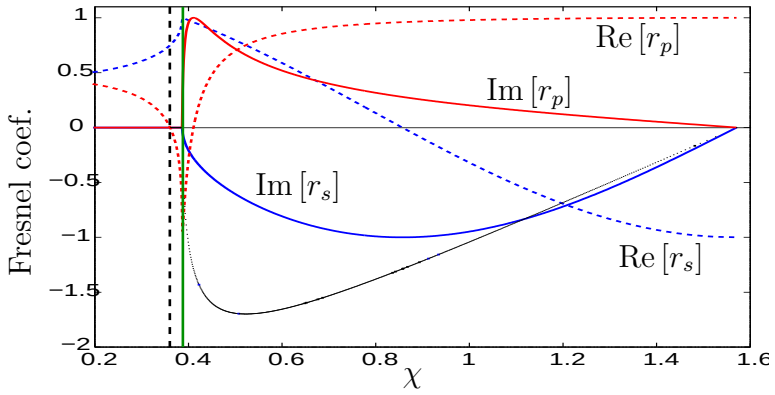

Figure 7.2: Fresnel coefficients for total internal reflection at interface with $n_o = 1$ and $n = 2.65$. In red we have r_p, in blue r_s. (real part dashed, imaginary solid). The curve in black is the phase shift between the two components. The vertical dashed black line indicates the Brewster angle at which $r_p = 0$ and the vertical green line is the critical angle (CA).

From Snell's law Eq. (7.2) we see that there exist a critical angle

$$\chi_{crit} \equiv \arcsin \frac{n_o}{n} \tag{7.7}$$

at which we have no transmitted ray; for a curved surface there are correction [11] to this result, already discussed in Section 6.3 below. The outgoing angle α does still exist, but is now a complex number, leading to a polarization dependent phase shift. We write

$$\sin\alpha = \frac{n}{n_o}\sin\chi \tag{7.8}$$

$$\cos\alpha = i\sqrt{\frac{n^2}{n_o^2}\sin^2\chi - 1} \qquad (\chi > \chi_{crit}). \tag{7.9}$$

Thus we can write the Fresnel reflection coefficients as

$$r_s = \frac{\frac{n}{n_o}\cos\chi - i\sqrt{\frac{n^2}{n_o^2}\sin^2\chi - 1}}{\frac{n}{n_o}\cos\chi + i\sqrt{\frac{n^2}{n_o^2}\sin^2\chi - 1}} \tag{7.10}$$

$$r_p = -\frac{\frac{n_o}{n}\cos\chi - i\sqrt{\frac{n^2}{n_o^2}\sin^2\chi - 1}}{\frac{n_o}{n}\cos\chi + i\sqrt{\frac{n^2}{n_o^2}\sin^2\chi - 1}}. \tag{7.11}$$

These are complex numbers of modulus unity, leading to the well-known TE, TM phase shifts on TIR shown in Fig. 7.2.

Now we recall that for the $k_z = 0$ resonances of the dielectric cylinder we have either $B_z = 0$ (TM mode) or $E_z = 0$ (TE mode) and we are interested in the

semiclassical limit, $m, kR \gg 1$ where the reflection at the boundary is locally like that of the plane wave. Hence the resonances in this case are shifted by the appropriate TE and TM Fresnel phase shifts for the TIR resonances; this phase shift contributes directly to the wavevector of the resonance (see Eq. (6.28)). For the above barrier resonances there is (in this limit) no phase shift, only a loss upon reflection which is determined by the Fresnel leakage in the TE and TM cases and gives $\mathrm{Im}\,[\gamma]$ for these resonances. When curvature corrections are taken into account, there is some small $\mathrm{Im}\,[\gamma]$ in the TIR case and some small energy shift for the above-barrier resonances. Thus the TE and TM Fresnel laws enter the quantization conditions directly.

However our review of polarization of plane waves indicates a complication that will arise for $k_z \neq 0$. Imagine we are in the semiclassical limit so we can think of a ray as a plane wave spiraling up or down the dielectric cylinder; it is easy to see and we will show below, that the plane of incidence will change with each reflection from the boundary for all cases except for $\sin\chi = 0$ (diametral motion in the transverse plane). Therefore a polarization which is purely E_p or E_s on the first bounce will appear as some linear combination of the two on the next bounce, and in fact the polarization would have to change with z, violating the translational symmetry required of resonances. Therefore we shall see that the polarization must be an eigenvector of particular reflection times rotation matrix in order to restore translational symmetry and in fact this condition determines the vector solutions of the problem with $k_z \neq 0$ and the polarization properties in the far-field of the emitted light. The eigenvalues of this problem are precisely the quantities $\Lambda = re^{i\zeta}$ that we inserted without detailed analysis into the resonance condition, Eq. (6.28)

7.3 Jones Algebra

To keep track of the polarization of polarized light, R. Clark Jones introduced in 1941 [106] the 2-d matrix algebra, where the polarization state is given with a Jones vector, and the optical element is described by a Jones matrix. The Jones vector is written as

$$\boldsymbol{E} = \begin{pmatrix} E_p \\ E_s \end{pmatrix} = \begin{pmatrix} E_{0p} e^{i\phi_p} \\ E_{0s} e^{i\phi_s} \end{pmatrix} \tag{7.12}$$

with E_{0s} and E_{0p} being the magnitude of the electric field and the phases ϕ_s and ϕ_p. Any optical element can now be written as a 2-d matrix. In our case we are interested in the Jones matrix for the reflection and transmission at a dielectric interface, which writes as

$$J_r = \begin{pmatrix} -r_p & 0 \\ 0 & r_s \end{pmatrix} \quad \text{(for reflection)}, \qquad J_t = \begin{pmatrix} t_p & 0 \\ 0 & t_s \end{pmatrix} \quad \text{(for transmission)} \tag{7.13}$$

This mechanism only works when all reflections lie in the same plane. If we deviate from the plane we need to rotate the coordinate system such that it lies in the new plane of incidence. If the angle between the two planes is given by ξ we can do this

by multiplying the Jones vector by the rotation matrix

$$\mathfrak{R}(\xi) = \begin{pmatrix} \cos\xi & \sin\xi \\ -\sin\xi & \cos\xi \end{pmatrix} \quad \begin{array}{l}\text{(rotation of coordinates through} \\ \text{an angle } \xi \text{ in negative direction)}\end{array} \tag{7.14}$$

In the next Section we will determine this angle ξ for a general cylindrical symmetry. The Jones version of the R-matrix will then be the product of J_r and the rotation matrix.

Rotation matrix for the Polarization

In order to be able to consider polarization we orient our electric field $\boldsymbol{E}$ in the $s,p-$direction of our ray. E_s is the perpendicular *senkrecht* direction and E_p in the parallel direction of the plane $\mathfrak{N}$ spanned by the incoming and outgoing ray $\mathfrak{N}^0 = \mathfrak{P}^0 \wedge \mathfrak{P}^1$. E_s points in the direction $\mathfrak{N}^0$. After the reflection we need to transform the electric field into the local coordinates for the reflection $\mathfrak{P}^1 \to \mathfrak{P}^2$, where the normal is given by $\mathfrak{N}^1 = \mathfrak{P}^1 \wedge \mathfrak{P}^2$. This can be achieved by a rotation of both components by ξ, where $\xi = \sphericalangle(\mathfrak{N}^0, \mathfrak{N}^1)$. This angle can be calculated using

$$\begin{aligned}
|\mathfrak{P}^0 \times \mathfrak{P}^1||\mathfrak{P}^1 \times \mathfrak{P}^2| \cos\xi &= \langle \mathfrak{P}^0 \times \mathfrak{P}^1 | \mathfrak{P}^1 \times \mathfrak{P}^2 \rangle \\
&= \langle \mathfrak{P}^0|\mathfrak{P}^1\rangle\langle\mathfrak{P}^1|\mathfrak{P}^2\rangle - \langle\mathfrak{P}^1|\mathfrak{P}^1\rangle\langle\mathfrak{P}^0|\mathfrak{P}^2\rangle \\
&= \left[(1+\tan^2\theta)\cos 2\eta^0\right]\left[(1+\tan^2\theta)\cos 2\eta^1\right] \\
&\quad - (1+\tan^2\theta)(p_x^0 p_x^2 + p_y^0 p_y^2 + \tan^2\theta) \\
&= (\cos 2\chi^0 - \tan^2\theta)(\cos 2\chi^1 - \tan^2\theta) \\
&\quad + (1+\tan^2\theta)(-(p_x^0 p_x^2 + p_y^0 p_y^2) - \tan^2\theta) \\
&= (\cos 2\chi^0 - \tan^2\theta)(\cos 2\chi^1 - \tan^2\theta) \\
&\quad + (1+\tan^2\theta)(\cos(\pi - 2\chi^0 - 2\chi^1) - \tan^2\theta)
\end{aligned} \tag{7.15}$$

where we used Eq. (3.74) and the fact that $-(p_x^0 p_x^2 + p_y^0 p_y^2)$ represents the angel between the rays $\sphericalangle(\boldsymbol{p}^0, \boldsymbol{p}^2)$. We further note that

$$\begin{aligned}
|\mathfrak{P}^0 \times \mathfrak{P}^1| &= |\mathfrak{P}^0||\mathfrak{P}^1| \sin\sphericalangle(\mathfrak{P}^0, \mathfrak{P}^1) \\
&= (1+\tan^2\theta)\sin 2\eta^0 \\
&= (1+\tan^2\theta)\sqrt{1-\cos^2 2\eta^0} \\
&= (1+\tan^2\theta)\sqrt{\frac{(1+\tan^2\theta)^2 - (\cos 2\chi^0 - \tan^2\theta)^2}{(1+\tan^2\theta)^2}} \\
&= \sqrt{(1+\tan^2\theta)^2 - (\cos 2\chi^0 - \tan^2\theta)^2} \\
&\ldots \quad \text{some identities later:} \\
&= 2\cos\chi^0 \sqrt{\sin^2\chi^0 + \tan^2\theta}
\end{aligned} \tag{7.16}$$

we can thus write the angle $\xi = \xi(\chi^0, \chi^1, \theta)$. All the information is thus given in terms of the 2-d picture plus the conserved inclination angle θ.

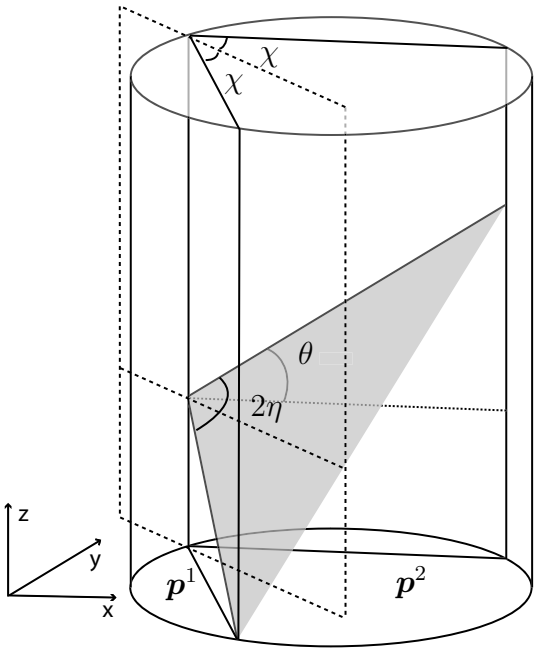

Figure 7.3: Schematic for the rays traveling in a 3-d cylinder.

7.4 Polarization resonance condition for the cylinder

We have seen in the previous section that the polarization vector gets in general mixed at every reflection from the boundary. Thus, the polarization would have to change along z. As this would be a violation of the translational symmetry we have to require that the polarization vector remains unchanged after a rotation and reflection, up to a constant

$$\nu_{1,2} \begin{pmatrix} E_p \\ E_s \end{pmatrix}_{1,2} = \mathfrak{R}(\xi) J_r \begin{pmatrix} E_p \\ E_s \end{pmatrix}_{1,2} \equiv \mathfrak{J} \begin{pmatrix} E_p \\ E_s \end{pmatrix}_{1,2} \tag{7.17}$$

where E_p, E_s are the given in the local plane of incidence spanned by $(\mathfrak{P}^1, \mathfrak{P}^2)$ with the normal $\mathfrak{N}$. This condition reduces now to the the eigenvalue problem of the 2×2 matrix $\mathfrak{J} = \mathfrak{R}(\xi) J_r$ with the two eigenvalues $\nu_{1,2}$. Each of two different eigenpolarizations $\binom{E_p}{E_s}_{1,2}$ represent either the TE or TM like resonances (in the limit where they are distinguishable).

In Fig. 7.4 we plot both the eigenvalues of the $\mathfrak{J}$ and R matrix vs. $\sin\chi$. We can clearly see that they are equivalent. In the next section we will show that both matrices are similar.

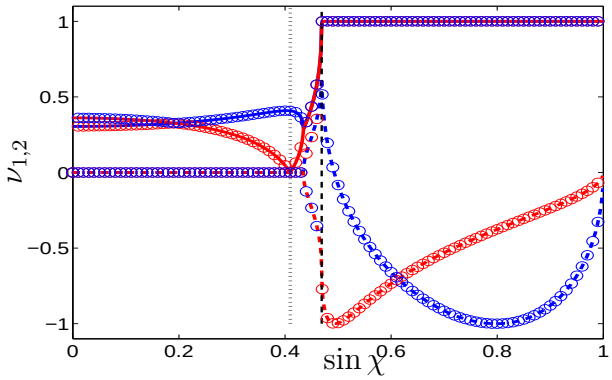

Figure 7.4: Absolute value of the two eigenvalues $\nu_{1,2}$ of the rotated Jones matrix (solid red and blue). Imaginary part of the eigenvalues is plotted in dashes. The Eigenvalues become complex at the point where the two curves meet and join. This point lies between the Brewster angle (dashed vertical black) and the effective critical angle (solid vertical green). In dots we plot the eigenvalues of the Λ for the R-matrix given in Chapter 6. Calculated for $\tan\theta = 0.2$, $n = 2$.

7.5 Similarity of $\mathfrak{J}$ and R

We have shown in Fig. 7.4 that the eigenvalues of the Jones-Rotation matrix $\mathfrak{J} = \mathfrak{R}(\xi)J_r$ are indeed the same as that of the R-matrix. In order to show that both matrices are similar, i.e. $R = \mathfrak{J}^{-1}R\mathfrak{J}$. We need to show that there exist an invertible $\boldsymbol{\Theta}$ such that $\mathfrak{a} = \boldsymbol{\Theta}\mathfrak{b}$, where $\mathfrak{a}$ are the eigenvectors of $\mathfrak{J}$ and $\mathfrak{b}$ the eigenvectors of R. Here we will now derive this $\boldsymbol{\Theta}$.

In Section 2.2 we have derived the properties of the wave equation in terms E_z and B_z. First we will adopt a local coordinate system shown in Figure 2.3 and use the normal and tangential derivatives in Eqs 2.53 in Eqs 2.18 and 2.19. This leads to:

$$\begin{pmatrix} E_x \\ E_y \end{pmatrix}^i = \begin{pmatrix} E_t \\ E_n \end{pmatrix}^i = \begin{pmatrix} \sin\chi & \cos\chi \\ \cos\chi & -\sin\chi \end{pmatrix} \begin{pmatrix} \tan\theta & 0 \\ 0 & \frac{1}{n\cos\theta} \end{pmatrix} \begin{pmatrix} E_z \\ B_z \end{pmatrix}^i, \quad \text{and} \tag{7.18}$$

$$\begin{pmatrix} B_x \\ B_y \end{pmatrix}^i = \begin{pmatrix} B_t \\ B_n \end{pmatrix} = \begin{pmatrix} -\cos\chi & \sin\chi \\ \sin\chi & \cos\chi \end{pmatrix} \begin{pmatrix} \frac{n}{\cos\theta} & 0 \\ 0 & \tan\theta \end{pmatrix} \begin{pmatrix} E_z \\ B_z \end{pmatrix}^i. \tag{7.19}$$

We can invert these equations and get for the electric field component

$$\begin{pmatrix} E_z \\ B_z \end{pmatrix}^i = \begin{pmatrix} \cot\theta & 0 \\ 0 & n\cos\theta \end{pmatrix} \begin{pmatrix} \sin\chi & \cos\chi \\ \cos\chi & -\sin\chi \end{pmatrix} \begin{pmatrix} E_x \\ E_y \end{pmatrix}^i \tag{7.20}$$

$$\begin{pmatrix} E_z \\ B_z \end{pmatrix}^r = \begin{pmatrix} \cot\theta & 0 \\ 0 & n\cos\theta \end{pmatrix} \begin{pmatrix} \sin\chi & -\cos\chi \\ -\cos\chi & -\sin\chi \end{pmatrix} \begin{pmatrix} E_x \\ E_y \end{pmatrix}^r \tag{7.21}$$

$$\begin{pmatrix} E_z \\ B_z \end{pmatrix}^t = \begin{pmatrix} \cot\alpha & 0 \\ 0 & n\cos\alpha \end{pmatrix} \begin{pmatrix} \sin\sigma & \cos\sigma \\ \cos\sigma & -\sin\sigma \end{pmatrix} \begin{pmatrix} E_x \\ E_y \end{pmatrix}^t. \tag{7.22}$$

All we need to do is to write E_p and E_s in terms of E_x and E_y. For this we note that E_s is parallel to the normal of the plane spanned by $\mathfrak{P}^0, \mathfrak{P}^1$:

$$\hat{k} = \mathfrak{P}^0 = \begin{pmatrix} \sin\chi \\ \cos\chi \\ \tan\theta \end{pmatrix}, \qquad \text{and} \qquad |k| = \sqrt{1+\tan^2\theta} \tag{7.23}$$

$$\hat{s} = \mathfrak{P}^0 \times \mathfrak{P}^1 = \begin{pmatrix} \tan\theta \\ 0 \\ -\sin\chi \end{pmatrix}, \qquad \text{and} \qquad |s| = \sqrt{\tan^2\theta + \sin^2\chi} \tag{7.24}$$

The E_p component lies in the plane thus we can write it as a sum of the two vectors $\mathfrak{P}^0, \mathfrak{P}^1$:

$$\hat{p} = -\left(\mathfrak{P}^0\cos 2\eta + \mathfrak{P}^1\right) = \begin{pmatrix} -\sin\chi\cos^2\eta \\ \cos\chi\sin^2\eta \\ -\tan\theta\cos^2\eta \end{pmatrix} \tag{7.25}$$

$$|p| = \sqrt{\sin^2\chi\cos^4\eta + \cos^2\chi\sin^4\eta + \tan^2\theta\cos^4\eta} \tag{7.26}$$

We can now write

$$\begin{pmatrix} E_x \\ E_y \\ -E_z \end{pmatrix} = \begin{pmatrix} s_x & p_x & k_x \\ s_y & p_y & k_y \\ s_z & p_z & k_z \end{pmatrix} \begin{pmatrix} 1/|s| & 0 & 0 \\ 0 & 1/|p| & 0 \\ 0 & 0 & 1/|k| \end{pmatrix} \begin{pmatrix} E_s \\ E_p \\ 0 \end{pmatrix} \tag{7.27}$$

thus

$$\begin{pmatrix} E_z \\ B_z \end{pmatrix}^i = \begin{pmatrix} \cot\theta & 0 \\ 0 & n\cos\theta \end{pmatrix} \begin{pmatrix} \sin\chi & \cos\chi \\ \cos\chi & -\sin\chi \end{pmatrix} \begin{pmatrix} s_x & p_x \\ s_y & p_y \end{pmatrix} \begin{pmatrix} 1/|s| & 0 \\ 0 & 1/|p| \end{pmatrix} \begin{pmatrix} E_s \\ E_p \end{pmatrix}^i \tag{7.28}$$

A good test of the equation is to check the value of

$$E_z = -\frac{E_s}{|s|}s_z - \frac{E_p}{|p|}p_z \tag{7.29}$$

$$= \cot\theta\left(\frac{E_s}{|s|}(s_x\sin\chi + s_y\cos\chi) + \frac{E_p}{|p|}(p_x\sin\chi + p_y\cos\chi)\right) \tag{7.30}$$

We have now connected both eigenvectors, via a matrix $\mathbf{\Theta}$. Thus the Jones matrix approach is equivalent to the R matrix approach. With this we are able to write the quantization condition in a completely analytical form! Right at the PCA the eigenvalues are complex conjugates and thus the resonances will get both a shift in the energy and width. From the CA on we just have a shift in energy.

7.6 Polarization critical angle

We have seen in the last section that the connection matrix between R and $\mathfrak{J}$, $\mathbf{\Theta}$ is real. We can infer from this that if the eigenvalues are real so are the eigenvectors.

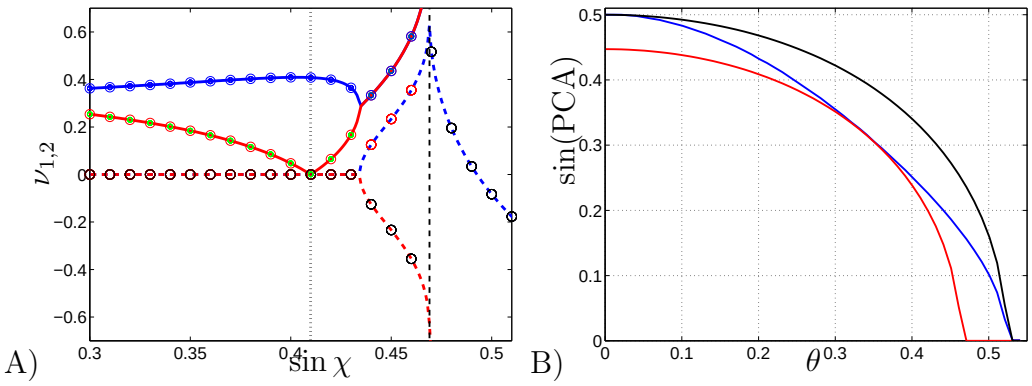

Figure 7.5: A) Absolute value of the two eigenvalues $\nu_{1,2}$ of the rotated Jones matrix (solid red and blue). Imaginary part of the eigenvalues is plotted in dashes. The Eigenvalues become complex at the point where the two curves meet and join. This point lies between the Brewster angle (dashed vertical black) and the effective critical angle (solid vertical green). In dots we plot the eigenvalues of the Λ for the R-matrix given in Chapter 6. Calculated for $\tan\theta = 0.2$, $n = 2$. B) (blue) The sine of the polarization critical angle PCA at which the eigenvalue of R gets complex. (red) sin of the Brewster Angle, (black) sin of the critical Angle, were total internal reflection occurs.

If the eigenvalues have a relative phase, so will E_z and B_z. We will show later that then also the far-field E_z and B_z components have a phase shift, thus show general polarization.

For the $\mathfrak{J}$ we can analyze the eigenvalues by writing the matrix explicitly in terms of the rotation angle ξ and the Fresnel reflection coefficiants r_s and r_p. The eigenvalues then read as

$$\nu_{1,2} = \frac{1}{2}\cos\xi\,(r_s - r_p) \pm \frac{1}{2}\sqrt{\cos^2\xi\,(r_s - r_p)^2 + 4r_p r_s}. \tag{7.31}$$

In the preceeding section we noticed that if the eigenvalues are complex, the polarzation will be in general elliptical. In Fig. 7.5 A) zoom into the plot of the eigenvalues vs. $\sin\chi$ for the region where the eigenvalues become complex. From Fig. 7.2 we know that $r_s > 0\ \forall\ \sin\chi$ and only r_p changes its sign (right at the Brewster angle). We can thus see that the discriminant in Eq. 7.31 will be always positive below the Brewster angle. At the critical angle (CA) both r_s and r_p get complex and we get eigenvalues with unit magnitude. The interesting part is the region between the Brewster angle and the critical angle. At some value of $\sin\chi$ in this interval, the discriminant gets negative (but both r_s and r_p are real) and thus leading to complex conjugate eigenvalues. This elliptical polarization will occurring *before* the critical angle. We name this angle the *polarization critical angle* PCA. In Fig. 7.5 B) we analyse the functional relation of the PCA with respect to θ and compare it to the Brewster angle and the CA. We see that for small θ the onset of the elliptical phase is at the CA. As θ varies new PCA moves close to the Brewster angle and then for θ

close to the CA, where for any $\sin\chi$ we will have TIR, the PCA returns to the CA.

We can make here an interesting observation, that the eigenvalues of the rotated Jones matrix are related exactly to the resonant lifetimes of the resonant problem in Section 6.3.1 by the relation Eq. (6.20).

In the next section we will now investigate the properties of the eigenvectors for both the Jones and R matrix approach.

7.7 Spinor ratios

In the last sections we only considered the eigenvalues of the Jones and R matrix. Here we will compare the eigenpolarizations. As we will later see we are going to be able to relate them to the polarization of the refracted light, effectively the far-field polarization derived in Section 4.9. The spinor has the two components E_z and B_z and it will be useful to look at the ratio nB_z/E_z and the phase difference between the two components. In the next section we will link these values to the ellipticity of the polarization. As we have derived the real transformation matrix $\mathbf{\Theta}$ know that if the spinor $\binom{E_z}{B_z}$ has a phase shift so will the polarization vector $\binom{E_s}{E_p}$, thus we already can infer that if the spinor is real the polarization is going to be linear along some axis.

In Fig. 7.6 the ratio of the eigenvalues and their phase difference is plotted for the Jones (circle) and EBK (solid lines) matrices is plotted. We observe that they are identical. In Fig. 7.6 A) we show the phase difference vs. $\sin\chi$ and in B) the ratio of the z components of the EM field. We can see for the phase that for a small angle of incidence in the projected plane $\sin\chi$ the phase is $\pm\pi$, thus the field is linearly polarized. This result should come as no surprise as for $\chi = 0$ we have a ray 'zig-zagging' in the transverse plane, effectively reducing the reflection to the two dimensional system. In the other extreme the phase is $\pm\pi/2$. This is the limit of the WG resonances, that are TIR reflected. The ratios of the components is shown in Fig. 7.6 B). We can see that in for small χ the fields have either $B_z = 0$ or $E_z = 0$. Somewhere between the Brewster angle and the CA the magnitudes become identical. This is right at the point, where they aquire a non-trivial phase. After the CA the amplitudes become distinguishable with a phase shift of $\pi/2$.

limiting cases

Here we check the limiting cases of θ, where θ is close to the CA and where it is almost vanishing. We can see in Fig. 7.7 that above the critical angle for θ the phase difference between the two polarizations is constant at $\pm\pi/2$. The two polarizations are linear at $\sin\chi = 0$, as we can see that the ratios diverge. For finite $\sin\chi > 0$ and θ close to the critical angle the ratio gets constant at $B_z/E_z = 1$, for large $\theta \gg \chi_c$ the ratio diverges further. For θ slightly above the critical angle and finite $\sin\chi$, we can see that the TM like resonances (red) are circularly polarized as the ratio between $B_z/E_z = 1$ and the phase difference is $\pi/2$. For the TE like resonances (black) the

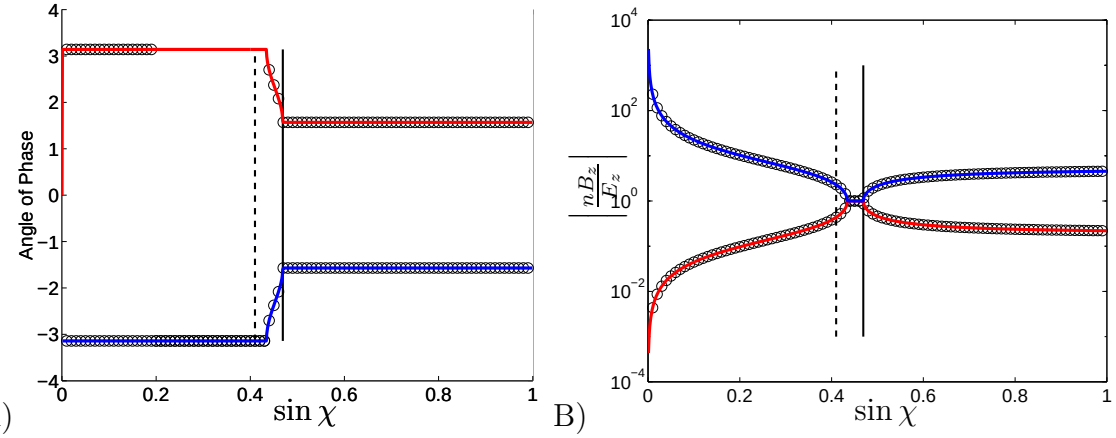

Figure 7.6: A) , B) (blue and red solid) Ratio of the z component of the two eigenvectors of the electric and magnetic field from the R matrix. The black circles are the Jones eigenvectors after the transformation $\mathbf{\Theta}$. For $n = 2$, $\tan\theta = 0.2$. The solid vertical black line is the effective critical angle, the dashed line the effective Brewster angel.

ratio is $B_z/E_z > 1$, thus we get elliptic polarization.

7.8 Far-field polarization

We have noted before that one of the most standard experimental observable for for dielectric microcavities is the far-field radiation. In Section 4.9 we showed that for a dielectric rod with arbitrary cross-section we can always define a polarization in the far-field. We were able to relate this to the E_z and B_z components of the field, and showed that if the detector is positioned perpendicular to the propagation direction of the field that the polarization is just given by the Spinor $\binom{B_z}{E_z}$ in the far-field.

In the preceeding section we only have looked at the internal polarization, here we now want to link it to the outside field components.

7.8.1 Polarization of exact resonance solutions of the cylinder

First we derive the magnitude of the B_z and E_z field for the cylinder to compare later with results from EBK and ray-models. Using our abbreviation from Eqs. (4.14) we can rewrite the matrix equation 4.10 for each of the components as

$$\xi_m = -ik_z \frac{\tau m}{kG^{TE}} \alpha_m \tag{7.32}$$

$$\alpha_m = ik_z \frac{\tau m}{kG^{TM}} \xi_m \tag{7.33}$$

In the limit close to a TM resonance $|G^{TE}| > 0$ and we can see if we fix α_m that the B_z component of the field vanishes for $k_z \to 0$. The same holds for the E_z component

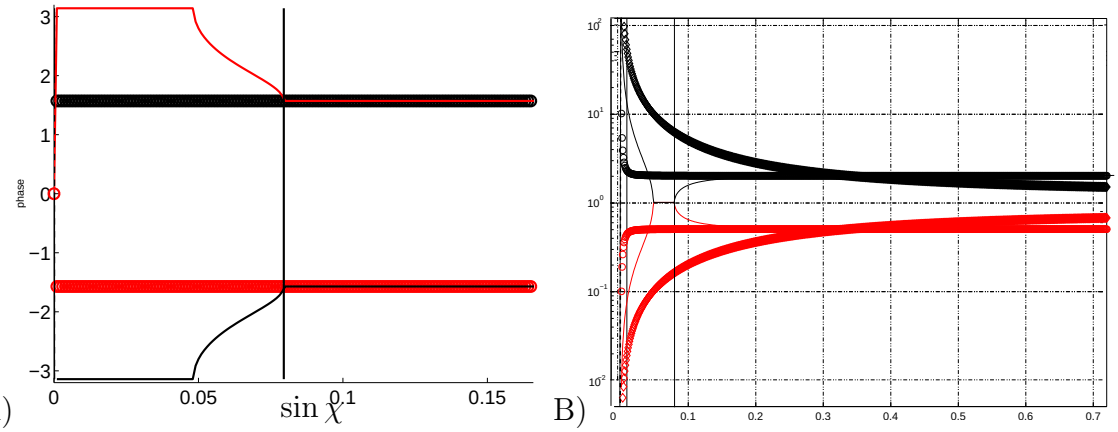

Figure 7.7: Limiting cases close to the critical angle. A) Phase, B) Ratio of the z component of B_z/E_z with $n = 2$ vs. $\sin\chi$ of the with $\tan\theta = 1.2700$ (diamond), $\tan\theta = 0.5774$ (circle) and $\tan\theta = 0.5700$ (solid), the values of θ are far above, slightly above and slightly below the critical angle. The solid vertical black line is the critical angle for $\tan\theta = 0.5700$.

in the vicinity of a TE resonance. There are also the other two choices of equations, but we note that since $|G^{TE}| \approx 0$ close to a TM resonance the equation will become highly unstable as we have a quotient of small k_z and $|G^{TE}|$.

The ratio of nB_z/E_z is easily written down in the exact form as

$$P = \frac{nB_z^>}{E_z^>} = \frac{\xi_m}{\alpha_m} = -ik_z \frac{\tau m}{kG^{TE}}. \tag{7.34}$$

Note that for interior fields the same relation $P = B_z^</E_z^<$ hold, as ξ_m and α_m are related to the outside fields through Eq. (4.9) by the same pre-factor. We will now make this connection in the EBK approach

7.8.2 Far-field in the EBK approach

In Section 2.4 we studied the semiclassical limit of and the reflection, transmission at a dielectric boundary. There we derived a relation for the incoming and outgoing field

$$\Psi^t = T\Psi^i \tag{7.35}$$

where $\Psi = \binom{B_z}{E_z}$ is the spinor. We show in Fig. 7.8 that the phase and the spinor ratio is not changed by the transmission matrix T. This should come as no surprise as we have shown in the preceeding section that this effect should follow directly out of the continuity boundary condition for the wave equation.

7.8.3 Ray-dynamical far-field polarization

Now we will derive the far-field for in terms of the Jones formalism. For this we first apply the Jones matrix J_t, and then need to describe the polarization with respect

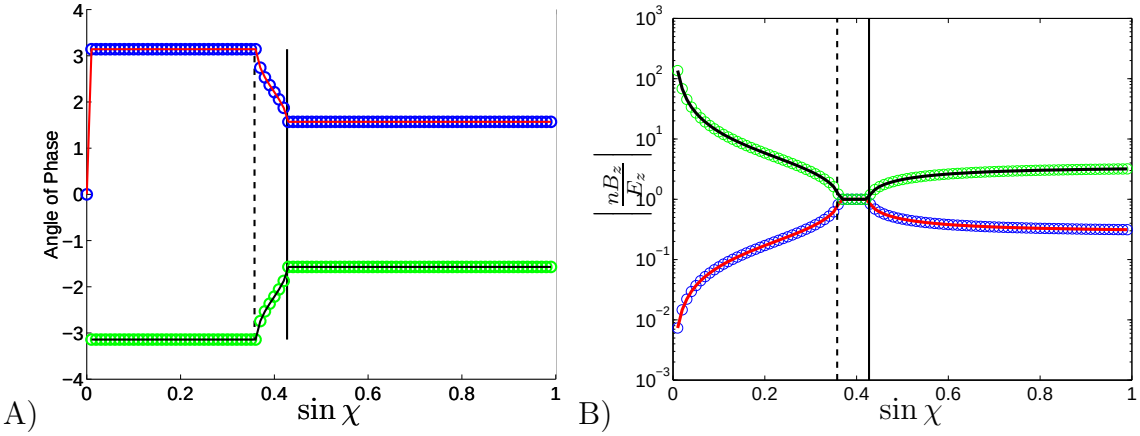

Figure 7.8: A) Phase difference and B) Ratio (black and red solid) of the z component of the two eigenvectors of the electric and magnetic field from the R matrix. The circles indicate the outside compoenent of the vector, given by Eq. (7.35). For $n = 2$, $\tan\theta = 0.3$. The solid vertical black line is the effective critical angle, the dashed line the effective Brewster angel.

to the $(x, y) \sim E_\phi$ plane and $z' \sim E'_z$ (see Section 4.9). This can be realized by a simple rotation of the angle

$$\sin\zeta = \cos\frac{\pi}{2} + \zeta = \frac{\langle\mathfrak{N}|\hat{E}'_p\rangle}{|\mathfrak{N}||\hat{E}'_p|} \tag{7.36}$$

$$= \frac{\tan\theta\cos\chi}{\sqrt{\Big(\tan^2\theta + \sin^2\chi\Big)\Big(\cos^2(1-\lambda)^2 + \sin^2(1+\lambda)^2\Big)}} \tag{7.37}$$

where $\hat{E}'_p$ is the vector perpendicular to the direction $\mathfrak{R}$, Eq. (B.6) and parallel to the (x, y) plane, given by

$$\hat{E}'_p = \begin{pmatrix} -(p_y^1 + \lambda p_y^2) \\ p_x^1 + \lambda p_x^2 \\ 0 \end{pmatrix}, \quad \mathfrak{N} = \mathfrak{P}^1 \times \mathfrak{P}^2 = \begin{pmatrix} \tan\theta(p_y^1 - p_y^2) \\ \tan\theta(p_x^2 - p_x^1) \\ p_x^1 p_y^2 - p_y^1 p_x^2 \end{pmatrix} \tag{7.38}$$

We have also chosen a local coordinate system at the point of incidence resulting in:

$$p_x^1 = \sin\chi, \qquad p_x^2 = \sin\chi \tag{7.39}$$

$$p_y^1 = \cos\chi, \qquad p_y^2 = -\cos\chi \tag{7.40}$$

The final polarization vector thus will be

$$R(-\zeta)J_t|\mathfrak{a}\rangle \tag{7.41}$$

and similarly for $|\mathfrak{b}\rangle$.

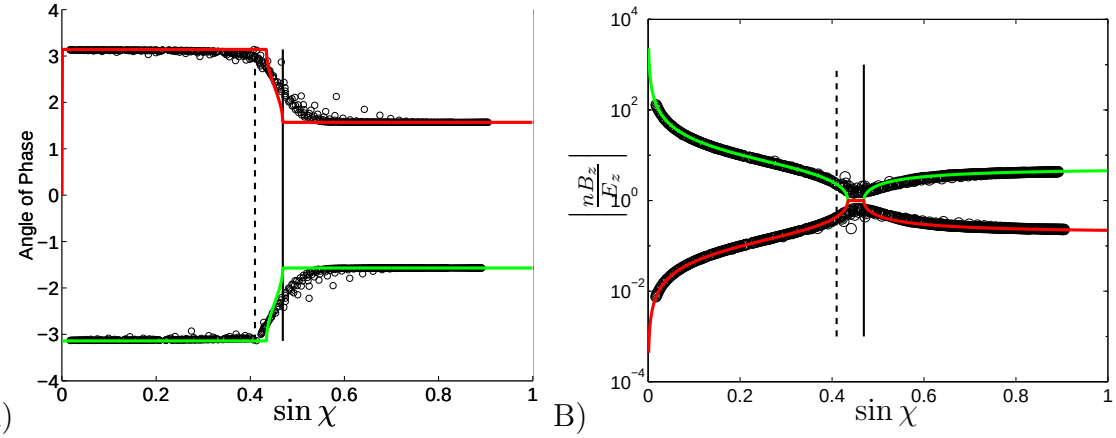

Figure 7.9: A) Phase difference , B) Ratio (green and red solid) of the z component of the two eigenvectors of the electric and magnetic field from the R matrix. The black circles are the exact numerical solutions following Eq. (4.16) ($m \in [0, 50]$ and $\gamma_1 < 50$). For $n = 2$, $\tan\theta = 0.2$. The solid vertical black line is the effective critical angle, the dashed line the effective Brewster angel.

7.8.4 Comparison in the far-field

In the last section we derived the far-fields for the exact numerics, the EBK ansatz and the Jones formalism. Here we will compare them. We have already seen in Fig. 7.6 that the Jones and EBK approach yield the same results for the eigenpolarization, thus here we will just focus on the comparison between wave and EBK. We can see in Fig. 7.9 A) that the in the limit for $\sin\chi = 0$ and $\sin\chi = 1$ both formalisms agree. Most notable is the difference in the region around the critical angle (CA). Here we see that the numerical solutions do not show the abrupt behavior of the EBK method. For the spinor relations in Fig. 7.9 B) we see the same behavior that the numerical solutions smoothen the behavior seen in the EBK method. We can conclude from this that both the EBK as well as the Jones formalism are appropriate tools to study the polarization of radiation from a cylinder.

7.8.5 Gaussian optical approach

In Section 6.5 we found that the arguments for the eigenvalues of the polarization matrix R went over to stable orbit modes via the Gaussian optics method, with the small modifications of a transverse energy shift (Floquet phase) and the necessity of including the full round trip R matrix to get the appropriate values. Essentially identical considerations apply to extending the above results to describe far-field polarization of hybrid modes based on stable 2d periodic orbits.

Preliminary studies confirm these predictions but will not be presented here at this time.

7.9 Conclusion

In this Chapter we derived a ray-dynamical understanding for the resonance shifts encountered at the EBK quantization condition in Chapter 6. We used the Jones algebra to construct an eigenpolarization problem and where able to write the eigenvalues in a physically appealing way. Comparing the analytic results of this and the last Chapter with numerical solutions from Chapter 4 we showed that the Jones and EBK approach is a valid description to characterize the far-field polarization from a cylinder. We gave an outlook of what to expect from a Gaussian optics construction of the far-field for stable orbits.

Chapter 8

GaN Experiment

8.1 Introduction

In the preceding chapters we learned how to describe dielectric micro-cavities theoretically. In Chapter 5 we described experiments done on dye-doped polymer micro-cavities with a low index of refraction ($n = 1.49$). In this chapter we will cover the experimental setup and the investigation of asymmetric Gallium Nitride (GaN) and Indium Gallium Nitrite (InGaN) micro-cavities, where the index of refraction is significantly higher ($n = 2.65$). For the first time we will provide experimental data from ARC micro-cavities with only one symmetry axis. GaN has many unique properties and possible applications are numerous, due to its being a wide-bandgap semiconductor with a bandgap of about 3.45eV (360nm). The InGaN studied here has a bandgap of 3.07eV and emits at 404nm. This wide-bandgap makes GaN an

Figure 8.1: Traffic lights in New Haven, CT. The green LED uses InGaN. The red and yellow LED use aluminum gallium arsenide AlGaAs. More recently, aluminum indium gallium phosphide has emerged as a promising material for red, amber, and yellow LEDs.

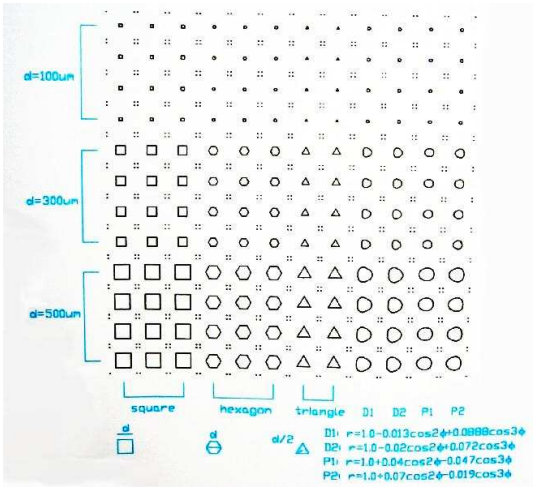

Figure 8.2: The structure of the Photolithographic Mask.

ideal semiconductor for development of green to ultra-violet (UV) opto-electronic devices, such as light-emitting diodes (LED) or laser diodes (LD). The applications range from green traffic light LED's (Fig. 8.1) to higher storage DVD's, finer printing techniques and huge TV LCD screens. It has been shown by Rex in his thesis [59] that GaN based micro-cavities can function as highly directional micro-lasers. At the end of this chapter we give an overview of experiments done on elliptic, quadrupolar and quadrupole-hexadecapole deformations, and the respective theory of resonant modes. Current developments following those ideas have lead to the first uni-directional GaN micro-cavity laser, based on a spiral shape, which has been reported by Chern *et al.* [17].

8.1.1 The Photolithography Masks

We use a photolithography mask with special shapes present on the mask `B2449` are squares, hexagons, triangles and four specially designed shapes.

$$D1 : r = d(1.0 - 0.013\cos 2\phi + 0.0888\cos 3\phi) \tag{8.1}$$
$$D2 : r = d(1.0 - 0.02\cos 2\phi + 0.072\cos 3\phi) \tag{8.2}$$
$$P1 : r = d(1.0 + 0.04\cos \phi - 0.047\cos 3\phi) \tag{8.3}$$
$$P1 : r = d(1.0 + 0.07\cos \phi - 0.019\cos 3\phi) \tag{8.4}$$

For each shape we have four samples at three different diameters ($d = 100\mu$m, $d = 300\mu$m and $d = 500\mu$m) each column. For the squares and hexagons we have three columns, two for the triangle and one column each for the special shapes. The mask was designed in `AutoCAD` by Grace Chern and send to the Palo Alto Research Center (PARC) to produce the photolithography mask. The special shapes were suggested by us for reasons discussed in the next section.

8.1.2 Discussion of Special Shapes

We selected the four special shapes for a number of reasons and possible applications in integrated optical components. In the following we will analyze the ray-dynamics and show the dominant stable periodic orbits and the surface of section for each of the shapes. We will also indicate why we chose the sample. The index of refraction for InGaN is $n = 2.65$, the critical angle is $\sin\chi_{crit} = 1/n = 0.377$.

D1 Shape — smooth uni-directional laser?

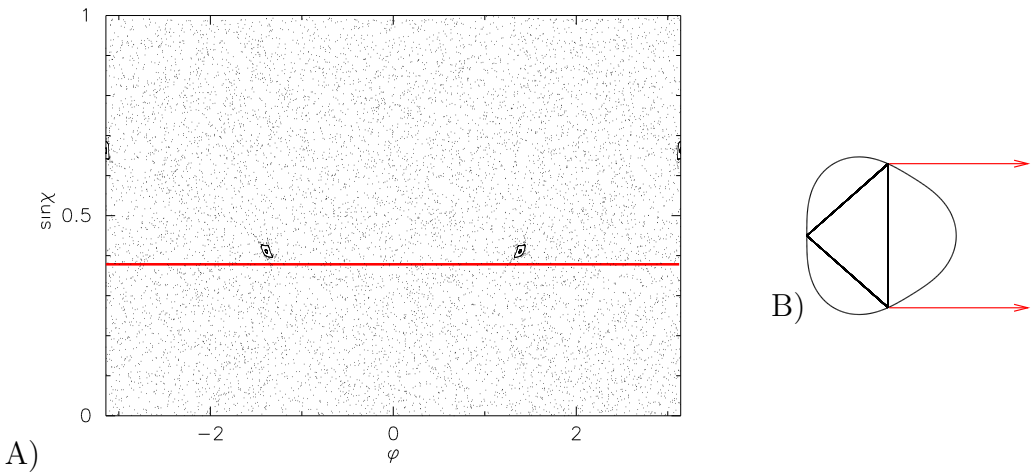

Figure 8.3: The surface of section for shape D1 and its main periodic orbit. The fix-points of the periodic orbit are $(\phi_o, \sin\chi_o) = (\pm 1.38, 0.41), (\pm\pi, 0.66)$. The line of critical angle of incidence at $\sin\chi_c = 1/n = 0.377$ is indicated by the red horizontal line.

All previous experiments on ARC s focused on shapes with double reflection symmetry for which stable orbit modes give multiple output beams. Here we design a shape with onlt one symmetry axis (a "space-capsule") and the possibility of stable orbit modes with two output points and only one beam direction. Note that for shape D1, only one dominant stable orbit is present in the SOS. With flood pumping of the cavity we would expect the orbit to be chosen that is close to the critical line. Two islands for this orbit are close to the critical line. We thus would expect both islands as output portals and emitting in the same direction. Siumulations show that they emit mainly into the 0° direction in the far-field.

D2 Shape — smooth uni-directional laser?

Shape D2 is similar to D1, but with an bigger island. Only one dominant stable orbit is present in the SOS. We again expect the orbit to be chosen and emission mainly into the 0° far-field.

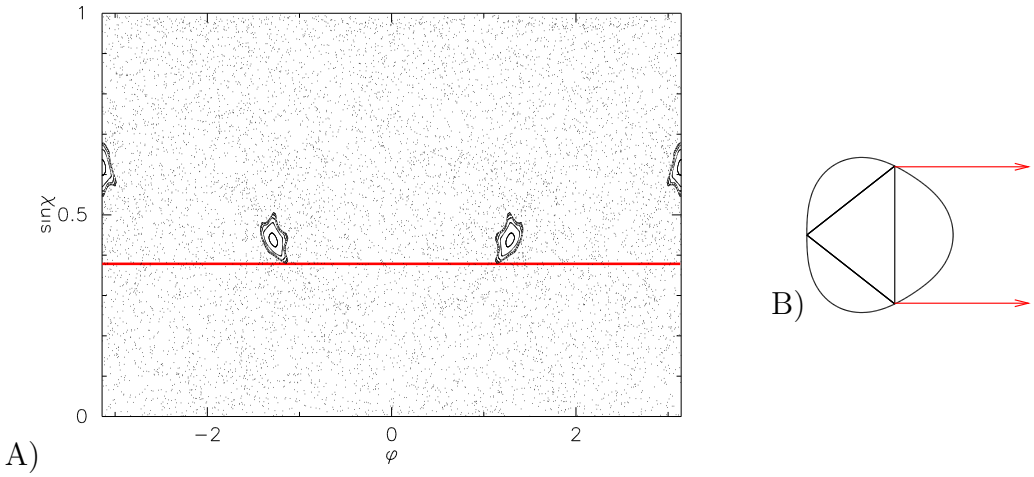

Figure 8.4: The surface of section for shape D2 and its main periodic orbit. The fix-points of the periodic orbit are $(\phi_o, \sin\chi_o) = (\pm 1.28, 0.43), (\pm\pi, 0.7998)$. The line of critical angle of incidence at $\sin\chi_c = 1/n = 0.377$ is indicated by the red horizontal line.

P1 Shape — A one portal amplifier?

For shape P1 only one dominant stable orbit is present in the SOS. With flood-pumping the cavity we would expect the orbit to be chosen that is close to the critical line. The dominant orbit in this case has one island close to the critical line. We expect emission out of this portal in two directions. This cavity might be used as an amplifier.

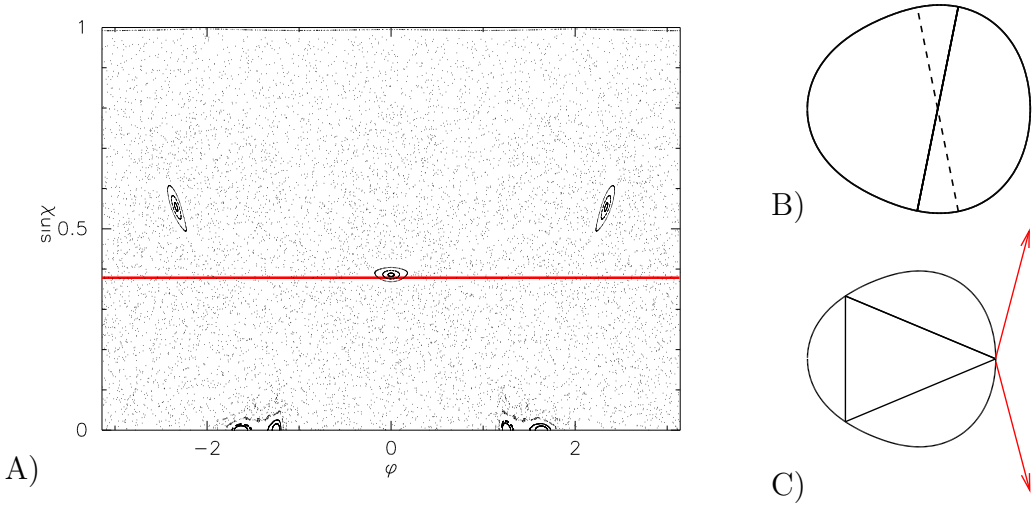

Figure 8.5: A) The surface of section for shape P1. B) Two BB orbits. C) The main periodic orbit with the fixed-points $(\phi_o, \sin\chi_o) = (\pm 2.33, 0.552), (0.0, 0.3854)$. The line of critical angle of incidence at $\sin\chi_c = 1/n = 0.377$ is indicated by the red horizontal line.

P2 Shape — Switching light?

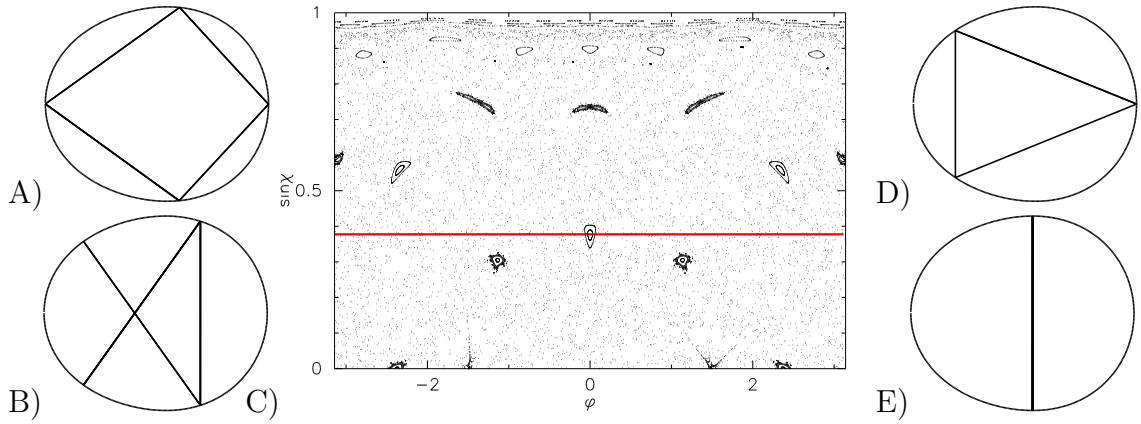

Figure 8.6: center C) The surface of section for shape P2. A) 'Kite'-orbit with fix-points $(\phi_o, \sin\chi_o) = (\pm\pi, 0.584), (0.0, 0.73)$. B) 'Fish'-orbit with fix-points $(\phi_o, \sin\chi_o) = (\pm 2.37, 0.0), (1.136, 0.3049)$. D) Triangular orbit with fix-points $(\phi_o, \sin\chi_o) = (\pm 2.34, 0.558), (0.0, 0.376)$. E) Center BB orbit $(\phi_o, \sin\chi_o) = (\pm\pi/2, 0.0)$. The line of critical angle of incidence at $\sin\chi_c = 1/n = 0.377$ is indicated by the red horizontal line.

The dynamics in this shapes has a number of stable orbits. Some like the hexagon and other clearly WG type orbits are high above the critical line and we thus do not expect them to play a major role in this semiconductor resonator. The four bounce 'Kite' orbit has three refection points clearly above the critical line and one closer to it. Its spatial overlap is considerable with the the triangular orbit that has one dominant island just at the critical line. The other two orbits are probably not of too much importance as they both are self-retracing orbits, and thus have reflection points with normal incidence and are expected to be very lossy. This cavity might be useful for optical switching of modes. As the different modes have considerable overlap we might be able to excite the triangular or 'kite' orbit via flood pumping and by shining light from the sidewall into the direction of the 'fish' we might be able to deplete the resonance mode and thus change the lasing output. As both the triangle and the 'kite' have the same sidewall angle $\phi = 0.0$ with an island we might be able to get different output from the same point on the sidewall.

8.2 GaN growth, etching & quality

As we are interested in the difference of the radiation patterns for the only slightly differing samples, the sidewall quality of the sample is going to be an important factor. We expect the quality of the sidewall to be good up to the order of the wavelength. There are a number of different ways to etch InGaN. The wet etching techniques (mainly using chemicals) are not useful for our applications as they etch along crystallographic planes and as we are interested in exact defined shapes this

would be not feasible. Dry techniques employ physical methods. Both of the methods alone will not produce smooth enough sidewalls (For a detailed discussion see Ref. [59]). It has been shown that *chemically assisted ion beam etching* (CAIBE) produces the smoothest sidewalls in InGaN [107]. CAIBE is a well-known technique to etch III-V semiconductor materials such as GaAs, InP, and related alloys. The material removal comes as a result of collisions of argon ions accelerated by a voltage applied in a vacuum chamber. This process is aided by the introduction of chlorine which, reacts with the semiconductor substrate making it softer and, thus, increasing the etching rate. Xerox PARC etched the InGaN using CAIBE. In Fig. 8.7 we show the sidewall quality of the cavity and the shape preservation.

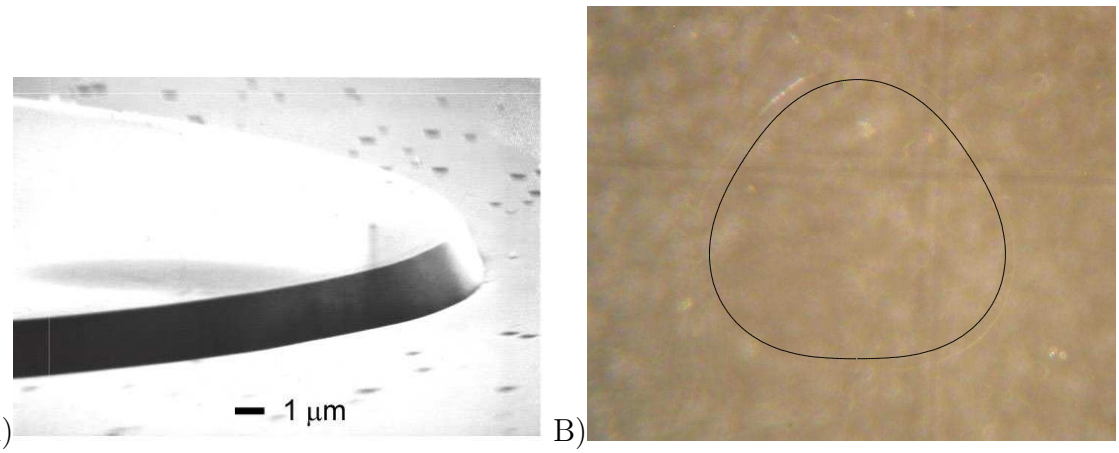

Figure 8.7: A) Sidewall Photo of a GaN cavity etched with CAIBE. B) Optical microscope picture of the D2 cavity with $d = 500\mu$m. In black we overlaid the exact shape of D2 scaled a bit smaller to see the faint boundary of the cavity.

8.3 Optical Excitation of InGaN

InGaN has a bandgap energy of 3.07eV, corresponding to emission at 404nm, we thus are required to excite in the near UV. For this we used a laser diode pumped Spectra-Physics X-30 Q-switched, Nd:YAG laser. It has a fundamental 1.046μm infrared beam and its second harmonic at 532nm (green), both of the beams are emitted simultaneously. To excite the InGaN close to its bandgap we will use an external 3^{rd} harmonic generator which combines both wavelengths to create a 355nm beam. The pulse duration of the X-30 is approximately 30ns with a maximum energy up to 80μJ per pulse.

8.4 Experimental Setup

The laser is positioned horizontally in the plane of the operating table. It passes through the 3^{rd} harmonic generator. We use two narrow band filters to filter the

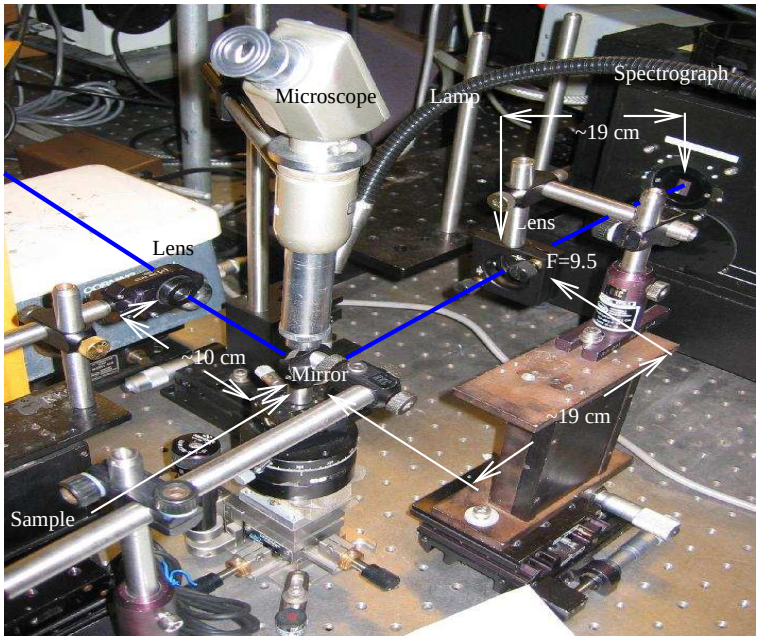

Figure 8.8: Setup for the Spectral Analysis

fundamental frequencies out of the beam, thus allowing only the 532nm beam to propagate. A quartz lens narrows the beam an we clean it by passing it through an aperture. By adding normal density ND filters the intensity can be reduced and it passes through a lens onto a 45° tilted dielectric mirror, which is coated to reflect 532nm. Two vertical stages and a rotational stage are positioned right below the mirror allowing the sample to be freely positioned. The rotational stage is tilted by an angle of about 3° away from the ICCD camera (spectroscope) to allow the radiation of the single cavity to pass by the other obstructing cavities on the chip. The rotational stage is used to investigate the micro-cavity as an function of the angle. Behind the sample we can position either an aperture and the spectroscope or an imaging lens and the ICCD camera. This setup is favored to rotating the CCD camera as we need to have large magnification for high resolution imaging. For the imaging experiment we will increase the path-length by placing a 45° mirror behind the imaging lens. Above the sample and the dielectric mirror we position an optical microscope with a cross-hair, this allows us to fine adjust (and find) the micro-cavity on the chip. We can also use it to fine adjust the excited micro-cavity as the spontaneous emission of the InGaN illuminates the cavity in a light blue.

8.4.1 Spectral Setup

To obtain spectral information of the micro-cavity we focus the emitted radiation of the cavity through a $f = 9.5$cm lens onto the spectrometer. We use an electronically controlled Acton Research Corporation 0.5m focal-length spectrometer with three gratings 150, 300 and 1500 lines/ mm. A Princeton Instruments intensified CCD

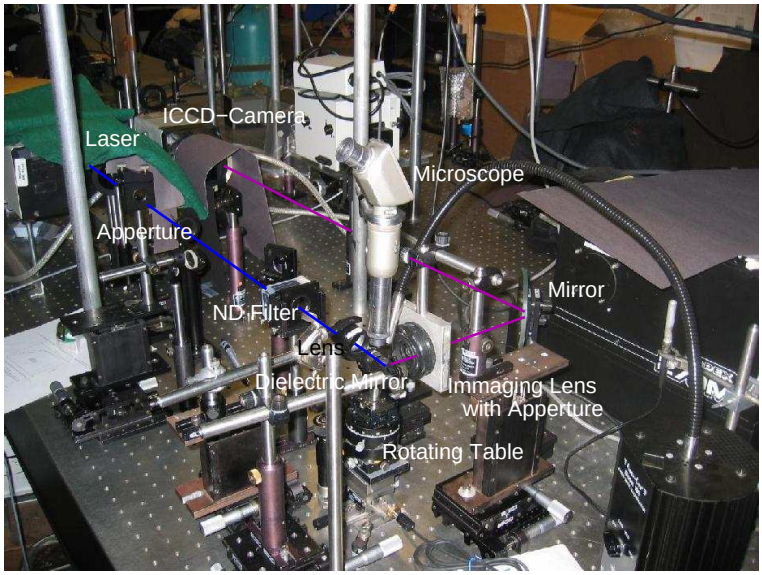

Figure 8.9: Setup for the Imaging

camera with a resolution of 256x1024 pixel is used behind the spectrometer to collect the spectrum. The camera needs to be synchronized to the pulsed laser and gets calibrated with the known spectrum of a Hg lamp (For a picture of the setup see Fig. 8.8).

8.4.2 Imaging Setup

For the imaging setup we use a short focal length camera lens ($f = 1.4$cm) with an adjustable aperture. This aperture is set to accept a light cone of approximately $2\mu = 5°$, resulting in a numerical aperture NA

$$NA = n_{air} \sin \mu = 0.047 \tag{8.5}$$

and a depth of field d

$$d = \lambda \frac{\sqrt{n_{air}^2 - NA^2}}{NA^2} \approx 200\mu\text{m}. \tag{8.6}$$

This depth of field assures that the cavity in its entirety is always in focus as we rotate it. The light reflects through a 45° tilted mirror into the ICCD camera. The intensity can be reduced by inserting ND filters (not saturate the ICCD camera). We use the same Princeton Instruments ICCD camera used in the spectral setup. In front of the ICCD camera we mount a band pass filter restrict the light to the stimulated emission region of the micro-cavity. The aperture in the imaging lens has an important role of defining a window in the direction space ($\Delta \sin \chi$), so that a given pixel on the camera can be identified up to a diffraction limited resolution with a pair $(\phi, \sin \chi)$. Mathematically, the effect of the lens-aperture combination is equivalent to a windowed Fourier transform of the incident field on the lens [108].

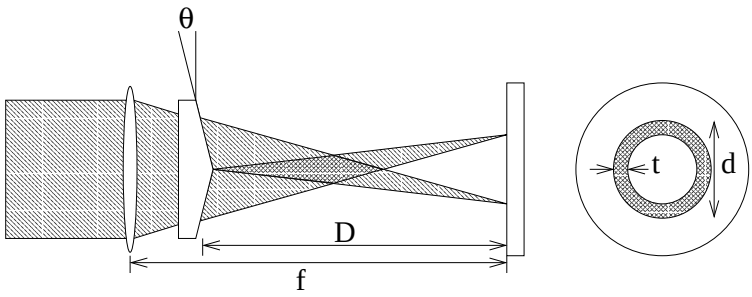

Figure 8.10: An axicon lens generating a ring-shaped beam. The use of a converging lens of focal length f allows for the control of the thickness t of the ring. The diameter d depends on the distance D. In the actual setup we will add another converging lens to shorten the distance D.

Note that the infinite aperture limit is simply a Fourier transform of the incident field and we lose all the information about direction $\sin\chi$. It has to be emphasized that we are only probing the far-field, and hence the image data does not contain the "near-field" details we would see in a typical numerical solution, nor does it contain information about the internally reflected components of the internal cavity field (see Ref. [66] for further details). On the other hand, it provides us with valuable information about the $\sin\chi - \phi$ correlations of the emitted field, allowing us to put forward a ray interpretation of the emission and hence the internal resonance.

8.4.3 A Ring of lasing light: Axicon lens

In 1950 J. H. McLeod introduced a conically shaped optical element, termed *axicon* [109, 110]. In conjunction with a spherical lens, a Gaussian laser beam can be focused to a hollow ring, of variable radius and ring thickness. Based on this a patent was filed for precision laser machining [111, 112]. The schematic used in our setup is shown in Fig. 8.10. As our experiment is in the UV we use an axicon made from fused silica. The angle of the axicon is $\theta = 5$mrad. For the actual setup we add after the 3^{rd} harmonic generator a set of telescoping lenses to expand the beam, then clean it through an aperture and send it through the axicon and focus the ring with an additional converging lens onto the sample.

8.5 Stimulated emission

One of our main interests in the micro-cavities is to use them as lasers or amplifiers. For both we need to study the stimulated emission in the cavity. In order to determine the threshold for lasing in the InGaN cavity we use the setup described in Section 8.4.1. The laser is adjusted to give 62μJ power and we cut the power by inserting ND filters. We flood pump the cavity, meaning that we un-focus the beam to a size just bigger than the cavity. In Fig. 8.11 A) we investigate the 500μm D1

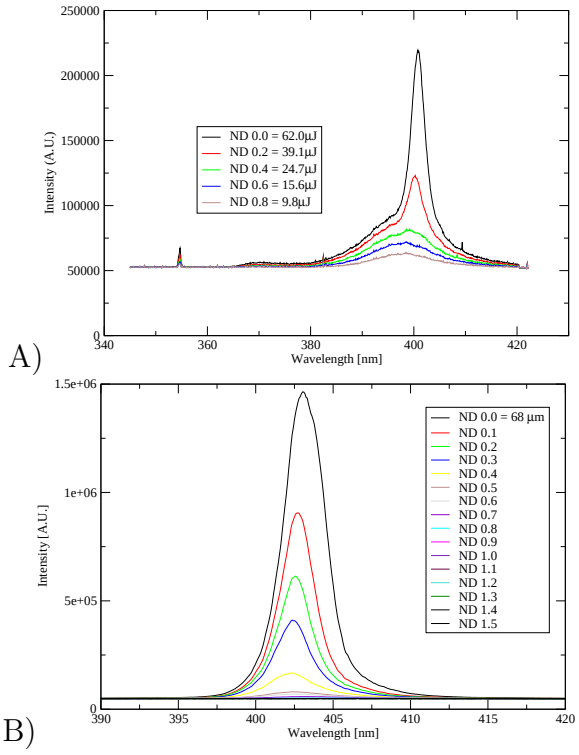

Figure 8.11: Spectral profile for the D1 shape (A) and a hexagon (B), pumped at different pump intensities.

shape. On the left side of the graph at 354nm we can see the small peak of scattered light from the pump beam. A better understanding of the lasing threshold is gained by a log–log plot of the integrated intensity vs. pump power shown in Fig. 8.12 A). We can see that our pump intensity was not sufficient to fully start lasing emission,

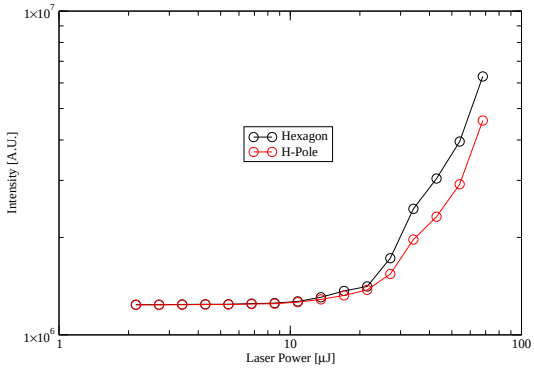

Figure 8.12: A) Log–log plot of the Integrated Spectra of the hexagon and D1 shape, pumped at different pump intensities. The slight difference in the intensity lies most likely in the fact that the area of the hexagon: ($A = 0.398\text{mm}^2$) is slightly larger than that of D1: ($A = 0.274\text{mm}^2$).

but we were well in the stimulated emission region. More pump power would on the other hand have destroyed our micro-cavity and as we are mainly interested in the directional emission properties we spared the cavity and refer to Rex's thesis Ref. [59] where a more detailed analysis was performed.

8.6 Imaging Experiments of deformed Microcavities

In this section we show the results of the imaging experiment described in Section 8.4.2. The relative angle is accurate to plus or minus 5° degrees and is determined by making laser-emission measurements from a square-shaped micro-cavity, specifically designed on the photographic mask to serve the purpose of alignment. All the other microstructures, during the mask designing time, are aligned relative to the square. The square, acting as a calibration marker, emits laser radiation (8 beams) only at its four corners and propagates parallel to its edges. Therefore, when the CCD camera is normal to one edge of the square, two equally bright spots should appear from the two edges. The relative angle is varied by either rotating the sample while keeping the CCD camera stationary or vice versa. Another powerful method

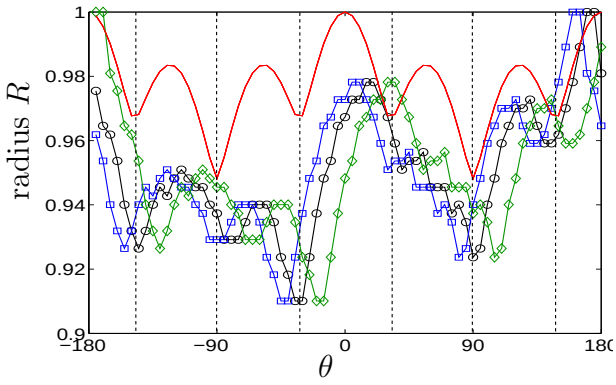

Figure 8.13: Relative width of the boundary of shape D1 vs. far-field angle (angle of the tangents). (red) mathematical shape; (blue), (black), (green) width of the CCD camera image with a fixed cutoff (at 91.000) with a shift far-field angle shift of 15° , 5° , −10°, all normalized to one. A clear correlation of the minima is visible and allows for fine adjustment of the far-field angle. The 5° far-field shift appears to be the best fit. Human selection of the cutoff for each image graph will get an even better fit.

is shown in Fig. 8.13. We use here the observation that the width of the cavity is a function of the far-field angle. By calculating the width of the mathematical shape and overlaying it onto the relative width of the emission pattern recorded by the CCD camera (we chose here a constant cut-off to mark the boundary of the shape) we can clearly find the zero degree far-field.

8.6.1 D1 Shape

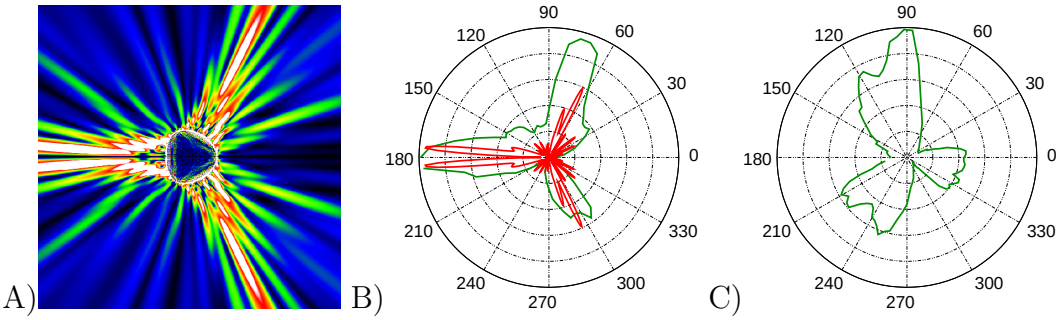

Figure 8.14: A) wavefunction real-space plot (the outside and inside field are scaled to the same intensity for display purpose), B) theoretical and experimental far-field emission, C) experimental near-field. The numerical mode is at $kR = 29.0147 - 0.009307i$, with a $Q = 6,235$.

In Section 8.1.2 we discussed the ray dynamics in the D1 shape, and hoped for a stable resonance localized on the triangular orbit. The pump intensity and the beam quality where not sufficient to uniformly flood pump the sample for the imaging experiment. The 3^{rd} Harmonic generator generated a diffraction pattern in the beam which made it non-uniform. Defocusing the beam to produce a nearly uniform beam, at the loss of power, was not possible, as our sample needed all the power to have emission over the background noise. Flood pumping and thus exiting the uni-directional mode was therefore not possible with the current setup and sample. We were however able to use an axicon lens to excite a whispering gallery mode. In Fig. 8.14 B) we show the experimental far-field data and compare it to a numerical calculation. From the numerics we can learn that the resonance is of WG type. The angular momentum components of the mode are strongly localized around $|m| = 75 \sim 82$. Emission occurs at the points of highest curvature Fig. 8.14 C) in an almost tangent direction. In Chapter 5 we have shown that a ray-dynamical

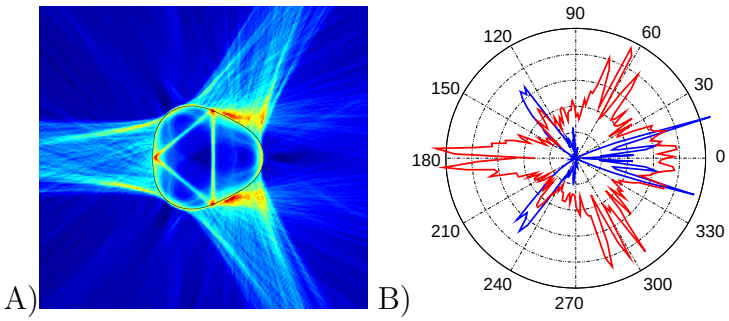

Figure 8.15: A) real-space picture of random initial conditions above the critical line. B) far-field intensity of random initial condition (red) and far-field for Gaussian bundle started on the periodic orbit (blue). In all graphs 6000 initial conditions iterated for 300 times.

description for high $\sin\chi$ modes can be appropriate. Following this thought we start in a ray simulation a bundle of rays above the critical line. We can see in Fig. 8.15 that the random bundle indeed shows the pattern seen in the experiment and in the numerical simulation. As we started uniformly above the critical line a number of rays were also started in the island of the triangular orbit. The axicon pumping seems to have favored just the WG component of the far-field.

In future we hope to obtain a better quality sample with a lower lasing threshold so that we can excite the resonance we found numerically solving the Helmholtz equation following Chapter 4. Here, we can indeed find resonances localized on this periodic orbit. A ground state with its far-field directionality is shown in Fig. 8.16.

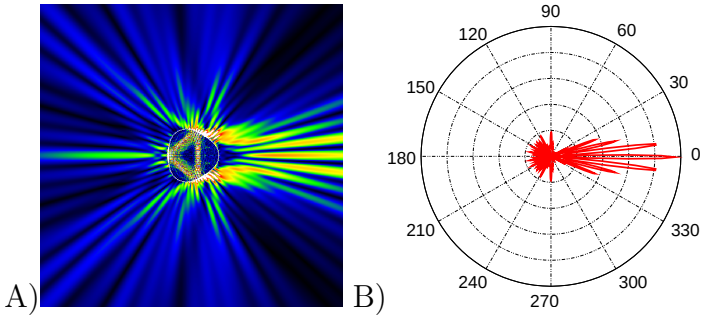

Figure 8.16: A) wavefunction real-space plot (the outside and inside field are scaled to the same intensity for display purpose), B) far-field emission of the dominant stable triangular orbit with a resonance at $kR = 30.1808 - 0.01388i$ and a $Q = 4,349$.

8.6.2 Ellipse: $\varepsilon = 0.16$ & $\varepsilon = 0.20$

In this section we analyze and interpret GaN data previously obtained by Nathan Rex [59] from elliptical cavities. The image data is collected for the lower deformation in Fig. 8.17, and for the higher deformation in Fig. 8.20. We can see a large shift in the far-field emission (Figs. C) with deformation. This is in contrast to the quadrupolar shape studied in the same material. In his thesis Rex argued that the change might be due to the onset of a bouncing ball type resonance (For a detailed discussion of the ray-dynamics in the ellipse refer to Section 3.3.3). For the lower deformation, clearly a WG-type resonance was chosen by the micro laser. From the Husimi distribution in Fig. 8.18 we can infer that the mode is mainly localized above the critical line at $\sin\chi_c = 0.377$ and only 'dips' at the points of highest curvature below the critical line. The expected emission is in the 90° range as we have seen from the experimental data. At higher deformation the structure in the phase-space remains similar, as the ellipse is integrable. One possible explanation for the drastic far-field shift between both deformations, could be that a bouncing ball type orbit might become broad enough in angle to be confined above the critical line, to have enough gain to be the dominant mode. We show the bouncing ball mode with the closest overlap in the far-field in Fig. 8.19 A). In part B) of the figure we show its theoretical image field data. Clearly the image field is *completely* different than that of Fig. 8.20.

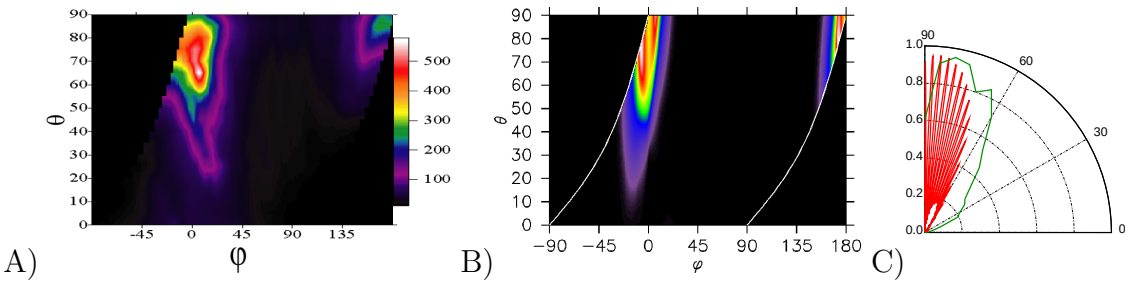

Figure 8.17: A) image data for the GaN ellipse with $\varepsilon = 0.16$. B) theoretical image data projecting the Husimi distribution into the far-field. C) The experimental far-field (green) and the calculated far-field (red). The mode used is shown in Fig. 8.18.

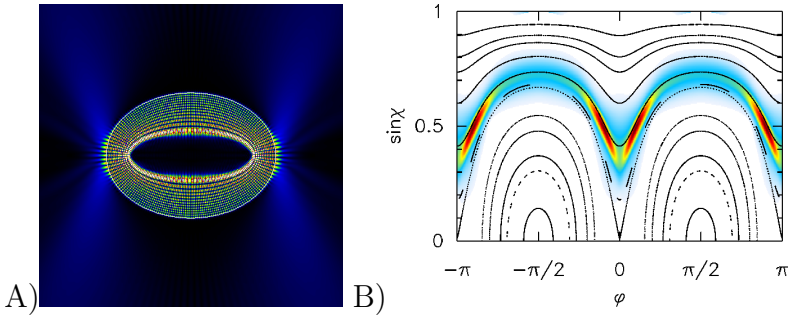

Figure 8.18: A) real-space and B) phase-space projection of a resonance in the ellipse with $n = 2.65, \varepsilon = 0.16$ and $kR = 49.908 - 0.00597i$, $Q = 16,722$. We clearly see that the associated mode for the image data is an whispering gallery type orbit.

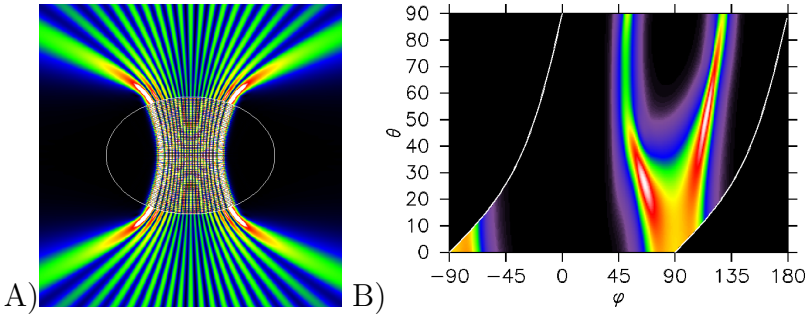

Figure 8.19: A) real-space and B) image of a 'bouncing-ball' type resonance in the ellipse who's main peak is in the far-field direction comparable to Fig. 8.21 with $n = 2.65, \varepsilon = 0.20$ and $kR = 49.945 - 0.1034i$, $Q = 966$. The image data is *very* different from that in Fig. 8.21.

We find that the emitting state is actually a separatrix state. In the real space wavefunction plot Fig. 8.21 A) we can see that the whispering gallery orbit starts to self-focus. This self focusing is the main reason that the far-field direction gets shifted into the 25° region. We have seen in this section that although the type of resonance selected stays the same the far-field can shift considerably. This further emphasizes

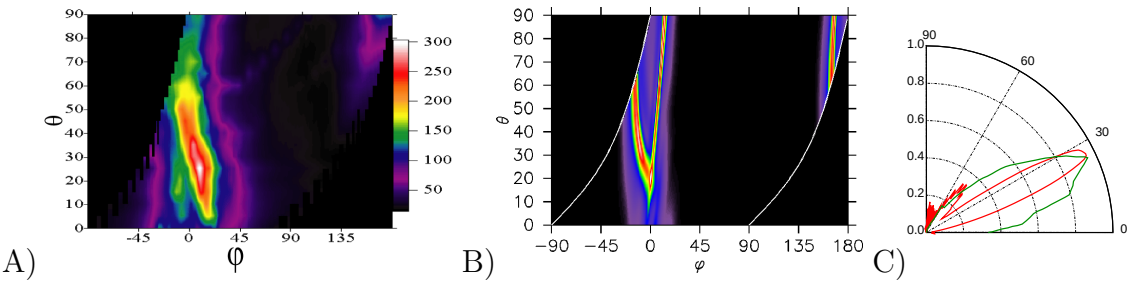

Figure 8.20: A) image data for the GaN ellipse with $\varepsilon = 0.20$. B) theoretical image data projecting the Husimi distribution into the far-field. C) The experimental far-field (green) and the calculated far-field (red). The mode used is shown in Fig. 8.21.

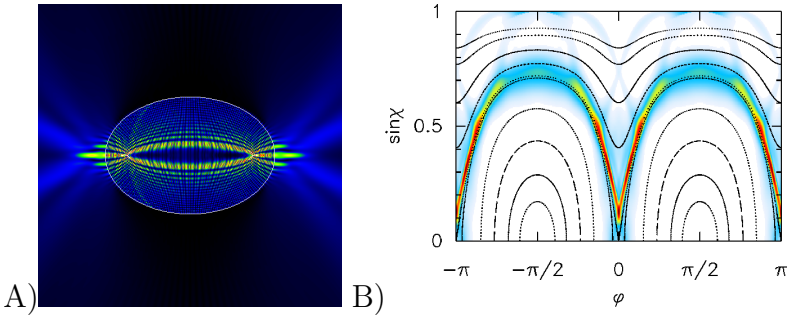

Figure 8.21: A) real-space and B) phase-space projection of a resonance in the ellipse with $n = 2.65, \varepsilon = 0.20$ and $kR = 49.659 - 0.05197i$, $Q = 1,911$. The associated mode for the image data is of whispering gallery type.

that the combination of farfield and image strongly constrains the possible resonances and allows good theoretical identification of the lasing mode.

8.6.3 Scar of David[1]

In this section we review briefly the experiment and theory of the first observed lasing scar in a GaN sample [3, 16]. Experimental data shown in Fig. 8.22 is for the quadrupolar deformation $\varepsilon = 0.12$. We observe a far-field angle $\theta \approx 74°$, which correlates with emission from the region of the sidewall around $\phi \approx +17°$. The data also show a secondary bright spot at slightly negative $\phi \approx -5°$ and another one at $\phi \approx 162°$ which do not lead to strong maxima in the first quadrant in the far-field. Observation of a small number of well-localized bright spots on the sidewall suggests a lasing mode based on a short periodic ray trajectory, contrary to the lasing from a WG orbit in the previous Section. In Fig. 8.23, we have indicated the approximate positions of the four bright spots on the boundary (the image-field can be unfolded to the range $\theta = 0 \ldots 2\pi$ using the symmetry of the quadrupole). The image-fields for the polymer lasers showed more bright spots and a variable number of them,

[1]See our paper in Ref. [3]

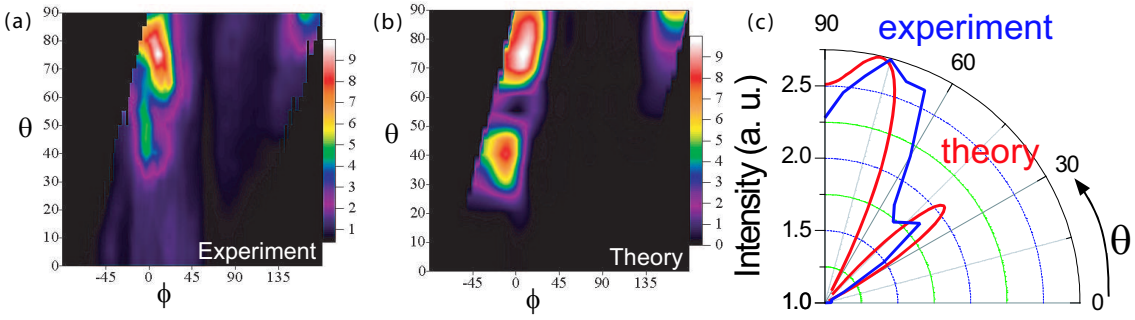

Figure 8.22: (a) Experimental data showing in color scale the CCD images (converted to sidewall angle ϕ) as a function of camera angle θ. Three bright spots are observed on the boundary for camera angles in the 1st quadrant, at $\phi \approx 17°, 162°, -5°$. (b) Calculated image field corresponding to the scarred mode shown in Fig. 8.25. (c) Calculated and experimental far-field patterns obtained by integrating over ϕ for each θ.

inconsistent with as single short periodic orbit. In the same figure is shown a view of the SOS at this deformation.

The only stable structures to result in localized modes in the framework of the previous section, are the bouncing ball, the bowtie, fish and diamond islands. For comparison, the stable bouncing ball mode would emit from $\phi = \pm 90°$ in the direction $\theta = \pm 90°$. The stable four-bounce bowtie mode, dominant in the devices of Ref. [8], is also ruled out by our data. It is very low-Q at this deformation due to its small

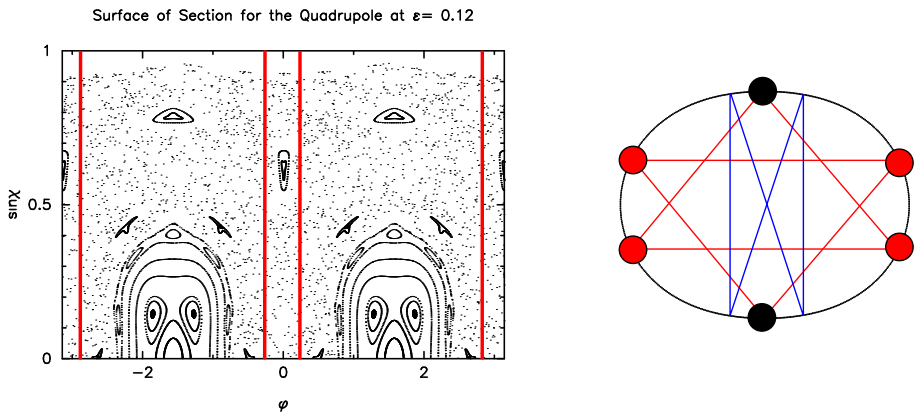

Figure 8.23: The SOS of the quadrupolar billiard at a deformation of $\varepsilon = 0.12$. The red vertical lines indicate the values of ϕ at which the bright spots in the image-field are observed. On the right is a schematic indicating in red the experimental bright spots in the real space. The location of these spots is strongly inconsistent with the bowtie orbit at this deformation but is consistent with modes based the two triangle orbits shown. These orbits would have the two "dark" bounce points (indicated in black) that are well above total internal reflection for the index of $n = 2.65$

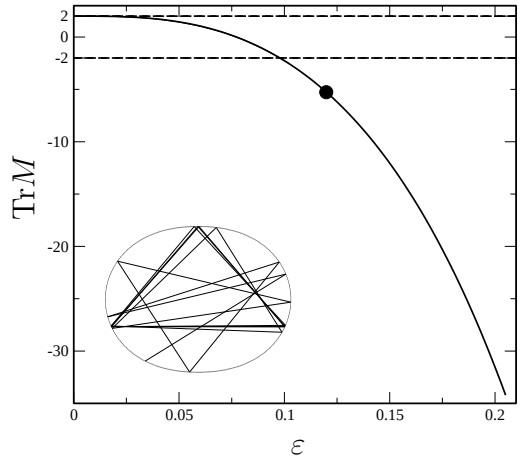

Figure 8.24: The variation of the trace of the monodromy matrix with respect to the quadrupolar deformation ε. The black circle indicates the experimental value $\varepsilon = 0.12$, at which $\mathrm{Tr}M = -5.27$. The two dashed lines delimit the regime $-2 < \mathrm{Tr}M < 2$ at which the triangular orbit is stable. In the inset is shown real space simulation of a ray orbit started with initial conditions which are away from the triangle fixed point at least by $\delta\phi = 10^{-3}$, $\delta \sin\chi = 10^{-4}$, followed for 20 bounces.

angle of incidence and would give bright spots at $\phi = \pm 90^\circ \pm 17^\circ$, far away from the brightest spot at $\phi = 17^\circ$ (see Fig. 8.23). There is however a pair of symmetry-related isosceles triangular periodic orbits with bounce points very close to the observed bright spots (see Fig. 8.23). The two equivalent bounce points of each triangle at $\phi = \pm 17^\circ$ and $180^\circ \pm 17^\circ$ have $\sin\chi \approx 0.42$, very near to the critical value, $\sin\chi_c = 1/n = 0.38$, whereas the bounce points at $\phi = \pm 90^\circ$ have $\sin\chi = 0.64$ and should emit negligibly (Fig. 8.23). This accounts for the three bright spots observed experimentally in Fig. 8.22(a) (the fourth spot at $\phi \approx 197^\circ$ is completely blocked from emission into the first quadrant). Note furthermore the proximity of the four emitting bounce points to critical incidence; a simple application of Snell's law to these rays would lead to far-field maxima in reasonable agreement with the observed peaks in the far-field distribution Fig. 8.22(c) (however not with the image-field data, see below).

These basic observations could be explained with generalized Gaussian modes [93], were it not for the fact that the triangular periodic orbit is unstable at this deformation. In Fig. 8.24, we plot the trace of the monodromy matrix as a function of deformation (see Section 3.2.5), which shows that at deformation $\varepsilon = 0.12$, $\mathrm{Tr}M = -5.27$. The triangular periodic orbit is unstable with a Lyapunov exponent of $\lambda \approx 1.62$ (see Fig. 8.24). The Gaussian optics approach which was useful for the modes localized on a stable bowtie periodic orbit modes will fail here as the width of the Gaussian becomes imaginary (see Section 6.5). Failure of the method however doesn't mean that localized modes do not exist. In fact, numerical solution of the quasi-bound states at this deformation, using the method of Chapter 4, finds modes localized on the triangular orbit, as seen in the configuration space plot in Fig. 8.25(a). A much

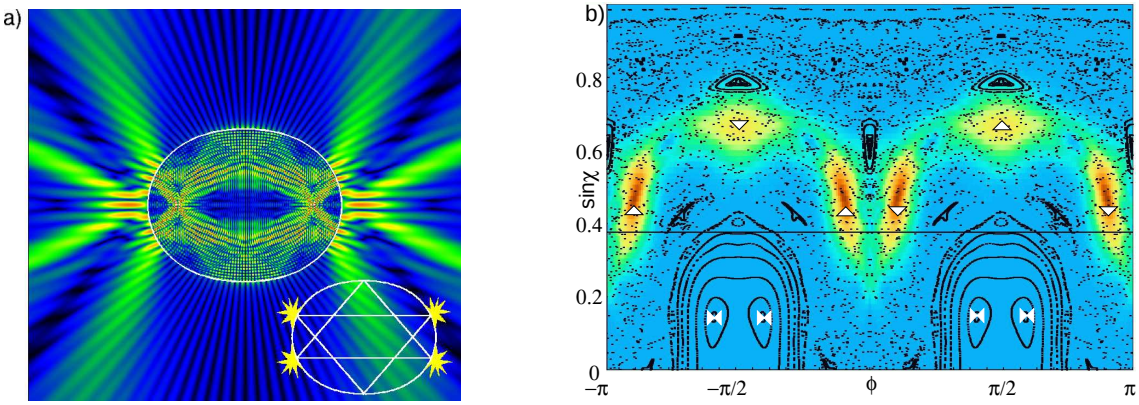

Figure 8.25: (a) Real-space false color plot of the modulus of the electric field for a calculated quasi-bound state of $nkR_0 \approx 129$ (n is the index of refraction, k is the real part of the resonant wave-vector) and $\epsilon = 0.12$ which is scarred by the triangular periodic orbits shown in the inset (M. V. Berry has termed this the "Scar of David"). The four points of low incidence angle which should emit strongly are indicated. (b) Husimi (phase-space distribution) for the same mode projected onto the surface of section of the resonator. The x-axis is ϕ_W and the y-axis is $\sin\chi$, the angle of incidence at the boundary. The surface of section for the corresponding ray dynamics is shown in black, indicating that there are no stable islands (orbits) near the high intensity points for this mode. Instead the high intensity points coincide well with the bounce points of the unstable triangular orbits (triangles). The black line denotes $\sin\chi_c = 1/n$ for GaN; the triangle orbits are just above this line and would be strongly confined whereas the stable bowtie orbits (bowtie symbols) are well below and would not be favored under uniform pumping conditions.

clearer picture, free of interference fringes, is provided by the Husimi plot of this mode in Fig. 8.25(b) projected onto the SOS. The brightest spots clearly coincide with the triangular fixed points, and the whole density is localized in the midst of the chaotic sea. This mode is an instance of a *scarred state* and is one of the most surprising and esoteric objects of quantum chaos theory.

However closer inspection of the image-field in Fig. 8.22(a) presents an intriguing puzzle from the point of view of ray optics. A mode localized on these triangular orbits might be expected to emit from the four bounce points approximately in the tangent direction according to Snell's law; this means that the bright spot at $\phi = 17°$ should emit into the direction $\theta \approx 115°$ (Fig. 8.26 A), whereas the data clearly indicate that the $\phi = 17°$ bright spot emits in the direction $\theta = 72°$. (Note that the Snell's law argument worked well for the polymer lasers in Chapter 5.) Thus the emission pattern here violates the intuitive expectations of ray optics by 43°, a huge discrepancy (see Fig. 8.26 A). Moreover, $\lambda/nR = 2.8 \times 10^{-3}$, so we are far into the regime in which the wavelength is small compared to the geometric features of the resonator and ray optics would be expected to be a good approximation. To ensure that this discrepancy did not arise from some error in the experimental

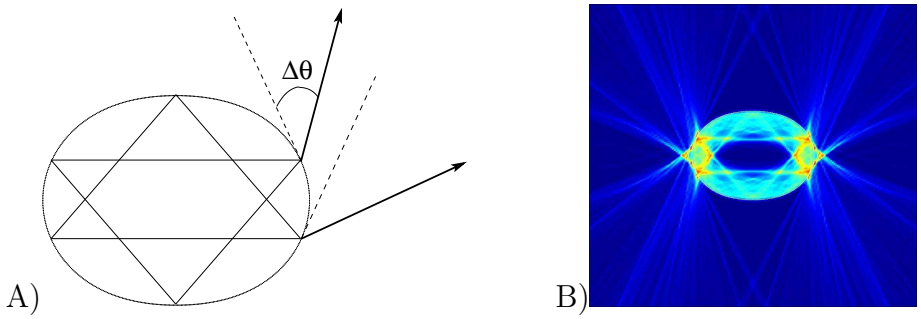

Figure 8.26: A) Schematics showing the three emitted "beams" detected in the experiment (solid lines) and illustrates their strong deviation from Snell's law (dashed tangent lines). B) Ray-dynamical simulation using the intensity of the Husimi distribution in Fig. 8.25 as intensity for a bundle of rays in the SOS. The ray intensities are then projected into real-space.

image-field we used the intensity distribution of the Husimi projection and used it as intensity distribution for an ensemble of rays started in the SOS. We followed the rays as described in Chapter 3 and note the far-field and project them into the real space shown in Fig. 8.26 B). To back this with a wave description we simulated the full experimental set-up, starting with our numerically-determined scarred solution (Fig. 8.25(a)) inside the resonator and propagating it through an aperture and lens into the far-field, reproducing the expected image-field. The way to do this is described in Ref. [66]. The image-field corresponding to the numerical resonance calculated in this manner is reproduced in Fig. 8.22(b). The good agreement with the experimental data in Fig. 8.22(a) indicates that the effect is real and is robust over a range of wavelengths, it has been termed 'Fresnel filtering' [3, 113]. In the next section we will observe a resonance located on a periodic orbit as it changes from an elliptic to a hyperbolic fix-point.

8.6.4 Quadrupole Hexadecapole: Stable & Scar

In this section we again refer to experimental data obtained by Rex [59] for the quadrupole-hexadecapolar deformations, defined by the mathematical equation:

$$r(\phi) = 1 + \varepsilon(\cos^2\phi + \frac{3}{2}\cos^4\phi). \tag{8.7}$$

The far-field emission data are reproduced in Fig. 8.27. All the deformations above $\varepsilon = 0.12$ show a well-localized emission which has approximately the same character over a wide range of deformations. Looking at the SOS of the quadrupole-hexadecapole at $\varepsilon = 0.12$, we note that there is a stable orbit – a triangular one – this time however rotated 90° from the one observed in the quadrupole [3], with bounce points at $\phi = 0°$ and $\phi = 180°$, at which points the trajectory is incident just above the critical angle for TIR. These are also the points where the maximum emission is emanating from the boundary, according to the imaging data. Unlike

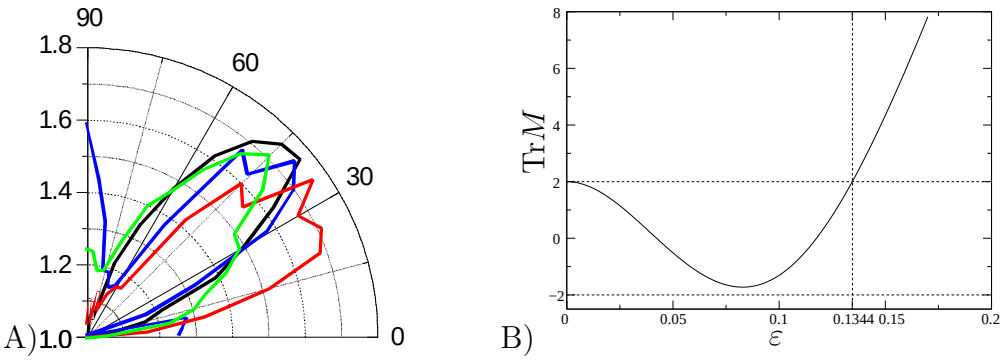

Figure 8.27: A) Far-field emission data for quadrupole-hexadecapole for deformations of $\varepsilon = 0.12$ (blue), $\varepsilon = 0.16$ (red), $\varepsilon = 0.18$ (green), and $\varepsilon = 0.2$ (black). B) trace of the monodromy matrix vs. deformation for the triangular orbit in the quadrupole-hexadecapole. For $|\mathrm{Tr}M| < 2$ the orbit is stable, otherwise unstable, see Section 3.2.5.

the quadrupole lasers then, for this shape there is a stable orbit with bounce points near the critical angle. We expect Gaussian modes [93] similar to the bowtie modes seen in the QC lasers [8]. An example of such a mode localized on the stable triangular orbit and resulting in emission consistent with the experimental results is shown in Fig. 8.28. For this shape, these triangular orbits become unstable above a deformation of $\varepsilon = 0.13$, and despite this change, the far-field data don't change in any appreciable way (Fig. 8.28). Figure 8.29 shows results of calculations for the deformation $\varepsilon = 0.16$. The Husimi projection of this mode reveals that it's localized on the triangular periodic orbit, in the vicinity of which complete chaos reigns. Thus, the laser operates on a mode which is based on one and the same classical periodic orbit, insensitive to whether it's stable or unstable.

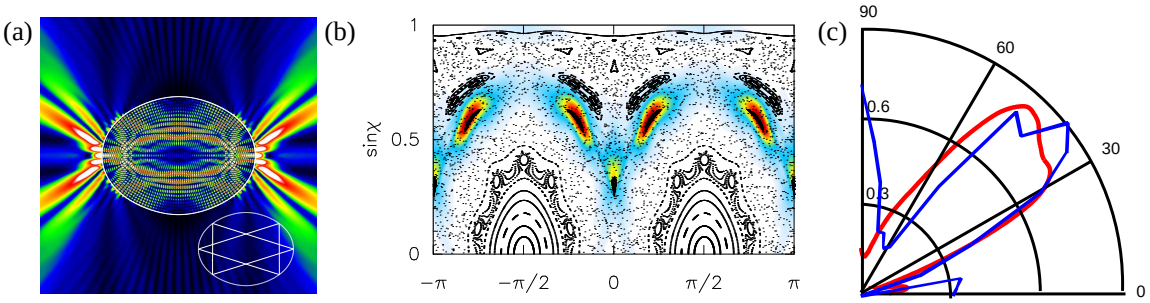

Figure 8.28: (a) A numerically calculated mode for a quadrupole-hexadecapolar deformation of $\varepsilon = 0.12$ and $n = 2.65$. (b) Husimi projection of the mode in (a). Clearly, the projection is localized on a reflection symmetric pair of stable triangular periodic orbits. (c) The calculated far-field emission pattern.

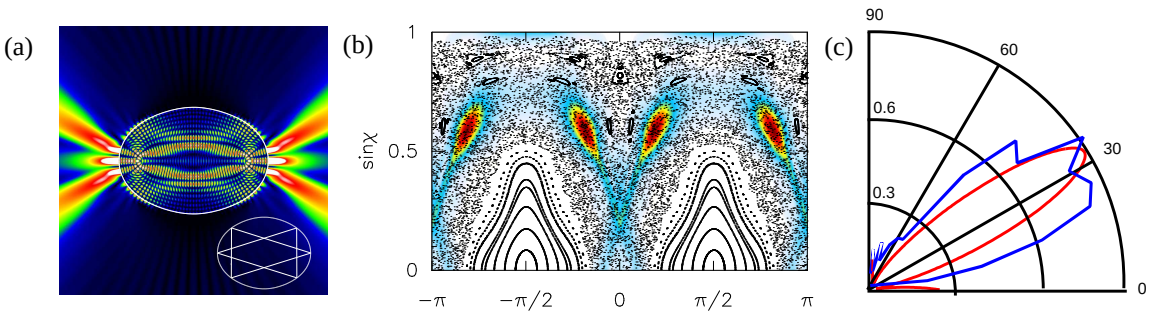

Figure 8.29: (a) A numerically calculated mode for a quadrupole-hexadecapolar deformation of $\varepsilon = 0.16$ and $n = 2.65$. (b) Husimi projection of the mode in (a). The projection is localized on a triangular orbit of the same geometry as the one in Fig. 8.29, but at this deformation the motion in its vicinity is unstable, leading to chaotic motion. The resulting mode is hence a scarred state. (c) The calculated far-field emission pattern.

8.7 Conclusion

We have presented the first data from samples with only one axis of symmetry, and we hope to soon be able to provide experimental data to report the first unidirectional laser based on a smooth boundary. From the review of all of the experiments in GaN it is clear that lasing modes of cylindrical micro-resonators need not be based on 'regular' modes such as stable orbits or whispering gallery modes, but also can get feedback from unstable ray trajectories. It is worth remarking that unstable Fabry-Perot laser resonators have been known since almost the initial conception of the laser [114, 115] and for many purposes are the best design for high-gain laser devices [85] because of their large modal volumes. In ARC micro-lasers such unstable lasing action arises naturally as one increases the deformation, with the SOS being dominated by more and more chaotic motion. Whether there is any advantage of micro-lasers based on unstable modes remains to be seen. One crucial point that needs emphasis is that there do exist many complicated chaotic modes which are not related to any single periodic orbit. Indeed in the passive cavity these modes dominate the spectrum as $kR \to \infty$. However, it may be that the non-linear effects in lasing cavities, either by averaging over fluctuating modes or by mode-locking, enhance the role of modes based on short periodic orbits, whether stable or unstable. It is striking that all of the experiments on semiconductor ARC lasers can be interpreted as demonstrating lasing from such modes.

Chapter 9

Conclusion and Open Questions

In this thesis we studied asymmetric dielectric resonant cavities. Due to the lack of symmetry these cavities in general give rise to non-integrable ray dynamics. We presented and expanded tools from the theory of non-linear dynamical systems to understand the emission directionality for various deformed polymer microlasers. The importance of short term dynamics in the chaotic region of the phase space was analyzed and linked to unstable manifolds of short unstable periodic orbits. We were able to show that the effect known as dynamical eclipsing is not dependent on the regular structures of the phase space but rather the unstable ones in the chaotic portion of the SOS. This theory lead to the prediction of directional emission from a completely chaotic stadium microlaser. We hope that experimental data for such an experiment will soon be available. As we explained the emission directionality just in terms of ray-dynamics. The next step could be to write the time propagation of a wavepacket localized in this vicinity of the relevant region of phase space.

Experiments were done on a "space-capsule" GaN microcavity to confirm our theoretical predictions. The shape was designed in such a way that it is supposed to have uni-directional emission. We were unfortunately unable to excite the specific three bounce orbit giving rise to this emission as the sample and pump quality was not efficient for strong flood pumping. Nevertheless, we were able to report the first one-fold symmetric whispering gallery orbit laser, which emits in three distinct directions. Hopefully we will be able to repeat the experiment with a new sample of better quality. If we had success with this experiment the way for phase space engineering of resonator emission properties would be open!

As all the experiments are done on three dimensional structures we derived the vector wave-equation for a dielectric rod with arbitrary cross-section. For the special case of the rotationally symmetric rod, the cylinder, we presented the EBK quantization scheme. We realized that the condition of the translational symmetry for the polarization induces a non-trivial phase shift in the resonance condition. This polarization critical angle has to our knowledge not been observed before!

For a rod with arbitrary cross-section we derived a quantization scheme based on the parabolic equation method. This scheme allows us to find the resonance conditions and construct wave solutions for stable periodic orbits of the projected

motion. For the set of resonances which do not correlate to regular structures of the phase space no such methods exist. There are a number of interesting questions to be explored in this context. We have developed an efficient numerical method to solve the vector wave-equation for dielectric rods with arbitrary cross-section and thus can analyse polarization properties of resonances numerically. With the help of the Jones algebra approach, we build a polarization ray-tracing routine to investigate this domain. So far we were not able to obtain specific results. Some open questions are:

- Identifying the nature of the lasing mode in ARCs is somtimes difficult. Can we use polarization properties to pin down which mode is lasing and where its main weight is in the mixed phase space.
- Do ARCs have useful properties as polarization filters or analyzers?
- What is a proper measure for polarization in a ray-dynamical experiment, the proper starting conditions?
- What are the effects of unstable manifolds on polarization?
- In a scattering experiment with a polarized plane wave, what are the effects of regular structures/ chaos?
- Generalize the formalism for non-uniform fiber width.

Overall, we have shown that the wonderful study of non-integrable dynamics and the rise of chaos in billiards has a very fruitful connection to the emission properties of microlasers. Various optical phenomena bear important implications to micro-photonic device design which needs further exploration.

Appendix A

Ray-dynamical properties of special orbits

A number of special periodic orbits will frequently show up in this thesis. Here we will combine their properties.

A.1 The Quadrupole

We define the quadrupolar shape by

$$r(\phi)/R_o = \frac{1}{\sqrt{1+1/2\varepsilon^2}}(1+\cos 2\phi) \tag{A.1}$$

where the prefactor insures that the area of the quadrupole is fixed constant at π, R_o is just the overall scale.

A.1.1 Bouncing Ball type orbits

Period-2 Orbits: Bouncing Ball Orbit

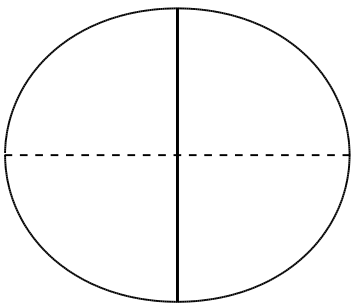

Figure A.1: Both Bouncing Ball orbits in the quadrupole of $\varepsilon = 0.08$. The solid orbit is the stable two-bounce, the dashed the unstable orbits.

At $\varepsilon = 0$ we have an infinite number of period-2 orbits. For a small perturbation $\varepsilon \neq 0$ we have seen that the infinite set breaks down and only two remain. One stable orbit along the minor axis of the quadrupole and one unstable along the major axis (Fig. A.1).

Period-4 Orbits: Bowtie & Bird

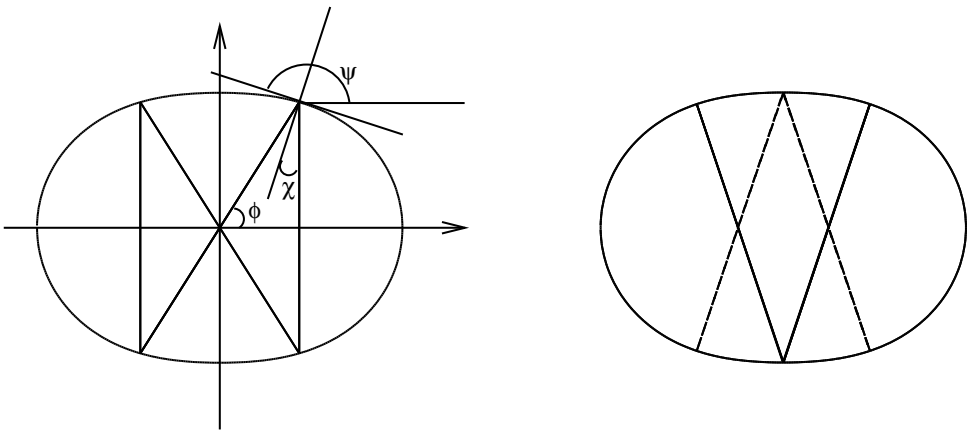

Figure A.2: Bowtie & Bird orbits born from the period doubling bifurcation of the stable two bounce orbit at $\varepsilon = 1/9$. Here shown at $\varepsilon = 0.15$. Note for the Bird that there are two separate orbits but the same number of fixed-points in the SOS. For the Bowtie we see that $\chi = \frac{\pi}{4} - \frac{\phi}{2}$ and $\Psi = 3/4\pi + \phi/2$.

We noted before that the stable BB-orbit undergoes a period doubling bifurcation at $\varepsilon = 1/9$. Following the geometry for the Bowtie in Fig. A.2 we can solve the equation

$$-\frac{\cos\phi}{1+\sin\phi} = \tan\Psi = \frac{dy}{dx} = \frac{\cos\phi}{\sin\phi} \cdot \frac{\varepsilon + 1 - 6\varepsilon\sin^2\phi}{\varepsilon - 1 - 6\varepsilon\cos^2\phi} \tag{A.2}$$

to give the analytic solution of the position of the bowtie bounce coordinates to be

$$\phi(\varepsilon) = \arcsin\left(-\frac{1}{3} + \sqrt{\frac{5}{18} + \frac{1}{6\varepsilon}}\right) \quad \text{and} \quad \sin\chi(\varepsilon) = \sqrt{\frac{4}{6} - \frac{1}{2}\sqrt{\frac{5}{18} + \frac{1}{6\varepsilon}}} \tag{A.3}$$

The bowtie becomes unstable at $\varepsilon \approx 0.2308$ where it bifurcates with $\mathrm{Tr}M = 2$ into two period-4 tilted bowties. For the 'Bird' we will not go into these details, as it is and will remain unstable.

Period-6 Orbits: Fish & Hexagram

In the 'Fish' orbit we encounter an orbit that has normal incidence on the boundary. We might wonder if it is a general statement that every orbit needs to have an even number of normal reflections (note that zero is an even number). We have seen that

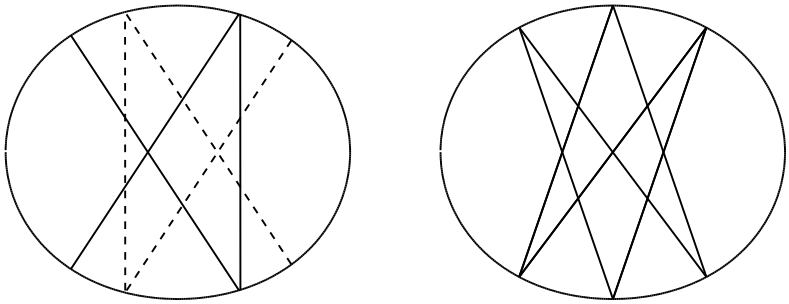

Figure A.3: Fish (stable) and the Hexagram (unstable) orbits born from the bifurcation of the stable two-bounce orbit at $\varepsilon \approx 0.0588$. Here shown at $\varepsilon = 0.08$.

for the BB, the 'Bird' and the Fish this is the case. Proof: Every periodic orbit retraces itself after N-reflections. At normal incidence the reflection will return the way it came. To fulfill the statement that every periodic orbit retraces itself after N-reflections, it needs to reflect upon itself at least another time. The maximum number of times it can reflect upon itself is two as we defined the period of an PO to have the smallest number of reflections before retracing itself.

A.1.2 Whispering gallery type orbits

Period-3 Orbits: Triangles

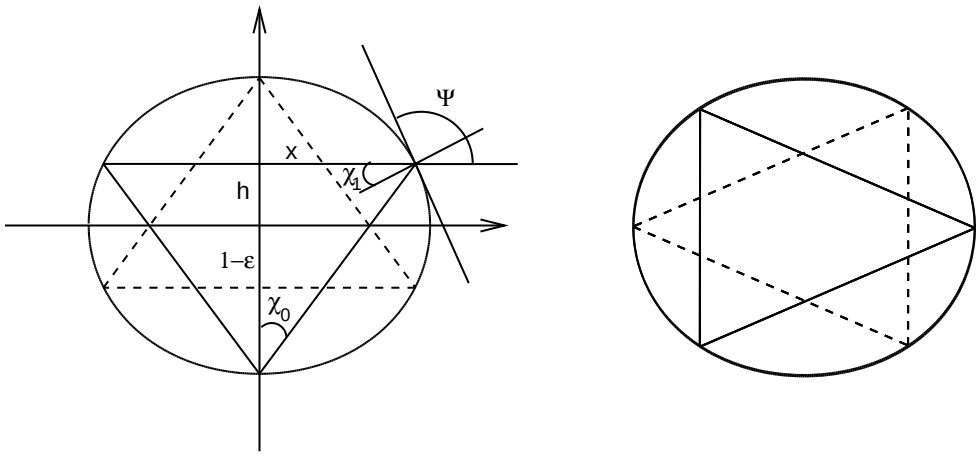

Figure A.4: Triangular PO in quadrupole with $\varepsilon = 0.07$. The left PO is stable 'Star of David', the right unstable. We note for the 'Star of David': $\Psi = \pi/2 + \chi_1$.

The period-3 triangular orbits are the shortest orbits that exist in the whispering gallery-type class. It is not born through a bifurcation, but exists already in the circle. Once $\varepsilon \neq 0$ the infinite set of triangles breaks down into a set of two orbits, stable and unstable. We can calculate the position of the 'Star of David' triangle

Table A.1: Positions of the two triangular orbits in the quadrupole with respect to deformation.

	'Star of David'		other Triangle				
ε	ϕ	$\sin\chi_1$	ϕ_o	$\sin\chi_o$	ϕ_1	$\sin\chi_1$	TrM
0.00	0.523598	0.50000	0.0	0.5000	1.0472	0.5000	2.0000
0.01	0.498268	0.49250	0.0	0.4849	1.0206	0.5075	2.0045
0.02	0.474303	0.48505	0.0	0.4697	0.9930	0.5149	2.0361
0.03	0.451751	0.47766	0.0	0.4545	0.9646	0.5223	2.1209
0.04	0.430610	0.47035	0.0	0.4394	0.9357	0.5294	2.2834
0.05	0.410835	0.46313	0.0	0.4246	0.9067	0.5364	2.5452
0.06	0.392360	0.45602	0.0	0.4103	0.8781	0.5430	2.9241
0.07	0.375103	0.44900	0.0	0.3965	0.8500	0.5493	3.4331
0.08	0.358977	0.44209	0.0	0.3833	0.8229	0.5553	4.0797
0.09	0.343895	0.43526	0.0	0.3708	0.7969	0.5609	4.8662
0.10	0.329769	0.42852	0.0	0.3591	0.7722	0.5661	5.7901
0.11	0.316521	0.42187	0.0	0.3481	0.7488	0.5709	6.8446
0.12	0.304075	0.41529	0.0	0.3377	0.7268	0.5754	8.0201
0.13	0.292362	0.40878	0.0	0.3281	0.7061	0.5796	9.3049
0.14	0.281319	0.40234	0.0	0.3191	0.6867	0.5835	10.6865
0.15	0.270890	0.39596	0.0	0.3107	0.6685	0.5871	12.1521
0.16	0.261022	0.38964	0.0	0.3028	0.6514	0.5904	13.6891
0.17	0.251671	0.38338	0.0	0.2955	0.6354	0.5935	15.2858
0.18	0.242794	0.37717	0.0	0.2886	0.6204	0.5964	16.9313
0.19	0.234354	0.37100	0.0	0.2822	0.6064	0.5991	18.6158
0.20	0.226316	0.36488	0.0	0.2762	0.5932	0.6016	20.3304

pair following Fig. A.4, where we note that

$$\cot\chi_o = \tan 2\chi_1 = \frac{(1-\varepsilon) + r\sin\phi}{r\cos\phi} \tag{A.4}$$

further the tangent at the bounce point $(\phi_o, \sin\chi_o)$ is given by

$$-\frac{dy}{dx} = \tan\Psi \quad \text{and} \quad \tan(\pi/2+\chi_1) = -\cot\chi_1 \tag{A.5}$$

thus

$$\frac{(1-\varepsilon) + r\sin\phi}{r\cos\phi} = \tan 2\chi_1 = \frac{2\tan\Psi}{\tan^2\Psi - 1} = \frac{2\frac{dy}{dx}}{\frac{dy}{dx}^2 - 1} \tag{A.6}$$

this we can solve numerically getting the positions of the bounce points with respect to the deviation shown in Tab. A.1. The triangle becomes unstable at $\varepsilon \approx 0.0978$. Where Tr$M = -2, R = 1, l/m = 1/2$, thus a period doubling bifurcation ($N \times m = 3 \times 2$) resulting in a period-6 orbit. The fixed-point becomes inversion hyperbolic. With similar calculations we can calculate the positions and stability of the other triangle (given in Tab. A.1). Note that this fixed-point is also inversion hyperbolic.

Period-4 Orbits: Diamond & Rectangle

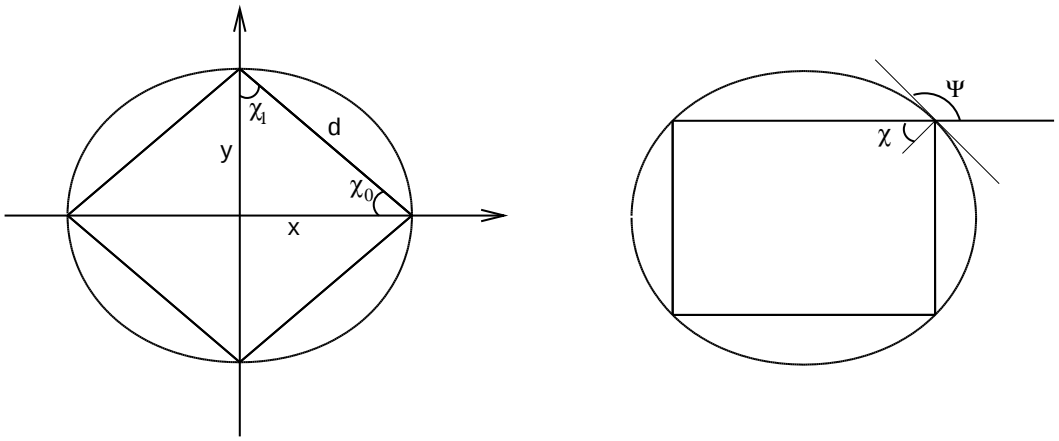

Figure A.5: Diamond and Rectangular PO in quadrupole with $\varepsilon = 0.08$. The left PO is stable, the right unstable.

The next relevant set of periodic orbits bifurcates out of the square in the circle. Upon $\varepsilon \neq 0$ they separate into the Diamond (stable) and Rectangle (unstable) (see Fig. A.5). For the 'Diamond' we note:

$$\sin\chi_o = \arctan\frac{1-\varepsilon}{1+\varepsilon}, \quad \sin\chi_1 = \arctan\frac{1+\varepsilon}{1-\varepsilon} \tag{A.7}$$

The trace of the monodromy matrix of the 'Diamond' is simply

$$\mathrm{Tr}(M) = \mathrm{Tr}(m)^2 - 4, \quad \text{with} \quad \mathrm{Tr}(m) = 4\frac{d(d-y_0-y_1)}{y_o y_1} + 2 \tag{A.8}$$

For the rectangle, finding the reflection point is not as trivial as for the diamond, though its angle of incidence is conserved with $\chi = \pi/4$, thus the tangent angle is $\Psi = 3/4\pi$ and we can write the condition for the reflection point.

$$\frac{\cos\phi}{\sin\phi}\cdot\frac{\varepsilon+1-6\varepsilon\sin^2\phi}{\varepsilon-1-6\varepsilon\cos^2\phi} = \tan\Psi = \tan\left(\frac{3}{4}\pi\right) = -1 \tag{A.9}$$

The Diamond gets unstable at $\varepsilon \approx 0.1367$ where it undergoes a simple bifurcation ($\mathrm{Tr}M = 2, R = 0, l/m = 1/1$) leading to two displaced 'Kites', the original fixed-point gets normal hyperbolic. In Tab. A.2 we calculate the reflection points and the angle of incidence for both of the PO for different deformations.

A.2 Ray-dynamics in the Spiral

The Spiral shape has attracted a lot of attention lately [17] as it lead to the first uni-directional microcavity InGaN laser. Its shape is defined as

$$r = 1 + \frac{\varepsilon}{2\pi}\phi, \quad \text{with} \qquad \phi = 0..2\pi \tag{A.10}$$

Table A.2: Positions of the two period-4 orbits in the quadrupole with respect to deformation.

	'Diamond'		Rectangle	
ε	$\sin\chi_o$	$\sin\chi_1$	ϕ_o	$\sin\chi_o$
0.00	0.7071	0.7071	0.7854	0.7071
0.01	0.7000	0.7141	0.7654	0.7071
0.02	0.6928	0.7211	0.7456	0.7071
0.03	0.6856	0.7280	0.7261	0.7071
0.04	0.6783	0.7348	0.7070	0.7071
0.05	0.6709	0.7415	0.6885	0.7071
0.06	0.6635	0.7482	0.6706	0.7071
0.07	0.6560	0.7548	0.6534	0.7071
0.08	0.6485	0.7612	0.6370	0.7071
0.09	0.6409	0.7676	0.6213	0.7071
0.10	0.6332	0.7740	0.6064	0.7071
0.11	0.6256	0.7802	0.5922	0.7071
0.12	0.6178	0.7863	0.5787	0.7071
0.13	0.6100	0.7924	0.5660	0.7071
0.14	0.6022	0.7983	0.5539	0.7071
0.15	0.5944	0.8042	0.5424	0.7071
0.16	0.5865	0.8099	0.5315	0.7071
0.17	0.5786	0.8156	0.5212	0.7071
0.18	0.5707	0.8212	0.5115	0.7071
0.19	0.5627	0.8267	0.5022	0.7071
0.20	0.5547	0.8321	0.4934	0.7071

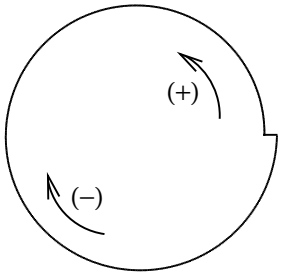

Figure A.6: spiral of deformation $\varepsilon = 0.10$

This shape is of theoretical interest as it does not obey any symmetry and is non-convex. Here we will mention just a few of its properties. We can see immediately that the radius of the spiral boundary increased constantly away from the notch. The notch has two discontinuities. As the curvature is positive everywhere the angle of incidence will increase with every refection on the same sheet $0 < \phi < 2\pi$. Lets first assume a negative sense of rotation (see Fig. A.6 for definition). The angle of incidence will increase with every reflection of the boundary, till we have almost normal incidence, and then the the rotational sense will change, still increasing $\sin\chi$ at every iteration. A jump over the notch will increase the angle of incidence even more. This can clearly be seen in Fig. A.7 where we plot the angle of incidence vs. the number of iterations. The notch is only visible for the positive sense of rotation. If we hit the notch, the sense of rotation changes sign, (and so does $\sin\chi$) and the angle of incidence continues to increase.

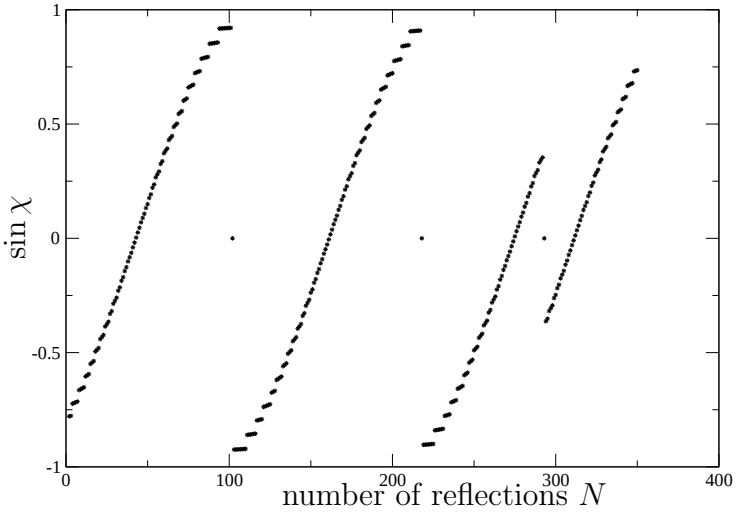

Figure A.7: $\sin\chi$ vs. the number of iterations in the spiral with $\varepsilon = 0.07$ for an initial $\sin\chi = -0.8682$ and $\phi = 2\pi - 0.008$. The constant curvature of the spiral results into a monotonic increase in the angle of incidence, so does a jump over the notch. A reflection at the notch results into a change in the rotational sense, note the refection point at the notch.

An interesting point to observe from this is that there cannot be any periodic orbits which do not have a reflection on the notch. Furthermore we state that due to the monotonic increase of the angle of incidence with every reflection, that any periodic orbit must be at least once have normal incidence on the curved boundary.

Appendix B

Geometric derivation of generalized Snell's law

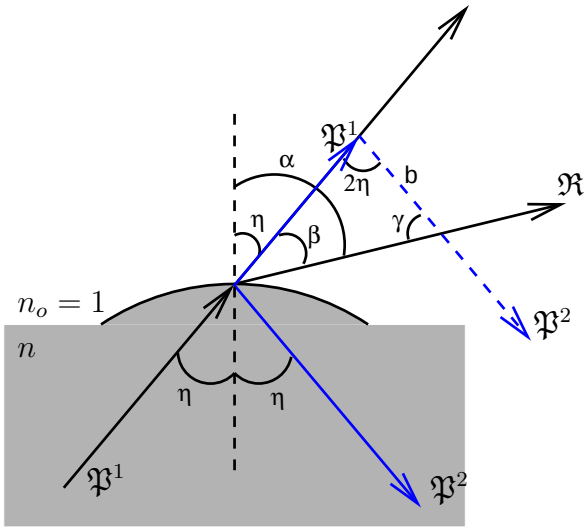

Figure B.1: Ray-picture for far-field.

We have derived in Section 2.4.1 a generalized *Snell's law*. Here we will derive this generalized Snell's law in a purely geometric fashion. An incoming ray $\mathfrak{P}^1$ with angle of incidence η gets reflected into $\mathfrak{P}^2$ and refracted into $\mathfrak{R}$. The 2-d Snell's law Eq. (3.76) gives us the angle $\alpha = \arcsin(n \sin \chi)$ in the plane of incidence. As the refracted ray lies in the plane of $\mathfrak{P}^1$ and $\mathfrak{P}^2$ we can write it as a sum of the incoming and reflected ray.

$$\mathfrak{R} = \mathfrak{P}^1 + \lambda \mathfrak{P}^2 \tag{B.1}$$

We can calculate b through the geometry of Fig. B.1.

$$b = \frac{\sin \beta}{\sin \gamma} |\mathfrak{P}^1| \tag{B.2}$$

we write further

$$\frac{\sin\beta}{\sin\gamma} = \frac{\sin(\alpha-\eta)}{\sin(\alpha+\eta)} = \frac{\sin\alpha\cos\eta - \cos\alpha\sin\eta}{\sin\alpha\cos\eta + \cos\alpha\sin\eta}, \quad \text{with} \quad \gamma = \pi - 2\eta - \beta = \pi - \eta - \alpha \tag{B.3}$$

$$= \frac{n\cos\eta - \sqrt{1-n^2\sin^2\eta}}{n\cos\eta + \sqrt{1-n^2\sin^2\eta}} = \lambda(\eta) \tag{B.4}$$

using for the far-field angle the angle of incidence and Snell's law

$$\sin\alpha = n\sin\eta \quad \text{and} \quad \cos\alpha = \sqrt{1-n^2\sin^2\eta}. \tag{B.5}$$

It is interesting to note that $\lambda(\eta)$ coincides exactly with the Fresnel reflection coefficient for the perpendicular field (r_s), i.e. E_z-field (TM-mode). We currently do not have a clear enough understanding to make intuitive sense out of this interesting fact. We can now come to our final result and write the vector of our refracted ray as

$$\mathfrak{R} = \mathfrak{P}^1 + \lambda(\eta)\frac{|\mathfrak{P}^1|}{|\mathfrak{P}^2|}\mathfrak{P}^2. \tag{B.6}$$

From this equation we can conclude that the far-field for the general 3-d ray $\mathfrak{P}^1$ does not have the same far-field directionality as its projection onto the (x, y)-plane. There we would get

$$\boldsymbol{r} = \boldsymbol{p}^1 + \lambda(\chi)\frac{|\boldsymbol{p}^1|}{|\boldsymbol{p}^2|}\boldsymbol{p}^2 \tag{B.7}$$

and as $\chi \neq \eta$ we will in general not get the same far-field direction. A usefull quantity that we can calculate with this idea is the projected farfield angle σ (See Fig. 2.3 C)):

$$\cos\sigma = \frac{\cos\chi(1-\lambda)}{\sqrt{\cos^2\chi(1-\lambda)^2 + \sin^2\chi(1+\lambda)^2}} \tag{B.8}$$

and

$$\sin\sigma = \frac{\sin\chi(1+\lambda)}{\sqrt{\cos^2\chi(1-\lambda)^2 + \sin^2\chi(1+\lambda)^2}} \tag{B.9}$$

$$= \frac{n\cos\theta\,\sin\chi}{\sqrt{1-n^2\sin^2\theta}} \tag{B.10}$$

Appendix C

Phase-shift between E_z and B_z

Just following Maxwell's equation we can derive a nice little result relating to a general phase difference between the z components of the EM field. For this we will assume that E_z has the simple phase dependence $E_z \sim \cos m\varphi$. The divergence equations states that the divergence of the electric field with no sources vanishes.

$$0 = \boldsymbol{\nabla} \cdot \boldsymbol{E} = \partial_\rho E_\rho + \frac{1}{\rho}\partial_\varphi E_\varphi + \partial_z E_z \tag{C.1}$$

Assuming a dependence $E_z \sim \cos m\varphi$ we know from linear algebra that the terms in the divergence need to be linear dependent in order to vanish. We need at least another $\sim \cos m\varphi$ to cancel the E_z component. The remaining term would then need either to be zero or linearly dependent. The ∂_ρ derivative does not change the field, but the ∂_φ does. Therefore, $E_\rho \sim \cos m\varphi$ and $E_\varphi \sim \sin m\varphi$, thus the E_φ component has a $\pi/2$ phase shift in ϕ. Now we should apply the curl theorem to determine the phase of the B_z component.

$$\boldsymbol{B} = \boldsymbol{\nabla} \times \boldsymbol{E} = \begin{pmatrix} \frac{1}{\rho}\partial_\varphi E_z - \partial_z E_\varphi \\ \partial_z E_\rho - \partial_\rho E_z \\ \partial_\rho E_\varphi - \frac{1}{\rho}\partial_\varphi E_\rho \end{pmatrix} = \begin{pmatrix} \sim \sin m\varphi \\ \sim \cos m\varphi \\ \sim \sin m\varphi \end{pmatrix} \tag{C.2}$$

From here we can conclude that the B_z and E_z are each in different symmetry classes. A similar argument can be formulated for the deformed case. As we will see in Section 4.12 they will project onto either $\cos m\varphi$ or $\sin m\varphi$. As $\sin m\varphi$ and $\cos m\varphi$ are linearly independent, we can make the above argument for every component and thus can make a statement about the symmetry class of the E_z and B_z solutions.

Appendix D

Normal and Tangential derivatives of the field

Throughout this thesis we will refer to normal and tangential derivatives. Here we will write down these derivatives explicitly. In terms of polar coordinates $(\hat{\phi}, \hat{r})$ we write the tangent and normal as

$$\hat{\boldsymbol{t}} = \frac{1}{\sqrt{r'^2 + r^2}} \left[r'(\phi)\hat{\boldsymbol{\phi}} + r(\phi)\hat{\boldsymbol{r}} \right] \qquad \hat{\boldsymbol{n}} = \frac{1}{\sqrt{r'^2 + r^2}} \left[r(\phi)\hat{\boldsymbol{\phi}} - r'(\phi)\hat{\boldsymbol{r}} \right] \tag{D.1}$$

We can write the gradient in polar coordinates as

$$\nabla_{(r,\phi)} = \frac{\partial}{\partial r}\hat{\boldsymbol{r}} + \frac{1}{r}\frac{\partial}{\partial \phi}\hat{\boldsymbol{\phi}} \tag{D.2}$$

and defining $\Gamma = \sqrt{r'^2 + r^2}$ we can now write the tangential and normal derivative as

$$\partial_t = \hat{\boldsymbol{t}} \cdot \nabla = \frac{1}{\Gamma}\left\{ r'(\phi)\frac{\partial}{\partial r} + \frac{r(\phi)}{r(\phi)}\frac{\partial}{\partial \phi} \right\} \tag{D.3}$$

$$\partial_n = \hat{\boldsymbol{n}} \cdot \nabla = \frac{1}{\Gamma}\left\{ r(\phi)\frac{\partial}{\partial r} - \frac{r'(\phi)}{r(\phi)}\frac{\partial}{\partial \phi} \right\} \tag{D.4}$$

$$\tag{D.5}$$

Appendix E

Resonance conditions in the 2-d

For completeness sake we list here the two resonance conditions for the case of separable polarizations at $k_z = 0$. Later in Chapter 7 we will be able use them for asymptotic descriptions of the resonances.

TM case

The boundary conditions for the E_z component are Eq. (2.32) and Eq. (2.35) which reduce with $k_z = 0$ to:

$$E_{z1}\Big|_{\partial D} = E_{z2}\Big|_{\partial D} \tag{E.1}$$

$$\partial_n E_{z1}\Big|_{\partial D} = \partial_n E_{z2}\Big|_{\partial D} \tag{E.2}$$

Using the ansatz Eq. (4.8) we get the system of equations

$$\begin{pmatrix} J_m & -H_m \\ \partial_\rho J_m & -\partial_\rho H_m \end{pmatrix} \begin{pmatrix} \alpha_m \\ \gamma m \end{pmatrix} = 0 \tag{E.3}$$

We thus have to ensure that the determinate of the matrix vanishes.

$$H_m \partial\rho J_m - J_m \partial\rho H_m = 0 \tag{E.4}$$

Using the relations for the Bessel-functions

$$\partial\rho J_m = n\left(J_{m-1} - \frac{m}{nkR} J_m\right) \quad \text{and} \quad \partial\rho H_m = \left(H_{m-1} - \frac{m}{kR} H_m\right) \tag{E.5}$$

We find

$$J_m H_{m-1} = n H_m J_{m-1} \tag{E.6}$$

TE case

The boundary conditions for the B_z component are Eq. (2.33) and Eq. (2.34) which reduce with $k_z = 0$ to:

$$B_{z1}\Big|_{\partial D} = B_{z2}\Big|_{\partial D} \tag{E.7}$$

$$\partial_n B_{z1}\Big|_{\partial D} = n^2 \partial_n B_{z2}\Big|_{\partial D} \tag{E.8}$$

Using the ansatz Eq. (4.8) we get the system of equations

$$\begin{pmatrix} J_m & -H_m \\ \partial_\rho J_m & -n^2 \partial_\rho H_m \end{pmatrix} \begin{pmatrix} \alpha_m \\ \gamma m \end{pmatrix} = 0 \tag{E.9}$$

We thus have to ensure that the determinate of the matrix vanishes.

$$H_m \partial\rho J_m - n^2 J_m \partial\rho H_m = 0 \tag{E.10}$$

We find using the above mentioned recursion relations for the Bessel-functions

$$J_{m-1} H_m + \frac{m}{x}\left(n - \frac{1}{n}\right) H_m J_m - n H_{m-1} J_m = 0 \tag{E.11}$$

E.1 Above Barrier expansion for the circle

Using the large argument expansion $kR \gg m$ for the Bessel functions (see Appendix G)

$$J_m \approx \sqrt{\frac{2}{\pi n k R}} \cos\left(nkR - m\frac{\pi}{2} - \frac{\pi}{4}\right) \tag{E.12}$$

$$H_m \approx \sqrt{\frac{2}{\pi k R}} \exp i\left(kR - m\frac{\pi}{2} - \frac{\pi}{4}\right) \tag{E.13}$$

we can calculate the ratio of two Bessel-functions:

$$\frac{J_{m-1}}{J_m} = -\tan\left(nkR - m\frac{\pi}{2} - \frac{\pi}{4}\right) \tag{E.14}$$

$$\frac{H_{m-1}}{H_m} = \exp\left\{i\frac{\pi}{2}\right\} = i \tag{E.15}$$

TM case

For the TM case the resonance condition Eq. (E.6) writes as

$$n\frac{J_{m-1}}{J_m} = \frac{H_{m-1}}{H_m} \tag{E.16}$$

and using the above relations yields

$$-n\tan\left(nkR - m\frac{\pi}{2} - \frac{\pi}{4}\right) = i. \tag{E.17}$$

Solving for nkR we get

$$nkR = \pi\left(\frac{m}{2} + \frac{1}{4} + j\right) + \arctan\left(-\frac{i}{n}\right). \tag{E.18}$$

With the complex relation for the arctan

$$\arctan z = -\frac{i}{2}\ln\frac{1+iz}{1-iz}, \tag{E.19}$$

we can state our final asymptotic resonance condition for the TM resonances

$$kR = \frac{\pi}{n}\left(j + \frac{m}{2} + \frac{1}{4}\right) - \frac{i}{2n}\ln\frac{n+1}{n-1} \tag{E.20}$$

TE case

For the TE case the resonance condition Eq. (E.11) writes as

$$\frac{J_{m-1}}{J_m} = \frac{m}{x}\left(n - \frac{1}{n}\right) - n\frac{H_{m-1}}{H_m} \tag{E.21}$$

using the above relation as in the TM case we get

$$\tan\left(nkR - m\frac{\pi}{2} - \frac{\pi}{4}\right) = \frac{m}{kR}\left(n - \frac{1}{n}\right) - in \tag{E.22}$$

noting that we are interested in the limit $kR \gg m$ we write

$$\begin{aligned}
kR &\approx \frac{\pi}{n}\left(j + \frac{m}{2} + \frac{1}{4}\right) - \frac{i}{2n}\ln\frac{1+n}{1-n} \\
&\approx \frac{\pi}{n}\left(j + \frac{m}{2} + \frac{1}{4}\right) - \frac{i}{2n}\ln(-1)\frac{n+1}{n-1} \\
&\approx \frac{\pi}{n}\left(j + \frac{m}{2} + \frac{1}{4}\right) - \frac{i}{2n}\left(\ln\frac{n+1}{n-1} + \ln(-1)\right) \\
&\approx \frac{\pi}{n}\left(j + \frac{m}{2} + \frac{1}{4}\right) - \frac{i}{2n}\left(\ln\frac{n+1}{n-1} + i\pi\right) \\
&\approx \frac{\pi}{n}\left(j + \frac{m}{2} + \frac{1}{4}\right) + \frac{\pi}{2n} - \frac{i}{2n}\ln\frac{n+1}{n-1}.
\end{aligned}$$

We can now stat the final asymptotic expression for the TE resonance as

$$kR \approx \frac{\pi}{n}\left(j + \frac{m+1}{2} + \frac{1}{4}\right) - \frac{i}{2n}\ln\frac{n+1}{n-1} \tag{E.23}$$

Table E.1: First twenty resonances for the TM and TE fields, given in kR. The asymptotic resonances $\widetilde{E_z}$ are given by Eq. E.20

j	$E_z(m=1,j)$	$\widetilde{E_z}(m=1,j)$	$B_z(m=1,j)$	$E_z(m=2,j)$
0	$1.4706-0.5106i$	$1.5707-0.5364i$	$2.4487-0.5806i$	$2.2835-0.4521i$
1	$3.6204-0.5310i$	$3.6651-0.5364i$	$4.6266-0.5487i$	$4.5316-0.5166i$
2	$5.7308-0.5342i$	$5.7595-0.5364i$	$6.7485-0.5422i$	$6.6829-0.5275i$
3	$7.8328-0.5352i$	$7.8539-0.5364i$	$8.8570-0.5398i$	$8.8069-0.5314i$
4	$9.9316-0.5357i$	$9.9483-0.5364i$	$10.9599-0.5386i$	$10.9194-0.5332i$
5	$12.0289-0.5359i$	$12.0427-0.5364i$	$13.0601-0.5380i$	$13.0261-0.5341i$
6	$14.1253-0.5360i$	$14.1371-0.5364i$	$15.1586-0.5376i$	$15.1293-0.5347i$
7	$16.2213-0.5361i$	$16.2315-0.5364i$	$17.2561-0.5373i$	$17.2304-0.5351i$
8	$18.3168-0.5362i$	$18.3259-0.5364i$	$19.3530-0.5371i$	$19.3300-0.5354i$
9	$20.4121-0.5362i$	$20.4203-0.5364i$	$21.4494-0.5370i$	$21.4286-0.5356i$
10	$22.5073-0.5363i$	$22.5147-0.5364i$	$23.5454-0.5369i$	$23.5265-0.5357i$
11	$24.6023-0.5363i$	$24.6091-0.5364i$	$25.6411-0.5368i$	$25.6238-0.5358i$
12	$26.6972-0.5363i$	$26.7035-0.5364i$	$27.7367-0.5368i$	$27.7206-0.5359i$
13	$28.7921-0.5363i$	$28.7979-0.5364i$	$29.8320-0.5367i$	$29.8171-0.5360i$
14	$30.8869-0.5363i$	$30.8923-0.5364i$	$31.9273-0.5367i$	$31.9134-0.5360i$
15	$32.9816-0.5364i$	$32.9867-0.5364i$	$34.0224-0.5367i$	$34.0094-0.5361i$
16	$35.0763-0.5364i$	$35.0811-0.5364i$	$36.1175-0.5366i$	$36.1052-0.5361i$
17	$37.1710-0.5364i$	$37.1755-0.5364i$	$38.2125-0.5366i$	$38.2009-0.5362i$
18	$39.2656-0.5364i$	$39.2699-0.5364i$	$40.3074-0.5366i$	$40.2964-0.5362i$
19	$41.3602-0.5364i$	$41.3643-0.5364i$	$42.4023-0.5366i$	$42.3918-0.5362i$
20	$43.4548-0.5364i$	$43.4586-0.5364i$	$44.4971-0.5366i$	$44.4871-0.5362i$

E.2 A perturbative approach for narrow width resonances in the circle

Here we will describe a perturbative approach to calculate the resonance width of long-lived states $\gamma = x + iy$, with $x, y \in \mathbb{R}$, where $|y| \ll x$. This is the region of whispering gallery modes. In this limit we can expand the Bessel functions in the resonance condition as

$$J_m(nkR) \simeq J_m(nx) + inyJ'_m(nx), \quad \text{and} \tag{E.24}$$
$$H^+_m(kR) \simeq H^+_m(x) + inyH^{+\prime}_m(x) \tag{E.25}$$

where $'$ describes the derivative with respect to the argument. When the argument is clear we will omit it in the following equations. All calculations are done here just for the TM case. Similar arguments hold for the TE case. For the TM condition Eq. (E.6) we get

$$\begin{aligned}\left\{nJ_{m-1}H^+_m - J_mH^+_{m-1}\right\} + \\ iy\left\{nJ_{m-1}H^{+\prime}_m + n^2J'_{m-1}H^+_m - J_mH^{+\prime}_{m-1} - nJ'_mH^+_{m-1}\right\} = 0\end{aligned} \tag{E.26}$$

Another perturbations can be used if we only consider a small image nary part of the index of refraction $n = n_R + in_I$ with $n_R \gg n_I$

$$J_m(nx) \simeq J_m(n_Rx) + in_IxJ'_m(n_Rx). \tag{E.27}$$

To first order in y and n_I and considering that the argument of J is only the real part of the index of refraction

$$\begin{aligned}\left[n_RJ_{m-1}H^+_m - J_mH^+_{m-1}\right] \\ +iy\left[\frac{1}{x}\Big\{J_mH^+_{m-1} - n_RJ_{m-1}H^+_m\Big\} + \Big(1 - n_R^2\Big)J_mH^+_m\right] \\ +in_I\left[\Big\{mJ_{m-1} - n_RxJ_m\Big\}H^+_m - \Big\{xJ_{m-1} - \frac{m}{n_R}J_m\Big\}H^+_{m-1}\right] = 0.\end{aligned} \tag{E.28}$$

Let us write the equations as

$$\mathcal{A}(x) + iy\mathcal{B}(x) + in_I\mathcal{C}(x) = 0 \tag{E.29}$$

where

$$\begin{aligned}\mathcal{A}(x) &= \left[n_RJ_{m-1}H^+_m - J_mH^+_{m-1}\right] \\ \mathcal{B}(x) &= \left[\frac{1}{x}\Big\{J_mH^+_{m-1} - n_RJ_{m-1}H^+_m\Big\} + \Big(1 - n_R^2\Big)J_mH^+_m\right] \\ \mathcal{C}(x) &= \left[\Big\{mJ_{m-1} - n_RxJ_m\Big\}H^+_m - \Big\{xJ_{m-1} - \frac{m}{n_R}J_m\Big\}H^+_{m-1}\right].\end{aligned}$$

We can now recognize $\mathcal{A}$ as the known resonance condition. The resonance width can be determined by

$$\begin{aligned} y &= i\frac{\mathcal{A}}{\mathcal{B}} - n_I\frac{\mathcal{C}}{\mathcal{B}} \\ &= -\left\{\frac{1}{n_R^2}\ln\frac{n_R+1}{n_R-1}\right\}\frac{J_mN_{m-1}-J_{m-1}N_m}{J_m^2+N_m^2} - n_I\frac{\mathcal{C}}{\mathcal{B}}. \end{aligned} \tag{E.30}$$

The coefficient $\mathcal{C}/\mathcal{B}$ unfortunately does not simplify nicely and we are forced to let it sit like it is.

Appendix F

Symmetry reduction in the wave-equation

Most structures in this thesis have symmetries. Here we analyse the symmetries found in the quadrupolar deformation type. We also considered quadrupole-hexadecaploar and elliptical deformations in Chapter 5. A general symmetric shape like Fig. F.1 has the following symmetries in respect to the x and y axis

$$\begin{array}{lllllll} \phi & \rightarrow & & & \phi & : & 1 \\ \phi & \rightarrow & & - & \phi & : & \sigma_x \\ \phi & \rightarrow & \pi & - & \phi & : & \sigma_y \\ \phi & \rightarrow & \phi & - & \pi & : & \sigma_{xy} \end{array} . \tag{F.1}$$

We can combine these to give us the the symmetry group

$$\{1, \sigma_x, \sigma_y, \sigma_{xy}\} \tag{F.2}$$

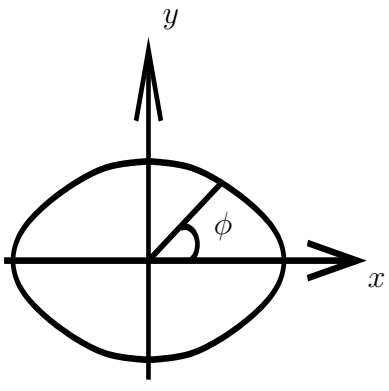

Figure F.1: Symmetric Shape

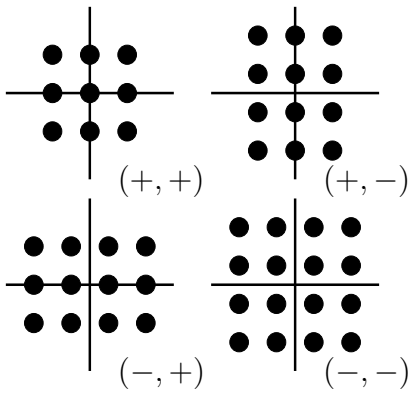

Figure F.2: Nodal appearance in the wavefunction for the four different symmetries.

namely the $C_2 \otimes C_2$ point group. We can now apply this symmetry class on the Helmholtz equation to construct symmetrized wave functions

$$\begin{array}{rclcccccl} \Psi_{++} & = & (1 & + & \sigma_y & + & \sigma_x & + & \sigma_{xy})\,\Psi \\ \Psi_{+-} & = & (1 & + & \sigma_y & + & \sigma_x & - & \sigma_{xy})\,\Psi \\ \Psi_{-+} & = & (1 & - & \sigma_y & + & \sigma_x & - & \sigma_{xy})\,\Psi \\ \Psi_{--} & = & (1 & - & \sigma_y & - & \sigma_x & + & \sigma_{xy})\,\Psi \end{array} . \tag{F.3}$$

As the Bessel functions in our Ansatz depend only on the the radius at an angle ϕ and are thus invariant under the symmetry operation

$$1r(\phi) = \sigma_x r(\phi) = \sigma_y r(\phi) = \sigma_{xy} r(\phi), \tag{F.4}$$

only the exponents are effected by the symmetry operators. We can write this out in terms of the Ψ_{++} internal wave function

$$\begin{aligned} \Psi_{++} &= \sum_{m=-\infty}^{\infty} \Big(\alpha_m H_m^+(kr) + \beta_m H_m^-(kR)\Big) \left[e^{im\phi} + e^{im(\pi-\phi)} + e^{-im\phi} + e^{im(\phi-\pi)}\right] \\ &= \sum_{m=-\infty}^{\infty} \Big(\alpha_m H_m^+(kr) + \beta_m H_m^-(kR)\Big) \left[e^{im\phi}(1+e^{-im\phi}) + e^{-im\phi}(1+e^{im\phi})\right] \\ &= \sum_{m=-\infty}^{\infty} \Big(\alpha_m H_m^+(kr) + \beta_m H_m^-(kR)\Big)\, 4 \cdot \cos m\phi \qquad \forall\, m \text{ even} \\ &= \sum_{m=0}^{\infty} \Big((\alpha_m + \alpha_{-m}) H_m^+(kr) + (\beta_m + \beta_{-m}) H_m^-(kR)\Big)\, 4 \cdot \cos m\phi \qquad \forall\, m \text{ even} \\ &= \sum_{m=0}^{\infty} \Big(\overline{\alpha}_m H_m^+(kr) + \overline{\beta}_m H_m^-(kR)\Big)\, 4 \cdot \cos m\phi \qquad \forall\, m \text{ even.} \end{aligned} \tag{F.5}$$

We see that these symmetry considerations reduced the matrix size by a factor of four! The same arguments holding for the other symmetries, gives respectively

$$\Psi_{++} = \sum_{m=0}^{\infty} \Big(\overline{\alpha}_m H_m^+(kr) + \overline{\beta}_m H_m^-(kr)\Big)\, 4 \cdot \cos m\phi \qquad \forall \quad m \text{ even} \tag{F.6}$$

$$\Psi_{+-} = \sum_{m=0}^{\infty} \Big(\overline{\alpha}_m H_m^+(kr) + \overline{\beta}_m H_m^-(kr)\Big)\, 4i \cdot \sin m\phi \qquad \forall \quad m \text{ odd} \tag{F.7}$$

$$\Psi_{-+} = \sum_{m=0}^{\infty} \Big(\overline{\alpha}_m H_m^+(kr) + \overline{\beta}_m H_m^-(kr)\Big)\, 4 \cdot \cos m\phi \qquad \forall \quad m \text{ odd} \tag{F.8}$$

$$\Psi_{--} = \sum_{m=1}^{\infty} \Big(\overline{\alpha}_m H_m^+(kr) + \overline{\beta}_m H_m^-(kR)\Big)\, 4i \cdot \sin m\phi \qquad \forall \quad m \text{ even} \tag{F.9}$$

These Ansätze together with the boundary conditions can be written as a generalized eigenvalue problem with a block matrix size of $(N+1) \times (N+1)$, compared to the

$(2N+1) \times (2N+1)$ size in the non symmetry reduced problem. We have not only noticed a huge speed increase for the calculation, but also an increase in numerical stability. The effect of the symmetry can easily be seen at a wavefunction plot, when we compare the nodal structure. In Fig. 4.16 we have related the nodal structure of the real space wave function to our definition of the symmetries for the convenience of the reader.

Appendix G

Bessel function relations

Bessel functions whether we like them or not show up throughout this thesis. This collection of identities have been usefull, and will be used throughout the thesis.

G.1 Definition of Hankel function

The Hankelfunction can be defined as the sum of the Besselfunction of the first kind J_m and the Neuman function N_m (sometimes given as Y_m)

$$H_m^{\pm} = J_m \pm iN_m \tag{G.1}$$

from this follows the relation that we will use

$$H_m^{+} + H_m^{-} = (J_m + iN_m) + (J_m - iN_m) = 2J_m. \tag{G.2}$$

G.2 Recursion relation for Bessel functions

The follwoing is true for of $J_m(x), H_m^{\pm}(x), N_m(x)$

$$\frac{2m}{x}Q_m(x) = Q_{m-1}(x) + Q_{m+1}(x) \tag{G.3}$$

$$2\frac{d}{dx}Q_m(x) = Q_{m-1}(x) - Q_{m+1}(x) \tag{G.4}$$

where Q can be either of J, H, N

G.3 Derivative relation for Bessel functions

The derivative of $J_m(x), H_m^{\pm}(x), N_m(x)$ is given by

$$\frac{d}{dx}Q_m(x) = Q_{m-1}(x) - \frac{m}{x}Q_m(x) \tag{G.5}$$

$$\frac{d}{dx}Q_m(x) = \frac{m}{x}Q_m(x) - Q_{m+1}(x) \tag{G.6}$$

$$\tag{G.7}$$

where Q can be either of J, H, N

G.3.1 $J_m\partial_\rho H_m$ and $H_m\partial_\rho J_m$

These two forms show up all the time in the resonance conditions here we give them in with the recursion relations:

$$J_m(\gamma_1 x)\partial_\rho H_m(\gamma_2 x) = \gamma_2 J_m(\gamma_1 x)\left[H_{m-1}(\gamma_2 x) - \frac{m}{\gamma_2}H_m(\gamma_2 x)\right] \tag{G.8}$$

$$H_m(\gamma_2 x)\partial_\rho J_m(\gamma_1 x) = \gamma_1 H_m(\gamma_2 x)\left[J_{m-1}(\gamma_1 x) - \frac{m}{\gamma_1}J_m(\gamma_1 x)\right] \tag{G.9}$$

$$\tag{G.10}$$

G.4 Large argument expansion $x \gg m$

Using the large argument expansion $x \gg m$ for the Bessel functions:

$$J_m \approx \sqrt{\frac{2}{\pi x}}\cos\left(x - m\frac{\pi}{2} - \frac{\pi}{4}\right) \tag{G.11}$$

$$H_m \approx \sqrt{\frac{2}{\pi x}}\exp i\left(x - m\frac{\pi}{2} - \frac{\pi}{4}\right) \tag{G.12}$$

we can calculate the ratio of two Bessel-functions:

$$\frac{J_{m-1}}{J_m} = -\tan\left(x - m\frac{\pi}{2} - \frac{\pi}{4}\right) \tag{G.13}$$

$$\frac{H_{m-1}}{H_m} = \exp\left\{i\frac{\pi}{2}\right\} = i \tag{G.14}$$

Bibliography

[1] H. E. Tureci, H. G. L. Schwefel, Ph. Jacquod, and A. Douglas Stone. Modes of wave-chaotic dielectric resonators. to be published Progress in Optics, 2005.

[2] Harald G. L. Schwefel, Nathan B. Rex, Hakan E. Tureci, Richard K. Chang, A. Douglas Stone, Tahar Ben-Messaoud, and Joseph Zyss. Dramatic shape sensitivity of directional emission patterns from similarly deformed cylindrical polymer lasers. *J. Opt. Soc. Am. B*, 21:923–934, 2004.

[3] N. B. Rex, H. E. Tureci, H. G. L. Schwefel, R. K. Chang, and A. D. Stone. Fresnel filtering in lasing emission from scarred modes of wave-chaotic optical resonators. *Phys. Rev. Lett.*, 88:art. no. 094102, 2002.

[4] J. P. Reithmaier. SEM of a VCSEL. `http://opto.physik.-uni-wuerzburg.de`, 2004. Optoelectronic Device Group; Julius-Maximilians-Universität, Würzburg.

[5] CMPL. SEM of edge-emitting laser. `http://www.nip.upd.edu.ph/cmpl/-index.html`, 2004.

[6] A. F. J. Levi. SEM of a microdisks laser. `http://www.usc.edu/alevi`, 2004.

[7] R. Seaman. Whispering Gallery in St. Pauls cathedral London. `http://www.richard-seaman.com/`, 2004.

[8] C. Gmachl, F. Capasso, E. E. Narimanov, J. U. Nöckel, A. D. Stone, J. Faist, D. L. Sivco, and A. Y. Cho. High-power directional emission from microlasers with chaotic resonators. *Science*, 280:1556–1564, 1998.

[9] R. H. G. Helleman. Self generated chaotic behavior in nonlinear mechanics. In E. G. D. Cohen, editor, *Fundamental Problems in Statistical Mechanics V*, pages 165–233. North-Holland Publ. Comp., 1980.

[10] A. W. Poon, R. K. Chang, and J. A. Lock. Spiral morphology-dependent resonances in an optical fiber: Effects of fiber tilt and focused Gaussian beam illumination. *Opt. Lett.*, 23:1105–1107, 1998.

[11] J. U. Nöckel. *Resonances in nonintegrable open systems*. PhD thesis, Yale University, New Haven, USA, 1997.

[12] J. U. Nöckel, A. D. Stone, and R. K. Chang. q-spoiling and directionality in deformed ring cavities. *Opt. Lett.*, 19:1693–1695, 1994.

[13] J. U. Nöckel, A. D. Stone, G. Chen, H. L. Grossman, and R. K. Chang. Directional emission from asymmetric resonant cavities. *Opt. Lett.*, 21:1609–1611, 1996.

[14] J. U. Nöckel and A. D. Stone. Ray and wave chaos in asymmetric resonant optical cavities. *Nature*, 385:45–47, 1997.

[15] R. K. Chang and A. K. Campillo, editors. *Optical Processes in Microcavities*. World Scientific, Singapore, 1996.

[16] H. G. L. Schwefel, H. E. Tureci, A. Douglas Stone, and R. K. Chang. Progress in asymmetric resonant cavities: Using shape as a design parameter in dielectric microcavity lasers. In K. J. Vahala, editor, *Optical Processes*. World Scientific, 2004.

[17] G. D. Chern, H. E. Tureci, A. D. Stone, R. K. Chang, M. Kneissl, and N. M. Johnson. Unidirectional lasing from InGaN multiple-quantum-well spiral-shaped micropillars. *Appl. Phys. Lett.*, 83:1710–1712, 2003.

[18] H. Soda, K. Iga, C. Kitahara, and Y. Suematsu. GaInAsP/InP surface emitting injection lasers. *Jpn. J. Appl. Phys*, 18:2329–2330, 1979.

[19] B. R. Johnson. Theory of morphology-dependent resonances – shape resonances and width formulas. *J. Opt. Soc. Am. A.*, 10:343–352, 1993.

[20] Lord Rayleigh. On waves propagated along the plane surface of an elastic solid. *Proc. Lond. Math. Soc.*, 17:4–11, 1885.

[21] Lord Rayleigh. *The problem of the whispering gallery*, pages 617–620. Cambridge University, Cambridge, UK, 1912.

[22] G. Chen, R. K. Chang, S. C. Hill, and P. W. Barber. Frequency splitting of degenerate spherical cavity modes – stimulated Raman-scattering spectrum of deformed droplets. *Opt. Lett.*, 16:1269–1271, 1991.

[23] G. Chen, M. M. Mazumder, Y. R. Chemla, A. Serpenguzel, R. K. Chang, and S. C. Hill. Wavelength variation of laser-emission along the entire rim of slightly deformed microdroplets. *Opt. Lett.*, 18:1993–1995, 1993.

[24] S. L. McCall, A. F. J. Levi, R. E. Slusher, S. J. Pearton, and R. A. Logan. Whispering-gallery mode microdisk lasers. *Appl. Phys. Lett.*, 60:289–291, 1992.

[25] R. E. Slusher, A. F. J. Levi, U. Mohideen, S. L. McCall, S. J. Pearton, and R. A. Logan. Threshold characteristics of semiconductor microdisk lasers. *Appl. Phys. Lett.*, 63:1310–1312, 1993.

[26] A. F. J. Levi, R. E. Slusher, S. L. McCall, T. Tanbunek, D. L. Coblentz, and S. J. Pearton. Electrically pumped, room-temperature microdisk semiconductorlasers with submilliampere threshold currents. *IEEE Trans. Electron Devices*, 39:2651–2651, 1992.

[27] B. E. Little, J. S. Foresi, G. Steinmeyer, E. R. Thoen, S. T. Chu, H. A. Haus, E. P. Ippen, L. C. Kimerling, and W. Greene. Ultra-compact Si-SiO_2 microring resonator optical channel dropping filters. *IEEE Photonics Technol. Lett.*, 10:549–551, 1998.

[28] Y. Yamamoto and R. E. Slusher. Optical processes in microcavities. *Phys. Today*, 46:66–73, 1993.

[29] B.E. Little, S.T. Chu, H.A. Haus, J. Foresi, and J.-P. Laine. Microring resonator channel dropping filters. *Lightwave Technology, Journal of*, 15:998–1005, 1997.

[30] A. F. J. Levi, R. E. Slusher, S. L. McCall, J. L. Glass, S. J. Pearton, and R. A. Logan. Directional light coupling from microdisk lasers. *Appl. Phys. Lett.*, 62:561–563, 1993.

[31] D. Y. Chu, M. K. Chin, W. G. Bi, H. Q. Hou, C. W. Tu, and S. T. Ho. Double-disk structure for output coupling in microdisk lasers. *Appl. Phys. Lett.*, 65:3167–3169, 1994.

[32] C. Gmachl, E. E. Narimanov, F. Capasso, J. N. Baillargeon, and A. Y. Cho. Kolmogorov-Arnold-Moser transition and laser action on scar modes in semiconductor diode lasers with deformed resonators. *Opt. Lett.*, 27:824–826, 2002.

[33] K. M. Lee, P. T. Leung, and K. M. Pang. Iterative perturbation scheme for morphology-dependent resonances in dielectric spheres. *J. Opt. Soc. Am. A-Opt. Image Sci. Vis.*, 15:1383–1393, 1998.

[34] H. M. Lai, P. T. Leung, K. Young, P. W. Barber, and S. C. Hill. Time-independent perturbation for leaking electromagnetic modes in open systems with application to resonances in microdroplets. *Phys. Rev. A.*, 41:5187–5198, 1990.

[35] E. B. Becker, G. F. Carey, and J. T. Oden. *Finite Elements*. Pentice-Hall, KEnglewood Cliffs, N.J., 1981.

[36] J. B. Davies. Finite element analysis of waveguides and cavities – a review. *IEEE Transactions on Magnetics*, 29:1578, 1993.

[37] C. A. Brebbia, editor. *Progress in Boundary Element Methods*. Halstead Press, 1981.

[38] M. V. Berry. Quantizing a classically ergodic system – Sinai billiard and the KKR method. *Ann. Phys.*, 131:163–216, 1981.

[39] J. Wiersig. Boundary element method for resonances in dielectric microcavities. *J. Opt. Soc. Am. A*, 5:53–60, 2003.

[40] S. D. Frischat and E. Doron. Quantum phase-space structures in classically mixed systems: A scattering approach. *J. Phys. A-Math. Gen.*, 30:3613–3634, 1997.

[41] G. D. Birkhoff. On the periodic motion of dynamical systems. *Acta Math.*, 50:359–379, 1927.

[42] M. V. Berry. Regularity and chaos in classical mechanics, illustrated by three deformations of a circular billiard. *Eur. J. Phys.*, 2:91–102, 1981.

[43] V. I. Arnold. *Mathematical methods of classical mechanics*. Springer, New York, USA, 1989.

[44] V. F. Lazutkin. *KAM theory and semiclassical approximations to eigenfunctions*. Springer, New York, USA, 1993.

[45] M. Robnik and M. V. Berry. Classical billiards in magnetic-fields. *J. Phys. A-Math. Gen.*, 18:1361–1378, 1985.

[46] A. Mekis, J. U. Nöckel, G. Chen, A. D. Stone, and R. K. Chang. Ray chaos and Q-spoiling in lasing droplets. *Phys. Rev. Lett.*, 75:2682–2685, 1995.

[47] S. Chang, R. K. Chang, A. D. Stone, and J. U. Nöckel. Observation of emission from chaotic lasing modes in deformed microspheres: Displacement by the stable-orbit modes. *J. Opt. Soc. Am. B-Opt. Phys.*, 17:1828–1834, 2000.

[48] A. Dodabalapur, E. A. Chandross, M. Berggren, and R. E. Slusher. Applied physics – organic solid-state lasers: Past and future. *Science*, 277:1787–1788, 1997.

[49] Z. Bao, J. A. Rogers, A. Dodabalapur, A. J. Lovinger, H. E. Katz, V. R. Raju, Z. Peng, and M. E. Galvin. Polymer light emitting diodes: new materials and devices. *Opt. Mater.*, 12:177–182, 1999.

[50] L. Collot, V. Lefevreseguin, M. Brune, J. M. Raimond, and S. Haroche. Very high-Q whispering-gallery mode resonances observed on fused-silica microspheres. *Europhys. Lett.*, 23:327–334, 1993.

[51] F. Treussart, N. Dubreuil, J. C. Knight, V. Sandoghdar, J. Hare, V. Lefevre-Seguin, J. M. Raimond, and S. Haroche. Microlasers based on silica microspheres. *Ann. Telecommun.-Ann Telecommun.*, 52:557–568, 1997.

[52] S. X. Qian, J. B. Snow, H. M. Tzeng, and R. K. Chang. Lasing droplets – highlighting the liquid-air interface by laser-emission. *Science*, 231:486–488, 1986.

[53] S. X. Qian and R. K. Chang. Multiorder stokes emission from micrometer-size droplets. *Phys. Rev. Lett.*, 56:926–929, 1986.

[54] M. M. Mazumder, G. Chen, R. K. Chang, and J. B. Gillespie. Wavelength shifts of dye lasing in microdroplets – effect of absorption change. *Opt. Lett.*, 20:878–880, 1995.

[55] J. Popp, M. H. Fields, and R. K. Chang. Injection seeding of lasing in microdroplets. *Opt. Lett.*, 22:139–141, 1997.

[56] S. S. Chang, N. B. Rex, and R. K. Chang. Chemical lasing in pendant droplets: lasing-spectra, emissionpattern, and cavity-lifetime measurements. *J. Opt. Soc. Am. B-Opt. Phys.*, 16:1224–1235, 1999.

[57] E. J. Heller. *Wavepacket dynamics and quantum chaology*, pages 547–663. North Holland, Amsterdam, 1989.

[58] K. Husimi. Some formal properties of the density matrix. *Proc. Phys. Math. Soc. Jpn.*, 22:264–314, 1940.

[59] N. B. Rex. *Regular and chaotic orbit Gallium Nitride microcavity lasers*. PhD thesis, Yale University, New Haven, USA, 2001.

[60] Takanori Okoshi. *Optical fibers*. Academic Press, Inc., London, 1982.

[61] Jeff Hecht. *Understanding fiber optics*. Prentice-Hall, Upper Saddle River, New Jersey, 2002.

[62] J. D. Jackson. *Classical electrodynamics*. John Wiley & Sons, Inc., New York, USA, 1998.

[63] B. Cowan. Dealing with cylindrical structures. Technical Report ARDB328, Stanford Linear Accelerator Center – Accelerator Research Department B, 2003.

[64] A. Sommerfeld and J. Runge. Anwendung der Vektorrechnung auf die Grundlagen der geometrischen Optik. *Annalen der Physik*, 35:277–298, 1911.

[65] M. Born and E. Wolf. *Principles of Optics*. Cambridge University Press, Cambridge, UK, 1980.

[66] Hakan E. Türeci. *Wave chaos in dielectric resonators: Asymptotic and numerical approaches*. PhD thesis, Yale University, New Haven, USA, 2003.

[67] A. Einstein. Zum Quantensatz von Sommerfeld und Epstein. *Verhandl. Deut. Physik. Ges.*, 19:82–92, 1917.

[68] L. Brillouin. Remarques sur la mécanique ondulatoire. *Le Journal de Physique et le Radium*, 12:353–368, 1926.

[69] J. B. Keller. Corrected Bohr-Sommerfeld quantum conditions for nonseparable systems. *Ann. Phys.*, 4:180–188, 1958.

[70] W. Nolting. *Elektrodynamik*. Vieweg & Sohn, Braunschweig, Germany, 1997.

[71] M. V. Berry. Regular and irregular motion. *Am. Inst. Phys. Conf. Proc.*, 46:16–120, 1977.

[72] W. Nolting. *Analytische Mechanik*. Vieweg & Sohn, Braunschweig, Germany, 1998.

[73] A. N. Kolmogorov. On the conservation of conditionally periodic motions for a small change in Hamilton's function. *Dokl. Akad. Nauk. SSSR*, 98:527, 1954.

[74] V. I. Arnol'd. Proof of a theorem of A. N. Kolmogorov on the invariance of quasi-periodic motions under small perturbations of the Hamiltonian. *Russ. Math. Surv.*, 18, No. 6:85–192, 1963.

[75] J. Moser. On the theory of quasiperiodic motions. *SIAM Review*, 8:145–172, 1966.

[76] H. Poincaré. Sur le problème des trois corps et les équations de la dynamique. *Acta Math.*, 13:67, 1890.

[77] S. Smale. Differentiable dynamical systems. *Bull. Amer. Math. Soc.*, 73:747–817, 1967.

[78] Edoh Y. Amiran. Integrable smooth planar billiards and evolutes. *New York J. Math.*, 3:32–47, 1997.

[79] J. U. Nöckel. Angular momentum localization in oval billiards. *Phys. Scr.*, T90:263–267, 2001.

[80] R. Douady. *Applications du theorémè des tores invariants*. PhD thesis, Université Paris VII, 1982.

[81] J. M. Greene. Two-dimensional measure-preserving mappings. *Journal of Mathematical Physics*, 9(5):760–768, 1968.

[82] J. M. Greene, R. S. MacKay, F. Vivaldi, and M. J. Feigenbaum. Universal behaviour in families of area-preserving maps. *Physica D*, 3(3):468–486, 1981.

[83] K. R. Meyer. Generic bifurcation of periodic points. *Trans. Am. Math. Soc.*, 149:95–&, 1970.

[84] J.-M. Mao and J. B. Delos. Hamiltonian bifurcation theory of closed orbits in the diamagnetic Kepler problem. *Phys. Rev. A.*, 45(3):1746, 1991.

[85] A. E. Siegman. *Lasers.* University Science Books, Mill Valley, California, 1986.

[86] SLATEC. SLATEC Common Mathematical Library (Version 4.1), July 1993. `http://www.netlib.org/slatec/`.

[87] Lord Rayleigh. On the dynamical theory of gratings. *Proc. Roy. Soc.*, A79:399–416, 1907.

[88] P. M. van den Berg and J. T. Fokkema. The rayleigh hypothesis in the theory of diffraction by a perturbation in a plane surface. *Radio Sci.*, 15:723–732, 1980.

[89] E. Doron and U. Smilansky. Semiclassical quantization of chaotic billiards – a scatteringtheory approach. *Nonlinearity*, 5:1055–1084, 1992.

[90] B. Dietz, J. P. Eckmann, C. A. Pillet, U. Smilansky, and I. Ussishkin. Inside-outside duality for planar billiards – a numerical study. *Phys. Rev. E.*, 51:4222–4231, 1995.

[91] E. Anderson, Z. Bai, C. Bischof, S. Blackford, J. Demmel, J. Dongarra, J. Du Croz, A. Greenbaum, S. Hammarling, A. McKenney, and D. Sorensen. *LAPACK Users' Guide.* Society for Industrial and Applied Mathematics, Philadelphia, PA, third edition, 1999.

[92] N. B. Rex, R. K. Chang, and L. J. Guido. Threshold lowering in GaN micropillar lasers by means of spatially selective optical pumping. *IEEE Photonics Technol. Lett.*, 13:1–3, 2001.

[93] H. E. Tureci, H. G. L. Schwefel, A. D. Stone, and E. E. Narimanov. Gaussian-optical approach to stable periodic orbit resonances of partially chaotic dielectric micro-cavities. *Opt. Express*, 10:752–776, 2002.

[94] E. J. Heller. Scars and other weak localization effects in classically chaotic systems. *Phys. Scr.*, T90:154–161, 2001.

[95] E. J. Heller. Bound-state eigenfunctions of classically chaotic Hamiltonian systems – scars of periodic-orbits. *Phys. Rev. Lett.*, 53:1515–1518, 1984.

[96] P. M. Morse and H. Feshbach. *Methods of Theoretical Physics, Part I and II, Section 2.3, "Motion of Fluids".* McGraw-Hill, New York, NY, USA, 1953.

[97] J. U. Nöckel and A. D. Stone. *Chaotic Light: a theory of asymmetric cavity resonators*, chapter 11, pages 389–426. World Scientific, Singapore, 1996.

[98] S. Lacey, H. Wang, D. H. Foster, and J. U. Nöckel. Directional tunnel escape from nearly spherical optical resonators. *Phys. Rev. Lett.*, 91:033902, 2003.

[99] S. Chang, N. B. Rex, R. K. Chang, G. B. Chong, and L. J. Guido. Erratum: Stimulated emission and lasing in whispering gallery modes of GaN microdisk cavities (vol 75, pg 166, 1999). *Appl. Phys. Lett.*, 75:3719–3719, 1999.

[100] M. Hentschel and H. Schomerus. Fresnel laws at curved dielectric interfaces of microresonators. *Phys. Rev. E.*, 65:art. no.–045603, 2002.

[101] J. B. Keller and S. I. Rubinow. Asymptotic solution of eigenvalue problems. *Ann. Phys.*, 9:24–75, 1960.

[102] V. M. Babič and V. S. Buldyrev. *Asymptotic Methods in Shortwave Diffraction Problems*. Springer, New York, USA, 1991.

[103] C. M. Bender and S. A. Orszag. *Advanced mathematical methods for scientists and engineers*. Springer, New York, USA, 1999.

[104] J. Kevorkian and J. D. Cole. *Multiple scales and singular perturbation methods*. Springer, New York, USA, 1996.

[105] V. P. Maslov and M. V. Fedoriuk. *Semi-Classical Approximation in Quantum Mechanics*. Reidel, Boston, USA, 1981.

[106] R. C. Jones. A new calculus for the treatment of optical systems. I. description and discussion of the calculus. *J. Opt. Soc. Am.*, 31:488–493, 1941.

[107] J. Burm. Properties, processiong, and applications of gallium nitride and related semiconductors. In J. H. Edgar, S. Strite, I. Akasaki, H. Amano, and C. Wetzel, editors, *Properties, Processiong, and Applications of Gallium Nitride and Related Semiconductors*, page 5690. INSPEC, London, UK, 1999.

[108] J. W. Goodman. *Introduction to Fourier Optics*. Mc Graw-Hill, New York, USA, 1996.

[109] J. H. McLeod. The axicon – a new type of optical element. *Journal Of The Optical Society Of America*, 44:592–597, 1954.

[110] J. H. McLeod. Axicons and their uses. *Journal Of The Optical Society Of America*, 50:166–169, 1960.

[111] M. Rioux, R. Tremblay, and P. A. Belanger. Linear, annular, and radial focusing with axicons and applications to laser machining. *Applied Optics*, 17:1532–1536, 1978.

[112] R. B. Barber. Laser optical apparatus for cutting holes. United States Patent 3,419,321, December 1968.

[113] H. E. Tureci and A. D. Stone. Deviation from snell's law for beams transmitted near the critical angle: application to microcavity lasers. *Opt. Lett.*, 27:7–9, 2002.

[114] A. E. Siegman. Laser beams and resonators: The 1960s. *IEEE J. Sel. Top. Quantum Electron.*, 6:1380–1388, 2000.

[115] A. E. Siegman. Laser beams and resonators: Beyond the 1960s. *IEEE J. Sel. Top. Quantum Electron.*, 6:1389–1399, 2000.

Index